

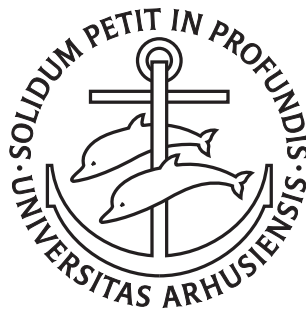
---

# Investigating decadal- to millennial-scale solar variability based on instrumental observations and cosmogenic nuclides

Fadil Inceoglu

---

PhD Dissertation



Department of Physics and Astronomy  
Aarhus University  
Denmark



Investigating decadal- to millennial-scale  
solar variability based on  
instrumental observations  
and cosmogenic nuclides

A Dissertation  
Presented to the Faculty of Science and Technology  
of Aarhus University  
for the PhD Degree

by  
Fadil Inceoglu  
October 31, 2014



# Abstract

On Earth, we live in close proximity to an active and variable star - the Sun. The Sun is not only the main energy source for the Earth's climate system, it also protects us from harmful galactic cosmic rays. A better understanding of changes in solar activity over time and underlying physical mechanisms will provide a much better understanding of what drives changes in solar radiation and how these changes affect the Earth's climate.

During my PhD project I have studied changes in solar activity over different time scales based on observations of the solar photosphere, the Sun's magnetic field, the presence of neutrons in the Earth's atmosphere, sunspots and cosmogenic isotopes, such as  $^{10}\text{Be}$  in ice cores and  $^{14}\text{C}$  in tree rings. The cosmogenic isotopes can be used to reconstruct changes in solar activity over the last centuries and millennia. Another important aspect of my PhD has been to produce new  $^{10}\text{Be}$  data based on material from an ice core in order to study the Sun's influence on the production of  $^{10}\text{Be}$ .

The first part of my PhD project focused on the study of the relationship between the amount of neutrons in the atmosphere, which is an indicator of the flow of cosmic particles from space, and the number of sunspots based on the hysteresis effect. This study resulted in a new empirical model which I then used to reconstruct the detailed changes in the number of sunspots over the last six centuries. During this time I was also involved in a study of "missing" solar cycle (4b) - a solar cycle apparently failed to appear or disappear around the year 1820.

In an effort to increase our understanding of phenomena such as solar maxima and solar minima - periods when solar activity is abnormally high and low, respectively - I analysed the available  $^{14}\text{C}$  data from tree rings (IntCal13) and  $^{10}\text{Be}$  data from the Greenland GRIP ice core over the last 8250 years, which is the period where the two datasets overlap in time. The use of two different cosmogenic isotopes with different geochemical characteristics made it possible to identify the solar maxima and solar minima back in time with high accuracy and reliability. The new knowledge made it possible subsequently to compare past solar maxima and solar minima of solar activity over the last decades. This comparison shows that the Sun probably is in the initial phase of a solar minimum and solar activity can therefore be expected to fall in the coming decades.

My study of an ice core from Mongolia resulted in the first continuous  $^{10}\text{Be}$  data sets from mid-latitudes, which has contributed a new perspective on our understanding of the link between the presence of  $^{10}\text{Be}$  in ice cores, solar variability and regional climate processes. Overall, my PhD project contributed to an increased understanding of how solar activity has varied over the decades, centuries and millennia, which provides better foundation to study the Sun's influence on Earth's climate.



# Resumé

Her på Jorden lever vi i nærheden af en aktiv og meget dynamisk stjerne - Solen. Solen er ikke kun den dominerende energikilde for Jordens klimasystem, den beskytter os også mod den strøm af skadelige partikler fra rummet der konstant bombarderer Jorden. En bedre forståelse af ændringer i solens aktivitetsniveau gennem tiden, og de bagvedliggende fysiske mekanismer, vil give en meget bedre forståelse af hvad der driver ændringer i Solens udstråling og hvorledes disse ændringer påvirker Jordens klima.

Under mit PhD-projekt har jeg studeret ændringer i Solens aktivitet over forskellige tidsskalaer baseret på observationer af Solens fotosfære, Solens magnetfelt, forekomsten af neutroner i Jordens atmosfære, solpletter og kosmogene isotoper, såsom  $^{10}\text{Be}$  i iskerner og  $^{14}\text{C}$  i træringe. De kosmogene isotoper kan bruges til at rekonstruere ændringer i solens aktivitet over de sidste århundreder og årtusinder. Et andet væsentligt aspekt af min PhD har bestået i at frembringe nye  $^{10}\text{Be}$  data baseret på materiale fra en iskerne med henblik på det studere Solens indflydelse på produktionen af  $^{10}\text{Be}$ .

Den første del af mit PhD-projekt fokuserede på studier af sammenhængen mellem mængden af neutroner i atmosfæren, hvilket er en indikator for strømmen af kosmiske partikler fra rummet, og antallet af solpletter baseret på hysterese-effekten. Dette studie resulterede i en ny empirisk model som jeg efterfølgende anvendte til at rekonstruere detaljerede ændringer i antallet af solpletter over de sidste 6 århundreder. Under dette forløb var jeg også involveret i et studie af "den forsvundne" sol-cyklus (4B) – en sol-cyklus der tilsyneladende udeblev eller forsvandt omkring år 1820.

I bestræbelserne op at øge vores forståelse af fænomener som sol-maksima og sol-minima - erioder hvor Solens aktivitet er hhv. unormalt høj og lav - analyserede jeg de tilgængelige  $^{14}\text{C}$  data fra træringe (IntCal13) og  $^{10}\text{Be}$  data fra den grønlandske GRIP-iskerne over de sidste 8250 år, hvilket er den periode hvor de to datasæt overlapper hinanden tidsmæssigt. Brugen af to forskellige kosmogene isotoper, med vidt forskellige geokemiske egenskaber, gjorde det muligt at identificere forekomsten af sol-maksima og sol-minima tilbage i tid med høj nøjagtighed og troværdighed. Den nye viden gjorde det efterfølgende muligt at sammenligne fortidens sol-maksima og sol-minima med Solens aktivitet over de sidste årtier. Denne sammenligning viser, at Solen sandsynligvis befinder sig i den indledende fase af et sol-minimum og at sol-aktiviteten derfor kan forventes at falde de kommende årtier.

Mit studie af en iskerne fra Mongoliet resulterede i det første kontinuerlige  $^{10}\text{Be}$  datasæt udenfor Arktis og Antarktis, hvilket har bidraget med et nyt perspektiv på vores forståelse af sammenhængen mellem forekomsten af  $^{10}\text{Be}$  i iskerner, Solens variabilitet og regionale klimaprocesser. Overordnet set har mit PhD-projekt bidraget med en øget forståelse af hvorledes Solens aktivitet har varieret over årtier, århundreder og årtusinder, hvilket giver bedre fundament for at studere Solens indflydelse på Jordens klima.



# Acknowledgments

I would like to start by expressing my thanks to my PhD supervisors, Mads Faurschou Knudsen, Jesper Olsen, Christoffer Karoff and Jan Heinemeier, who have been amazing sources of support and knowledge in different scientific fields, and who were always available for great scientific discussions during the course of my PhD research. I also thank Rosaria Simoniello of Laboratoire AIM, CEA/DSM-CNRS-Université Paris Diderot, IRFU/SAP, Centre de Saclay, who has been an invaluable help by providing me with useful advice, feedback, and knowledge on the solar dynamo mechanisms. I really look forward to continue to work together with her on the solar dynamo processes and models, and magnetic cycles observed in sun-like stars in the future. I also would like to thank Margit Schwikowski and Pierre-Alain Herren for providing me the Tsambagarav ice core samples, and being very patient with me during my stay at the Paul Scherrer Institute, Switzerland. Also, I thank Ann-Marie Berggren and Anna Sturevik Storm of Uppsala University for helping me with the  $^{10}\text{Be}$  chemistry during my stay in Uppsala, Sweden.

Funding for this PhD research project was provided jointly by the Aarhus University Graduate School of Science and Technology (GSST) and the Stellar Astrophysics Center and the Villum Foundation.

Finally, I thank my amazing family Hulya Okten, Mustafa Inceoglu, and Henrik Rostved Horak, for their support and patience during my PhD studies.

*Fadil Inceoglu,  
Aarhus, October 31, 2014.*



# Contents

<b>Abstract</b>	<b>i</b>
<b>Resumé</b>	<b>iii</b>
<b>Acknowledgments</b>	<b>v</b>
<b>Contents</b>	<b>vii</b>
<b>I Overview</b>	<b>1</b>
<b>1 Background</b>	<b>3</b>
1.1 Introduction . . . . .	3
1.2 The Sun . . . . .	3
1.3 The Sun's large-scale magnetic field . . . . .	4
1.4 Solar activity on different time scales . . . . .	5
1.5 Galactic Cosmic Rays and Production of Cosmogenic Radionuclides . . . . .	7
1.6 Geochemical Behaviours of $^{10}\text{Be}$ and $^{14}\text{C}$ in the Earth system . . . . .	9
1.7 The Relationship between cosmogenic radionuclides and solar activity . . . . .	11
1.8 Solar Variability and Earth's Climate . . . . .	13
<b>2 Aim of the Ph.D. Project</b>	<b>21</b>
2.1 Summary of Paper I . . . . .	21
2.2 Summary of Paper II . . . . .	24
2.3 Summary of Paper III . . . . .	26
2.4 Summary of Paper IV . . . . .	30
2.5 Summary of Paper V . . . . .	31
2.6 Summary of Paper VI . . . . .	33
<b>3 Work in Progress</b>	<b>35</b>
3.1 Modelling Surface Ocean $^{14}\text{C}$ Variability during MIS 3 with GENIE-1: An outline . . . . .	35
<b>4 Future Work</b>	<b>39</b>
4.1 Investigating the Astrophysical Origin of short-lived Cosmic Ray events and their impact on Earth's environment . . . . .	39
<b>II Publications</b>	<b>41</b>
<b>5 Modeling the Relationship between Neutron Counting Rates and Sunspot Numbers Using the Hysteresis Effect</b>	<b>43</b>

5.1	Introduction . . . . .	43
5.2	Data Analysis . . . . .	44
5.3	Hysteresis Effect . . . . .	47
5.4	Modeling the Relationship between NCRs and SSNs . . . . .	51
5.5	Discussion and Conclusions . . . . .	56
<b>6</b>	<b>Reconstruction of Sub-Decadal Changes in Sunspot Numbers based on the NGRIP <math>^{10}\text{Be}</math> Record</b>	<b>61</b>
6.1	Introduction . . . . .	62
6.2	Data . . . . .	63
6.3	Analysis . . . . .	63
6.4	Results . . . . .	70
6.5	Discussion . . . . .	73
6.6	Conclusions . . . . .	75
<b>7</b>	<b>Grand solar minima and maxima deduced from <math>^{10}\text{Be}</math> and <math>^{14}\text{C}</math>: Magnetic dynamo configuration and polarity reversal</b>	<b>77</b>
7.1	Introduction . . . . .	78
7.2	Long term solar variability based on cosmogenic radionuclide data . . . . .	79
7.3	Results . . . . .	84
7.4	Discussion . . . . .	90
7.5	Conclusions . . . . .	92
<b>8</b>	<b>Are we entering a Grand Solar Minimum?: Comparison between current and previous solar dynamics</b>	<b>93</b>
8.1	Introduction . . . . .	94
8.2	The characterisation of the solar dynamics during the Holocene . . . . .	95
8.3	The Sun's large scale dipolar magnetic field over the last three solar cycles . . . . .	102
8.4	Interpreting and Predicting the future solar dynamics . . . . .	104
8.5	Discussion and Conclusion . . . . .	105
<b>9</b>	<b>A continuous ice core <math>^{10}\text{Be}</math> record from Mongolian mid-latitudes: Influences of solar variability and local climate</b>	<b>109</b>
9.1	Introduction . . . . .	109
9.2	Location . . . . .	110
9.3	Methods . . . . .	111
9.4	Data . . . . .	111
9.5	Results . . . . .	112
9.6	Discussion . . . . .	117
9.7	Conclusions . . . . .	118
9.8	Supplementary . . . . .	119
<b>10</b>	<b>The lost sunspot cycle: New support from <math>^{10}\text{Be}</math> measurements</b>	<b>121</b>
10.1	Introduction . . . . .	121
10.2	Observations . . . . .	123
10.3	Analysis . . . . .	125
10.4	Results . . . . .	128
10.5	Discussion . . . . .	129
	<b>Bibliography</b>	<b>131</b>

Part I

**Overview**



# Chapter 1

## Background

### 1.1 Introduction

This thesis is produced as a result of my PhD studies during the last three years at the Department of Physics and Astronomy and at the Department of Geosciences at Aarhus University. In this period, I studied the short- and long-term behaviour of the solar dynamo using various data sets, such as the available cosmogenic radionuclide records ( $^{10}\text{Be}$  and  $^{14}\text{C}$ ), neutron counting rates, as an indicator of the galactic cosmic ray intensity near the Earth environment, from neutron monitors located at different geographical locations and altitudes, and Wilcox Solar Observatory line-of-sight magnetogram data. I have also produced the first continuous ice core  $^{10}\text{Be}$  record from mid-latitudes.

The first part of this thesis is an overview, in which the first chapter briefly gives some background information on the Sun. This includes variations in solar magnetic activity on different time scales and associated connection with galactic cosmic ray intensity in the heliosphere, and hence cosmogenic radionuclides such as  $^{10}\text{Be}$  and  $^{14}\text{C}$  that are produced in the Earth's atmosphere. I also give specific examples of how the solar variation might effect the climate on Earth on different time scales. The second chapter of the overview part explains the aims of my PhD studies and provides brief summaries of six articles, five out of which I have first authored, that I produced during my PhD study period. The third chapter gives a general outline of the ongoing research I am involved in regarding the mechanisms behind the variations observed in the North Atlantic surface ocean  $^{14}\text{C}$  records during Marine Isotope Stage 3 ( $\sim 27\text{--}60$  kyr BP). Future work, which will be related to the short-lived cosmic ray events and their impact on the Earth can be found in the last chapter.

The second part of my thesis includes the six manuscripts that are published in, or submitted to, scientific journals.

### 1.2 The Sun

The Sun, which is simply a ball of plasma compressed under its own gravitational force, is a star of spectral type G2V with an age of  $\sim 4.5 \times 10^9$  years. The solar mass ( $M_{\odot}$ ) is roughly about  $1.99 \times 10^{30}$  kg and the mean solar radius ( $R_{\odot}$ ) is  $6.96 \times 10^5$  km (Foukal, 2004). The solar atmosphere consists of three regions with different physical properties. The lowest region of the solar atmosphere, called the photosphere, is a very thin plasma layer, where most of the solar radiation is emitted. Above the photosphere, there is a less dense and hence more transparent layer called the chromosphere. The outermost layer of the solar atmosphere, the corona, extends from

the top of a transition region, which is a region between the upper chromosphere and the corona, to the interplanetary space (Priest, 1981).

Observations of the Sun since 1610 A.D. show that it has magnetic activity structures on its photosphere, chromosphere and corona. These include sunspots and faculae on the photosphere, plages on the chromosphere, and coronal holes (Figure 1.1). The physical mechanism responsible for the generation of the Sun's large-scale magnetic field and hence the emergence of the observed magnetic activity structures on the Sun is called the solar dynamo (Charbonneau, 2010).

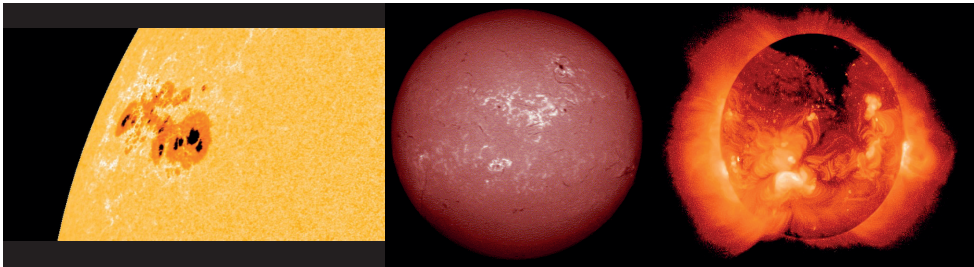


Figure 1.1: Solar Atmospheres; from left to right, photosphere, chromosphere ( $H\alpha$ ) and corona (X-Ray) (Image courtesy of NASA).

### 1.3 The Sun's large-scale magnetic field

The external magnetic field of the Sun mainly consists of two major components (Solanki et al., 2000). The first component emerges on the Sun in the form of small bipoles or ephemeral regions. The life times of these regions are relatively short with decay timescales  $<1$  day and basically represent a small-scale background noise. Wang & Sheeley (1991) suggested that due to the random axial orientations of bipoles, ephemeral regions almost have no contribution to the mean magnetic field of the Sun, being a factor of 6 smaller than what the axial dipole moment contributes (Solanki et al., 2000), even though they contribute to the total unsigned photospheric flux (Wang, 2004). The second component emerges on the latitudes where the sunspots form as large bipoles or active regions. In contrast to the ephemeral regions, the active regions have preferential axial orientations which result in an organised large-scale magnetic field (Wang, 2004).

The large-scale magnetic field consists of open and closed magnetic fields (see Figure 1.2). The majority of the total magnetic flux of the Sun originates from closed magnetic loops having each end connected in the Sun, forming sunspots and faculae (Wang, 2004). Therefore, closed magnetic field lines play a major role in controlling the total solar irradiance variations through time (Lean, 2000). On the other hand, the open solar magnetic flux leaves the solar atmosphere and forms the interplanetary magnetic field (IMF), since the magnetic field strength decreases rapidly as the magnetic loops exceed the heliocentric sphere of  $2.5 \times R_{\odot}$  (Wang, 2004; Lockwood, 2013). The open solar magnetic field thus affects geomagnetic activity and it is the source of the modulation of galactic cosmic rays (GCRs) in the heliosphere, which is responsible for the production of cosmogenic isotopes on the Earth (Lean et al., 2002). Figure 1.3 illustrates the incoming galactic cosmic rays and the heliosphere and its structure.

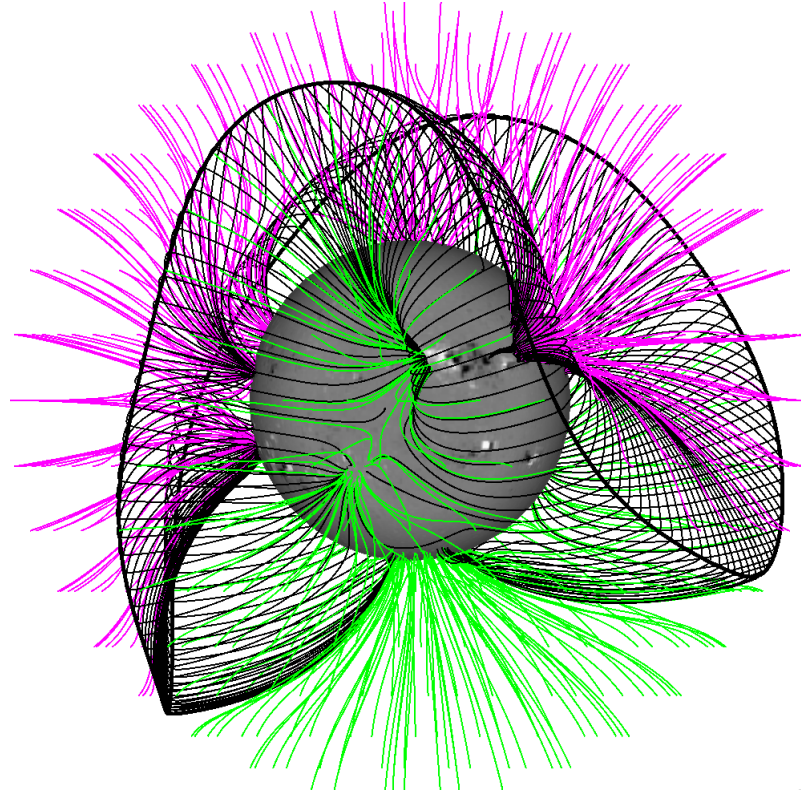


Figure 1.2: Potential field source surface extrapolation of the photospheric magnetic field on June 2012. Black lines show the closed magnetic field, whereas the green and magenta lines show the open magnetic field for different polarities.

## 1.4 Solar activity on different time scales

The Sun shows variations on various time scales with the most prominent being the 11-year sunspot cycle, which has a duration that changes from 9 to 14 years (Friis-Christensen & Lassen, 1991). This can be explained by a dipole-like dynamo configuration (dynamo mode), which is antisymmetric with respect to the equator and reverses its polarity very near the maximum of the 11-year solar activity cycle (DeRosa et al., 2012). The initial dipolar magnetic configuration (full magnetic cycle) is re-established after about 22 years, which corresponds to the Hale cycle.

Shorter-term periodicities found in various data sets, including sunspot data, range from a couple of weeks to years, such as  $\sim 160$  days,  $\sim 1.3$  and  $\sim 2$  years (Krivova & Solanki, 2002; Mursula et al., 2003; Zaqarashvili et al., 2010; Simoniello et al., 2013a). These periodicities are thought to be related to the magnetic configuration of the solar dynamo (Vecchio & Carbone, 2009). Zaqarashvili et al. (2010) suggested that the 160 day periodicity may be connected with the dynamics of magnetic Rossby waves in the tachocline, which is a transition region between the solar radiative zone and convective envelope, since it shows itself at certain times coinciding with the 11-year solar cycle maximum. A periodicity of  $\sim 1.3$  years found in sunspot areas and sunspot numbers has been suggested in accordance with a  $\sim 1.3$ -year periodicity in the solar rotation rate revealed by helioseismological data. This implies that variations in the solar rotation rate influence the solar dynamo mechanism, which is responsible for the emergence of the magnetic flux to the solar surface (Krivova & Solanki, 2002). A periodicity of  $\sim 1.3$  years has also been detected in various geomagnetic indices such as

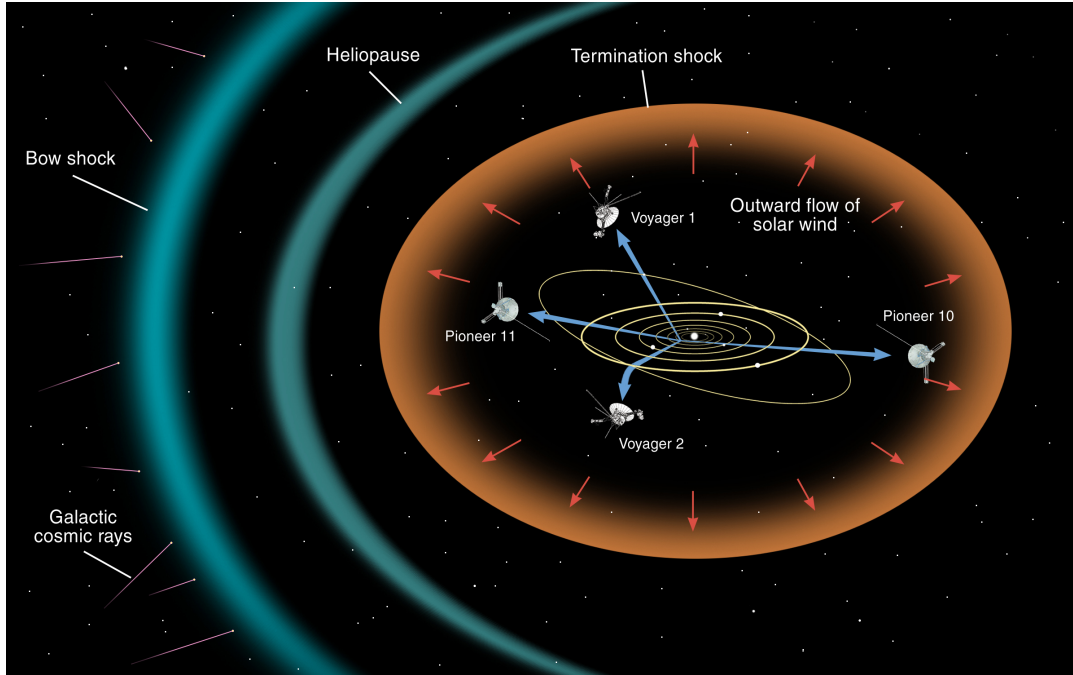


Figure 1.3: Heliosphere and its structure (Image courtesy of NASA).

the near-Earth interplanetary magnetic field and geomagnetic  $aa$ -index (Lockwood, 2001). The 2-year periodicity, namely the quasi-biennial oscillation (QBO), manifests itself in most solar activity proxies at certain times and its signal is stronger near the solar cycle maximum (Simoniello et al., 2013a). Simoniello et al. (2013a) used 17 years of high-resolution data provided by the Global Oscillation Network Group (GONG) that covers Solar Cycle 23 and the ascending phase of Solar Cycle 24 in their detailed analysis to obtain a better understanding of the physical mechanisms governing the QBO. As a result the authors suggest that the physical mechanism for the observed QBO is the beating between dipole and quadrupole dynamo modes (Simoniello et al., 2013a).

Observations of the Sun have also revealed that the magnetic activity level of the Sun varies on longer timescales, *e. g.* from the Maunder Minimum (1645 - 1715), when sunspots almost completely vanished from the solar surface, to the enhanced activity level since the middle of the 20<sup>th</sup> century, the Modern Maximum (Figure 1.4) (Usoskin et al., 2007).

Maunder minimum-like periods are believed to be special states of the solar dynamo and they represent a challenge for solar dynamo theory and models, since the models do not agree on the frequencies of these phenomena in the Sun's history, the processes that cause them and whether they represent regular or random characteristics of the solar dynamo (Charbonneau, 2010).

Information on solar variations prior to 1610 relies on past production rates of cosmogenic nuclides stored in terrestrial archives, such as  $^{10}\text{Be}$  in ice cores and  $^{14}\text{C}$  in tree rings (Bard & Frank, 2006). There are numerous studies concerning long-term changes in the solar magnetic activity levels, their characteristics, and hence long-term behaviour of the solar dynamo, based on cosmogenic radionuclides (Usoskin et al., 2003c; Solanki et al., 2004; Muscheler et al., 2007a; Usoskin et al., 2007; Knudsen et al., 2009; Inceoglu et al., 2014b). Usoskin et al. (2007) studied the statistical characteristics of the grand minima states of the solar activity using a SSN recon-

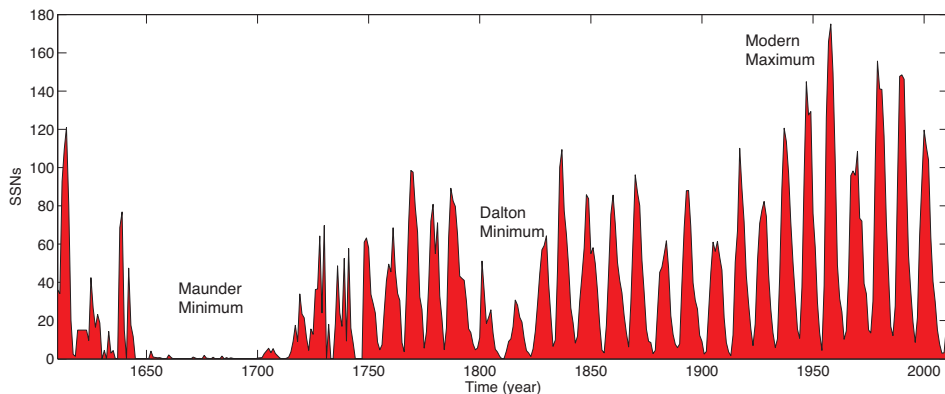


Figure 1.4: Temporal variations in sunspot numbers, using data from Hoyt and Schatten (1998).

struction based on  $^{14}\text{C}$ , and suggested that these low activity episodes of the Sun are observed in two different types of minima, *i. e.*, Maunder-like minima with shorter durations ranging between 30–90 years and Spörer-like minima with longer durations of  $>110$  years. Additionally, the authors claimed that the occurrences of these low activity episodes reflect an oscillatory behaviour (accumulate and release of energy). Muscheler et al. (2007a) reconstructed past solar activity at a high-resolution, with some periods at annual resolution, for the past 1000 years (between A.D. 1000–2002), by combining information based on six different  $^{10}\text{Be}$  records from ice cores from Greenland and Antarctica,  $^{14}\text{C}$  in tree rings, neutron counting rates, as indicators of galactic cosmic ray (GCR) intensity and geomagnetic field strength records. As a result of their analyses, Muscheler et al. (2007a) showed that even though the various  $^{10}\text{Be}$  records show the major changes in the past solar activity levels, there are many discrepancies observed because of local (core-site) changes in the atmospheric transport and deposition processes. The authors also concluded that the modern solar activity levels are relatively high compared with the levels prior to 1950 A.D., but this activity level is also observed several times during the past 1000 years. In order to investigate periodicities in the solar activity, Knudsen et al. (2009) used two solar activity reconstructions based on  $^{10}\text{Be}$  and  $^{14}\text{C}$ . They observed four dominant periodicities of  $\sim 88$  (Gleissberg Cycle),  $\sim 150$ ,  $\sim 220$  (Suess Cycle) and  $\sim 400$  years, which show amplitude variations throughout the Holocene. The authors also observed some differences between the power spectra of the two solar activity reconstructions based on  $^{10}\text{Be}$  and  $^{14}\text{C}$ . These differences are more pronounced when the amplitude of the signals, which are related to the periodicities, reach their maximum. Knudsen et al. (2009) suggested that this can be related to the potential link between the solar activity levels and climate system. Because the geochemical behaviour of  $^{10}\text{Be}$  and  $^{14}\text{C}$  and their transport and deposition in the earth system are influenced by the climate system, which is responding to the longer solar cycles.

## 1.5 Galactic Cosmic Rays and Production of Cosmogenic Radionuclides

Galactic cosmic rays (GCRs), which are accelerated by shock waves generated by supernova explosions (Blandford & Eichler, 1987; Hathaway, 2010), are charged particles with energy ranges from a few MeV to approximately  $10^{20}$  eV, impinging on the

Earth from all directions.

The majority of cosmic ray particles are atomic nuclei, but electrons, positrons, and other sub-atomic particles are also included. Before reaching the Earth, cosmic ray particles have to travel through the heliosphere, where they become modulated (Potgieter, 2013). According to the basic transport equation (Equation 1.1) derived by Parker (1965), modulation of cosmic ray particles in the heliosphere (part a of equation below) is a combination of convection of particles due to the out-blowing solar wind processes (part b), drift of the cosmic ray particles in the heliospheric magnetic field caused by gradients and curvatures in the global heliospheric magnetic field (part c), diffusion of particles due to magnetic inhomogenities (part d) and adiabatic cooling in expanding solar wind (part e) (Usoskin, 2013; Potgieter, 2013).

$$\underbrace{\frac{\partial f}{\partial t}}_a = -(\underbrace{\mathbf{V}}_b + \underbrace{\langle \mathbf{v}_d \rangle}_c) \cdot \nabla f + \underbrace{\nabla \cdot (\mathbf{K}_s \cdot \nabla f)}_d + \underbrace{\frac{1}{3}(\nabla \cdot \mathbf{V}) \frac{\partial f}{\partial \ln P}}_e \quad (1.1)$$

where  $f(r, P, t)$  represents the cosmic ray distribution function,  $P$ ,  $t$  and  $r$  denote rigidity, time and the position in 3 dimensions, respectively. The position in the 3-dimensional space is specified in a heliocentric spherical coordinate system with  $r$ ,  $\theta$  and  $\phi$ , where the equatorial plane is at a polar angle of  $\theta=90^\circ$ . Additionally, in the equation,  $\mathbf{V}$  and  $\langle \mathbf{v}_d \rangle$  are solar wind velocity and averaged particle drift velocity, while  $\mathbf{K}_s$  is the symmetrical diffusion tensor (Potgieter, 2013).

Therefore, GCRs are inversely proportional to, but out of phase with, the 11-year solar cycle and the temporal variation of the GCR intensity displays a distinct 11-year periodicity due to solar modulation of GCRs in the heliosphere (Singh et al., 2008). However, the 11-year cycle in GCRs is delayed, by a time span landing from a month to a year, with respect to the sunspots (Inceoglu et al., 2014a).

At the top of the Earth's atmosphere, the composition of GCRs includes protons (87 %), alpha particles (12 %), and heavier nuclei (1 %) (Dunai, 2010). Upon entering the Earth's atmosphere, GCRs produce cascading showers of particles as a result of spallation reactions with atmospheric elements, such as N and O, in the Earth's upper atmosphere (see Figure 1.6). Therefore, the composition of the cosmic ray particles changes from being proton dominated to neutron dominated during the cascade processes (Dunai, 2010). The temporal evolution of the cosmic-ray flux can thus be measured by neutron monitors (NMs) located around the globe at various geographical locations and altitudes (Hathaway, 2010; Usoskin, 2013). Figure 1.5 shows the temporal evolution of the neutron counting rates, as an indicator of galactic cosmic ray intensity near the Earth's environment, taken from the McMurdo and Thule Neutron Monitors.

Figure 1.6 illustrates the productions and geochemical pathways of  $^{10}\text{Be}$  and  $^{14}\text{C}$  in the earth system.  $^{10}\text{Be}$  is mainly produced via primary spallation reactions of secondary neutrons produced by the galactic cosmic rays in the atmosphere with atmospheric nitrogen and oxygen (Matthiä et al., 2013). For  $^{14}\text{C}$ , the main production reaction is the capture of a thermal neutron with typical energies around 0.025 eV (Gosse & Phillips, 2001; Dunai, 2010). The most important production channels of  $^{10}\text{Be}$  and  $^{14}\text{C}$  are as follows;

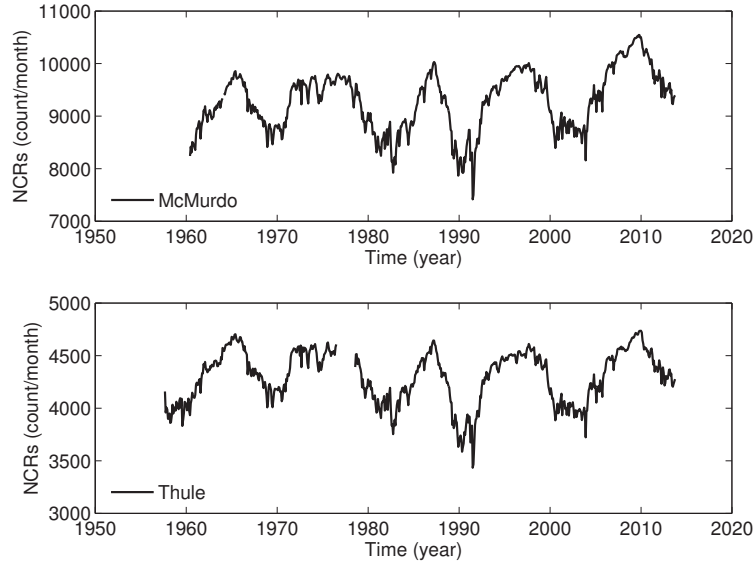
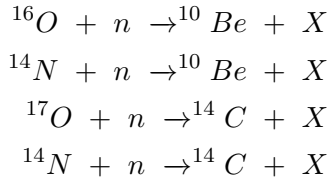


Figure 1.5: Temporal variations of NCRs, as an indicator of GCRs, measured by McMurdo and Thule NMs.



where "n" denotes a neutron that starts the reaction, while "X" represents the side-product of the reaction. The production rates of the cosmogenic nuclides are inversely correlated with solar magnetic activity and the geomagnetic field intensity due to the non-linear shielding effect of the solar magnetic field and the geomagnetic dipole field (Heikkilä et al., 2008b). A strengthening of the solar magnetic and geomagnetic fields results in a lower production rate of cosmogenic nuclides (Masarik & Beer, 1999), as well as lower neutron counting rates (NCRs) (Mavromichalaki & Petropoulos, 1984).

## 1.6 Geochemical Behaviours of ${}^{10}\text{Be}$ and ${}^{14}\text{C}$ in the Earth system

Production of the cosmogenic nuclides mostly occurs within the lower stratosphere and the upper troposphere. For  ${}^{10}\text{Be}$ , the production rates are estimated to be 67% in the stratosphere and 33% in the troposphere according to Lal & Peters (1967), while Masarik & Beer (1999) estimated these values as 56% and 44%, respectively.

After its production,  ${}^{10}\text{Be}$  is rapidly attached mainly onto atmospheric sulfate aerosols (Baroni et al., 2011). After a residence time around 1 to 2 years in the lower stratosphere (Raisbeck et al., 1981), the aerosols are transported into the lower troposphere by air mass exchanges taking place between the troposphere and stratosphere at mid-latitudes (Koch & Rind, 1998) and they are eventually deposited at the surface by both dry and wet deposition. The concentration of  ${}^{10}\text{Be}$  in terrestrial archives

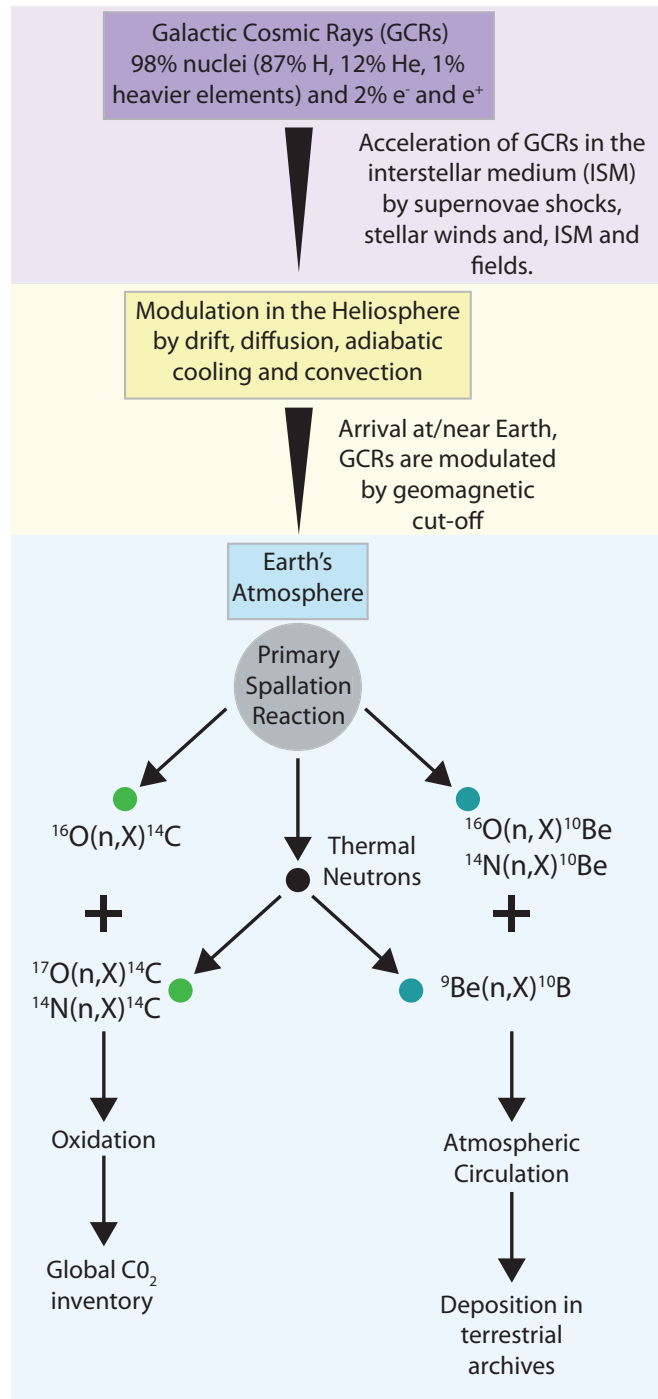


Figure 1.6: Illustration of the production of cosmogenic nuclides  $^{10}\text{Be}$  (blue dots) and  $^{14}\text{C}$  (green dots) and their fate in the Earth's environment.

is therefore not only influenced by changes in production rates caused by variable solar activity, but also by transport and deposition processes, atmospheric mixing, scavenging and snow accumulation rates at the coring site (Heikkilä et al., 2008b). The climate influence on the  $^{10}\text{Be}$  concentration rates measured in ice cores can be separated into two main effects, *i. e.* atmospheric mixing of  $^{10}\text{Be}$  tends to smooth out the latitudinal distribution of  $^{10}\text{Be}$  production, whereas the local meteorologic conditions at the coring site affects the precipitation of the  $^{10}\text{Be}$  from the atmosphere

(Heikkilä et al., 2013b).

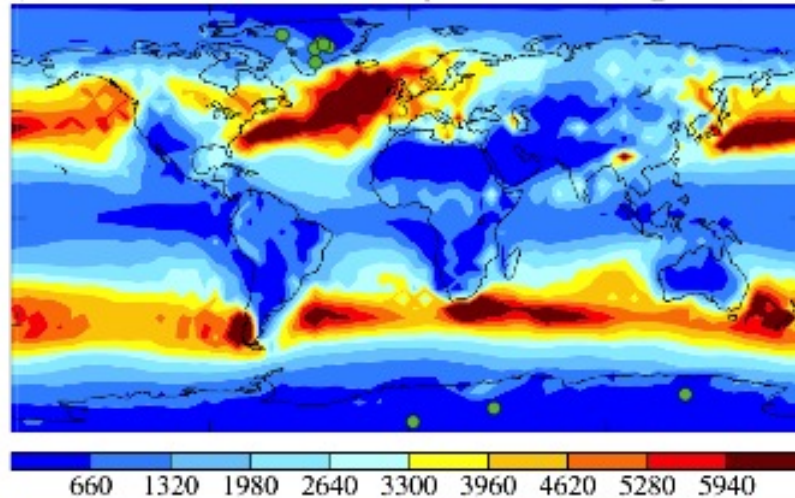


Figure 1.7: Annual mean wet  $^{10}\text{Be}$  deposition ( $10^{-27}\text{kg}/\text{m}^2/\text{s}$ ) at the surface of the Earth. The main exchange between the stratosphere and the troposphere occurs at mid-latitudes, resulting in a maximum of  $^{10}\text{Be}$  deposition at these latitudes. The existing  $^{10}\text{Be}$  records from ice cores (green circles) all derive from polar regions (modified from Field et al. (2006)).

Using a general circulation model, Field et al. (2006) and Heikkilä et al. (2013b) calculated that the maximum deposition of  $^{10}\text{Be}$  occurs at the temporal latitudes (Figure 1.7) instead of the polar regions, where all the currently available high-resolution  $^{10}\text{Be}$  records stem from. Thus,  $^{10}\text{Be}$  records obtained from polar regions may not completely reflect changes in global  $^{10}\text{Be}$  production rates.

For  $^{14}\text{C}$ , the contribution of the stratospheric production to the global production of  $^{14}\text{C}$  atoms is estimated as 56% by Lal & Peters (1967), while Masarik & Beer (1999) estimated this rate as 51%. After its production,  $^{14}\text{C}$  becomes oxidised and joins the atmospheric  $\text{CO}_2$  inventory. The atmospheric  $\text{CO}_2$  reservoir is part of the global carbon cycle, and it exchanges  $\text{CO}_2$  with Earth's carbon reservoirs, including the oceans, sediments, soils and biosphere (Bard et al., 1997). Therefore, the  $^{14}\text{C}$  in the natural archives, such as tree rings, is influenced by the exchange dynamics among Earth's carbon reservoirs (Baroni et al., 2011). The amount of  $^{14}\text{C}$  in the atmosphere is influenced by changes in the global production rate, but variations in the  $^{14}\text{C}$  concentration measured in tree rings are attenuated and delayed relative to its production due to the effect of the global carbon inventory and residence time in atmosphere (Roth & Joos, 2013).

## 1.7 The Relationship between cosmogenic radionuclides and solar activity

After removal of the climatic noise and/or carbon cycle influence and geomagnetic field effects, which can be done using independent reconstructions of the geomagnetic dipole field intensity (Knudsen et al., 2008), on the cosmogenic radionuclide records measured in terrestrial archives, such as  $^{10}\text{Be}$  in ice cores and  $^{14}\text{C}$  in tree rings, the remaining signal can be considered as changes in past production rates of the cosmo-

genic radionuclides that are related to changes in the solar magnetic field strength described by the solar modulation potential (Steinhilber et. al., 2008).

On the basis of some assumptions made in order to reduce the complexity of the Parker’s model (Equation 1.1), which explains the modulation of cosmic ray particles in the heliosphere, Gleeson & Axford (1968) derived the so-called force-field parameterization of the GCR energy spectrum:

$$J(E_p) = J_{\text{LIS}}(E_p + \Phi) \times \frac{E_p(E_p + 2m_p c^2)}{(E_p + \Phi)(E_p + 2m_p c^2 + \Phi)} \quad (1.2)$$

where  $J_{\text{LIS}}$  is the local interstellar cosmic ray flux,  $E_p$  and  $m_p c^2$  indicate the proton’s kinetic and rest energies, respectively. The solar modulation strength is given by  $\Phi$ , whereas  $c$  is the velocity of light. Steinhilber et. al. (2008) pointed out that using  $\Phi$  provides a good approximation for the solar modulation of cosmic rays in the Earth’s vicinity. In order to solve Equation (1.2) for the solar modulation strength,  $\Phi$ , the local interstellar cosmic-ray spectrum (LIS) has to be known. However, there are no measurements of this parameter and hence modelled values of the LIS have to be used in the production rate calculations of cosmogenic nuclides such as  $^{10}\text{Be}$  and  $^{14}\text{C}$  (Herbst et al., 2010).

Masarik & Beer (1999) provided a relationship, based on Monte Carlo method, to calculate the solar modulation potential as a function of production rates of cosmogenic nuclides, *i. e.*  $^{10}\text{Be}$  and  $^{14}\text{C}$ , and the geomagnetic field strength. Figure 1.8 shows the overall relationships between normalised production rates of the cosmogenic nuclides  $^{10}\text{Be}$  (left panel) and  $^{14}\text{C}$  (right panel), the geomagnetic field strength normalised according to today’s values and the solar modulation potential.

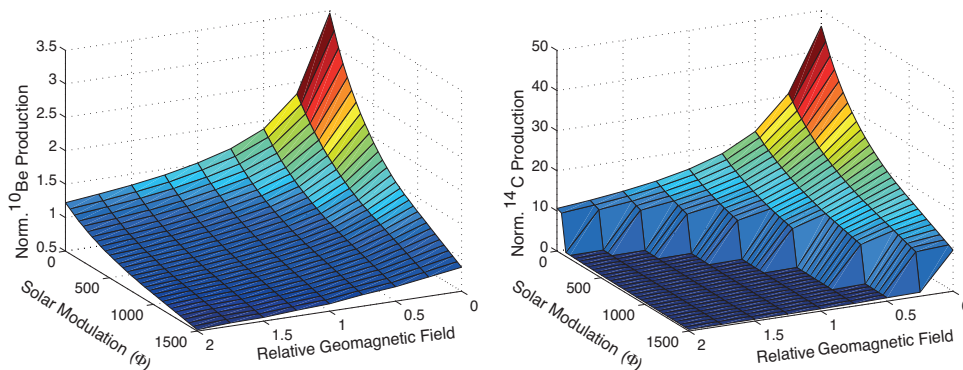


Figure 1.8: Solar modulation potential as a function of normalised production rates of  $^{10}\text{Be}$  (left) and  $^{14}\text{C}$  (right) and relative to today geomagnetic field intensity (Masarik & Beer, 1999).

It is consequently possible to use cosmogenic radionuclide measurements from terrestrial archives, such as  $^{10}\text{Be}$  in ice cores and  $^{14}\text{C}$  in tree rings, to reconstruct solar modulation potential, which is related to the open solar magnetic field that modulates the galactic cosmic rays in the heliosphere. Reconstructions of the solar modulation potential enable us to study the short- and long-term behaviour of the solar dynamo that is responsible for the emergence of the magnetic activity structures on the Sun and hence variations in the past activity levels of the Sun. Additionally, more robust identifications of grand minima and maxima periods in past solar activity levels will help us understand the link between the solar variability and its influence on Earth’s climate.

## 1.8 Solar Variability and Earth's Climate

The climate system of the Earth, which is mainly a result of multiple interactions between the atmosphere, the hydrosphere, the cryosphere, the land surface and the biosphere (Figure 1.9), is subjected to basically three natural forcing mechanisms that cause changes on various time scales ranging from millions of years (tectonic processes) to decades (variations of the activity level of the Sun) (Ruddiman, 2007). These forcing mechanisms introduce an externally imposed perturbation in the energy budget of the Earth's climate system (IPCC, 2007), which in turn leads the climate system to undergo some changes in order to adjust its energy balance.

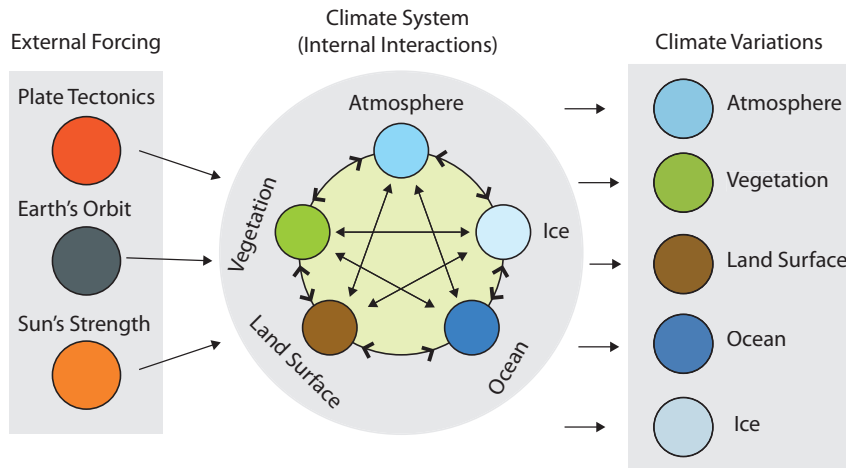


Figure 1.9: Forcing mechanisms, climate system and climate variations that we can measure/reconstruct from geological archives (Modified from Ruddiman (2007)).

In contrast to the tectonic and orbital forcing mechanisms, variations in the activity levels of the Sun, which is the main energy source for the Earth's climate system, occur on relatively short time scales. The absorption of solar radiation determines the radiation and energy budget of the Earth (Haigh, 2007). Therefore, understanding solar variability through time is important to decipher the solar influence on the climate of the Earth.

The thermal structure of the Earth's atmosphere can be effected by variations in the magnetic activity level of the Sun, which will cause global or regional climate fluctuations on different time scales (Haigh, 2007). The equilibrium between the energy received from the incident solar radiation and the energy lost to space via thermal infrared radiation from the Earth determines the global mean temperature of the Earth. This relationship is given by  $(1 - \alpha)I_{TS}/4 = \sigma T_s^4(1 - B)$ , where  $I_{TS}$  represents total solar irradiance (TSI), i.e. the total electromagnetic power per unit area of cross section arriving at the mean distance between the Earth and the Sun ( $\sim 1$  A.U.)  $\alpha$  is the Earth's visible albedo (reflectivity),  $\sigma$  denotes the Stefan-Boltzman constant,  $T_s$  is the Earth's surface temperature and  $B$  is the Earth's infrared albedo (Haigh, 2007; Gray et al., 2010). It is evident from the energy equilibrium definition that changes in the incoming irradiance and/or the reflective properties of the Earth will cause changes in the temperature structure of the air column due to the fact that the atmosphere-surface system tends to adjust itself in order to restore the energy equilibrium (Haigh, 2007).

The TSI received by the Earth's rotating sphere is  $\sim 340Wm^{-2}$ , which is the

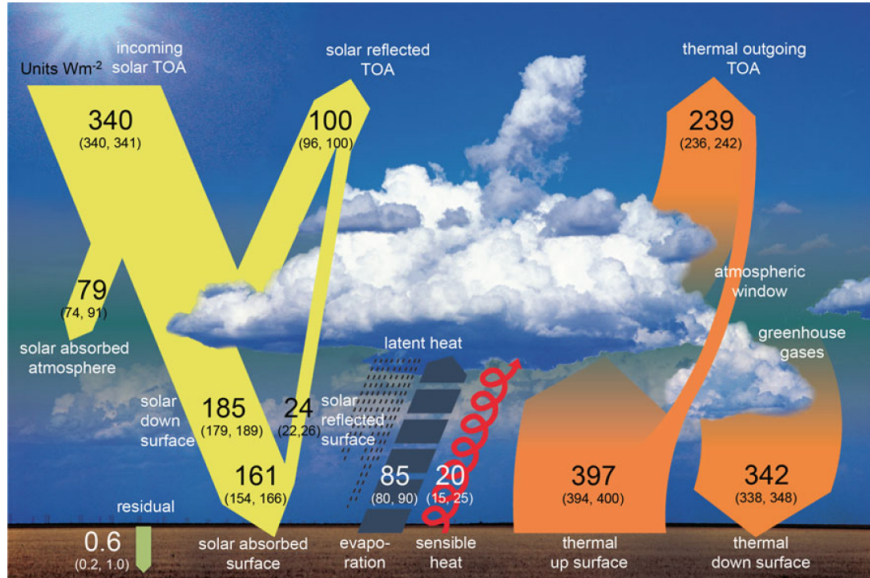


Figure 1.10: Globally averaged energy budget of the atmosphere (Wild et al., 2013).

averaged value of the TSI ( $\sim 1360 Wm^{-2}$ ) over the surface area of the Earth's rotating sphere. As shown in Figure 1.10, which illustrates the globally averaged energy budget of the atmosphere,  $100 Wm^{-2}$  of the incoming solar radiation is reflected back to space due to the albedo caused by clouds, aerosols, atmospheric molecules and the surface, so the remaining part of the incident solar radiation is absorbed by the Earth's surface and the atmosphere. Additionally, infrared radiation ( $397 Wm^{-2}$ ) is emitted from the surface of the Earth and a fraction of it escapes to space. The remaining outgoing energy is absorbed by clouds and atmospheric gases and return to the surface as infrared radiation ( $342 Wm^{-2}$ ) (Wild et al., 2013).

Atmospheric circulations are mainly driven by the latitudinal distribution of the absorbed incoming radiation by the atmosphere, which depends on the concentrations and spectral properties of the atmospheric components. The upper panel of Figure 1.11 shows two black body spectra at 5750 K and 245 K, representing the solar irradiance at the top of the atmosphere and the Earth's thermal radiation. The bottom panel of Figure 1.11 shows a spectrum of the atmospheric absorption pattern of incident solar radiation. As observed in the figure, molecular oxygen and ozone are the major absorbers of incoming UV radiation, whereas water vapor and  $CO_2$  are the major absorbers of infrared radiation (Haigh, 2007).

Changes in magnetic activity of the Sun on the 11 year time-scale are positively correlated with solar irradiance variations (Field et al., 2006). Direct satellite-based measurements of TSI, dates back to 1978. Observations show that the variation in TSI between solar cycle minima and maxima over the past two 11-year cycles is approximately 0.08% ( $1.1 Wm^{-2}$ ) (Fröhlich, 2006; Haigh, 2007; Gray et al., 2010). However, observations of TSI and solar spectral irradiance (*SSI*) made by the *SORCE* (Solar Radiation & Climate Experiment) satellite, which was launched in 2003, have revealed that the irradiance variability in the UV spectrum is two orders of magnitude higher than the TSI over the 11-year cycle (Gray et al., 2010). The top panel of Figure 1.12 shows the spectral variability of the irradiance, which is defined as the difference between solar cycle maxima and minima values, compared to the minima value, based on the last two solar cycles.

Incoming solar radiation and the solar energetic particles play a major role in

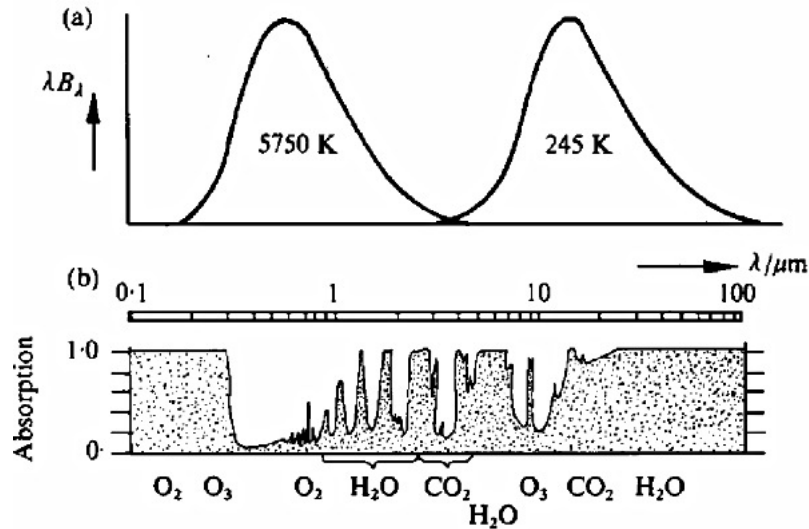


Figure 1.11: (a) Black body functions at the emitting temperatures of the Sun and the Earth. The functions are scaled to have equal area to represent the Earth's radiation balance. (b) Absorption by a vertical column of atmosphere. The gases responsible for the main absorption features are identified at the appropriate wavelengths (Haigh, 2007).

determining the atmospheric chemistry in the middle atmosphere through photochemical processes (Haigh, 1994, 2007; Gray et al., 2010). As a result, the thermodynamic structure of the stratosphere is strongly modulated by solar variability (Haigh, 2007) because the stratospheric ozone budget is determined by the solar UV radiation and its spectral composition. The solar-induced changes in stratospheric ozone produce perturbations to stratospheric and tropospheric circulation patterns and climate (Gray et al., 2010). Moreover, the amplitude of these perturbations is sensitive to the actual change in ozone in the stratosphere and its distribution (Haigh, 1996, 1999). Soukharev & Hood (2006) applied a multiple regression statistical analysis using three independent satellite ozone data spanning between 1985–2003 and Mg II core-to-wing ratio as a proxy for solar UV variation to investigate the influences of variations in SSI on the stratospheric ozone concentrations. The lower panel of Figure 1.12 represents the results of their analysis, which suggest that 6% changes in SSI over a solar cycle results in a statistically significant response of 2%–4% in the upper stratosphere where solar UV variations directly affect ozone production rates.

### Solar Variability and Its Influence on the Atmospheric Circulation

Ineson et al. (2011) designed an experiment to show the response of surface climate to variations in UV flux alone (200 - 300 nm), in which they imposed the solar spectral irradiance (SSI) forcing in a climate model. For simplicity, the authors used monthly climatological ozone values and ignored stratospheric ozone feedback, which would probably enhance the effects. As a result, their model produced a 1-2 K temperature decrease in the troposphere from solar maximum to solar minimum due to a decrease in ozone heating in the stratosphere, which is a direct result of decreased UV, and changes in the Arctic Oscillation (AO) / North Atlantic Oscillation (NAO)-like atmospheric circulation patterns (Ineson et al., 2011). Additionally, several other studies concerning the heating of the stratosphere by changes in solar UV concluded that

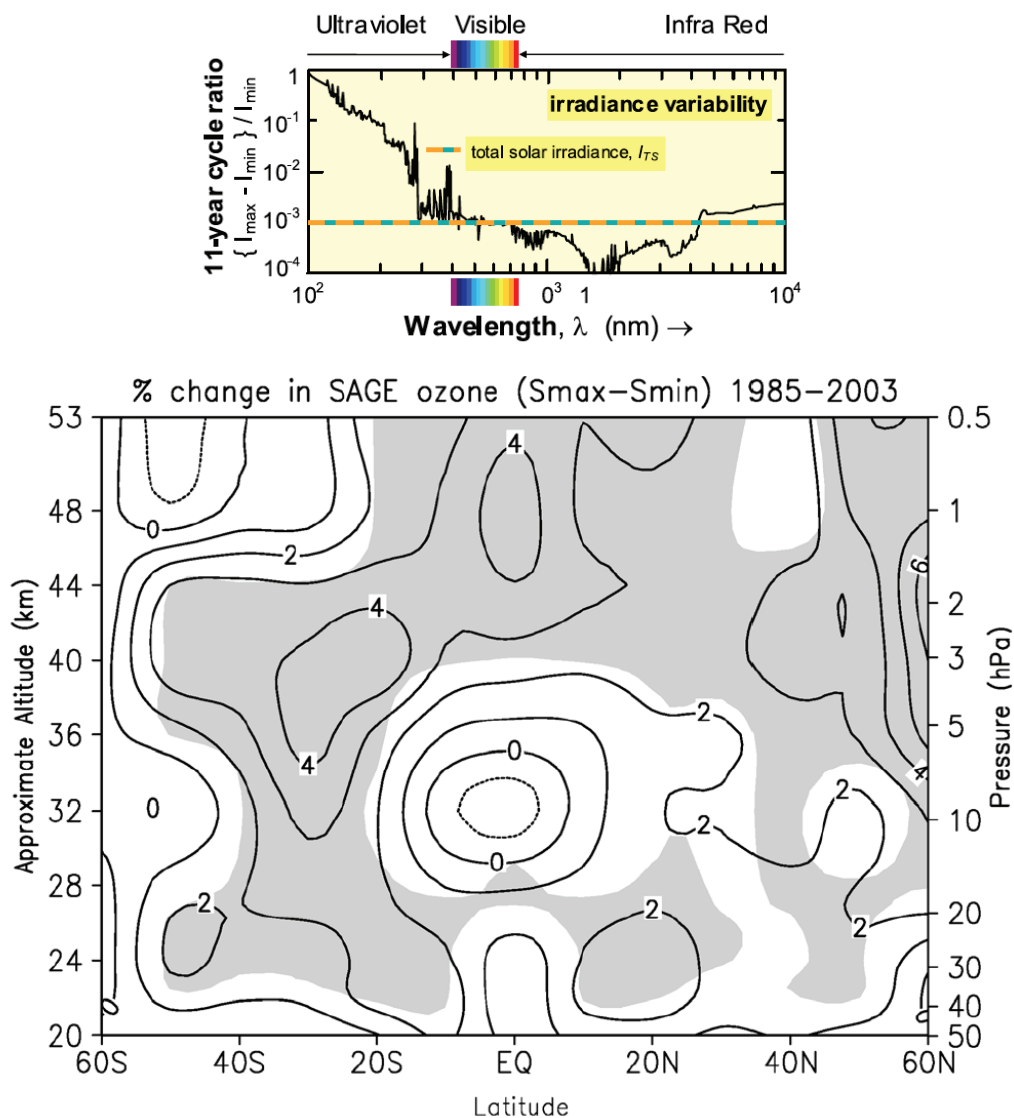


Figure 1.12: The Top panel shows the spectral variability of the irradiance. The horizontal dashed line gives the corresponding value for the total solar irradiance as the integral over all wavelengths (Gray et al., 2010). The bottom panel shows percentage change in stratospheric ozone over solar maximum minus solar minimum conditions ( $S_{max}-S_{min}$ ) for the time period from 1985 to 2003, whereas shaded areas indicate significant at the 5% level (Soukharev & Hood, 2006).

changes in UV radiation can perturb the thermal structure of ozone by photochemical processes which in turn can affect the atmosphere below. This can be experienced in changing weather patterns near the surface (Merkel et al., 2011; Oberländer et al., 2012).

The North Atlantic Oscillation is defined as a fluctuation in atmospheric pressure between a sub polar low-pressure zone over Iceland and a high-pressure zone over the Azores region (Figure 1.13). The NAO has two modes: negative and positive. During the positive NAO phase, the pressure is lower over Iceland and higher over the Azores, causing milder and wetter weather conditions over the eastern US and northwest Europe and cold and dry conditions over Greenland and northern Canada. The opposite

pattern is seen during negative modes of NAO (Lamb & Pepler, 1987; Castro-Diez et al., 2002; Ruddiman, 2007; Olsen et al., 2012a). The Arctic Oscillation is also an oscillation in which atmospheric pressure at polar and mid-latitude locations (Azores) fluctuates between positive and negative phases. The negative phase of the AO occurs when the polar pressure is higher than normal and the mid-latitude pressure is lower than usual, causing less cold stratospheric conditions, and vice versa for the positive phase (Thompson & Wallace, 1998; Bridgman & Oliver, 2006). The North Atlantic Oscillation (NAO) and the Arctic Oscillation (AO) are closely related. It is disputed whether one or the other is more fundamentally representing the dynamics of the atmosphere (p.c. Seidenkrantz, M.-S, 2012).

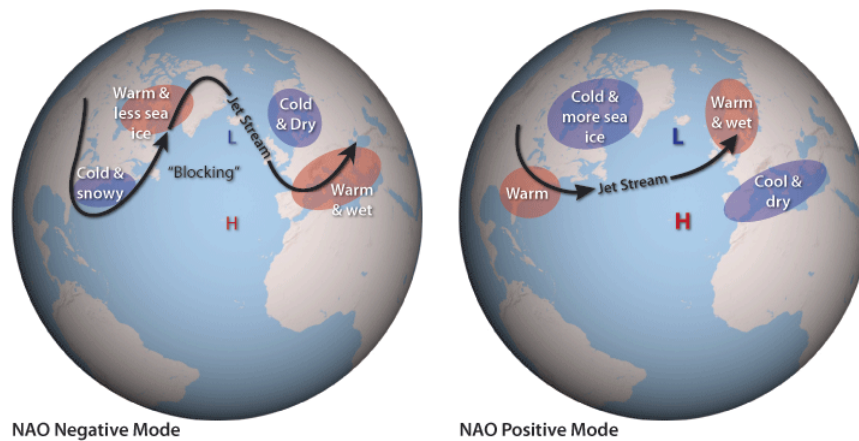


Figure 1.13: The North Atlantic Oscillation negative (left) and positive (right) modes (Image courtesy of NOAA).

## Solar Variability and Its Influence on the Monsoon Intensity

Neff et al. (2001) investigated the variations in the Indian Ocean Monsoon intensity using  $\delta^{18}\text{O}$  records measured in a stalagmite in Hoti cave located in northern Oman. Monsoons occur as a result of temperature difference between the land and the ocean, since the land responds to seasonal changes in solar radiation much quicker than the ocean does (Ruddiman, 2007). Neff et al. (2001) compared their  $\delta^{18}\text{O}$  records with  $\Delta^{14}\text{C}$  measurements from tree-rings and found that the temporal variations in both records are highly correlated, suggesting that the two records are responding to the same forcing mechanism, variations in the solar magnetic activity levels.

Wang et al. (2005) measured  $\delta^{18}\text{O}$  in a stalagmite from Dongge Cave in southern China, which is related to the variations in the precipitation rate over the region and hence characterising the Asian Monsoon intensity. In order to evaluate the link between the Asian Monsoon strength and solar variability, the authors compared their detrended  $\delta^{18}\text{O}$  record ( $\Delta^{18}\text{O}$ ) with detrended  $^{14}\text{C}$  record ( $\Delta^{14}\text{C}$ ), which is shown in Figure 1.14. As seen in Figure 1.14, during high solar activity periods, seen as low  $^{14}\text{C}$  values, the strength of the Asian Monsoon increases, seen as smaller  $\Delta^{18}\text{O}$  values in the figure. Wang et al. (2005) also identified periodicities of 558, 206 and 159 years in the  $\Delta^{18}\text{O}$  record, which they relate to the periodicities in the  $\Delta^{14}\text{C}$  record, suggesting a link between variations in solar activity and Asian Monsoon strength.

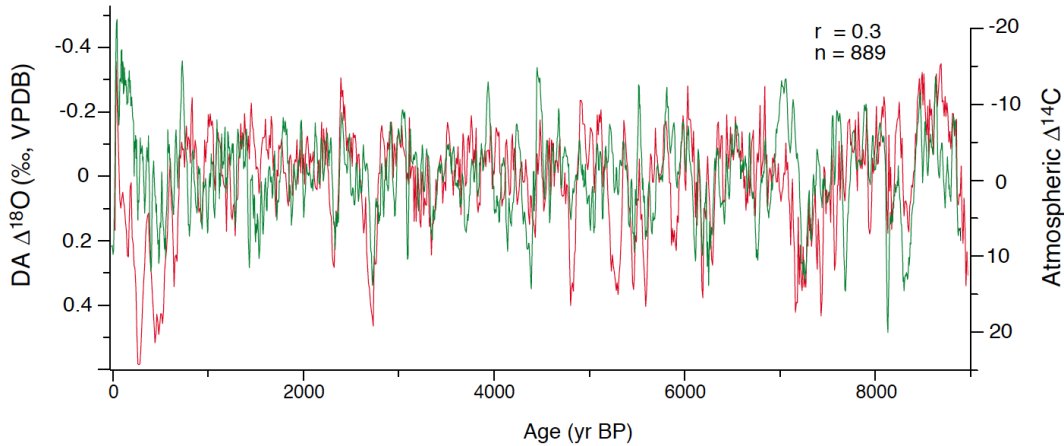


Figure 1.14: Time series of the  $\Delta^{18}\text{O}$  record (five-point running average, green line) and the  $\Delta^{14}\text{C}$  record (red line). All data have been detrended using singular spectrum analysis. Higher solar irradiance (smaller  $\Delta^{14}\text{C}$ ) corresponds to a stronger Asian Monsoon (smaller  $\Delta^{18}\text{O}$  value). The correlation coefficient is 0.30 for the entire profile and 0.39 between 9 and 6 ky B.P. (from Wang et al., 2005).

### Solar variability and Its Influence on the Ocean Dynamics

In addition to the studies concerning influences of solar irradiation variations on atmospheric circulation patterns, there are several studies investigating the long-term influence of the Sun on the climate of the North Atlantic region and ocean circulation patterns (Bond et al., 2001; Braun et al., 2005; Muscheler & Beer, 2006). In these studies, solar activity variations back in time are reconstructed by cosmogenic radionuclides  $^{10}\text{Be}$  and  $^{14}\text{C}$  records obtained from different natural archives.

Bond et al. (2001) used both  $^{10}\text{Be}$  records from Greenland ice cores and  $^{14}\text{C}$  records from tree rings to produce a combined record of production rates in order to interpret the relationship between solar activity and ice rafting episodes during the Holocene (last  $\sim 11,700$  years) known as the Bond events. As a result of their study, Bond et al. (2001) claimed that intervals with reduced solar irradiance coincide with increases in North Atlantic ice drift episodes in their records.

Braun et al. (2005) used an intermediate complexity climate model with glacial conditions to produce rapid climate shifts similar to the Dansgaard-Oeschger (D-O) events having a periodicity of  $\sim 1470$  years previously suggested by Schulz (2002). In order to generate a similar signal, Braun et al. (2005) used fresh water input to the North Atlantic Ocean as a forcing mechanism with periodicities of  $\sim 87$  and  $\sim 210$  years corresponding to the Gleissberg and the Suess solar cycles, respectively. Their results also showed that, even though no 1470-year periodicity has been found in solar activity records, observed 1470-year D-O cycles can be explained by a superposition of two shorter fresh water cycles. Braun et al. (2005), however, did not find evidence for the 1470-year cycle using the Holocene climate conditions, and the role of the 1470-year cycle during the Holocene is subject to debate. Studying  $^{10}\text{Be}$  and  $\delta^{18}\text{O}$  data, Muscheler & Beer (2006) suggested that they could not find any convincing evidence for a solar influence on the D-O events. Therefore, it remains unclear whether solar variability has an influence on the major climatic shifts within glacial intervals and hence the ocean circulation patterns.

D-O cycles are defined as rapid temperature oscillations over Greenland between extremely cold intervals called stadials and milder conditions called interstadials dur-

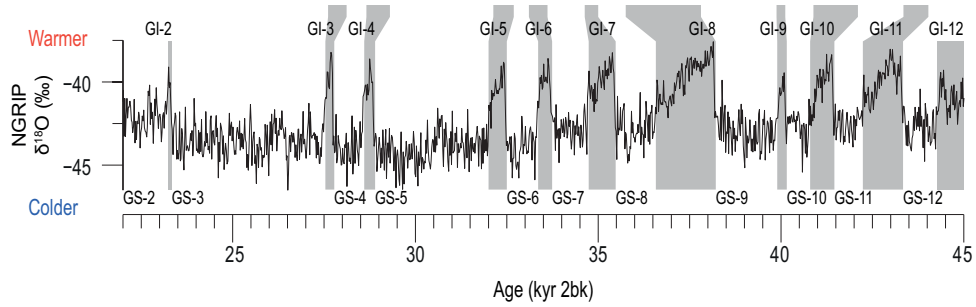


Figure 1.15: Temporal variation of  $\delta^{18}\text{O}$ , using data from Wolff et al. (2010) (p. c., Olsen, J., 2014).

ing glacial intervals, which is evident from  $\delta^{18}\text{O}$  measurements of Greenland ice cores (Dansgaard et al., 1993; Ruddiman, 2007) and marine cores (Bond et al., 1999). Figure 1.15 shows the measured  $\delta^{18}\text{O}$  concentrations in the North Greenland Ice Core Project (NGRIP) data (Wolff et al., 2010), where the D-O cycles can be observed as warmer and colder intervals, shaded in the figure (p. c., Olsen, J., 2014). GI and GS represents Greenland Interstadial and Greenland Stadial events, respectively.

Another pattern seen in marine core records, called Heinrich events (H events), are explained by episodes of unusual abundant ice rafting (Heinrich, 1988; Ruddiman, 2007). D-O cycles and H events are thought to be closely coupled to the surrounding ice sheets, which through release of icebergs and meltwater are likely to disturb the thermohaline circulation (THC), the currents driven by density differences primarily caused by surface fluxes of heat and fresh water across the sea surface and subsequent interior mixing of heat and salt (Rahmstorf, 2002), and in turn the Atlantic Meridional Overturning Circulation (AMOC), which carries warm waters from equatorial regions to Polar Regions where North Atlantic Deep Water formation occurs, and returns cold deep waters to the equatorial region. This heat transport mechanism is fundamental to the climate of the Northern Hemisphere and a reduced AMOC can have a strong impact on climate (Heinrich, 1988; Dansgaard et al., 1993; Bryden et al., 2005).

To interpret the basic relationships between solar activity and climate, it is necessary to study pre-industrial era, since in this period greenhouse gas concentrations were relatively stable and the degree of orbital forcing was relatively small. Even though climate variability during the Holocene shows evidence of the solar periodicities, e.g. 11 year, 22 year, 80-90 years, 208 years, 2300 years (Knudsen et al., 2009; Gray et al., 2010), we have a poor understanding of how the Sun influences the climate system, therefore the link between solar variability and climate system still needs to be investigated (Baroni et al., 2011).

Therefore, to study possible influences of solar activity on climate requires short and long-term reconstructions of solar activity parameters (Gray et al., 2010). Following the separation of the solar signal on the climate reconstructions from other influences, e. g. noise signals, the underlying mechanisms must be explained, since the solar irradiance variations are small and their effect on the climate must be amplified by feedback mechanisms or internal responses (see Figure 1.9). The coupling of lower atmosphere to ocean circulation and/or to the stratosphere represents important examples of internal responses of the climate (Haigh, 2001).



## Chapter 2

# Aim of the Ph.D. Project

The overall objective of my Ph.D. project is to study solar variability on different time scales using the solar photospheric magnetic field, open solar magnetic field, neutron counting rates, sunspot numbers and in particular solar modulation potential reconstructions based on cosmogenic nuclides,  $^{10}\text{Be}$  in ice cores and  $^{14}\text{C}$  in tree rings. This includes generating the first  $^{10}\text{Be}$  concentrations and fluxes measured in a midlatitude ice core deriving from the Tsambagarav mountain range in Mongolia.

Current  $^{10}\text{Be}$  records stem from polar ice cores from Greenland and Antarctica within the minimum  $^{10}\text{Be}$  deposition areas (see Figure 1.7), which implies that they may not reflect the global  $^{10}\text{Be}$  production signal (Field et al., 2006). Additionally, because of the local short-and long-term climatic noise, mentioned in Section 1.7, there are some discrepancies among current  $^{10}\text{Be}$  records that lead to some ambiguities regarding the current solar reconstructions (Muscheler et al., 2007a). For example, Bard et al. (1997, 2007) and Muscheler et al. (2007a,b) suggested that the solar activity at around  $\sim 1200$  A.D. and  $\sim 1780$  A.D. was at least as high as the activity around  $\sim 1950$ , while Solanki et al. (2004) suggest that the present level of solar activity is unusually high and long compared to the preceding 8000 years.

In order to achieve the objectives presented above, I studied five different, but interconnected, projects and I have published and submitted articles in various scientific journals. In the following I will present brief summaries of these studies, whose full versions can be found in Part II, including the published and submitted articles.

### 2.1 Summary of Paper I

#### Modeling the Relationship Between Neutron Counting Rates and Sunspot Numbers Using the Hysteresis Effect

Information on the past solar activity variations before the solar observations is mainly based on the past production rates of the cosmogenic radionuclides from terrestrial archives, such as  $^{10}\text{Be}$  in ice cores and  $^{14}\text{C}$  in tree rings (Bard & Frank, 2006). Cosmogenic radionuclides are produced when galactic cosmic ray particles, which are inversely correlated with solar activity levels, interacts with atmospheric N and O.

In order to gain a more detailed understanding of the relationship between sunspot numbers (SSNs), as an indicator of the solar magnetic activity levels, and NCRs, as indicator of GCR intensity near/at Earth, we investigated the hysteresis effect between SSNs and NCRs, over a time period that covers the last four solar cycles, we built up a non-linear empirical model that connects variations in NCRs and SSNs.

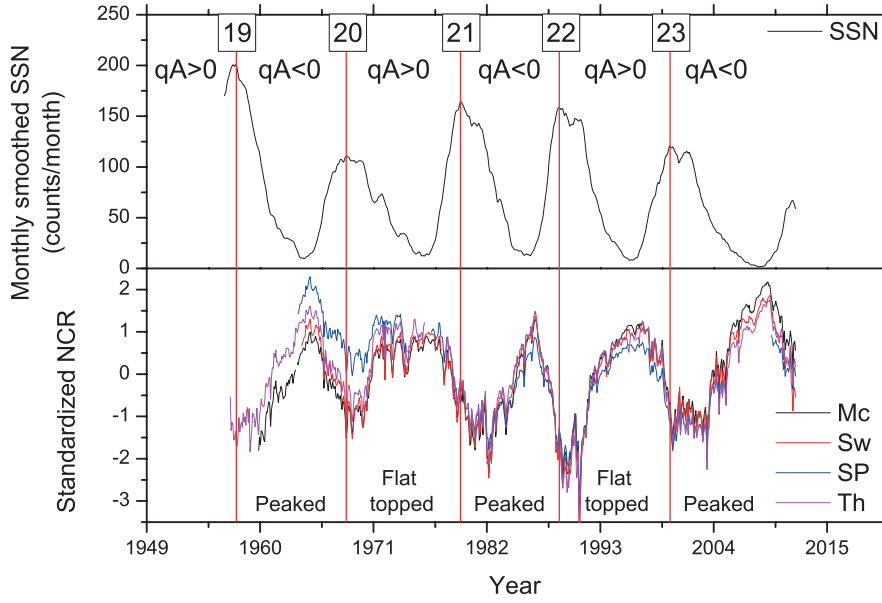


Figure 2.1: SSNs (top) and NCRs recorded by neutron monitors (bottom). Mc, Sw, SP, and Th denote McMurdo, Swarthmore, South Pole, and Thule neutron monitors, respectively.

To build our relationship, we used pressure-corrected NCRs from four different neutron monitors (NMs) located on the various places on the Earth. Three of these monitors (South Pole and McMurdo in Antarctica, and Thule in Greenland) are located close to the poles, whereas one, Swarthmore, is located in Pennsylvania. SSN data throughout the last four solar cycles were taken from the Solar Influences Data Center. Figure 2.1 shows standardised NCRs from different NMs together with the monthly smoothed SSNs. In the figure, we also showed the polarity state of the axial dipole component of the large-scale magnetic field of the Sun, which are indicated with  $qA>0$  and  $qA<0$  for positive and negative polarity states, respectively.

To investigate this relationship and the long-term modulation of GCRs, cross-correlation analysis was applied to the data covering the last four solar cycles as well as to the data for each solar cycle. The analysis yields an average time lag of 5 months between the SSNs and the GCRs, while cycle-wise cross correlation yields longer time-lags between NCRs and SSNs for odd-numbered solar cycles (12 months), such as solar cycle 21 and 23, and almost no time-lag during even-numbered solar cycles. This implies that the shape of the hysteresis curves between NCRs and SSNs during odd-numbered solar cycles are wider in comparison to those during even-numbered solar cycles. Figure 2.2 shows an example for the hysteresis curves for solar cycle 21 for four different NMs. As seen in Figure 2.2, the shape of the hysteresis loops, which are significantly wider compared to the even-cycle loops, enables us to use ellipse modeling, which improves the representation of the relationship between SSNs and NCRs, instead of a linear fit. However for even cycles, the hysteresis loops are narrow due to the fact that the time-lag between NCRs and SSNs are almost zero, favouring linear modelling.

In this work, we suggest a new non-linear empirical model between NCRs and SSNs based on the hysteresis effect to reconstruct NCRs and GCR intensity. This model uses linear- and ellipse-modeling procedures separately for even and odd cycles, respectively, due to the fact that the hysteresis loops for even and odd solar cycles

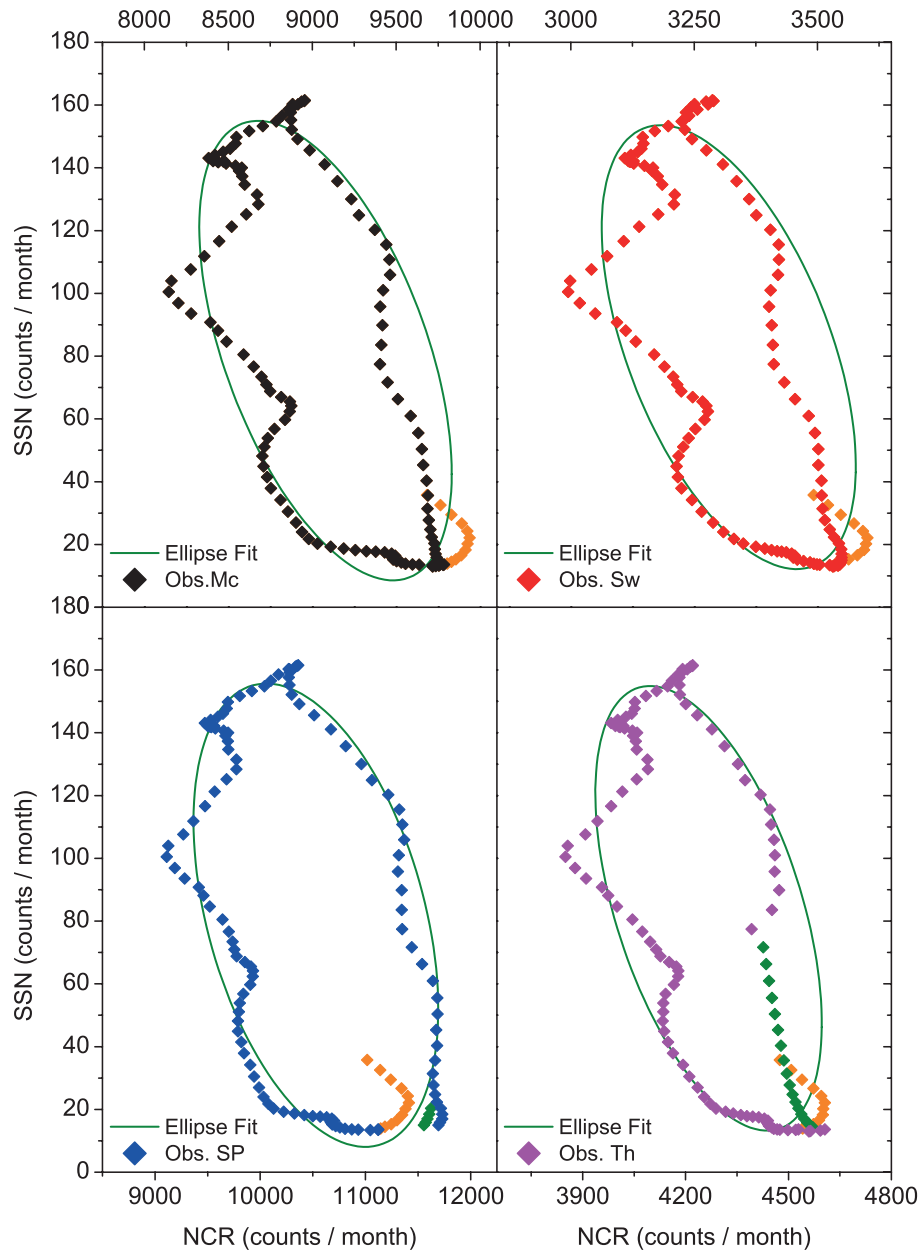


Figure 2.2: Ellipse fitting of NCRs recorded by four neutron monitors for the 21st cycle. Orange and green diamonds show extended (see the text) and interpolated data, respectively.

show different shapes, which is related to the polarity states of the Sun. By using this method, we reconstructed NCRs based on SSNs during solar cycles 20, 21, 22, and 23 (Figure 2.3). The NCRs reconstructed using the new approach are in good agreement with observed NCRs, as indicated by correlation coefficients of 0.95, 0.95, 0.94, and 0.95 for smoothed data from the neutron monitors McMurdo, Swarthmore, South Pole, and Thule, respectively. In comparison, we obtained correlation coefficients of 0.84, 0.84, 0.62, and 0.78 for smoothed data from the same NMs when applying linear fit to the whole data sets.

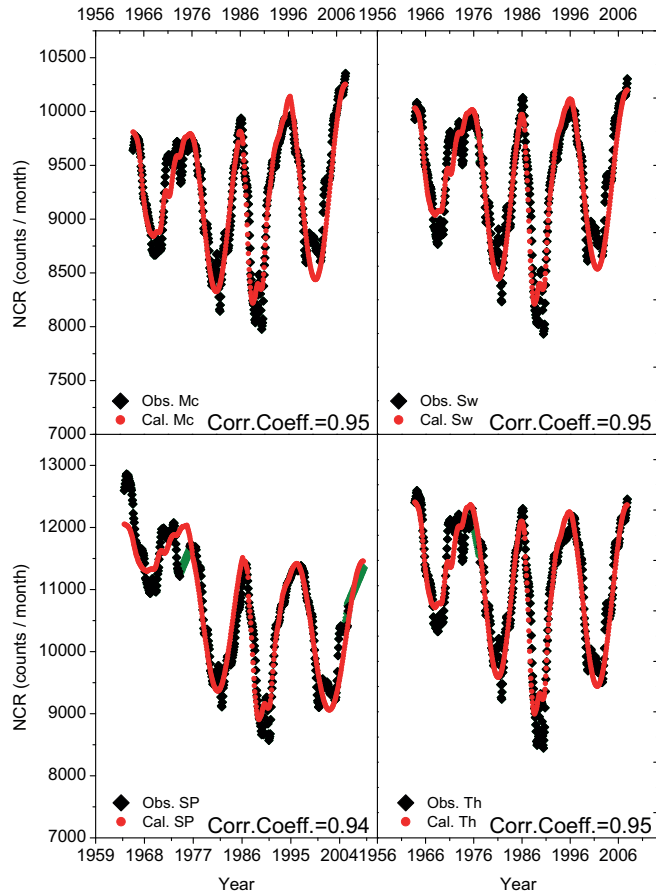


Figure 2.3: Observed and modeled NCRs variations in time with the relevant correlation coefficients for the neutron monitors. Black diamonds and red dots show observed and calculated values, respectively, whereas green diamonds show interpolated data.

## 2.2 Summary of Paper II

### Reconstruction of Sub-Decadal Changes in Sunspot Numbers based on the NGRIP $^{10}\text{Be}$ Record

After construction a relationship between SSNs and NCRs using the hysteresis effect, we investigated the relationship between the solar modulation strength,  $\Phi$ , calculated based on annually resolved  $^{10}\text{Be}$  measurements in the NGRIP (the North Greenland Ice Core Project) ice core from Greenland, and observed group sunspot numbers (Hoyt and Schatten, 1998) to reconstruct subdecadal changes in group sunspot numbers for the time period spanned by the ice-core  $^{10}\text{Be}$  record (Figure 2.4) between 1391 and 1985.

We first tested three simple empirical approaches, namely linear, ellipse-linear and ellipse models, (latter two are based on the hysteresis effect observed between GCRs, which are modulated through the heliosphere, and SSNs, Inceoglu et al., 2014a), in combination with a physics-based model (Usoskin et al., 2002a, 2004), to the annually-resolved  $^{10}\text{Be}$  measurements. By using these three approaches, we reconstruct high-resolution changes in SSNs including variations in the 11-year solar cycle. The highest cross-correlation between the reconstructed and observed group SSNs was found as 0.81 for a time lag of one year for the whole overlapping period from 1610 to 1985

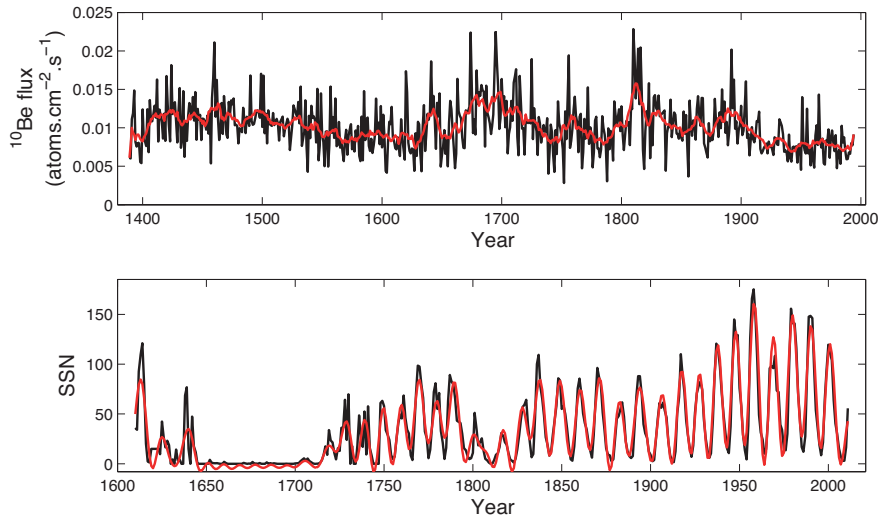


Figure 2.4: From top to bottom, the NGRIP  $^{10}\text{Be}$  flux and group SSNs. In the top panel, the black line shows the NGRIP  $^{10}\text{Be}$  flux data corrected for Earth's geomagnetic field following Knudsen et al. (2009) and the red line corresponds to the 11 year-moving-average of the NGRIP  $^{10}\text{Be}$  flux (see text). In the bottom panel, the black line shows the group SSNs and the red line corresponds to the low-pass filtered groups SSNs with a cut-off frequency of  $(1/9)$  year $^{-1}$  for the observed group SSNs.

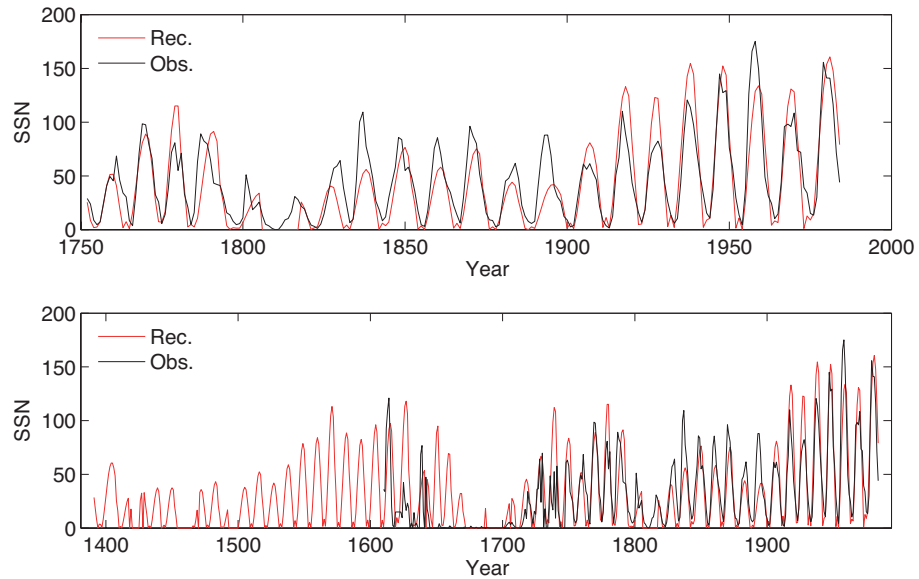


Figure 2.5: The top panel shows the resulting ellipse modeling reconstruction of group SSN, using data that were low-pass filtered with a cut-off frequency of  $(1/9)$  year $^{-1}$  (see text), and the observed group SSNs for the time period covering between 1619–1984. The bottom panel shows reconstructed and observed SSNs for the time period covering between 1391–1984. The black line corresponds to the observed group SSNs and the red line shows the reconstructed group SSNs based on the NGRIP ice core.

when we use ellipse approach. Because given the average residence time of  $^{10}\text{Be}$  in the atmosphere of one to two years, uncertainties related to the age-depth model of the

NGRIP ice core (Vinther et al., 2006), and climate-related noise, it was challenging to reconstruct well-defined hysteresis curves. In spite of the success of the ellipse-linear approach when applied to instrumental data (Inceoglu et al., 2014a), the ellipse approach clearly provides the most robust method to reconstruct subdecadal changes in group SSNs back in time based on the NGRIP  $^{10}\text{Be}$  flux, because it simply provides a much better representation of the observed group SSN data compared to the linear and ellipse-linear approaches. The resulting reconstruction is shown in Figure 2.5.

We also compared our long-term SSN reconstruction with three different SSN reconstructions by Usoskin et al. (2003c, 2014) and Solanki et al. (2004), which are shown in Figure 2.6 together with the observed group SSNs. Usoskin et al. (2003c) used  $^{10}\text{Be}$  concentrations in ice cores from Greenland and the South Pole, while Usoskin et al. (2014) and Solanki et al. (2004) used  $^{14}\text{C}$  from tree rings to reconstruct decadal-scale changes in group SSNs.

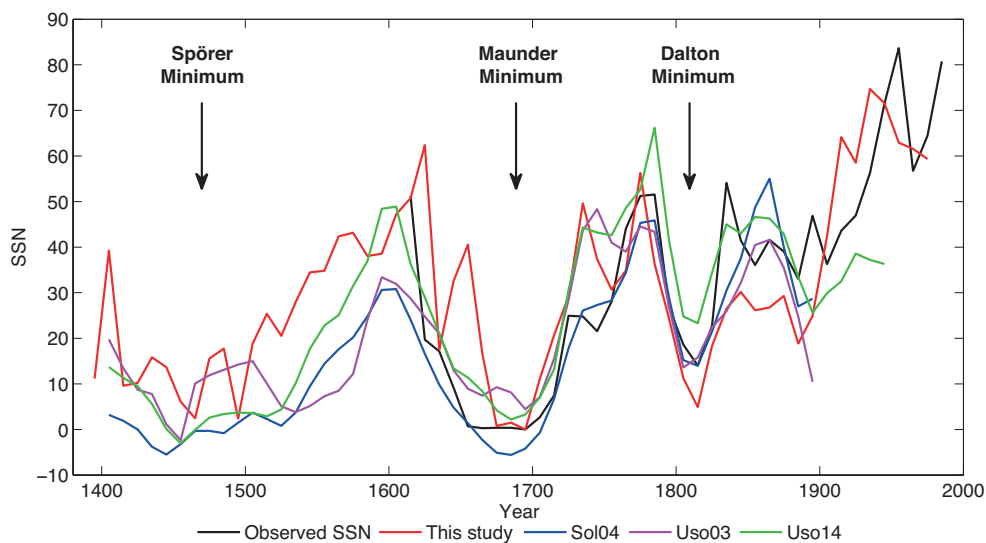


Figure 2.6: Reconstructed group SSNs in this study (10-year average, red line), decadal reconstructions of Usoskin et al. (2014) (Uso14, green line), Usoskin et al. (2003c) (Uso03, magenta line), Solanki et al. (2004) (Sol04, blue line), and decadal  $\text{SSNs}_{\text{Obs}}$  (black line).

We concluded that the long-term changes in reconstructed group SSNs based on the NGRIP ice core record agree reasonably well with the other group SSN reconstructions with some discrepancies. These discrepancies result from differences in the underlying proxy data for past solar activity, hereby demonstrating the potential influence of climatic noise. Therefore, to better resolve short-term changes in solar variability prior to 1610 A.D., which is necessary to improve our understanding of the Sun, we need more high-resolution  $^{10}\text{Be}$  records that extend farther back in time.

## 2.3 Summary of Paper III

### Grand solar minima and maxima deduced from $^{10}\text{Be}$ and $^{14}\text{C}$ : Magnetic dynamo configuration and polarity reversal

In this study, we aim, in particular, to improve our understanding on the origin of the long term solar variability from Grand Maximum to Grand Minimum, since achieving

a better understanding of the solar influence on Earth’s climate requires knowledge of past solar variability. To this aim we used the GRIP  $^{10}\text{Be}$  and IntCal13  $^{14}\text{C}$  records, in order to reconstruct the solar modulation potentials ( $\Phi$ ) for the overlapping time period spanning the last 8250 years, which are shown in Figure 2.7. We used, for the first time, the two solar modulation potential reconstructions simultaneously to detect grand minima and maxima periods.

As seen in the upper panel of Figure 2.7, even though there is a good agreement between short-term fluctuations, there are some discrepancies between the long-term variations of the two reconstructions. The observed long-term differences between the two reconstructions can be caused by long-term changes in the atmospheric transport and deposition of  $^{10}\text{Be}$  and undetected changes in carbon cycle (Vonmoos et al., 2006). In order to remove the observed long-term trends from the time series, we first calculated the long-term trends in data sets using polynomial fits of degree 5, then subtract the values of the long-term trends. After removal of the long-term trend from the two time series, we standardised the data using their mean and standard deviation values.

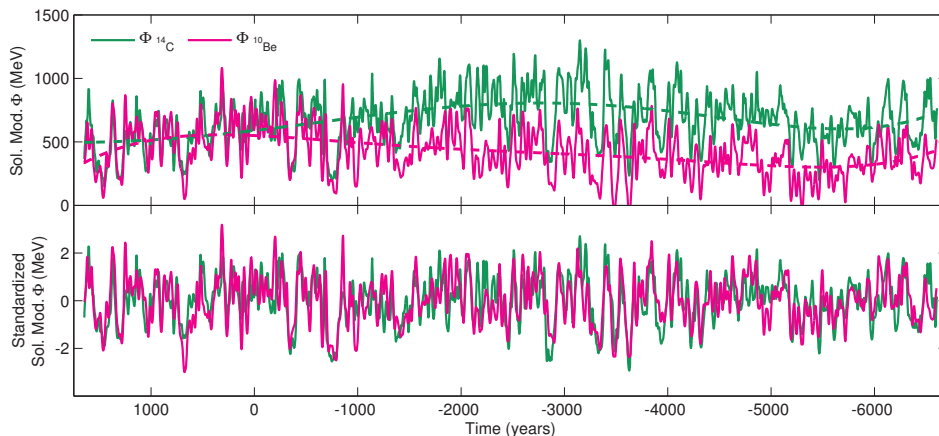


Figure 2.7: Top panel: Solar modulation potential based on the GRIP  $^{10}\text{Be}$  (magenta) and the IntCal13  $^{14}\text{C}$  (green) records. Dashed lines show the long-term trend observed in calculated solar modulation potentials. Bottom panel: Detrended and standardised solar modulation potential based on polynomial fits of degree 5.

The lower panel of Fig. 2.7 shows the detrended and standardised solar modulation potential reconstructions based on  $^{10}\text{Be}$  and  $^{14}\text{C}$ . Temporal variations in the detrended solar modulation potential reconstructions are in good agreement, implying that the short-term variations seen in the reconstructions reflect the solar component within the data.

Following to that, we defined three selection criteria to identify grand minima and maxima periods observed in the two data sets as follows;

(i) low/high activity periods have to occur simultaneously in the two time series for the overlapping period. Therefore, by using zero crossing method, we determined 160 events, peaks and dips, occurring in the two solar modulation potential reconstructions at the same time. Using the two reconstructions at the same time provides more robust identifications of these low/high activity periods,

(ii) the amplitudes of the low/high activity events have to be lower/higher than a certain threshold value. In order to calculate these threshold values, we fitted bimodal gaussian curves on the distributions of the events which were determined in (i),

(iii) the durations of these periods have to be longer than 22-year Hale cycle.

Using these criteria, we identified 32 grand minima and 21 grand maxima periods occurring in the both reconstructions at the same time.

In order to investigate the origin of the detected grand minimum and maximum activity states of the Sun and durations of these periods, we applied waiting time distribution analyses to the data. Waiting times can be considered as intervals the time intervals between subsequent peaks or dips in activity (Wheatland et al., 1998). The statistical distribution of the waiting times between discrete events has been broadly used in physical sciences to investigate whether the underlying mechanisms of such events are random processes or processes related to energy accumulation and release (Wheatland, 2000; Lepreti et al., 2001; Wheatland, 2003). An exponential waiting time distribution indicates that the mechanism causing such events is a Poisson process, which is a memoryless, purely random process, where the occurrence of an event is independent of the preceding one (Usoskin et al., 2007). On the other hand, if the waiting time distribution follows a power law, the occurrence is dependent of an event, implying that the mechanism has a memory of the previous events (Clauset et al., 2009).

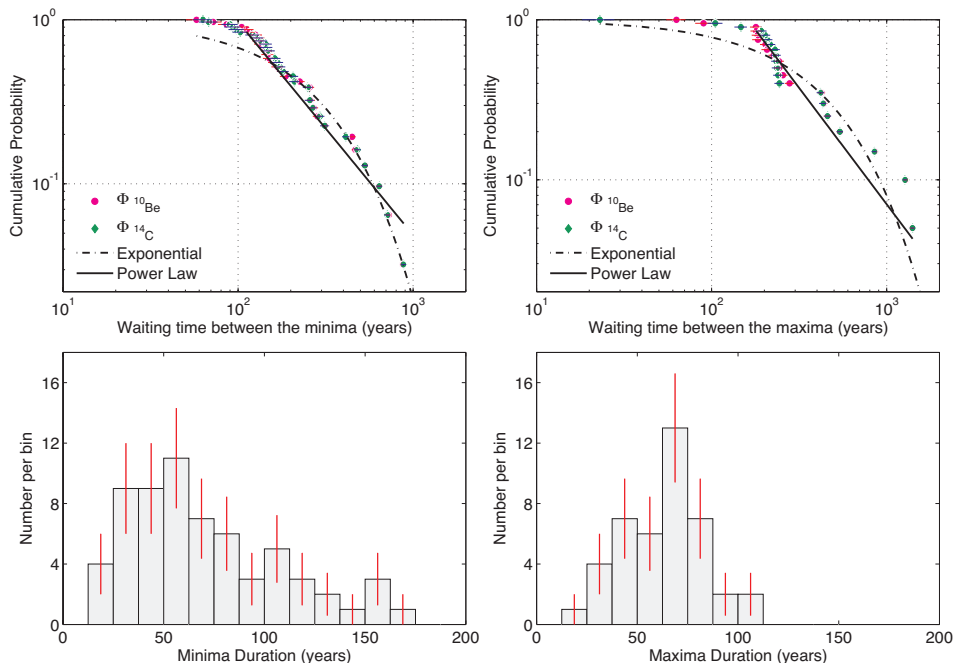


Figure 2.8: The results of the waiting time distribution analyses. Top panels show the complementary cumulative distribution function for grand minima and grand maxima together with the power-law and exponential fits using MLM. Bottom panels show the distributions of durations of the grand minima and maxima, respectively.

The results of the analysis, which are shown in the upper panel of Figure 2.8, suggest that the origin of the observed grand minima and maxima periods reflect processes related to energy accumulation and release, implying that the system has a memory effect and occurrences of these periods are not caused by stochastic noise. The lower panel of Figure 2.8 shows that there is an upper limit of  $\sim 100$  years for the duration of Grand Maxima, which shows a normal distribution with a mean duration of  $\sim 65$  years, while the duration of grand minima episodes exhibits a lognormal distribution with a mean value of  $\sim 70$  years, based on the criteria defined in this

study.

We have also constructed cross-wavelet periodograms of the two solar modulation potential based on  $^{10}\text{Be}$  and  $^{14}\text{C}$  in order to investigate the magnetic cycle lengths during grand minima and maxima periods. In fact, if these events are not memoryless as suggested by the results of the waiting time distribution analyses, we expect to observe regular patterns in the cycle length variation over Grand Minima and Maxima (Tobias1998REF).

The bottom panel of Fig. 2.9, which is focusing on the identified Grand Minima and Maxima based on the criteria defined in this study, show the resulting local cross-wavelet power spectra of high-pass filtered  $\Phi_{10Be}$  and  $\Phi_{14C}$  with a cut-off frequency of  $(1/30)\text{ year}^{-1}$  together with the solar modulation potential reconstructions based on  $^{10}\text{Be}$  and  $^{14}\text{C}$ , respectively (top panel). In the figure, we also show minimum and maximum solar activity periods identified based on the criteria defined in this study.

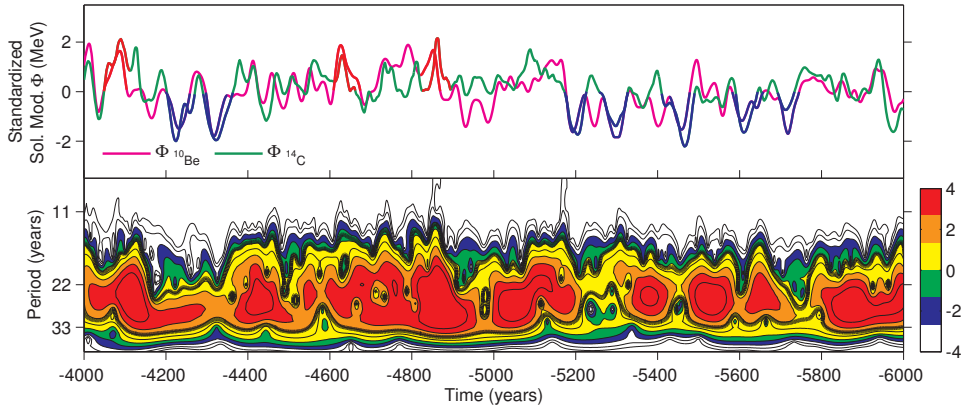


Figure 2.9: Top panel: Temporal change in  $\Phi_{10Be}$  and  $\Phi_{14C}$ . Blue and red lines show identified grand minima and maxima, respectively. Bottom Panel: Local Cross-wavelet spectrum of the high pass filtered  $\Phi_{10Be}$  and  $\Phi_{14C}$  with a cut-off frequency of  $(1/30)\text{ year}^{-1}$ , focusing on identified Grand Minima periods by criterion defined in this study.

One interesting feature observed in the cross-wavelet power spectra of the high-pass filtered solar modulation potential reconstructions, is that it is still possible to follow the temporal behaviour of the periods lower than 40 years that are present in the data. When the bottom panel of Fig. 2.9 is carefully examined, we might see that the significance of the 22-year Hale cycle during Grand Minimum/Maximum states decreases/increases, respectively, implying that the power of the 22-year periodicity under consideration becomes weaker during Grand Minima states, whereas the power of the 22-year Hale cycle signal seems stronger during Grand Maxima states.

Combined results from the analyses of  $^{10}\text{Be}$  and  $^{14}\text{C}$  data show that Grand Minimum/Maximum events are likely to reflect processes related to energy accumulation and release and there is an upper limit of  $\sim 100$  years for the duration of Grand Maxima based on the criteria defined in this study. This can be interpreted as a limit on the solar dynamo capability to sustain higher activity levels for longer periods and this number can be directly compared with predictions based on solar dynamos regarding the length of Grand Maxima.

## 2.4 Summary of Paper IV

### Is the Sun entering a Modern Minimum State? Interpreting the current solar magnetic activity characterising its behaviour during the Holocene period

The recent behaviour of solar magnetic activity has attracted a great interest, since it has become very modest soon after the end of the Modern Maximum in 2000. The minimum phase of Solar cycle 23, which has  $\sim 265$  spotless days, characterises Solar cycle 24, as it is the weakest in 140 years. Therefore, it is an open debate whether the Sun has entered a long quiescent activity period named grand minimum.

Therefore, we investigated distinct patterns in the occurrences of grand minima and maxima in the solar modulation potentials calculated based on the GRIP  $^{10}\text{Be}$  and the IntCal13  $^{14}\text{C}$  data during the Holocene epoch identified in the previous study. As variations in solar magnetic activity are driven by the Sun's dipole large-scale magnetic field, we also investigated how the single dipolar component developed over the last decades by studying their temporal evolution, as the strength of the forthcoming cycle is already established at the maximum of solar activity of the preceding cycle, when the axial dipole field is at its minimum. We then compared solar magnetic activity over the last three solar cycles with magnetic activity level of previous grand minima and maxima, as the solar modulation potential keeps the memory of the Sun's dipole magnetic field.

We used solar modulation potential reconstruction based on IntCal13  $^{14}\text{C}$  data to investigate the occurrence rate of grand minima and maxima during the Holocene period. We, then, used the Wilcox Solar Observatory data to track the temporal evolution of the dipolar components of the magnetic dynamo configuration.

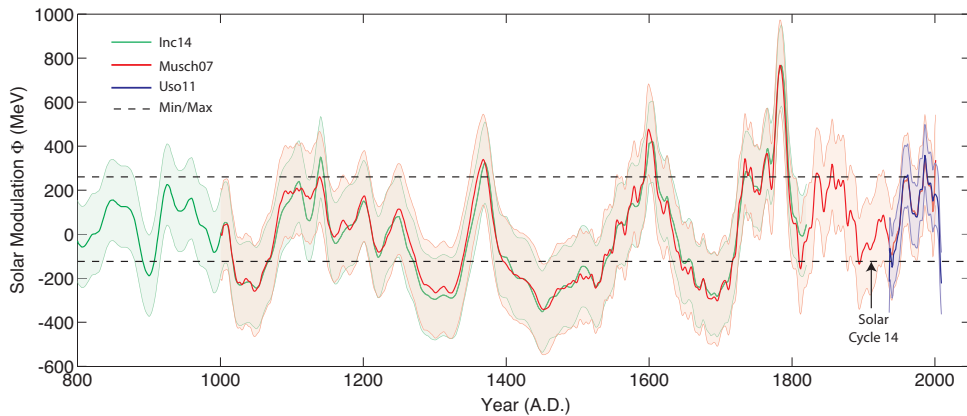


Figure 2.10: Solar modulation potential reconstructions by Inceoglu et al. (2014c) (green line, based on IntCal13  $^{14}\text{C}$ ), by Muscheler et al. (2007a) (red line, based on SHCal  $^{14}\text{C}$ , IntCal04  $^{14}\text{C}$  from 1000 to 1510 AD and annual  $^{14}\text{C}$  data from 1511 to 1950 AD) and by Usoskin et al. (2011) (blue line, based on neutron monitor data). Dashed lines show the threshold values for grand minima and maxima periods. Shaded areas indicate the %68 confidence interval calculated based on each dataset, separately. Note that here we only show the period from 800 to 2009 AD for visual purposes, even though the records extends from 6600 BC to 2009 AD.

The cosmogenic radionuclide data analysis showed that 71% of grand maxima are followed by a grand minimum and it also indicates that the activity level of the Sun, soon after 2000, is comparable to the previous grand minima (Figure 2.10). Over

the last three solar cycles, the axial and toroidal component of the Sun's dipole large scale magnetic field underwent a steady decrease, which are shown in Figure 2.11. Furthermore we also found lines of evidence showing that the axial dipolar component needed longer time to build up its magnetic configuration since 1980.

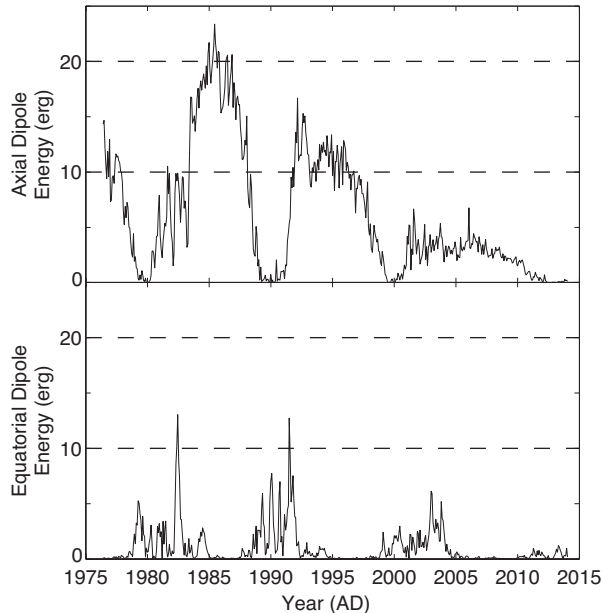


Figure 2.11: The top panel shows the temporal evolution of the total energy in the axial component of the dipole mode of the solar large-scale magnetic field, while the bottom panel represents the temporal evolution of the total energy in the equatorial component of the dipole mode.

The recent solar dynamics seem to be well represented by the pattern grand maxima followed by a grand minimum, as the Modern Maximum (1914–2000) has ended with Solar cycle 23 and the solar magnetic activity is comparable to previous grand minima since 2000. Furthermore, there are no signatures of an increase in the axial dipole magnetic field, which might suggest that Solar cycle 25 will be even weaker than Solar cycle 24. Therefore, it is possible that the Sun is already in a Modern Minimum state. The occurrence characteristics and rates of grand maxima and minima seem to support the scenario in which the dynamical non-linearity induced by the Lorentz force leads the Sun to act as a relaxation oscillator. Here the large-scale magnetic field of one parity (dipole or quadrupole) drives velocity perturbations and energy is exchanged between the magnetic field and the velocity.

## 2.5 Summary of Paper V

### **A continuous ice core $^{10}\text{Be}$ record from Mongolian mid-latitudes: Influences of solar variability and local climate**

Using a general circulation model, Field et al. (2006) calculated that the maximum deposition of  $^{10}\text{Be}$  occurs at temporal latitudes instead of polar regions, where all the currently available high-resolution  $^{10}\text{Be}$  records derive from. Therefore,  $^{10}\text{Be}$  measurements from a mid-latitude ice core will provide an important contribution towards our understanding of global production rates of cosmogenic nuclides.

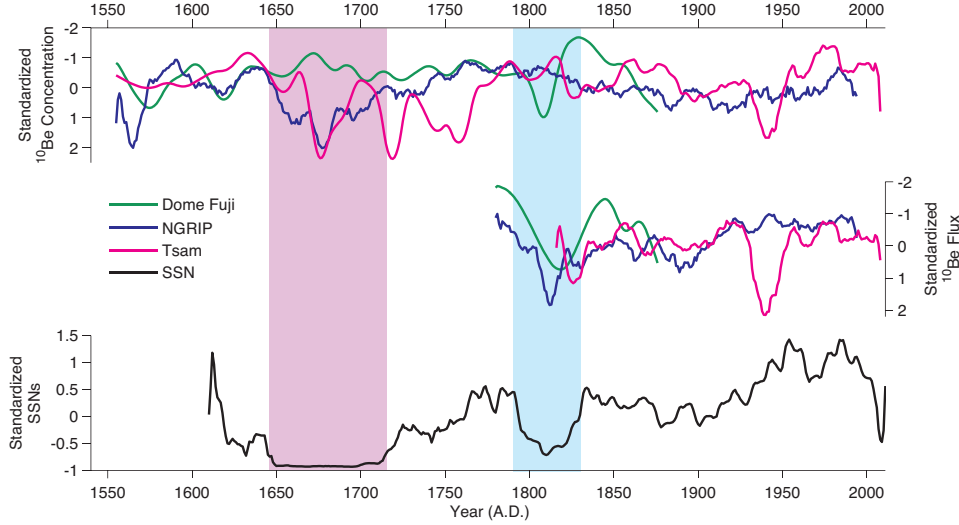


Figure 2.12: The top panel shows 11-year moving average values of the  $^{10}\text{Be}$  concentrations measured in the Tsambagarav (magenta-solid and red dashed), the NGRIP (blue) and the Dome Fuji (green) ice cores, whereas the middle panel shows the  $^{10}\text{Be}$  flux rates of the three ice cores. Notice that the x-axes of the top and mid-panels are reversed. The bottom panel shows 11-year moving average values of the observed group sunspot numbers. The purple and the blue bands show the Maunder Minimum and the Dalton Minimum, respectively.

In this study, we present  $^{10}\text{Be}$  measurements from a mid-latitude mountain glacier ice core from Tsambagarav, Mongolia, covering the period between  $\sim 1550$  and 2009. The Tsambagarav ice core was collected in 2009 in the Tsambagarav mountain range located in the Mongolian Altai and it extends back to 6000 B.P. (see Herren et al. (2013) for details). We also compared our results to two  $^{10}\text{Be}$  records from polar ice cores, the North Greenland Ice Core Project (NGRIP) (Berggren et al., 2009) and Dome Fuji (Horiuchi et al., 2008) and found that even though the long-term trends observed in the Tsambagarav  $^{10}\text{Be}$  concentration and flux records are reasonably similar to the NGRIP and the Dome Fuji  $^{10}\text{Be}$  records, there are some notable discrepancies between them. Figure 2.12 presents the 11-year moving averages of the  $^{10}\text{Be}$  concentrations and the fluxes from the three ice cores together with the 11-year moving averages of the observed group sunspot numbers (SSNs) (Hoyt and Schatten, 1998). The  $^{10}\text{Be}$  concentrations and flux rates of the each ice core and the group SSNs are standardised according to their individual mean and standard deviation values.

To investigate the possible influences of local climate, which may be the possible cause of the observed discrepancies between the Tsambagarav  $^{10}\text{Be}$  record and the NGRIP and the Dome Fuji  $^{10}\text{Be}$  records, and compare them to the effects of solar activity, we have applied multiple regression analysis to the Tsambagarav  $^{10}\text{Be}$  concentrations and fluxes using the major ion ( $\text{Ca}^{2+}$ ,  $\text{Mg}^{2+}$ ,  $\text{Na}^+$ ,  $\text{Cl}^-$ ,  $\text{SO}_4^{2-}$ ,  $\text{NH}_4^+$ ,  $\text{HCOO}^-$ ,  $\text{K}^+$ ,  $\text{NO}_3^-$ ) and  $\delta^{18}\text{O}$  records measured in the Belukha ice core (Eichler et al., 2009) as well as the group SSNs. We used the Belukha ice core from the Siberian Altai, located in relative close proximity to Tsambagarav, because the Tsambagarav major ion record was not available.

The results of our analyses suggested that grand solar minima, *i.e.*, the Maunder and Dalton Minima, influenced the  $^{10}\text{Be}$  record and moreover that the 11-year solar-cycle signal is present in the Tsambagarav ice core. However, some notable

discrepancies are observed between the Tsambagarav  $^{10}\text{Be}$  record and the two  $^{10}\text{Be}$  records from Greenland and the South Pole, potentially due to effects linked to regional meteorological phenomena, such as cyclonic versus anticyclonic conditions and storm tracks affecting the  $^{10}\text{Be}$  deposition in the Tsambagarav region.

## 2.6 Summary of Paper VI

### The lost sunspot cycle: New support from $^{10}\text{Be}$ measurements

It has been suggested that the Dalton minimum (1790 – 1830) might hide a lost sunspot cycle, sometimes referred to as cycle 4b. In this paper, we reanalyse  $^{10}\text{Be}$  measurements from the NGRIP ice core from North Greenland (Berggren et al., 2009) to evaluate the lost cycle hypothesis. The analysis built based on the hysteresis effect, which has been reported by various authors (Mavromichalaki & Petropoulos, 1984; Marmatsouri *et al.*, 1995; Gupta et al., 2006; Mavromichalaki et al., 2007; Inceoglu et al., 2014a).

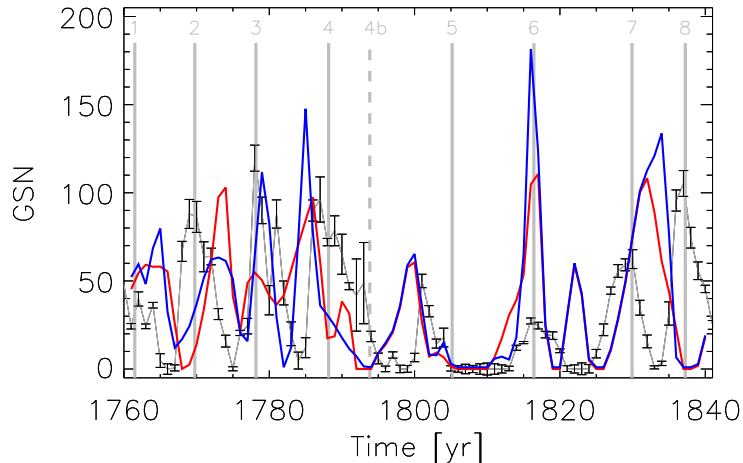


Figure 2.13: Comparison between the observed GSN (black line), the GSN calculated based on  $^{10}\text{Be}$  measurements and assuming a cycle 4b (blue line) and the GSN calculated based on  $^{10}\text{Be}$  measurements and not assuming a cycle 4b (red line). The calculation including cycle 4b is supported by the Bayesian analysis. Again, the solid grey lines indicate the midpoints of the canonical solar cycles, whereas the dashed line indicates the midpoint of cycle 4b.

To achieve these objectives, we first model the hysteresis effect using differential equations, which will not cause problems when linking even and odd cycles, and we adjust the physical model by Usoskin et al. (2002a, 2004) to work on a sub-cycle time scale. This makes it possible for us to compare two reconstructions of the GSN around the Dalton minimum – one with the lost cycle and one without.

Figure 2.13 shows the group SSN reconstruction based on the continuous model assuming cycle 4b (blue line) and not assuming cycle 4b (red line). Following to reconstructing the group SSNs, we applied the Bayesian analysis, which is provided by Feroz & Hobson (MULTINEST, 2008); Feroz et al. (MULTINEST, 2009), in order to evaluate which model (4b assuming or not assuming) represents the variations in the

observed group SSNs during the Dalton Minimum better. As a result of this analysis, we suggest that the NGRIP  $^{10}\text{Be}$  record supports the lost Solar cycle hypothesis.

## Chapter 3

# Work in Progress

### 3.1 Modelling Surface Ocean $^{14}\text{C}$ Variability during MIS 3 with GENIE-1: An outline

The overall aim of this project is to study the mechanisms behind the variations observed in the North Atlantic surface ocean  $^{14}\text{C}$  records during Marine Isotope Stage 3 (MIS3) ( $\sim 27 - 60$  ky BP). In order to investigate these mechanisms to explain the behaviour of temporal variation of  $^{14}\text{C}$  records, we have been using a 3D ocean, 2D atmosphere  $^{14}\text{C}$  coupled Earth-System model GENIE-1 of intermediate complexity. GENIE-1 was previously used to investigate the origin of atmospheric carbon increase during the Younger Dryas cold reversal period (12.9 - 11.7 kyr BP), which is an abrupt climate change during the transition from glacial to interglacial conditions (Singarayer et al., 2008). By comparing the model outputs and actual measurements of  $\Delta^{14}\text{C}$  from different oceans, Singarayer et al. (2008) concluded that  $\Delta^{14}\text{C}$  increase observed on the onset of the YD caused by ocean reorganisation.

The Dansgaard-Oeschger (D-O) cycles and Heinrich (H) events are dominant modes of climate change patterns in the North Atlantic during the glacial period (Bond et al., 1999). They are thought to be closely coupled to the surrounding ice sheets, and through release of icebergs and meltwater, they can disturb the AMOC, resulting in reduced ventilation in the deep ocean (Heinrich, 1988; Dansgaard et al., 1993). This, in turn, will change the carbon exchange rate between the atmosphere and the deep ocean leading to changes in the  $^{14}\text{C}$  activity of the surface ocean.

The top two panel of Figure 3.1 shows  $\Delta^{14}\text{C}$  values from different natural archives, e. g. speleothems from Bahamas (Hoffmann et al., 2010), marine sediments from Cariaco Basin (Hughen et al., 2006), speleothems from Hulu Cave (Southon et al., 2012), Suigetsu Lake (Ramsey et al., 2012), Marine09 (Reimer et al., 2009) and LINK15 (Olsen et al., 2014), where the upper-bottom panel shows calculated reservoir ages of LINK15 samples during MIS3. The difference between Cariaco Basin  $\Delta^{14}\text{C}$  and LINK15  $\Delta^{14}\text{C}$  values is shown in the lower panel of Figure 3.1. H3 and H4 show Heinrich events 3 and 4, and GI represents Greenland Interstadials, when the climatic conditions were milder during the glacial period.  $\Delta^{14}\text{C}$  is defined as per mil depletion or enrichment of the atmospheric  $^{14}\text{C}$  values with regard to standard normalised for isotope fractionation (Stuiver & Polach, 1977), whereas reservoir age is the difference between atmospheric and oceanic  $^{14}\text{C}$  ages. The reservoir age is a representative of the carbon exchange rate between these two dynamic systems and is defined as the age offset between the contemporaneous atmosphere and ocean. Higher reservoir ages, lower  $\Delta^{14}\text{C}$  in the figure, thought to be connected to lack of carbon exchange between the surface of the ocean and the atmosphere due to ice cover. The mechanism

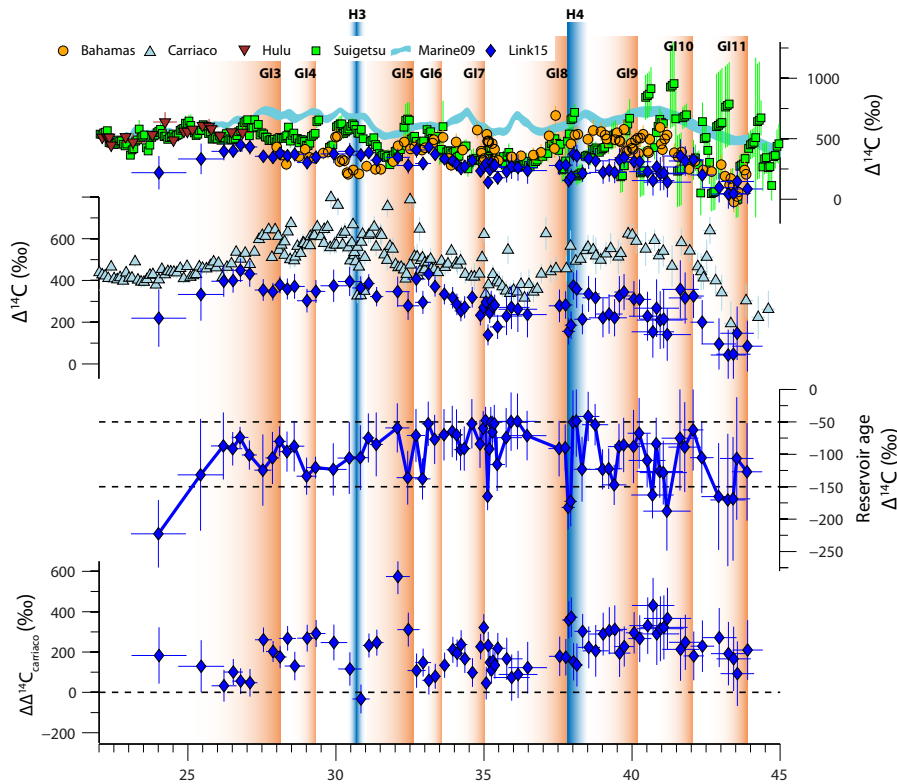


Figure 3.1:  $\Delta^{14}\text{C}$  values obtained from different natural archives as indicated on the upper most panel (see text) (p.c. Olsen, J., 2013).

behind the occurrence of transitions from Greenland interstadials to stadials (a.k.a. D-O Cycles) was suggested as slowing or ceasing the deep water formation due to decrease of the salinity of surface water caused by fresh water discharge, where deep water formation occurs. Slowing or ceasing THC, thus, will cause a weak AMOC, and weak heat transport from equatorial regions, and colder conditions in the Northern Hemisphere, where meltwater runoff and ice growth will take place (Broecker et al., 1985), resulting in cold periods referred to as Greenland stadials (GS). This can be seen in the bottom-mid panel of Figure 3.1. In the beginning of event H4, the reservoir age reached its minimum value ( $\sim -200\text{‰}$ ) and atmospheric  $^{14}\text{C}$  levels show a peak (bottom panel), implying that ocean-atmosphere exchange of carbon was minimum believed to be due to extended ice cover, where a weak or ceased AMOC is expected. After H4, towards GI8, a sharp increase in reservoir age ( $\sim -100\text{‰}$ ) and a decrease in atmospheric  $^{14}\text{C}$  levels are observed, implying that ocean ventilation occurs, where AMOC runs. However, the same pattern is not observed for event H3 in the reservoir age panel of Figure 3.1 as it is observed for event H4. In their work, van Meerbeek et al. (2009) perform climate simulations with a 3D earth system model in order to test the suggestion that MIS3 stadials and interstadials are caused by resumption of the THC from weak states during stadials to a relatively strong states during interstadials. They conclude that there was no significant reduction in sea-ice cover and no difference in sea surface temperatures between stadials and interstadials and surface ocean circulation and AMOC remained relatively unaltered (van Meerbeek et al., 2009).

Therefore, to reproduce surface ocean  $^{14}\text{C}$  variability of the North Atlantic during

MIS3 Stadial, MIS3 Interstadial and MIS3 Heinrich events and to investigate the possible forcing and driving mechanisms behind this variation (see Figure 3.1), we model  $^{14}\text{C}$  variation using GENIE-1 and compare the modelled values to observed  $^{14}\text{C}$  surface ocean variability in marine core LINK 15, which has been  $^{14}\text{C}$  dated in high detail (total 78 dating points).

Setting the boundary conditions to MIS3 Stadial conditions as  $\text{CO}_2=200$  ppmv,  $\text{CH}_4=450$  ppbv and  $\text{N}_2\text{O}=220$  ppbv following van Meerbeeck et al. (2009), we first ran the model for 20000 years so the model could reach an equilibrium. Following the equilibrium state of the generated stadial period, we introduced fresh water of 0.18 Sv into the North Atlantic for a hundred years to weaken the AMOC to produce a Heinrich event. Figure 3.2 represents sea-ice cover, ocean velocity and  $\Delta^{14}\text{C}$  values during the model stadial period and the Heinrich event. As seen in Figure 3.2, following the fresh water hosing into the North Atlantic, global ocean circulation, which is indicated by the ocean velocity in lower-top panel of the figure, weakens and thus the sea-ice cover in the North Atlantic retreats back. This is thought to be caused by the lack of humid and warm air transportation from the equatorial latitudes to the polar latitudes due to weakening of the global stream function. Additionally, reduction in ocean ventilation due to weakening of the global ocean circulation causes longer time for exchange of  $^{14}\text{C}$  between atmosphere and the ocean surface. This results in surface water  $\Delta^{14}\text{C}$  values that are closer to the values in the atmosphere, and consequently lower reservoir age, which are represented in the lower 2 panels of Figure 3.2.

The experimental run for the MIS3 Interstadial conditions and the control runs, in which the initial and boundary conditions are set to the pre-industrial era, together with the evaluation of the real data and model results are on the schedule to complete this study.

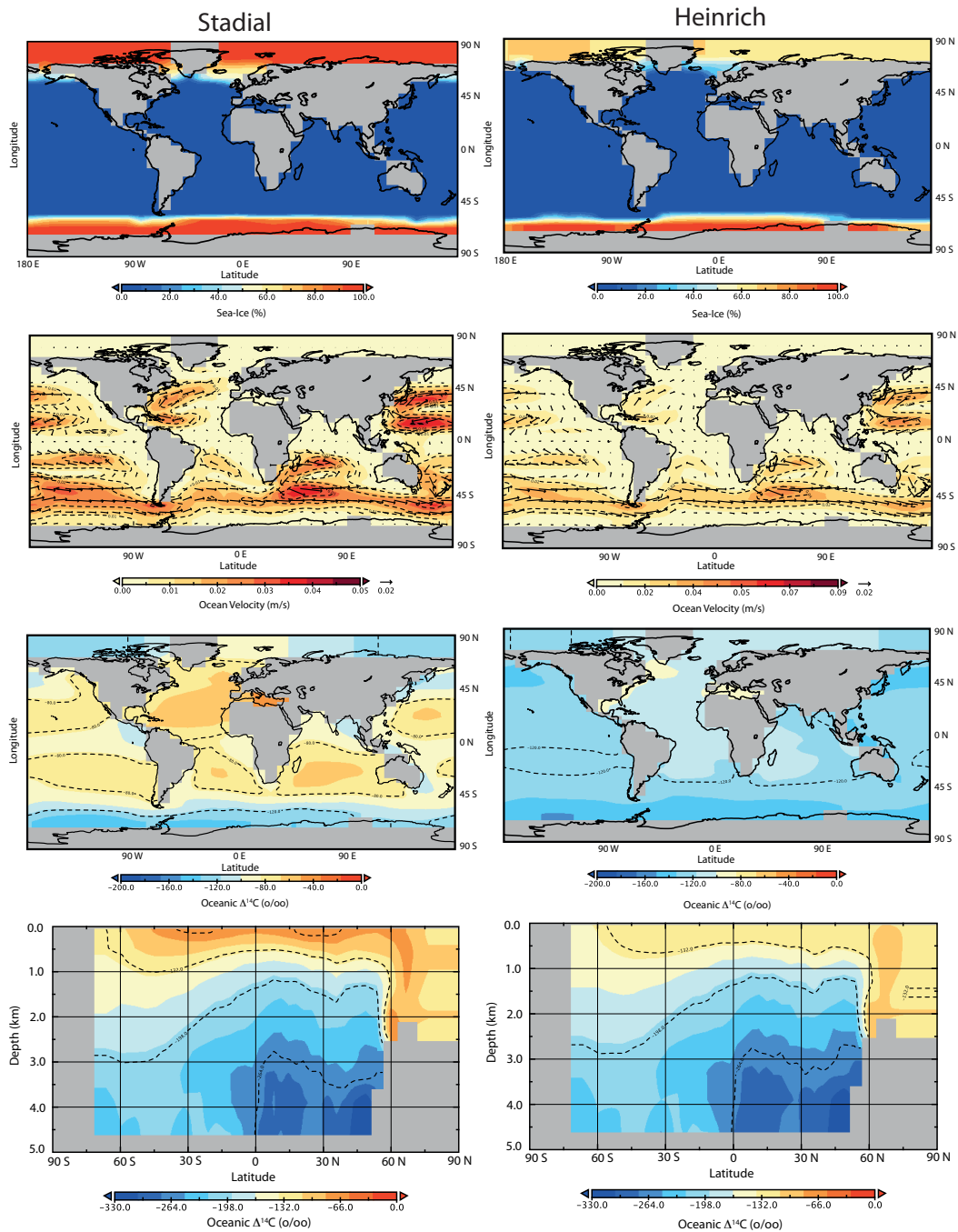


Figure 3.2: From top to bottom; sea-ice cover, ocean velocity, oceanic  $\Delta^{14}\text{C}$  in longitude-latitude, oceanic  $\Delta^{14}\text{C}$ -depth profile for the stadial period (left column) and the Heinrich event (right column).

## Chapter 4

# Future Work

### 4.1 Investigating the Astrophysical Origin of short-lived Cosmic Ray events and their impact on Earth's environment

Studying the Sun-Earth link is very important when we consider that we are living with a star that shows magnetic activity-related structures on its atmospheric layers, such as sunspots on the photosphere, flares on the chromosphere and coronal mass ejections on the corona. Located in the vicinity of these phenomena, the Earth, as a habitable planet, is vulnerable to high-energy solar flares and coronal mass ejections.

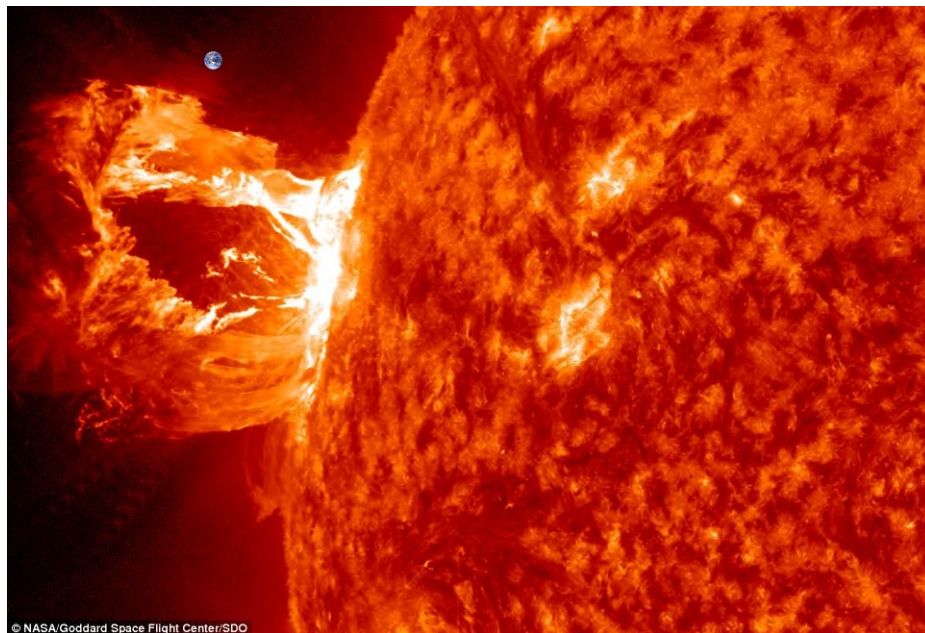


Figure 4.1: A solar flare and the Earth to scale (image courtesy of NASA).

My main motivation to pursue this research is to understand the possible effects of solar activity on Earth's atmosphere and climate. It is well known that the solar insolation has an influence on the climate due to changes in the tilt angle of the Earth and the eccentricity of the orbit, which occur on time scales of multiple ten thousands of years. These effects differ from those arising from solar magnetic activity variations, which take place on much shorter time scales. For shorter time scales, however, there is still an ongoing debate on the impacts of solar activity variations on the Earth

climate system and on the underlying physical mechanisms (Gray et al., 2010). In addition, the potential climate influences of impulsive solar activity events, such as solar flares and coronal mass ejections, remain open questions that are relevant for the general understanding of the mechanisms behind the sun-climate link.

Solar flares occur as a result of sudden energy releases, which has built up in the solar atmosphere in the vicinity of the spots observed on the photosphere of the Sun. Solar flares are generally followed by coronal mass ejections, where the Sun injects considerable amounts of plasma, that is composed of charged particles, from its corona into the interplanetary medium (see Figure 4.1 for scaled illustration) A powerful stream of these energetic charged particles will, when they hit Earth, introduce an extra amount of energy to the atmosphere changing its chemistry and hence its energy balance. To restore this balance, the atmospheric dynamics will undergo a chain of changes, which will lead to variations in atmospheric circulation patterns (Gray et al., 2010). In addition to influences of solar flares and coronal mass ejections on the atmospheric dynamics, they pose potential danger to the biosphere via changes in ozone as well as they can cause damages to our technology, for example on the satellites orbiting the Earth, power stations and power-grid networks and even on telecommunication lines (Thomas et al., 2013). Furthermore, from an astrobiological perspective, the understanding of the possible influence of stellar activity on habitable planets requires detailed studies of the Sun-Earth link, since our solar system is the only laboratory, where we can gain valuable information on this subject.

My future research career as a postdoc will focus on investigating how coronal mass ejections and solar flares interact with the upper atmosphere, and, hence, how this extra amount of energy and associated changes in atmospheric chemistry will affect the climate system. The effects of impulsive solar activity structures on the Earth's atmospheric circulation patterns are proposed to be studied with the chemistry-climate model SOCOL v3.0 (Solar Climate Ozone Link).

**Part II**

**Publications**



## Chapter 5

# Modeling the Relationship between Neutron Counting Rates and Sunspot Numbers Using the Hysteresis Effect

F. Inceoglu, M. F. Knudsen, C. Karoff, J. Olsen

*Published in Solar Physics (DOI 10.1007/s11207-013-0391-8)*

### Abstract

Several studies show that temporal variations in the galactic cosmic ray (GCR) intensity display a distinct 11-year periodicity due to solar modulation of the galactic cosmic rays in the heliosphere. The 11-year periodicity of GCRs is inversely proportional to, but out of phase with, the 11-year solar cycle, implying that there is a time lag between actual solar cycle and the GCR intensity, which is known as the hysteresis effect. In this study, we use the hysteresis effect to model the relationship between neutron counting rates (NCRs), an indicator of the GCR intensity, and sunspot numbers (SSNs) over the period that covers the last four solar cycles (20, 21, 22, and 23). Both linear and ellipse models were applied to SSNs during odd and even cycles in order to calculate temporal variations of NCRs. We find that ellipse modeling provides higher correlation coefficients for odd cycles compared to linear models, *e.g.* 0.97, 0.97, 0.92, and 0.97 compared to 0.69, 0.72, 0.53, and 0.68 for data from McMurdo, Swarthmore, South Pole, and Thule neutron monitors, respectively, during solar cycle 21 with overall improvement of 31% for odd cycles. When combined to a continuous model, the better correlation observed for the odd cycles increases the overall correlation between observed and modeled NCRs. The new empirical model therefore provides a better representation of the relationship between NCRs and SSNs. A major goal of the ongoing research is to use the new non-linear empirical model to reconstruct SSNs on annual time scales prior to 1610, where we do not have observational records of SSNs, based on changes in NCRs reconstructed from  $^{10}\text{Be}$  in ice cores.

Sun: activity – Sun: dynamo – Solar-terrestrial relations – Sunspots

### 5.1 Introduction

Galactic cosmic rays (GCRs) are charged particles with energy ranges from a few MeV to approximately  $10^{20}$  eV, impinging on the Earth from all directions. The majority of cosmic ray particles are atomic nuclei, but electrons, positrons, and other sub-atomic

particles are also included. At the top of the Earth’s atmosphere, the composition of GCRs includes protons (87%), alpha particles (12%), and heavier nuclei (1%) (Dunai, 2010). Upon entering the atmosphere, these particles interact with atmospheric atoms and produce secondary particles, primarily neutrons, via spallation and subsequent cascade processes. In order to observe the GCR intensity, neutron monitors were established at different latitudes on the Earth since the first half of the 20th century.

GCRs in the heliosphere are modulated by changes in the solar magnetic activity, and the number of sunspots on the surface of the Sun represents a widely used indicator of these activity variations. Sunspot numbers (SSNs) have been used to study past solar activity (Hoyt and Schatten, 1993; Lean, 2000; Solanki et al., 2004) and to predict the amplitudes of the forthcoming solar cycles (Owens et al., 2012), particularly the 24th solar cycle, which is the subject of much debate due to the extended minimum phase preceding this cycle (see *i.e.* Hathaway (2010) for a recent review).

Information on solar variations prior to 1610 relies on past production rates of cosmogenic nuclides, such as  $^{10}\text{Be}$  and  $^{14}\text{C}$  (Bard & Frank, 2006). Cosmogenic nuclides are produced in the atmosphere by interactions of GCR particles from space with atmospheric elements, such as N and O. Their production rates are inversely correlated with solar magnetic activity and the geomagnetic field intensity due to the non-linear shielding effect of the solar magnetic field and the geomagnetic dipole field (Heikkilä et al., 2008b).

Therefore, a more detailed understanding of the relationship between SSNs and neutron counting rates (NCRs), as indicator of GCRs, is needed since the time resolution of past cosmogenic nuclide production-rate reconstructions based on ice cores ( $^{10}\text{Be}$ ) and tree rings ( $^{14}\text{C}$ ) becomes increasingly higher (Baroni et al., 2011; Owens et al., 2012). Using such high-resolution records, it is possible to reconstruct GCR intensity further back in time prior to the instrumental measurements of NCRs. Information on the short- and long-term behavior of the GCR intensity obtained from cosmogenic nuclide production rate reconstructions will make it possible to reconstruct SSNs beyond 1610 AD and hence improve our understanding of the long- and short-term variations in solar activity cycles on millennial time scales.

In this study, we investigate the time lag between monthly SSNs and NCRs, as an indicator of GCR intensity, over a period that covers the last four solar cycles and we introduce a new model that links NCRs and SSNs and makes it possible to calculate temporal changes of NCRs based on the hysteresis effect. The layout of the paper is as follows. In Section 2, we describe the NCR data that we use. In Section 3, we study the hysteresis phenomenon. We then model the relationship between NCRs and SSNs in Section 4 and discussion and conclusions are found in Section 5.

## 5.2 Data Analysis

In order to study the long-term GCR modulation in the heliosphere over a time period covering solar cycles 20, 21, 22, and 23, we used pressure-corrected neutron counting rates (NCRs) obtained from four different neutron monitors (NMs). Three of these monitors (South Pole in Antarctica, McMurdo in Antarctica, and Thule in Greenland) are located close to the poles and have cut-off rigidities of 0.1–0.3 GV and thus record GCRs at essentially all energies, whereas one (Swarthmore) is located in Pennsylvania (39.9°N 75.4°E) and therefore has a cut-off rigidity of 2.4 GV. Since these stations are located around the globe at various geographical locations and altitudes, differences exist among the counting rates recorded at various neutron monitors (Usoskin et al., 1998, 1999, 2001a), but these differences do not affect the results presented in this

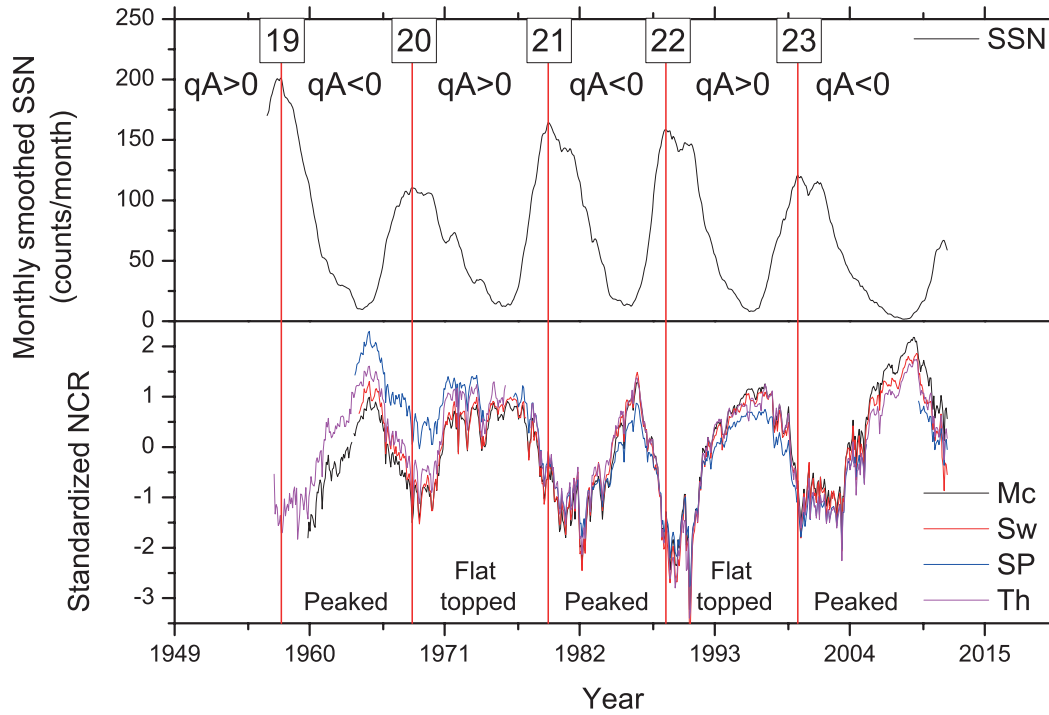


Figure 5.1: SSNs (top) and NCRs recorded by neutron monitors (bottom). Mc, Sw, SP, and Th denote McMurdo, Swarthmore, South Pole, and Thule neutron monitors, respectively.

paper. Additionally, it should be emphasized that there is a long-term trend in the counting rates of the South Pole NM, which may be due to improper normalization of its data and difficulties relating to maintenance of the NM (Ahluwalia and Ygbuhay, 2012). SSN data throughout the last four solar cycles were obtained from the Solar Influences Data Center <sup>1</sup>.

The pressure-corrected neutron counting rates from four different neutron monitors were standardized using their individual mean and standard deviation values. The standardization was used for plotting only. Temporal changes in neutron counting rates and monthly smoothed sunspot numbers are shown in Figure 5.1.

Although a strong correlation is observed between SSNs and NCRs it is also clear that the relationship between NCRs and SSNs varies from cycle to cycle. Especially, it is clear that NCRs show flat-topped maxima during transitions between declining phases of even cycles and inclining phases of odd solar cycles, whereas peaked-topped cycles are seen during transitions between declining phases of odd solar cycles and inclining phases of even solar cycles (Webber & Lockwood, 1988). This phenomenon is related to differences in the way the GCRs are modulated in the heliosphere during odd and even cycles, respectively, but no definitive explanation exists (Van Allen, 2000).

It is well known that the 11-year solar cycle is in fact a 22-year cycle, when the polarity of the large-scale solar magnetic field is taken into account (Hale et al., 1919). The varying relationships between NCRs and SSNs during odd and even cycles relate to the polarity of the large-scale solar magnetic field. The difference can be explained by including a drift term in the model due to Parker (1965) of

<sup>1</sup><http://sidc.oma.be/sunspot-data/>

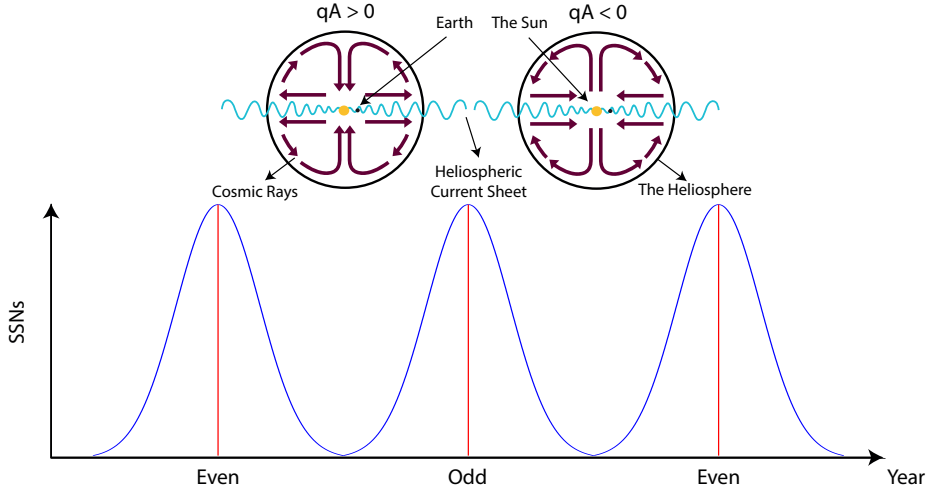


Figure 5.2: Illustration of trajectories of GCRs in the heliosphere under different solar polarity conditions (Modified from Jokipii, 2011).

Table 5.1: Cross-correlation coefficients and the corresponding time lags for each of the four neutron monitors for the period from 1957 to 2012.

Stations	Time lag (months)	Correlation coefficient	
		Without time-lag	With time-lag
McMurdo	5	-0.81	-0.86
Swarthmore	5	-0.81	-0.85
South Pole	5	-0.62	-0.66
Thule	6	-0.75	-0.79

the modulation of GCRs through the heliosphere as suggested by Jokipii, Levy, and Hubbard (1977) and Van Allen (2000). In this expanded model, the positively charged GCR particles ( $q > 0$ ) drift inward from the heliographic poles to the equator and outward along the current sheet when the polarity of the large-scale solar magnetic field is positive ( $qA > 0$ ), meaning that the direction of the polarity is aligned with the solar rotation axis (Figure 5.2). When the polarity of the large-scale magnetic field is negative ( $qA < 0$ ), the GCR particles experience an inward drift along the current sheet (Mavromichalaki et al., 1996, 1998) and therefore mainly enter the heliosphere through the equatorial regions. However, where the GCR particles experience an outward drift during the declining phase of even cycles and the onset of odd cycles ( $qA > 0$ ), they will experience an inward drift during the declining phase of odd cycles and onset of even cycles ( $qA < 0$ ) (Figure 5.2). This will lead to a slow recovery, which means longer time delays between changes in SSNs and GCRs (Van Allen, 2000) after maxima in odd cycles and a fast recovery after maxima in even cycles. In other words, the time it takes the GCRs to reach the Earth is smaller during the final phase of even cycles and the initial phase of odd cycles (Belov, 2000; Potgieter et al., 2001; Singh et al., 2008), resulting in a smaller delay between solar variability and cosmic ray particles reaching the Earth during even cycles. In addition, the observed peaked and flat-topped maxima in the temporal variation of NCRs are thought to be linked to these slow and fast recovery times (Van Allen, 2000; Ahluwalia and

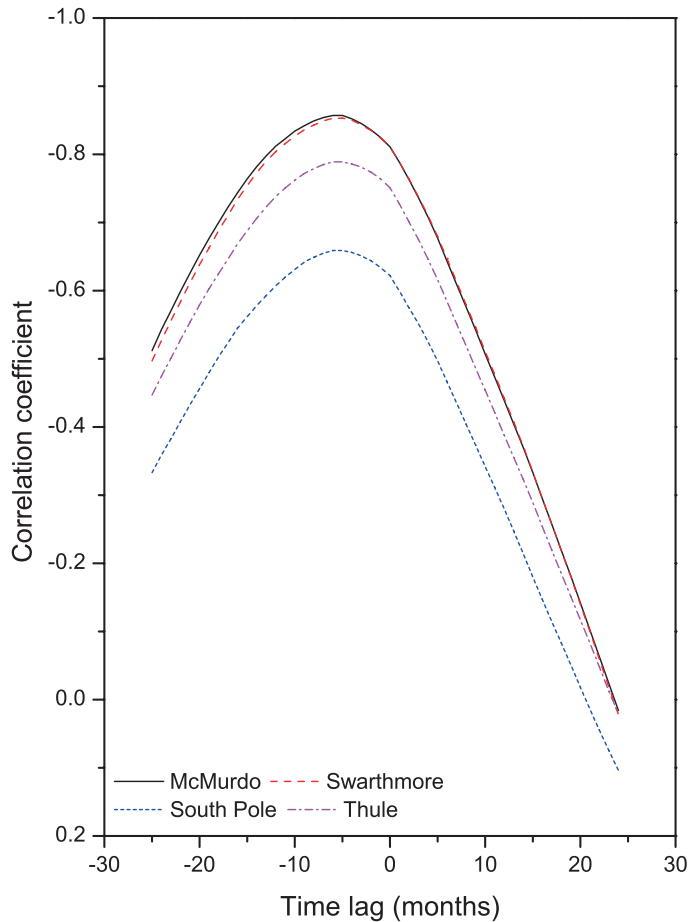


Figure 5.3: Corss-correlation coefficients between monthly NCRs and SSNs as a function of time lag.

Ygbuhay, 2012). Although this agrees with what is observed in Figure 5.1, where we also mark the polarity state of the large-scale solar magnetic field during the different cycles, it is not the only explanation for the varying, cycle-dependent relationships between NCRs and SSNs. Other explanations include *e.g.* the alignment between the polarity of the large-scale solar magnetic field and the galactic field (Nagashima & Morishita, 1980; Otaola et al., 1985). Additionally, it was found that GCRs experience a stronger modulation during positive solar polarity state conditions, whereas GCR particle modulation becomes relatively weaker during negative polarity states of the Sun (Alanko-Huotari et al., 2007).

To investigate this relationship and the long-term modulation of GCRs, cross-correlation analysis was applied to the data covering the last four solar cycles, using a time window of width  $T=50$  months centered at time  $t$ . Following the approach of Usoskin et al. (1998), we then calculated the cross-correlation for data shifted between  $t - T/2$  and  $t + T/2$ . The analysis yields an average time lag of 5 months between the SSNs and the GCRs (Figure 5.3 and Table 5.1).

### 5.3 Hysteresis Effect

The hysteresis effect and time lag between long-term variations in GCR intensity and solar activity have been reported before by various authors (Mavromichalaki &

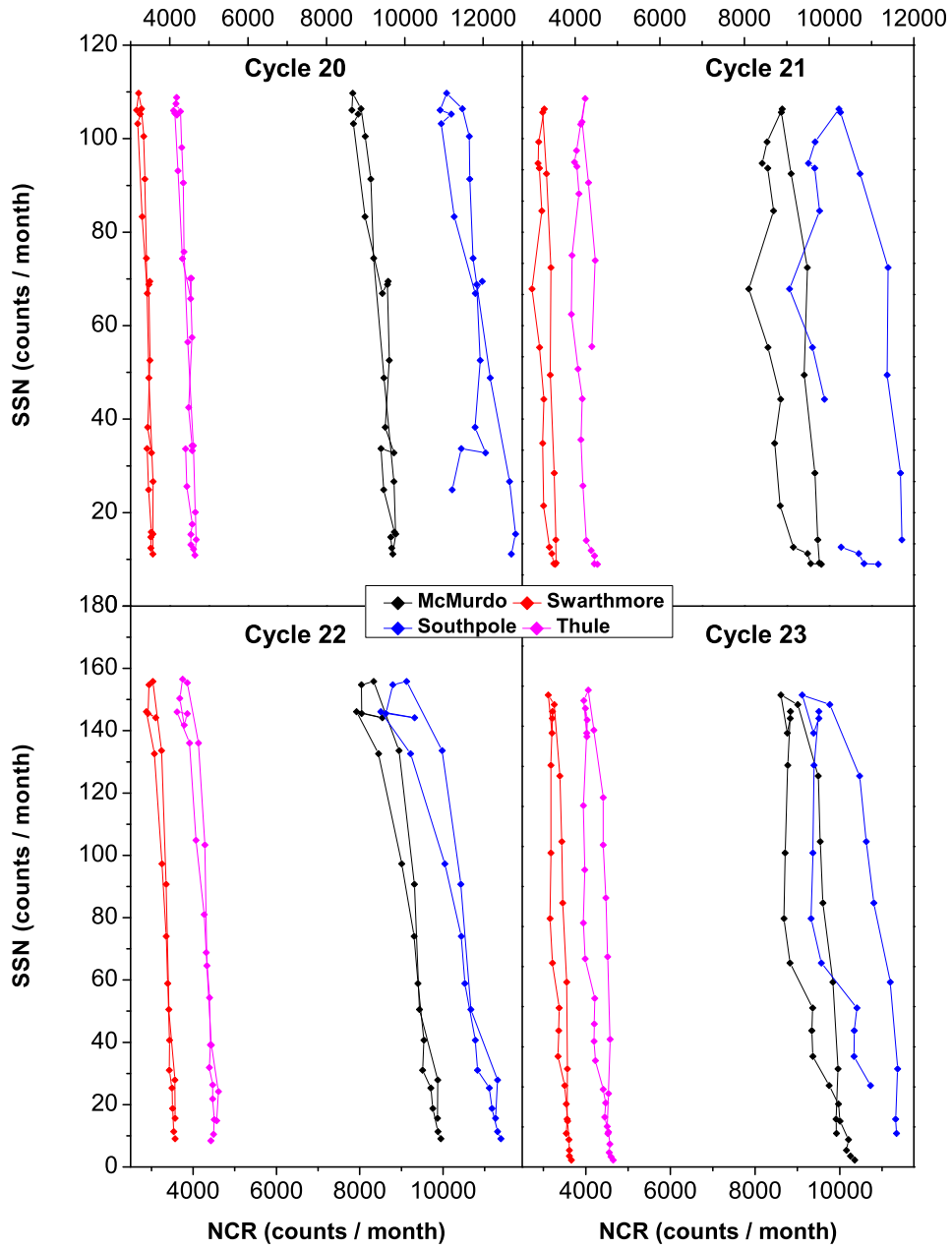


Figure 5.4: Hysteresis plots between NCRs as recorded by neutron monitors and SSNs for solar cycles 20 – 23. Data sets are averaged over a period equal to the 6-month time lag for plotting purposes.

Table 5.2: Cross-correlation coefficients and the corresponding time lags for each of the solar cycles 20, 21, 22, and 23 separately and for the four neutron monitors.

Stations	Time lag (months)	Correlation coefficient	
		Without time-lag	With time-lag
Cycle 20			
McMurdo	0	-0.88	-0.88
Swarthmore	0	-0.87	-0.87
South Pole	1	-0.80	-0.80
Thule	0	-0.85	-0.85
Cycle 21			
McMurdo	11	-0.61	-0.73
Swarthmore	9	-0.64	-0.72
South Pole	9	-0.48	-0.63
Thule	12	-0.48	-0.66
Cycle 22			
McMurdo	0	-0.94	-0.94
Swarthmore	0	-0.94	-0.94
South Pole	0	-0.95	-0.95
Thule	0	-0.93	-0.93
Cycle 23			
McMurdo	8	-0.82	-0.86
Swarthmore	8	-0.80	-0.86
South Pole	8	-0.73	-0.79
Thule	12	-0.74	-0.84

Petropoulos, 1984; Marmatsouri *et al.*, 1995; Gupta *et al.*, 2006; Mavromichalaki *et al.*, 2007). The underlying mechanism that causes this time lag is explained in detail above.

In this study, we use the hysteresis effect to reconstruct NCRs based on SSNs. To obtain hysteresis curves that properly take into account the average long-term time lag, each data set derived from the different NMs was averaged over a period equal to the 5-month time lag for plotting purposes. The hysteresis curves show that even cycles and odd cycles have different loop shapes and different time lags (Figure 5.4). We thus calculated the time lag for each individual solar cycle between two SSN minima (Figure 5.5 and Table 5.2). As clearly shown in Table 5.2, all the neutron monitors exhibit similar behavior regarding the hysteresis effect. During even cycles, almost no time lag is observed except for the South Pole station data (1 month). On the contrary, during odd cycles, the time lag varies from 8 months to 12 months among the NM stations. The time lag found for odd cycles are in good agreement with the calculated time lag of 13-14 months for solar cycle 23 in previous works (Mavromichalaki *et al.*, 2007; Paouris *et al.*, 2012) and slightly different from the results of Chowdhury, Kudela, and Dwivedi (2013) who obtained a time lag of 18 months. The reason for this difference is probably related to the fact that the latter estimate is based on NCR data from another NM with a different cut-off rigidity of 0.81 GV. The estimated time lag of Chowdhury, Kudela, and Dwivedi (2013), based on data from the Oulu NM (65.05°N 25.47°E), was computed using 27-day-averaged GCR intensity data, whereas our analyses are based on monthly averaged data.

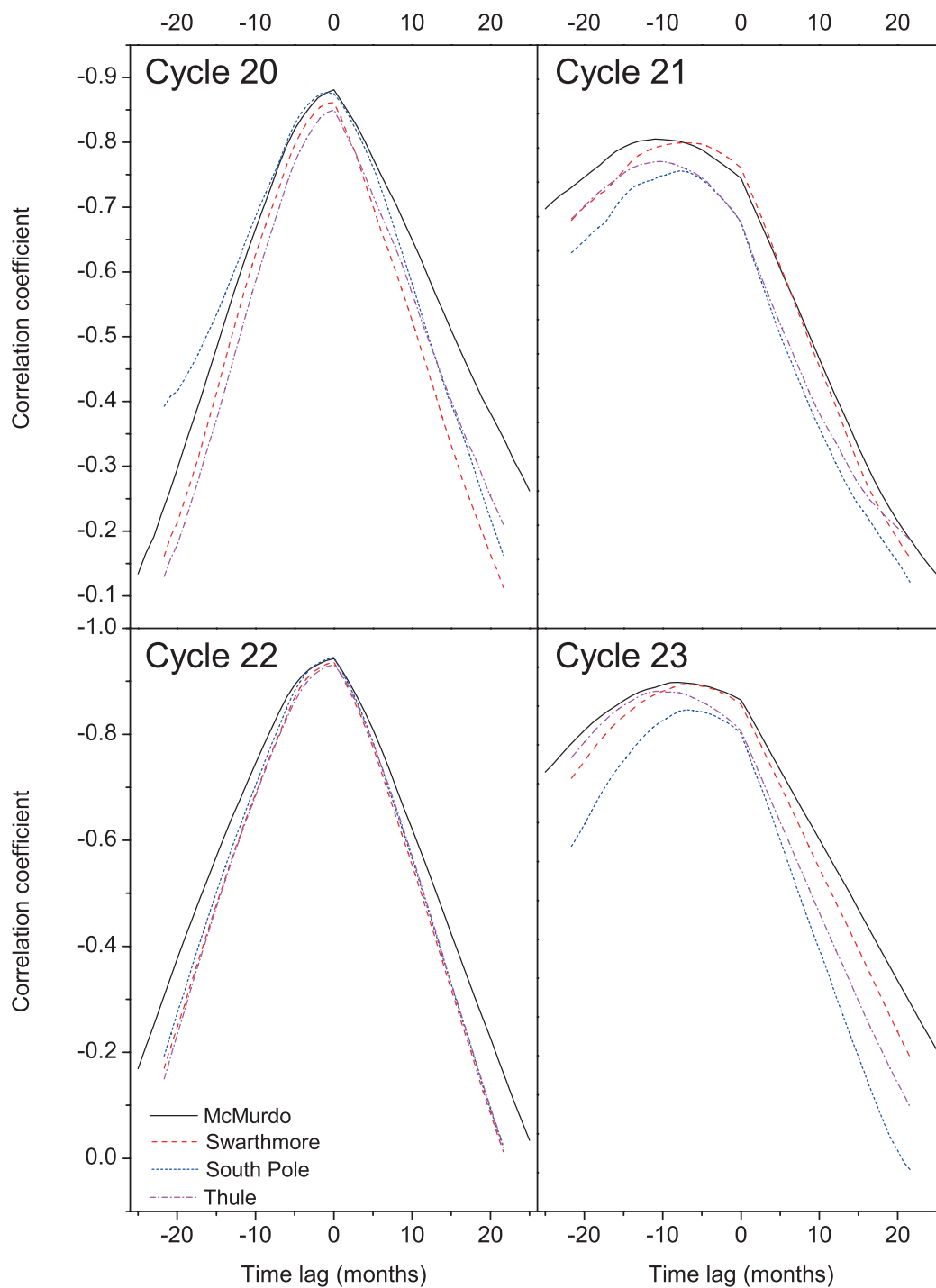


Figure 5.5: Cycle-wise cross-correlation coefficients between monthly NCRs and SSNs as a function of time lag.

Table 5.3: The parameters and correlation coefficients of linear modeling of NCRs for even cycles. The first value in each row shows the result for smoothed data, whereas the second value represents result for non-smoothed data. The linear regression equation is as follows:  $\text{NCR} = \alpha\text{SSN} + \beta$ .

Station	$\alpha$	$\beta$	Correlation coefficient
smoothed / unsmoothed			
Cycle 20			
McMurdo	9911/9912	-9.8/ - 9.8	0.91/0.88
Swarthmore	3604/3605	-3.2/ - 3.2	0.90/0.87
South Pole	12131/12137	-8.0/ - 8.0	0.58/0.57
Thule	4675/4675	-4.2/ - 4.2	0.88/0.85
Cycle 22			
McMurdo	10053/10051	-12.0/ - 12.0	0.97/0.94
Swarthmore	3610/3610	-4.0/ - 3.9	0.96/0.94
South Pole	11549/11545	-17.0/ - 17.0	0.97/0.94
Thule	4622/4620	-5.3/ - 5.3	0.96/0.93

Table 5.4: The parameters and correlation coefficients of linear modeling of NCRs for odd cycles. The first value in each row shows the result for smoothed data, whereas the second value represents result for non-smoothed data. The linear regression equation is as follows:  $\text{NCR} = \alpha\text{SSN} + \beta$ .

Station	$\alpha$	$\beta$	Correlation coefficient
smoothed / unsmoothed			
Cycle 21			
McMurdo	9609/9609	-6.6/ - 6.5	0.69/0.66
Swarthmore	3500/3500	-2.2/ - 2.2	0.72/0.69
South Pole	11084/11084	-8.0/ - 8.0	0.53/0.52
Thule	4485/4485	-2.7/ - 2.7	0.68/0.66
Cycle 23			
McMurdo	10039/10038	-11.0/ - 11.0	0.83/0.81
Swarthmore	3577/3576	-3.4/ - 3.4	0.83/0.80
South Pole	11210/11209	-15.0/ - 15.0	0.82/0.80
Thule	4521/4521	-4.3/ - 4.3	0.75/0.73

## 5.4 Modeling the Relationship between NCRs and SSNs

Prior to the modeling, the NCR data were linearly interpolated over the last four solar cycles to ensure continuity in the time series. This was necessary because small gaps exist in the data recorded by various neutron monitors, *e.g.* March 1978 for Swarthmore NM, July 1976 to June 1978 (24 months) for Thule NM, and November 1974 to January 1977 (27 months) and December 2005 to December 2008 (36 months) for South Pole NM. Additionally, in order to get rid of high-frequency fluctuations in the data sets, we smoothed the data in the time domain using a 7-month moving average. However, to make a comparison, we present analyses of both the smoothed and non-smoothed data series.

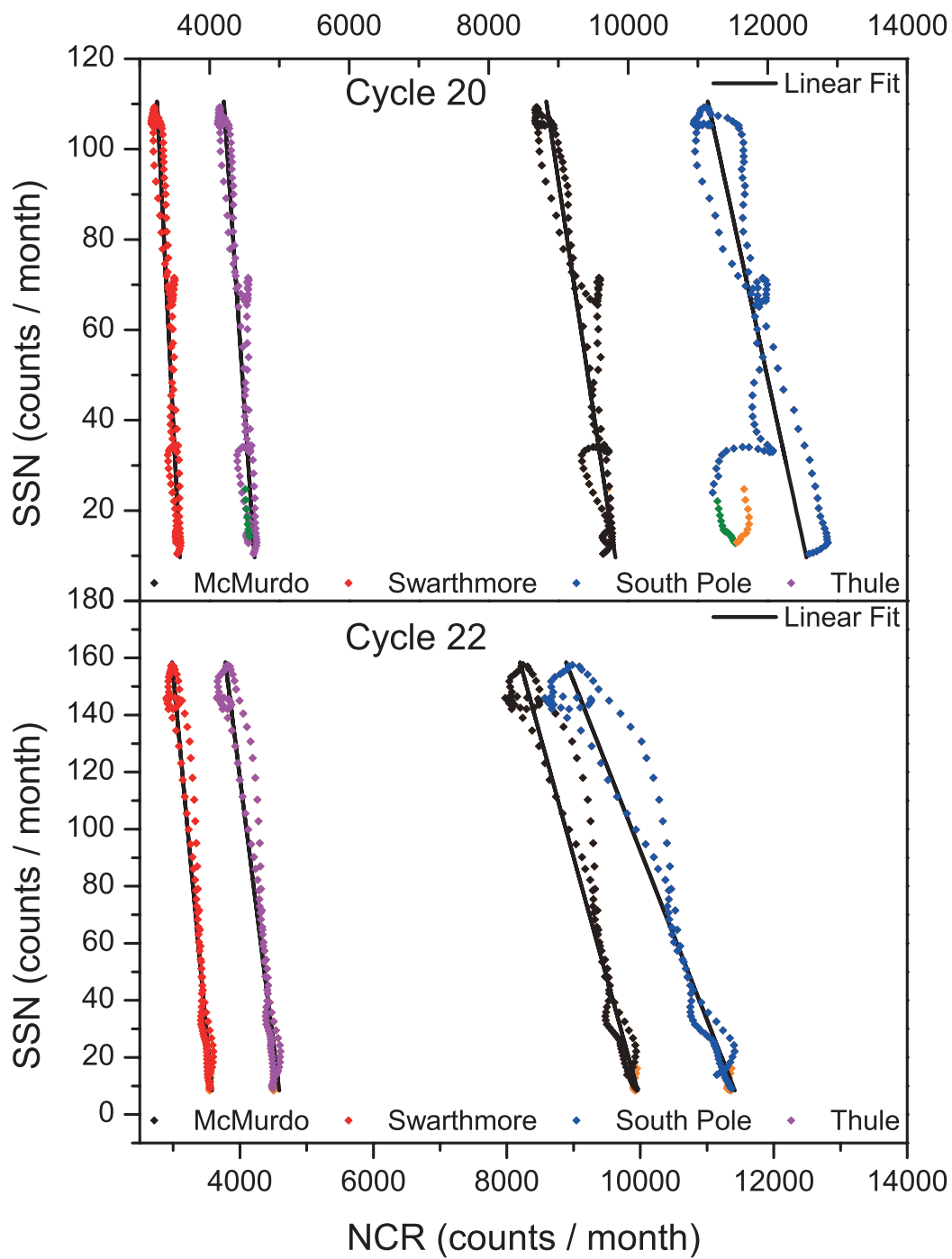


Figure 5.6: The hysteresis curves of even cycles (20 and 22) and corresponding linear fits. Orange and green diamonds show extended (see the text) and interpolated data, respectively.

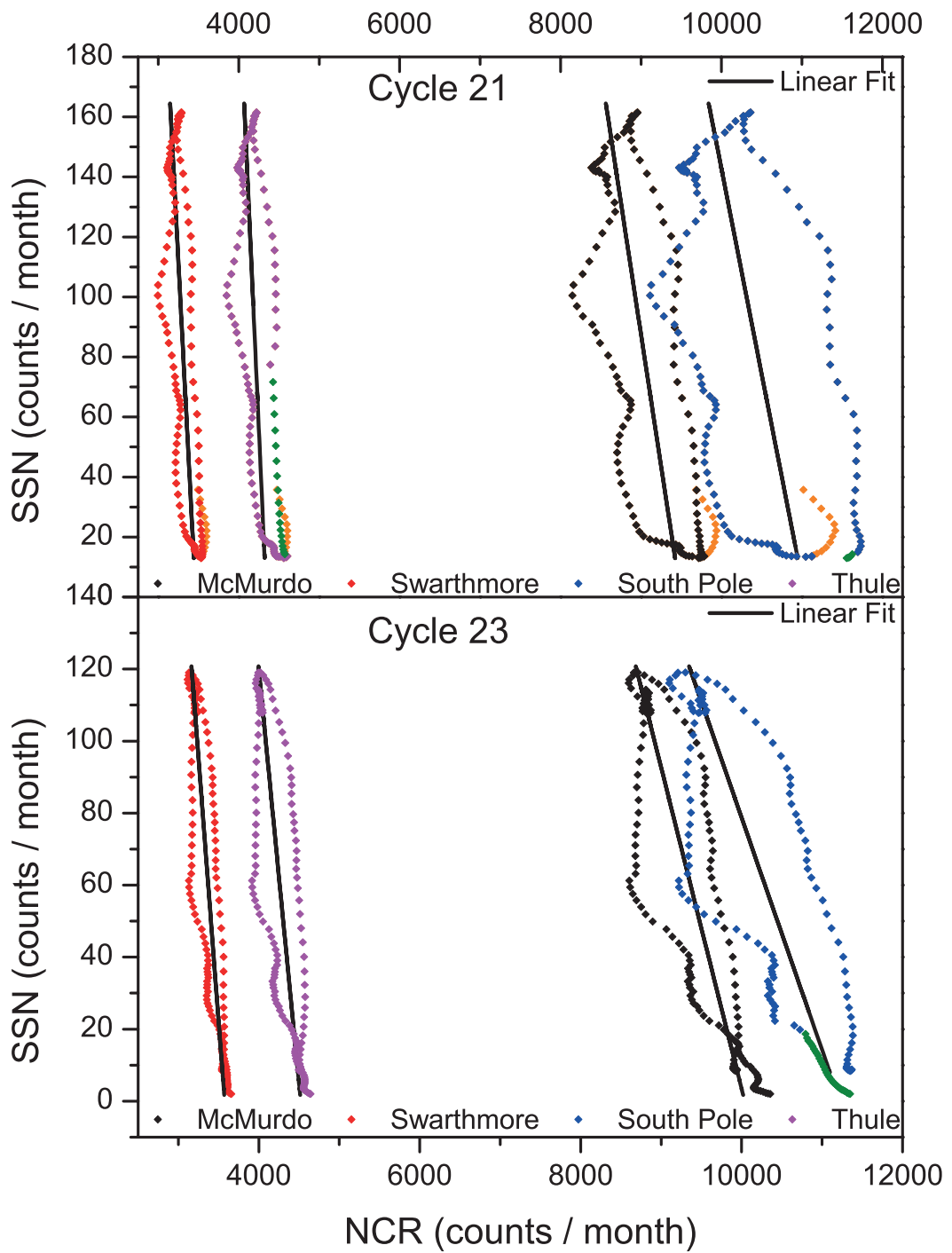


Figure 5.7: The hysteresis curves of odd cycles (21 and 23) and corresponding linear fits. Orange and green diamonds show extended (see the text) and interpolated data, respectively.

In order to reconstruct NCRs using SSNs, we have derived cycle-wise relationships based on the hysteresis effect. Since the link between SSNs and NCRs depends on whether the solar cycle is even or odd, this relationship also varies as a function of time. For even cycles, characterized by narrow hysteresis loops (Figure 5.4), linear regression was used, whereas for odd cycles, characterized by wider hysteresis loops (Figure 5.4), both linear and ellipse fitting were used to determine the best approach to calculate the relationship between NCRs and SSNs. In order to provide a smooth transition between odd and even cycles, we used a 12-month-overlapping period by extending the decreasing phase of the solar cycles by including the first 12 months of the subsequent cycle. Following this, we calculated weighted averages of these overlapping periods. This method ensures continuity of the model and calculated data.

### Even Cycles

In order to calculate the NCRs based on SSNs, a linear regression analysis was applied to the data associated with even cycles 20 and 22, because these hysteresis loops are sufficiently narrow to provide a good fit (Figure 5.6).

The linear relations are shown in Table 5.3 together with correlation coefficients between observed and calculated NCRs. These correlation coefficients are generally high: 0.91, 0.90, 0.58, and 0.88 for cycle 21 and 0.97, 0.96, 0.97, and 0.96 for cycle 23 for the McMurdo, Swarthmore, South Pole, and Thule NMs, respectively, which imply that the linear model is a good representation of the relationship between NCRs and SSNs during even solar cycles. The low correlation coefficient calculated for the South Pole NM results from a gap in the data.

### Odd Cycles

Linear regression analysis was used as a first approach to calculate NCRs during sunspot cycles 21 and 23. The applied linear regression fits (Table 5.4) are shown in Figure 5.7 together with the relevant hysteresis loops. It is obvious that linear fits do not provide a good representation of the relationship

Table 5.5: The parameters and correlation coefficients of ellipse modeling of NCRs for odd cycles [Equations (5.1) and (5.2)]. The first value in each row shows the result for smoothed data, whereas the second value represents result for non-smoothed data.

Station	$Z_1$	$Z_2$	$A$	$B$	$\alpha$	Correlation coefficient
	smoothed / unsmoothed					
	Cycle 21					
McMurdo	9079/9082	82/83	753/869	62/63	3.00/2.12	0.97/0.93
Swarthmore	3320/3325	83/84	261/308	59/62	8.81/6.09	0.97/0.92
South Pole	10529/10525	82/82	1164/1282	67/68	1.47/1.17	0.92/0.90
Thule	4267/4270	84/84	332/385	60/62	6.55/4.86	0.97/0.94
	Cycle 23					
McMurdo	9345/9364	62/62	908/1052	35/37	2.49/1.94	0.96/0.94
Swarthmore	3358/3354	62/62	269/311	35/39	8.58/6.56	0.95/0.93
South Pole	10258/10229	62/62	1199/1341	37/40	1.82/1.46	0.95/0.93
Thule	4261/4256	62/62	361/407	40/42	5.51/4.43	0.97/0.95

between SSNs and NCRs during odd solar cycles, in particular during solar cycle 21 where the correlation coefficients are much lower compared to those associated with even cycles.

The reason for these low correlations associated with the odd cycles is related to the shape of the hysteresis loops, which are significantly wider compared to the even-cycle loops. Therefore, to improve the representation of the relationship between SSNs and NCRs, ellipse modeling was applied to the data associated with the odd cycles (Figures 5.8 and 5.9).

The equations of the fitted ellipses in the parametric form are as follows:

$$\begin{bmatrix} \text{NCR} \\ \text{SSN} \end{bmatrix} = \begin{bmatrix} Z_1 \\ Z_2 \end{bmatrix} + Q(\alpha) \begin{bmatrix} A\cos\theta \\ B\sin\theta \end{bmatrix}, \quad (5.1)$$

$$Q(\alpha) = \begin{bmatrix} -\cos\alpha & \sin\alpha \\ -\sin\alpha & -\cos\alpha \end{bmatrix}, \quad (5.2)$$

where  $Z_1$  and  $Z_2$  are centroid points of the fitted tilted ellipse,  $Q(\alpha)$  is the rotation matrix,  $\alpha$  is the tilt angle,  $A$  and  $B$  are semi-axes, and  $0 \leq \theta \leq 2\pi$ . The rotation angle  $\theta$  is calculated for each data point in the time domain, extending from the beginning of an odd cycle to the first 12 points of the forthcoming cycle, which in turn provides the phase variation in time. The resulting parameters of the ellipse fitting are shown in Table 5.5 together with the correlation coefficients.

The obtained correlation coefficients between the observed and the calculated values are higher than those of the linear fits applied to odd cycles and as high as the linear approach applied to the even cycles. This justifies the use of ellipse fitting for odd cycles where the hysteresis loops are wider (Tables 5.4 and 5.5) and imply that we can obtain a good agreement between the observed and the calculated NCRs by using ellipse modeling.

By using different models for individual odd and even cycles, characterized by different hysteresis loop shapes, we calculated the temporal NCR variations observed at four different neutron monitors for cycles 20, 21, 22, and 23. The observed and calculated values are shown in Figure 5.10 together with corresponding correlation coefficients between  $\text{NCR}_{\text{Obs}}$  and  $\text{NCR}_{\text{Cal}}$ . Using this new model, we obtain the following correlation coefficients over the last four solar cycles: 0.95, 0.95, 0.94, and 0.95 for 7-month moving average smoothed data and 0.92, 0.91, 0.92, and 0.93 for non-smoothed data for the McMurdo, Swarthmore, South Pole, and Thule NMs, respectively. Application of linear regression analysis to the full data sets, *i.e.* both even and odd cycles, from the same NMs results in correlation coefficients of 0.84, 0.84, 0.62, and 0.78 for smoothed data and 0.82, 0.82, 0.61, and 0.76 for non-smoothed data, respectively. Comparing the correlation coefficients calculated using ellipse and linear models for the non-smoothed data for odd cycles (*i.e.* the last columns of Tables 5.4 and 5.5), we find that ellipse modeling, in general, improves the correlation with 31%. In other words, it is clear that inclusion of the hysteresis effect thus provides a substantially improved representation of the relationship between NCRs and SSNs.

## 5.5 Discussion and Conclusions

In the present work, we suggest a new empirical approach to model the link between NCRs and SSNs based on the hysteresis effect. Instead of using linear regression analysis, which is generally applied to both odd and even cycles in order to reconstruct NCRs and GCR intensity (see the multi-component analysis of Mavromichalaki &

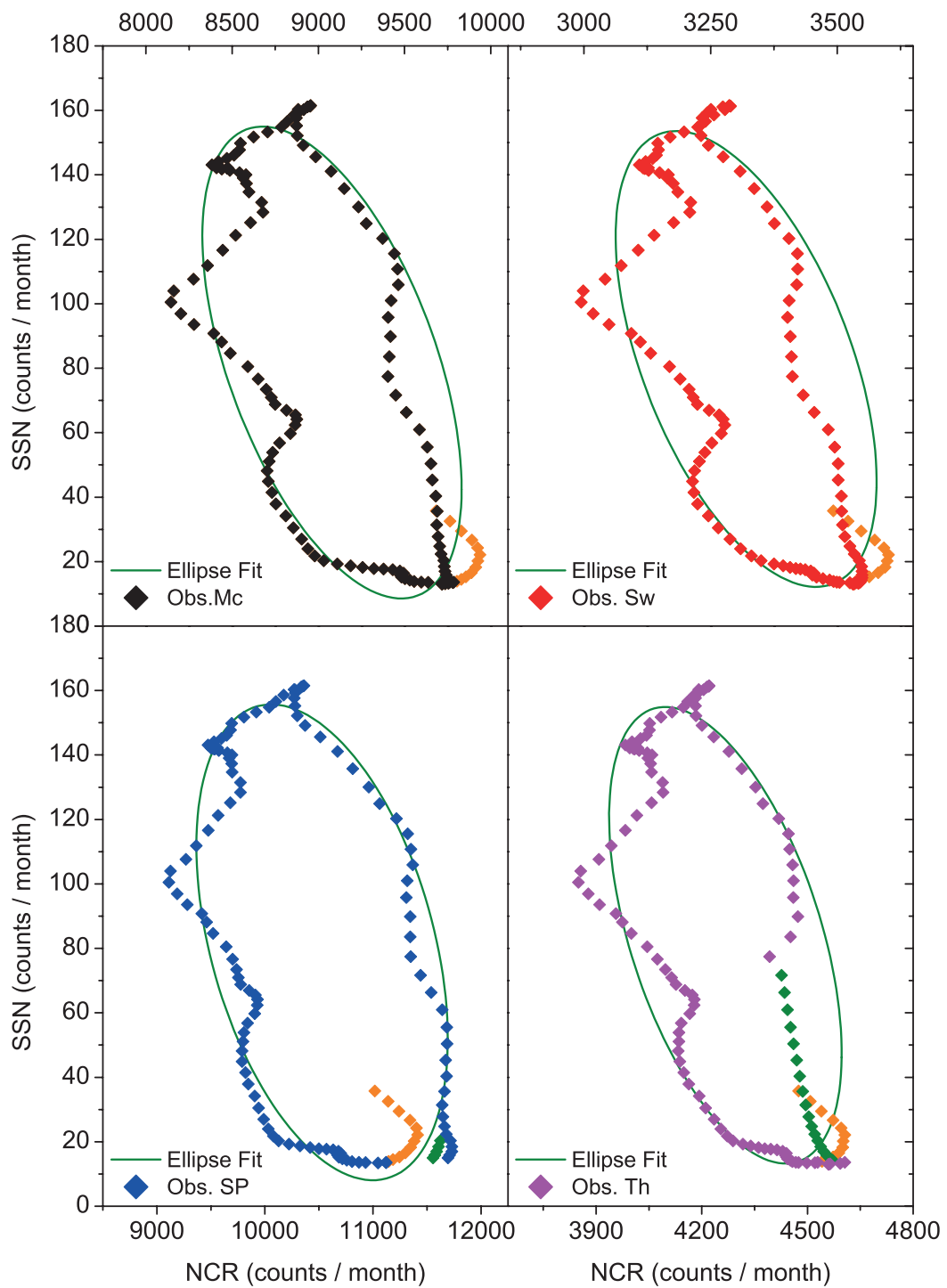


Figure 5.8: Ellipse fitting of NCRs recorded by four neutron monitors for the 21st cycle. Orange and green diamonds show extended (see the text) and interpolated data, respectively.

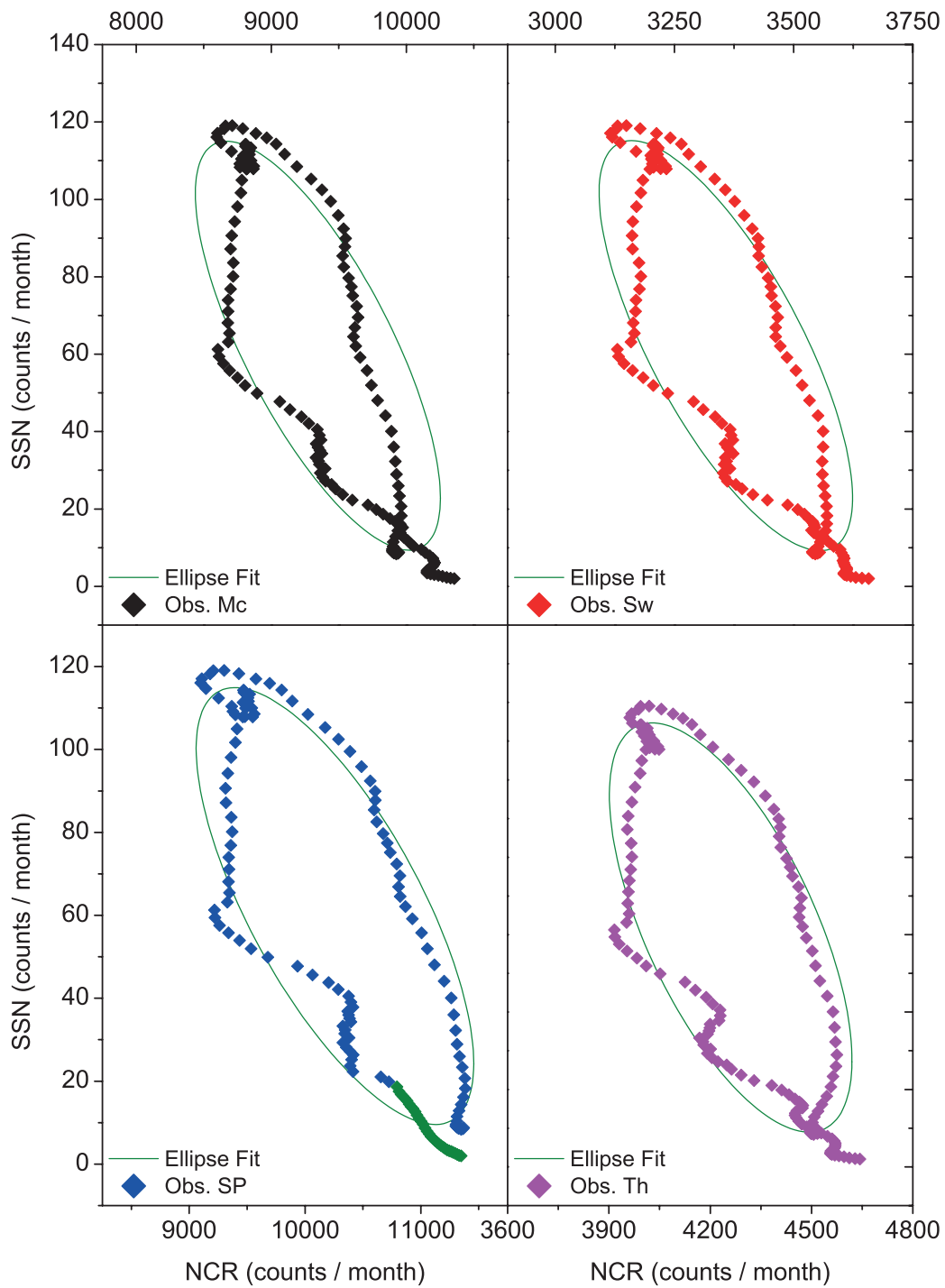


Figure 5.9: Ellipse fitting of NCRs recorded by four neutron monitors for the 23rd cycle. Green diamonds show interpolated data.

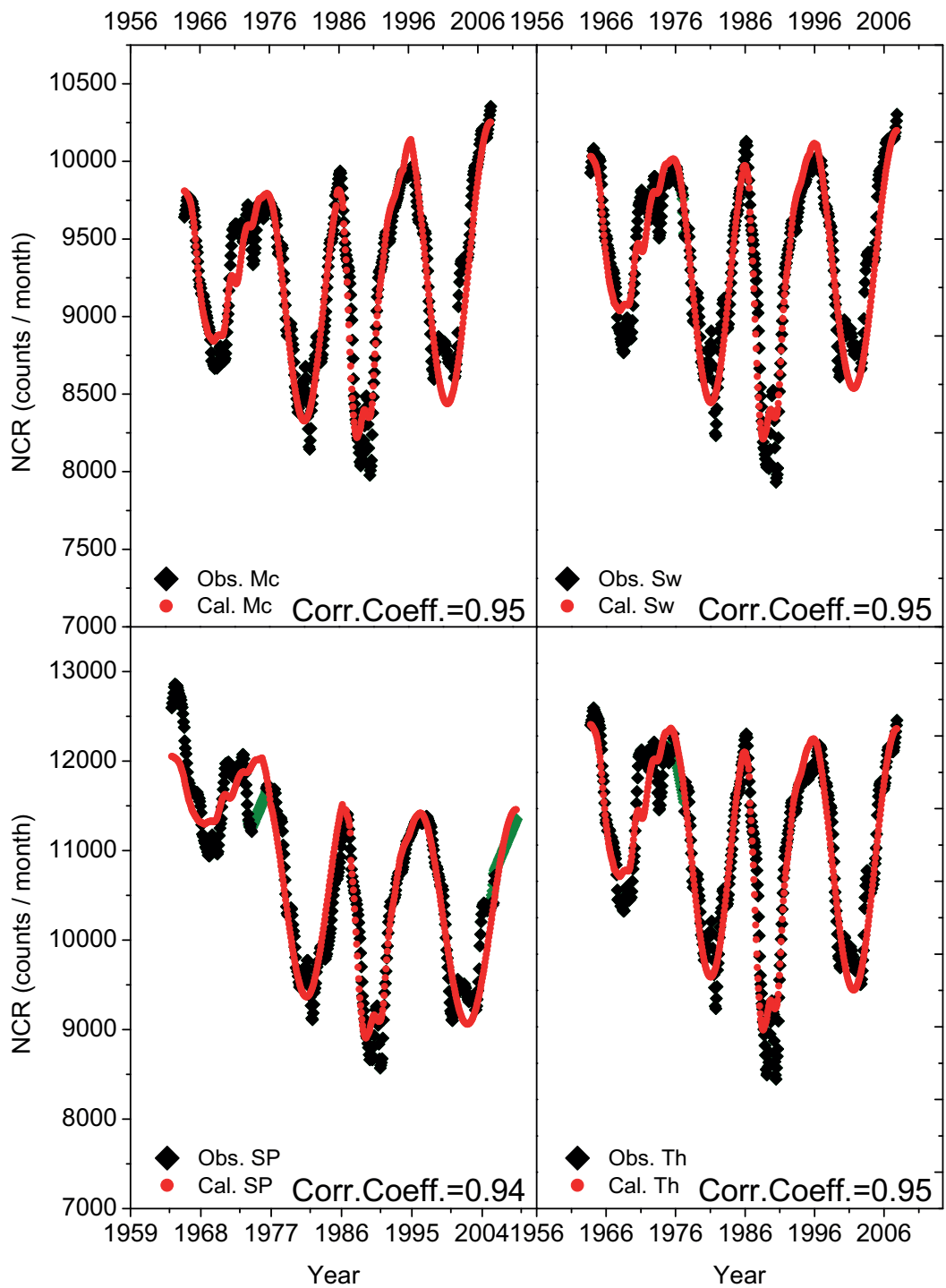


Figure 5.10: Observed and modeled NCRs variations in time with the relevant correlation coefficients for the neutron monitors. Black diamonds and red dots show observed and calculated values, respectively, whereas green diamonds show interpolated data.

Petropoulos (1987) and Mavromichalaki et al. (1990)), we used linear- and ellipse-modeling procedures separately for even and odd cycles, respectively. This approach relies on the fact that the hysteresis curves for even and odd solar cycles exhibit different loop shapes, which is related to the polarity states of the Sun. During even cycles, the hysteresis loops are narrow which favors linear modeling. However, the loops are relatively wide during odd cycles, where ellipse modeling provides a better representation of the data. By using this method, we reconstructed NCRs based on SSNs during solar cycles 20, 21, 22, and 23 (Figure 5.10). The NCRs obtained using the new approach are in good agreement with observed NCRs, as indicated by correlation coefficients of 0.95, 0.95, 0.94, and 0.95 for smoothed data from the neutron monitors McMurdo, Swarthmore, South Pole, and Thule, respectively. In comparison, we obtained correlation coefficients of 0.84, 0.84, 0.62, and 0.78 for smoothed data from the same NMs when applying linear fit to the whole data sets.

We emphasize that this study focuses on modeling the relationship between secondary cosmic ray particles, primarily neutrons, as an indicator of GCR intensity, and SSNs using a parameter that can be reconstructed for earlier periods. A major goal of this ongoing research is thus to improve our understanding of the relationship between high-resolution cosmogenic radionuclide ( $^{10}\text{Be}$  and  $^{14}\text{C}$ ) data, NCRs, and SSNs, in order to extend our knowledge of solar activity back in time beyond the interval from which instrumental data are available.

**Acknowledgements** Funding for the Stellar Astrophysics Centre is provided by the Danish National Research Foundation (Grant agreement no.: DNRF106). MFK, CK and JO acknowledged support from the Carlsberg Foundation. Neutron monitors of the Bartol Research Institute are supported by the United States National Science Foundation (Grant agreement numbers: ANT-0739620 and ANT-0838839), and by the University of Delaware Department of Physics and Astronomy and Bartol Research Institute.

## Chapter 6

# Reconstruction of Sub-Decadal Changes in Sunspot Numbers based on the NGRIP $^{10}\text{Be}$ Record

F. Inceoglu, M. F. Knudsen, C. Karoff, J. Olsen

*Published in Solar Physics (DOI 10.1007/s11207-014-0563-1)*

### Abstract

Sunspot observations since 1610 A.D. show that the solar magnetic activity displays long-term changes, from Maunder Minimum-like low activity states to Modern Maximum-like high activity episodes, as well as short-term variations, such as the pronounced 11-year periodicity. Information on changes in solar activity levels before 1610 relies on proxy records of solar activity stored in natural archives, such as  $^{10}\text{Be}$  in ice cores and  $^{14}\text{C}$  in tree rings. These cosmogenic radionuclides are produced by the interaction between Galactic cosmic rays (GCRs) and atoms in the Earth's atmosphere; their production rates are anti-correlated with the solar magnetic activity. The GCR intensity displays a distinct 11-year periodicity due to solar modulation of the GCRs in the heliosphere, which is inversely proportional to, but out of phase with, the 11-year solar cycle. This implies a time lag between the actual solar cycles and the GCR intensity, which is known as the hysteresis effect. In this study, we use the North Greenland Ice Core Project (NGRIP) records of the  $^{10}\text{Be}$  flux to reconstruct the solar modulation strength ( $\Phi$ ), which describes the modulation of GCRs throughout the heliosphere, to reconstruct both long-term and subdecadal changes in sunspot numbers (SSNs). We compare three different approaches for reconstructing subdecadal-scale changes in SSNs, including a linear approach and two approaches based on the hysteresis effect, *i.e.* models with ellipse-linear and ellipse relationships between  $\Phi$  and SSNs. We find that the ellipse approach provides an amplitude-sensitive reconstruction and the highest cross-correlation coefficients in comparison to the ellipse-linear and linear approaches. The long-term trend in the reconstructed SSNs is computed using a physics-based model and shows a good agreement with the other group SSN reconstructions. The new empirical approach, combining a physics-based model with ellipse-modeling of the 11-year cycle, therefore provides a method to reconstruct SSNs during individual solar cycles based on  $^{10}\text{Be}$  in ice cores. This, in turn, represents a new window for studying short-term changes in solar activity on unprecedented timescales, which may help improve our understanding of the solar dynamo.

Sun: activity – Sun: dynamo – Solar-terrestrial relations – Sunspots

## 6.1 Introduction

Observations of the Sun since 1610 A.D. reveal that the magnetic activity level of the Sun has varied from the Maunder Minimum (1645 - 1715), when sunspots vanished almost completely from the solar surface, to the enhanced activity level since the middle of the 20th century (Usoskin et al., 2007). Maunder Minimum-like periods are believed to represent a special state of the solar dynamo (Usoskin et al., 2014) and they pose a challenge for solar dynamo theory and models because the models do not agree on the frequency of these phenomena, the processes that cause them, or whether they represent regular or random characteristics of the solar dynamo (Charbonneau, 2010). Therefore, high-resolution time series are needed to test the solar dynamo models and to identify the nature of short and long-term changes in solar activity (Solanki et al., 2004; Brajša et al., 2009).

Information on solar variations prior to 1610 relies on past production rates of cosmogenic nuclides, such as  $^{10}\text{Be}$  and  $^{14}\text{C}$  (Usoskin, 2013), which are produced when Galactic cosmic ray (GCR) particles from space interact with atoms in the Earth's atmosphere (Dunai, 2010). The production rates of cosmogenic radionuclides are inversely correlated with solar magnetic activity and the geomagnetic field intensity. This inverse correlation is caused by the non-linear shielding effect of the solar magnetic field and the geomagnetic dipole field (Heikkilä et al., 2008b). In addition, the number of GCRs reaching Earth is inversely proportional to, but out of phase with, the 11-year solar cycle and temporal variations in the GCR intensity display a distinct 11-year periodicity owing to solar modulation of GCRs in the heliosphere (Potgieter, 2013). A strengthening of the solar magnetic and geomagnetic fields results in a lower production rate of cosmogenic nuclides (Masarik & Beer, 1999).

The production of the cosmogenic nuclides mostly takes place within the lower stratosphere and the upper troposphere. For  $^{10}\text{Be}$ , the production rates are estimated to be  $\sim 67\%$  in the stratosphere and  $\sim 33\%$  in the troposphere (Baroni et al., 2011). After they are produced, the  $^{10}\text{Be}$  atoms rapidly become adsorbed onto aerosols, mainly atmospheric sulfate particles. Following a residence time of one to two years in the lower stratosphere (Raisbeck et al., 1981), the aerosols are transported into the lower troposphere, where they eventually are deposited at the surface by both dry and wet deposition. As a consequence,  $^{10}\text{Be}$  concentrations in natural archives can be influenced by local, high-frequency meteorological changes (Berggren et al., 2009). In contrast, shortly after it is produced,  $^{14}\text{C}$  becomes oxidised and joins the atmospheric  $^{12}\text{CO}_2$  reservoir. The atmospheric  $^{12}\text{CO}_2$  reservoir is a part of the global carbon cycle, and it is exchanged among Earth's carbon reservoirs, including the oceans, sediments, soils and vegetation (Bard et al., 1997). The amount of  $^{14}\text{C}$  in the atmosphere is influenced by changes in the global production rate, but variations in the  $^{14}\text{C}$  concentration measured in tree rings are attenuated and delayed relative to its production because of the global carbon-inventory effect (Roth & Joos, 2013). Therefore, because of its simple geochemical behavior and direct transfer into the archives,  $^{10}\text{Be}$  is the most promising radionuclide for reconstructing short-term solar variability. Such reconstructions can potentially enable detailed studies of the short- and long-term behavior of the solar dynamo and help us identify possible influences of solar activity on the Earth's climate.

Earlier attempts to reconstruct short- and long-term variations in sunspot numbers (SSN) have not resolved subdecadal-scale changes because of insufficient data resolution and/or because the models were not designed to resolve the 11-year solar cycle or subdecadal changes (Usoskin et al., 2003c; Solanki et al., 2004; Vonmoos et al., 2006; Steinhilber et al., 2012).

In this article, we investigate the relationship between the solar modulation strength,  $\Phi$ , calculated based on annually resolved  $^{10}\text{Be}$  measurements in the NGRIP ice core from Greenland, and observed group sunspot numbers (Hoyt and Schatten, 1998) to reconstruct subdecadal changes in group sunspot numbers for the time period spanned by the ice-core  $^{10}\text{Be}$  record. By applying three simple empirical approaches (two of which are based on the hysteresis effect observed between GCRs, which are modulated through the heliosphere, and SSNs, Inceoglu et al., 2014a), in combination with a physics-based model (Usoskin et al., 2002a, 2004), to the annually-resolved  $^{10}\text{Be}$  measurements, we reconstruct high-resolution changes in SSNs including variations in the 11-year solar cycle. In Section 2, we describe the data used in the analyses and present the methods in Section 3. The results can be found in Section 4, while in Section 5 we discuss the results. We conclude in Section 6.

## 6.2 Data

Webber et al. (2007) pointed out that in regions above a geomagnetic latitude of  $65^\circ\text{N}$ , the 11-year solar cycle has a modulation effect of 36% on the production rate of  $^{10}\text{Be}$ , but the amplitude of this effect is dampened because two thirds of the  $^{10}\text{Be}$  deposited in Greenland are produced in the stratosphere, where it is globally mixed (Heikkilä et al., 2008b). The deposition of  $^{10}\text{Be}$  at the surface is additionally influenced by climatic effects, including changes in the amount of sulfate aerosols in the atmosphere, which  $^{10}\text{Be}$  atoms become attached to after they are produced (Baroni et al., 2011). Nevertheless, despite the climatic noise and dampening, it is possible to detect the 11-year solar cycles in the NGRIP  $^{10}\text{Be}$  flux data (*e.g.* Berggren et al., 2009).

To reconstruct subdecadal changes in SSNs, we used the annually resolved NGRIP  $^{10}\text{Be}$  flux record (Berggren et al., 2009) that spans the time interval from 1389 to 1994 and group SSNs observed between 1610 and 2011 (Hoyt and Schatten, 1998). The first solar cycle has been defined from 1755 and onwards in the SSN data.

## 6.3 Analysis

A linear interpolation method was used to correct the data set for brief discontinuities observed in the NGRIP  $^{10}\text{Be}$  data (years 1482, 1507, 1516, 1520, 1524, 1534, 1716, 1721, 1797, 1833, 1834, 1835, 1843 and 1920). The NGRIP  $^{10}\text{Be}$  flux was corrected for changes in the Earth’s magnetic field following the approach of Knudsen et al. (2009), which takes into account a 20% polar enhancement of the solar signal in the  $^{10}\text{Be}$  flux (Field et al., 2006). The exact magnitude of this polar bias, which is a consequence of incomplete atmospheric mixing of  $^{10}\text{Be}$  combined with a latitude-dependent shielding effect of the Earth’s magnetic field, remains a subject of debate (Heikkilä et al., 2008b).

To reconstruct subdecadal and centennial-scale changes in group SSNs for the period from 1392 to 1985, we combined two different models. The first model, which we used to reconstruct the long term trend in SSNs, is a physics-based model described in great detail in Usoskin et al. (2002a, 2004). To reconstruct subdecadal changes superimposed on the long-term trend, we then tested three different approaches: linear, ellipse-linear and ellipse models of the relationship between the solar modulation strength,  $\Phi$ , and group SSNs.

## Reconstructing Long-Term Changes in SSNs

The production rates of cosmogenic nuclides, such as  $^{10}\text{Be}$ , depend on the intensity with which cosmic rays impinging the Earth's atmosphere. However, before reaching the Earth, cosmic-ray particles have to travel through the heliosphere, where they become modulated (Potgieter, 2013). According to Parker (1965), modulation of cosmic-ray particles in the heliosphere is a combination of drift, diffusion, adiabatic cooling, and convection processes. On the basis of some assumptions made to reduce the complexity of the Parker's model, Gleeson & Axford (1968) derived the so-called force-field parameterization of the GCR energy spectrum:

$$J(E_p) = J_{\text{LIS}}(E_p + \Phi) \times \frac{E_p(E_p + 2m_p c^2)}{(E_p + \Phi)(E_p + 2m_p c^2 + \Phi)} \quad (6.1)$$

where  $J_{\text{LIS}}$  is the local interstellar cosmic-ray flux,  $E_p$  and  $m_p c^2$  indicate the proton's kinetic and rest energies, respectively. The solar modulation strength is given by  $\Phi$ , whereas  $c$  is the velocity of light. Steinhilber et. al. (2008) pointed out that using  $\Phi$  provides a good approximation for the solar modulation of cosmic rays in the Earth's vicinity. To solve Equation (6.1) for the solar modulation strength,  $\Phi$ , the local interstellar cosmic-ray spectrum (LIS) has to be known. However, there are no measurements of this parameter and thus modeled values of the LIS have to be used in the production-rate calculations of  $^{10}\text{Be}$  (Herbst et al., 2010). Therefore, using different  $^{10}\text{Be}$  records can lead to different solar modulation strength reconstructions.

We reconstructed the long-term trend observed in group SSNs using a physics-based model. To achieve this objective, we first smoothed the NGRIP  $^{10}\text{Be}$  flux using an 11-year moving average to minimize the noise and increase the stability of the model (Usoskin et al., 2003c, 2004), which is shown in the top panel of Figure 6.1. We calculated the modulation strength ( $\Phi$ ) of cosmic rays in the heliosphere following the approach of Usoskin et al. (2002b) and the Sun's open magnetic flux ( $F_0$ ) using Equation (6.2) (Usoskin et al., 2004),

$$F_0 = 0.023 \times \Phi^{0.9}, \quad (6.2)$$

Subsequently, we calculated the time-averaged source function  $\langle S \rangle$  using the following relationship (Usoskin et al., 2004)

$$\langle dF_0/dt \rangle = \langle S \rangle - \langle F_0 \rangle / \tau, \quad (6.3)$$

where  $\tau=4$  represents the characteristic decay time of the open network flux of the Sun (Solanki et al., 2000) and the angular brackets indicate temporal averages of the open magnetic flux of the Sun and the source function. Following Usoskin et al. (2004), we then calculated 11-year averaged group SSNs based on Equation (6.4) and Equation (6.5).

$$S(N) = \alpha \times (24.35 + 22 \times N - 0.061 \times N^2) \quad \text{and} \quad (6.4)$$

$$\langle N^2 \rangle = 1.32 \langle N \rangle^2, \quad (6.5)$$

where  $N$  is the calculated long-term group sunspot numbers ( $\text{SN}_{LT}$ ) and the amplitude factor  $\alpha$  is taken as  $1.95 \times 10^{11} \text{ Wb year}^{-1}$  (Usoskin et al., 2004).

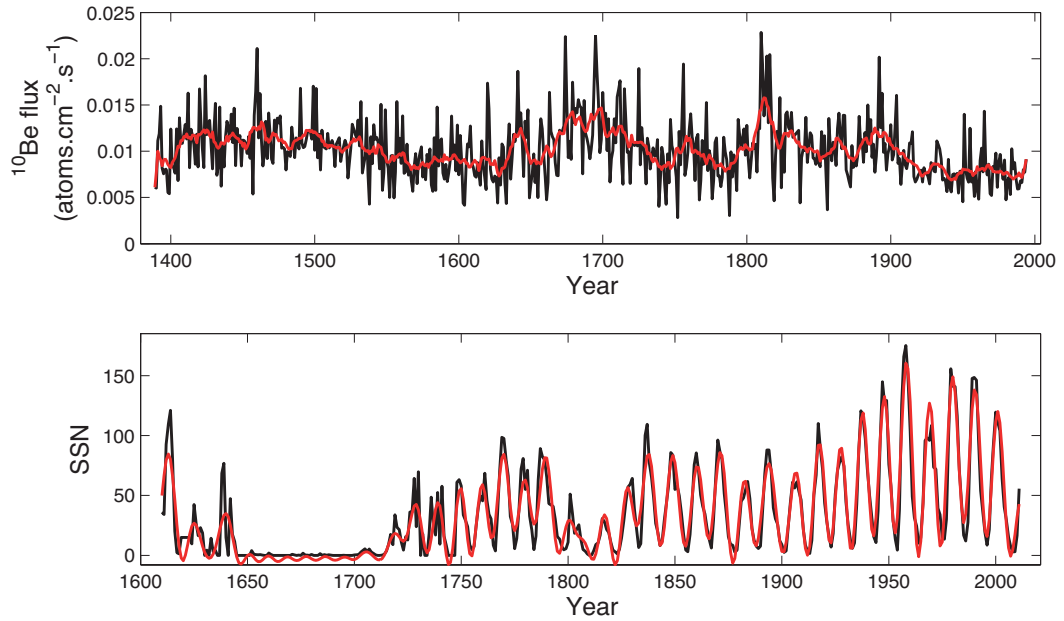


Figure 6.1: From top to bottom, the NGRIP  $^{10}\text{Be}$  flux and group SSNs. In the top panel, the black line shows the NGRIP  $^{10}\text{Be}$  flux data corrected for Earth’s geomagnetic field following Knudsen et al. (2009) and the red line corresponds to the 11 year-moving-average of the NGRIP  $^{10}\text{Be}$  flux (see text). In the bottom panel, the black line shows the group SSNs and the red line corresponds to the low-pass filtered groups SSNs with a cut-off frequency of  $(1/9)$  year $^{-1}$  for the observed group SSNs.

### Reconstructing Short-Term Changes in SSNs

The observed group SSNs were low-pass filtered using the Fourier-transform method with a cut-off frequency of  $(1/9)$  year $^{-1}$  to be able to reconstruct subdecadal changes in group SSNs. By using  $(1/9)$  year $^{-1}$  as a cut-off frequency for the low-pass filter, we ensured that the 11-year periodicity is maintained in the data, but remove high-frequency fluctuations. We also tried using another low-pass filter with a cut-off frequency of  $(1/3)$  year $^{-1}$  to investigate how the low-pass filter influences the resulting group SSN reconstructions. Following this step, the low-pass filtered observed group SSN data were used for all further analyses. The bottom panel of Figure 6.1 shows the low-pass filtered data with a cut-off frequency of  $(1/9)$  year $^{-1}$  (red line).

Prior to applying the three approaches to  $\Phi$  and to the SSN observed ( $\text{SSN}_{\text{Obs}}$ ) data to reconstruct subdecadal changes superimposed on the long-term trend, we separated the data into three time periods. The first period, which is called the model period, overlaps the observed SSNs, spanning the time interval from 1755 to 1985 and covering the first 21 solar cycles. The second period ranges from 1392 to 1755, covering a time period that precedes the observation of solar cycles based on sunspot numbers. The data set covering the most recent period (1755–1985) was used to train our model of the relationship between  $\Phi$  and  $\text{SSN}_{\text{Obs}}$ , *i.e.* we identified the optimum model parameters that provide SSNs that most accurately resemble the observed SSNs. Following this step, we used the obtained parameters to reconstruct annual changes in SSNs for the time period that extends back to 1392. Additionally, the period covering the 13 solar cycles prior to the first solar cycle (1610–1755) was used as a test period. We also introduced a sunspot formation threshold value of 125 MeV (Vonmoos et al., 2006) to the model because the production rate of  $^{10}\text{Be}$  and the

group sunspot numbers show significant differences in their sensitivity to changes in the solar activity levels (Vonmoos et al., 2006). For example, even though the sunspot numbers show that almost no sunspots were observed in the photosphere during the Maunder Minimum, the  $^{10}\text{Be}$  records from ice cores and in turn the modulation potential strengths calculated based on these records show that the 11-year solar cycle continued to exist during this interval (Beer et al., 1998; Vonmoos et al., 2006; Berggren et al., 2009). Therefore, any solar modulation strength under the introduced threshold value will result in a zero sunspot number, since the sunspot numbers can only be positive.

In Inceoglu et al. (2014a), we used hysteresis curve shapes to model the relationship between neutron counting rates (NCRs), which are indicators of GCRs, and  $\text{SSN}_{\text{Obs}}$ . This model treats the data associated with odd and even cycles differently. For odd cycles, the hysteresis curves are wider favoring an ellipse modeling, whereas the hysteresis curves are narrow during even cycles, which favors a linear modeling. The data used in Inceoglu et al. (2014a) were actual observations of SSNs and instrumental measurements of NCRs and they displayed distinct hysteresis curve shapes for even and odd cycles. In this study, however, we use  $^{10}\text{Be}$  data from the NGRIP ice core to reconstruct the solar modulation strength. Because of climate-related noise, age model uncertainties of the NGRIP ice core (Vinther et al., 2006), and an atmospheric residence time of  $^{10}\text{Be}$  of one to two years (Raisbeck et al., 1981), it may be difficult to observe a distinct hysteresis effect when plotting SSNs against reconstructed  $\Phi$ . Consequently, we test three different approaches to constrain the subdecadal relationship between  $\Phi$  and  $\text{SSN}_{\text{Obs}}$ . These include linear modeling, ellipse-linear modeling, and ellipse modeling.

### The Linear Approach

To build a linear relationship between  $\Phi$  and  $\text{SSN}_{\text{Obs}}$ , we first separated the data in the model period (1755–1985) into individual cycles. After standardising  $\Phi$  and  $\text{SSN}_{\text{Obs}}$  according to their cycle-wise mean and standard deviation values, we applied a simple linear regression approach to each cycle under consideration. In order to find the optimum parameters for the linear regression that give the best representation of the data, we averaged the parameters found for 21 solar cycles (Table 6.1). The uncertainties on the averaged parameters are calculated using Equation (6.6)

$$\delta = \frac{\left( \frac{1}{N-1} \sum_{i=1}^N (x_i - \hat{x})^2 \right)^{\frac{1}{2}}}{N-1}, \quad (6.6)$$

where  $N$  is the number of the values of the parameter as obtained for individual solar cycles,  $x_i$  and  $\hat{x}$  denote each parameter found and the mean of each parameter, respectively. Additionally, we used a two-year-overlapping period by extending the decreasing phase of the solar cycles including the first two years of the previous cycle (the reconstruction extends backwards in time starting from cycle 21) to ensure smooth transitions between the cycles. Following this, we calculated the arithmetic averages of these overlapping periods. This method ensures continuity of the model and calculated data. We then extend the relationship back to 1389.

### The Ellipse-Linear Approach

In this approach, we separated the data in the model period spanning the time interval from 1755 to 1985 into two groups, depending on whether they belong to odd- or even-

Table 6.1: The parameters of the SSN linear modeling. The linear regression equation is:  $SSN = \alpha\Phi + \beta$ . Units of the parameters are in standard deviation  $\sigma$  as the linear model is built based on standardized data (see text).

Linear Fit Parameters	
$\alpha$	$\beta$
$0.013 \pm 0.02$	$-1.12 \times 10^{-16} \pm 2.23 \times 10^{-17}$

Table 6.2: The parameters of the SSN ellipse-linear modeling for even and odd cycles. The linear regression equation is:  $SSN = \alpha\Phi + \beta$ . Units of the parameters, except for the tilt angle  $\phi$ , are in standard deviation  $\sigma$  as the ellipse-linear model is built based on standardized data (see text). See the text for ellipse equation.

Even Solar Cycles				
		$\alpha$	$\beta$	
		$-0.08 \pm 0.04$	$-2.03 \times 10^{-16} \pm 4.17 \times 10^{-17}$	
Odd Solar Cycles				
$Z_1$	$Z_2$	$A$	$B$	$\phi$ (radian)
$0.19 \pm 0.02$	$-0.31 \pm 0.08$	$1.51 \pm 0.05$	$1.82 \pm 0.08$	$0.03 \pm 0.06$

numbered solar cycles. Usoskin et al. (2009c) found evidence of an extra cycle, called 4b, during Solar Cycle 4 between 1784–1799. Even though this extra cycle might be real, our analysis did not reveal any evidence for this lost cycle in the NGRIP  $^{10}\text{Be}$  data. To train the model and to find the optimum parameters, we separately plot  $SSN_{\text{Obs}}$  against  $\Phi$ , both of which are standardized according to their cycle-wise mean and standard deviation values, for even and odd cycles. Similar to the approach described in Inceoglu et al. (2014a), we then fit ellipses individually for all odd solar cycles, while we used a linear fitting for even solar cycles. To construct the model, we then averaged the parameters found for ellipse and linear fits that provided the best representation of the data. However, one extreme case was observed, *i.e.* Solar Cycle 21, in which the model parameters are anomalously high. Therefore were excluded this from the calculations of the optimum parameters for the ellipse-linear model. Figure 6.2 shows a normal and an extreme case. Ellipse parameters were thus found using 10 odd cycles.

The equations associated with the fitted ellipses in the parametric form are as follows:

$$\begin{bmatrix} \Phi \\ SSN_{ST} \end{bmatrix} = \begin{bmatrix} Z_1 \\ Z_2 \end{bmatrix} + Q(\phi) \begin{bmatrix} A \cos \theta \\ B \sin \theta \end{bmatrix}, \quad (6.7)$$

$$Q(\phi) = \begin{bmatrix} -\cos \phi & \sin \phi \\ -\sin \phi & -\cos \phi \end{bmatrix}, \quad (6.8)$$

where  $Z_1$  and  $Z_2$  are centroid points of the fitted tilted ellipse,  $Q(\phi)$  is the rotation matrix,  $\phi$  is the tilt angle,  $A$  and  $B$  are the semi-axes, and  $0 \leq \theta \leq 2\pi$ . The rotation angle  $\theta$  is calculated for each data point in the time domain, extending from the beginning of an odd cycle to the first two points (two years) of the preceding cycle, which in turn provides the phase variation in time. The resulting average parameters of the ellipse and linear fitting with their uncertainties calculated based on Equation (6.6) are shown in Table 6.2.

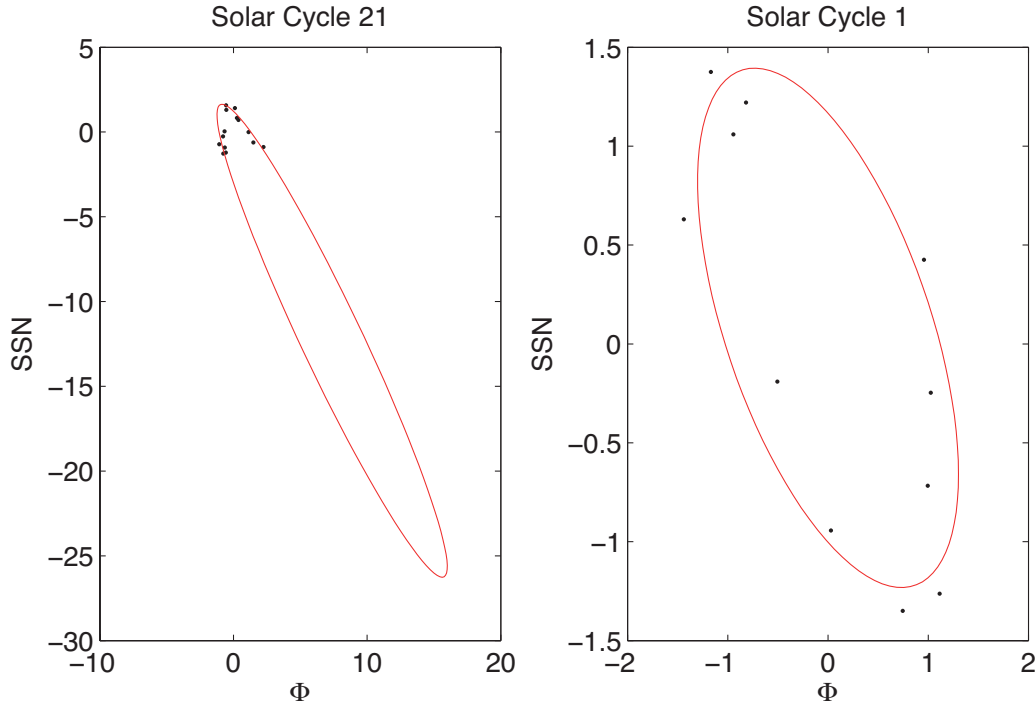


Figure 6.2: Hysteresis curves between group SSNs and  $\Phi$  after standardising  $\Phi$  and  $SSN_{Obs}$  according to their cycle-wise mean and standard deviation values. Right panel shows a regular hysteresis curve, whereas an extreme case is shown in the left panel (see text).

After testing the applicability of the ellipse-linear model, we then reconstructed SSNs back in time. To achieve this objective, we apply the above-mentioned procedure, to the data before 1755. The only exception is that we had to use an average solar-cycle length of 11 years for the rest of the data set spanning the time period from 1620 to 1389 because the solar-cycle lengths are not available for this period and we were unable to clearly distinguish them in the  $^{10}\text{Be}$  record.

### The Ellipse Approach

In the ellipse approach, we also separated the data in the model period (1755-1985) into individual cycles. Here, the data are not further separated into two groups consisting of odd or even cycles because ellipse fitting was applied to all the cycles regardless they are even- or odd-number cycles. After standardizing  $\Phi$  and  $SSN_{Obs}$  according to their cycle-wise mean and standard deviation values, we plot  $SSN_{Obs}$  against  $\Phi$  for all the solar cycles to define the associated hysteresis curves (Figure 6.3).

After obtaining the hysteresis curves, we fit ellipses to each solar cycle, where it is possible. It was not possible to represent the data associated with Solar Cycle 6 using ellipse fitting, most likely because of climatic noise and age model problems in the  $^{10}\text{Be}$  data. These problems might prevent detection of well-defined 11-year cycles. We therefore had to exclude this cycle. Additionally, one extreme case was excluded, that was also observed for the ellipse-linear model, *i.e.* Solar Cycle 21 (see Figure 6.2). We then averaged the ellipse parameters of 19 solar cycles out of 21. The parameters associated with the extreme case were excluded from this calculation because including them would change the optimum values, which in turn would affect

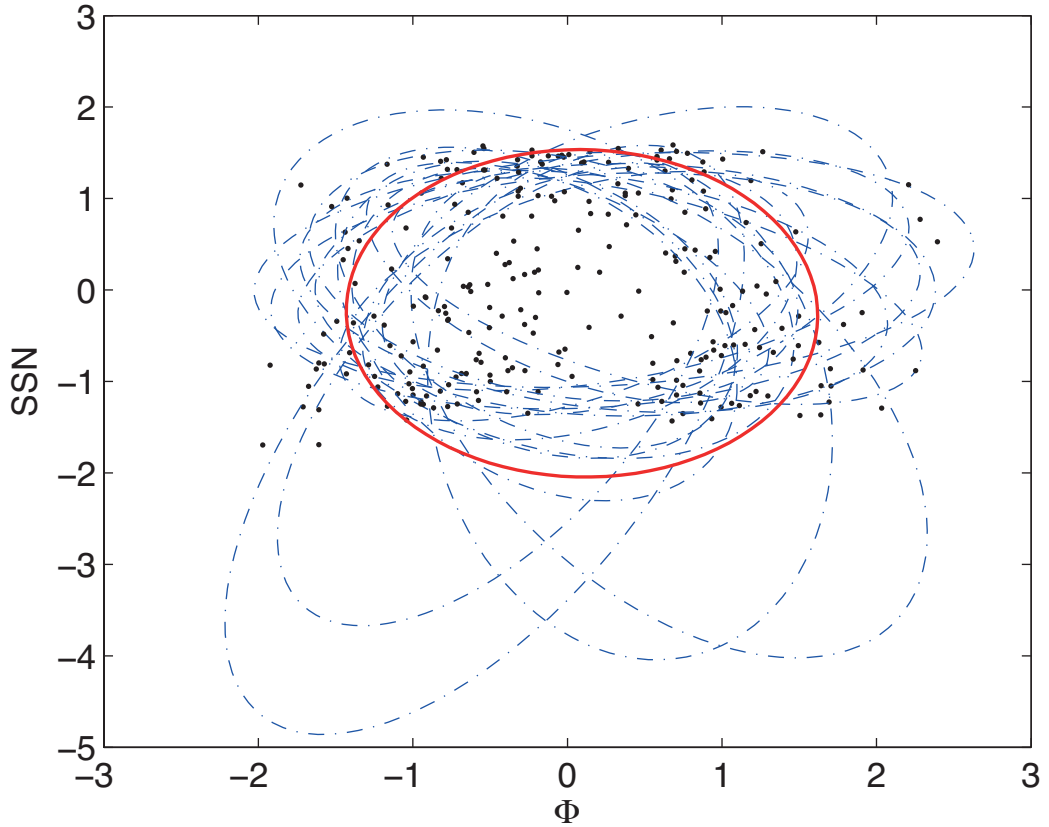


Figure 6.3: The hysteresis curves between observed group SSNs and  $\Phi$  after standardising  $\Phi$  and  $SSN_{Obs}$  according to their cycle-wise mean and standard deviation values. Blue line-dotted lines show the fitted ellipses, whereas the red solid line shows the mean ellipse fit.

Table 6.3: The parameters of the SSN ellipse modeling. Units of the parameters, except for the tilt angle  $\phi$ , are in standard deviation  $\sigma$  as the ellipse model is built based on standardized data (see text).

Ellipse Parameters				
$Z_1$	$Z_2$	$A$	$B$	$\phi$ (radian)
$0.08 \pm 0.01$	$-0.26 \pm 0.04$	$1.52 \pm 0.02$	$1.79 \pm 0.04$	$-0.05 \pm 0.03$

the goodness of the fit. The average ellipse parameters obtained are shown in Table 6.3 together with their uncertainties calculated using Equation (6.6).

### Superimposing Short-term Changes on the Long-term Trend

To superimpose short-term variations ( $SSN_{ST}$ ), calculated using the linear, ellipse-linear, and ellipse approaches, onto the long-term trend ( $SSN_{LT}$ ) computed with a physics-based model, we use Equation (6.9) for each solar cycle as follows:

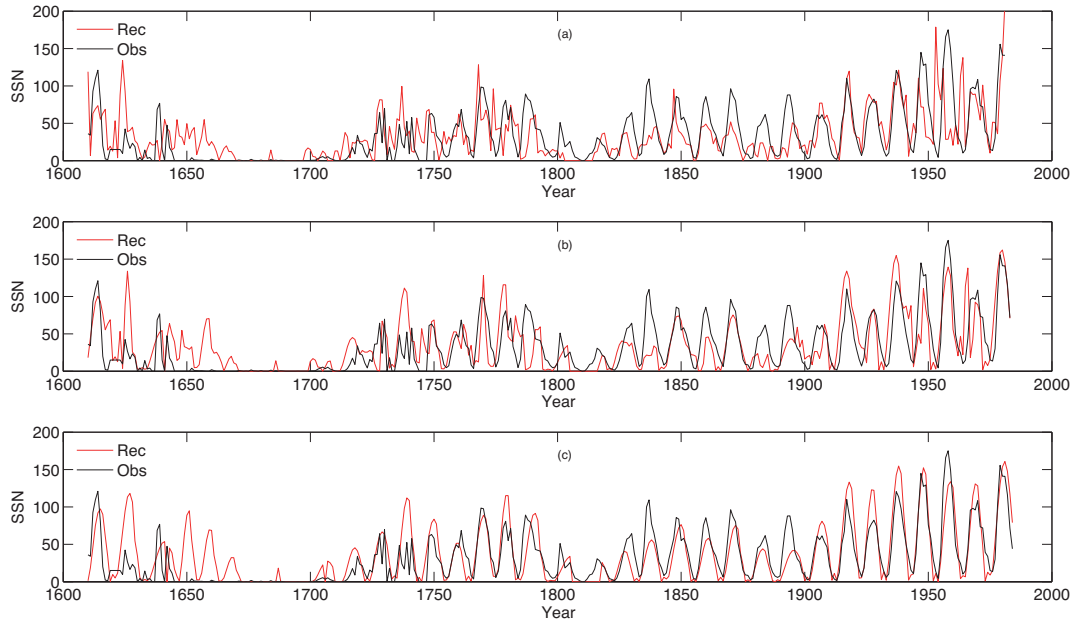


Figure 6.4: Reconstructed and observed group SSNs: (a) Linear fitting, (b) ellipse-linear fitting and (c) ellipse fitting for the period span by the NGRIP ice core. The ellipse approach clearly provides the best representation of the observed group SSNs.

$$SSN_{\text{Sup}}(i) = \frac{\left| \frac{SSN_{\text{ST}}(i)}{SSN_{\text{ST}}(i)_{\text{max}}} \right|}{\sum_{i=0}^n \left| \frac{SSN_{\text{ST}}(i)}{SSN_{\text{ST}}(i)_{\text{max}}} \right|} \times \mu_{SSN_{\text{LT}}} \times n, \quad (6.9)$$

where  $SSN_{\text{Sup}}$  indicates calculated annual values of the superimposed SSN during a solar cycle and  $i=1,2,\dots,n$  denotes the annual data points within a cycle,  $\mu_{SSN_{\text{LT}}}$  and  $n$  show the cycle-wise mean values of the long-term SSN reconstruction and the cycle length, respectively. By applying this method to each of the three approaches that provide subdecadal changes in group SSNs, we superimposed short-term changes on the long-term trend.

## 6.4 Results

### Superimposed Linear Approach

We applied a cross-correlation analysis to find the best possible correlation as a function of time lag. The highest cross-correlation coefficient between the observed group SSNs, which were low-pass filtered with a cut-off frequency of  $(1/9) \text{ year}^{-1}$ , and reconstructed group SSNs for the test period extending from 1610 to 1755 is 0.56 for a time lag of three years, while it is 0.54 with a time lag of four years for the model period from 1755 to 1985. For the whole overlapping period from 1610 to 1985, the highest cross-correlation is 0.56 for a time lag of four years. Therefore, we shifted the reconstructed group SSNs according to the obtained time-lag (Figure 6.4a).

## Superimposed Ellipse-Linear Approach

To find the highest correlation coefficient between the observed and the reconstructed group SSNs as a function of time lag, we performed a cross-correlation analysis for the test period between 1610–1755. The highest cross-correlation coefficient for this period is 0.62 for a time lag of two years. For the model period from 1755 to 1985, we obtained a highest cross-correlation coefficient of 0.69 for a time lag of two years, while the highest cross-correlation coefficient is 0.67 for a time lag of two years for the whole overlapping period extending from 1610 to 1985. The reconstructed group SSNs were then shifted accordingly (Figure 6.4b).

## Superimposed Ellipse Approach

After reconstructing group SSNs throughout the timespan covered by the NGRIP data, we performed a cross-correlation analysis for the period between 1755–1985. The highest cross-correlation coefficient between the observed group SSNs, which were low-pass filtered with a cut-off frequency of  $(1/9) \text{ year}^{-1}$ , and reconstructed group SSNs found for this period is 0.90 for a time lag of one year, while it is 0.81 for a time lag of one year for the whole overlapping period from 1610 to 1985. Additionally, for the test period spanning from 1610 to 1755, the highest cross-correlation coefficient is 0.65 for a time lag of two years. To estimate the statistical significance of the calculated correlation coefficients for the whole overlapping period and the test period, and to validate the method, we applied a nonparametric random-phase test using reconstructed and observed SSNs for the whole overlapping (1610–1755) and the test (1755–1985) periods. A nonparametric random-phase test provides robust results on the statistical significance levels of calculated correlation coefficients when the data sets have lagged correlation. Moreover, Ebisuzaki (1997) noted that using low-pass filtered data sets generally results in highly lagged correlation coefficients by reducing the variability in the original (unfiltered data) data. The random-phase test is a resampling method in the frequency domain based on fast Fourier transformation of the data series, which preserves the original power spectrum and the amplitudes of the signals, but changes the phase randomly and then back-calculates the data series (Ebisuzaki, 1997; Usoskin et al., 2006). For this method, we use 5000 phase-randomized data sets for each of the two periods and calculated correlation coefficients between randomized observed group SSNs and reconstructed SSNs, as well as randomized reconstructed SSNs and observed group SSNs. According to the result of the nonparametric random-phase test, the calculated correlation coefficients between  $\text{SSN}_{\text{Sup}}$  and  $\text{SSN}_{\text{Obs}}$  for the test period (1610–1755) are marginally significant on a  $p < 0.1$  level, while the calculated correlation coefficients for the whole overlapping period (1610–1985) are statistically significant on a  $p < 0.01$  level. The results of the applied nonparametric random-phase test imply that the method used to calculate subdecadal changes in SSNs back in time is valid. The resulting reconstruction of group SSNs both for the model-training period (1755–1985) and the whole period covering the timespan 1392 to 1985 are shown in Figure 6.5, while the dates and amplitudes of solar cycles prior to the group sunspot number series are listed in Table 6.4.

For comparison, we also reconstructed the group SSNs using observed group SSN data that were low-pass filtered with a cut-off frequency of  $(1/3) \text{ year}^{-1}$  as input variables for the ellipse approach. The resulting cross-correlation coefficient between the observed and calculated group SSNs for the model period was found to be 0.86 for a time lag of one year. The procedure described above was also applied to this

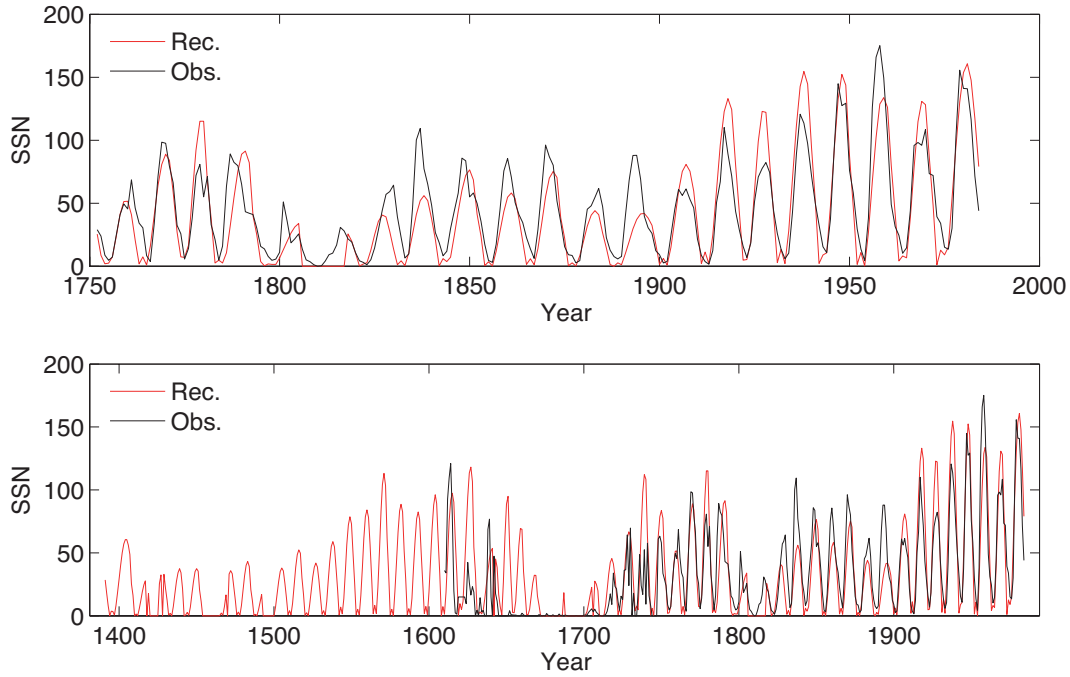


Figure 6.5: The top panel shows the resulting ellipse modeling reconstruction of group SSN, using data that were low-pass filtered with a cut-off frequency of  $(1/9) \text{ year}^{-1}$  (see text), and the observed group SSNs for the time period covering between 1619–1984. The bottom panel shows reconstructed and observed SSNs for the time period covering between 1391–1984. The black line corresponds to the observed group SSNs and the red line shows the reconstructed group SSNs based on the NGRIP ice core.

reconstruction. For the test period, which spans from 1610 to 1755, the highest cross correlation coefficient is 0.6 for a time-lag of two years. Following this step, we ran another cross-correlation analysis for the period between 1610–1985, where the reconstructed and observed group SSNs overlap. The highest cross-correlation coefficient is found to be 0.77 for a time-lag of one year. We then ran a nonparametric random-phase test, as we did for the data that were low-pass filtered with a cut-off frequency of  $(1/9) \text{ year}^{-1}$ , and found that the cross correlation coefficients found for the test period (1610–1755) and the whole overlapping period (1610–1985) are statistically significant on a  $p < 0.01$  level.

The results obtained demonstrate that using a lower cut-off frequency for observed group SSN helps improve the correlation between the observed and reconstructed group SSNs by 5% by removing high-frequency fluctuations. On the other hand the statistical significance of the correlation coefficient calculated using a higher cut-off frequency ( $(1/3) \text{ year}^{-1}$ ) for the test period spanning from 1610 to 1755 is higher than that calculated using the low-frequency cut-off of  $(1/9) \text{ year}^{-1}$ . Note, however, that the test period is dominated by the Maunder Minimum, where almost no sunspots were observed, whereas the  $^{10}\text{Be}$  and reconstructed  $\Phi$  show continued but slightly decreased activity levels. This implies that the test period is fundamentally different from the training period in the sense it contains a grand minimum without SSNs. The test period may therefore not be ideal compared with the training period, but reducing the model period to less than  $\sim 230$  years (1755–1985) would shorten the model period too much.

Table 6.4: Dates and amplitudes of solar cycles prior to the group sunspot number series obtained by the superimposed ellipse approach. In the table,  $t_{in}$  denotes the starting date of each Solar Cycle.

Solar Cycle Number	$t_{in}$ (year)	Amplitude (SSNs)
-13	1609	94
-14	1598	93
-15	1587	79
-16	1576	85
-17	1565	110
-18	1554	81
-19	1543	75
-20	1532	56
-21	1521	39
-22	1510	49
-23	1499	35
-24	1488	15
-25	1477	40
-26	1466	32
-27	1455	0
-28	1444	34
-29	1433	34
-30	1422	29
-31	1411	24
-32	1400	57

As for the ellipse-linear and linear approaches, the calculated cross-correlation coefficients using a cut-off frequency of  $(1/3) \text{ year}^{-1}$  are 0.65 compared with 0.67 for a time-lag of two years (between 1610–1985) and 0.52 for a time lag of three years compared with 0.56 for a time lag of four years (between 1610–1985).

## 6.5 Discussion

We reconstructed group SSNs for the period from 1392 to 1985 based on the  $^{10}\text{Be}$  flux recorded in the NGRIP ice core. Three different approaches were used to reconstruct short-term changes. These changes were subsequently superimposed on a physics-based model for reconstructing the long-term trend. The three approaches we used to reconstruct changes in the 11-year cycle are based on linear, ellipse-linear, and ellipse approaches, of which the latter two are based on the hysteresis effect observed between  $\Phi$  and SSNs (Inceoglu et al., 2014a). However, given the average residence time of  $^{10}\text{Be}$  in the atmosphere of one to two years, uncertainties related to the age-depth model of the NGRIP ice core (Vinther et al., 2006), and climate-related noise, it is challenging to reconstruct well-defined hysteresis curves. In spite of the success of the ellipse-linear approach when applied to instrumental data (Inceoglu et al., 2014a), the ellipse approach clearly provides the most robust method to reconstruct subdecadal changes in group SSNs back in time based on the NGRIP  $^{10}\text{Be}$  flux, because it simply provides a much better representation of the observed group SSN data compared to the linear and ellipse-linear approaches.

The ellipse-linear approach, which was proposed previously in Inceoglu et al.

(2014a), also seems problematic when considering reconstructed  $\Phi$  based on  $^{10}\text{Be}$  flux. Clearly, the main problem here is the transitions between cycles. This problem is likely also related to climate-related noise and/or uncertainties in the age-depth model of the NGRIP ice core.

We also compared our long-term group SSN reconstruction with three different group SSN reconstructions by Usoskin et al. (2003c, 2014) and Solanki et al. (2004). Usoskin et al. (2003c) used  $^{10}\text{Be}$  concentrations in ice cores from Greenland and the South Pole, while Usoskin et al. (2014) and Solanki et al. (2004) used  $^{14}\text{C}$  from tree rings to reconstruct decadal-scale changes in group SSNs. Neither of these previous studies attempted to reconstruct changes in group SSN over the 11-year solar cycle. The reconstruction obtained in this study is shown as 10-year-averaged values together with the reconstructions by Usoskin et al. (2003c) based on  $^{10}\text{Be}$  concentrations from the South Pole (Uso03), Usoskin et al. (2014) (Uso14) and Solanki et al. (2004) (Sol04) in Figure 6.6. Even though they generally match well, some discrepancies can be observed among the various reconstructions. During the ascending phase of the Dalton Minimum, between around 1825 and 1900, our reconstruction underestimates the group SSNs, similar to the Uso03 reconstruction, but shows the same two-peaked structure as seen in the observed group SSNs, while the Sol04 and the Uso14 reconstructions overestimate the group SSNs around 1850. Additionally, the peak occurring around 1650 and the higher levels of group SSNs during the ascending phase of the Spörer Minimum between around 1500 and 1600 in our group SSN reconstruction can also be observed with some time offset in the group SSN reconstruction based on the Dye-3 ice core (Greenland) (see Usoskin et al., 2003c, green curve in Figure 2 therein). Another peak observed in the reconstructed group SSNs in Figure 6.6 (also in Figure 2 of Usoskin et al., 2003c) around the termination of the Maunder Minimum ( $\sim 1730$ ) seems to be a common feature of group SSN reconstructions based on  $^{10}\text{Be}$  measurements from polar ice cores. This peak is also seen in the tree-ring based reconstruction by Uso14. However, these features cannot be seen in the directly observed group SSNs. The reconstruction obtained in this study based on the NGRIP record shows similar minimum values as observed group SSNs during the Maunder Minimum similar to Uso14, while Uso03 and Sol04 overestimate and underestimate the SSN, respectively. Additionally, our reconstruction, together with Uso14, better matches with the observed group SSN levels around the onset of the Maunder Minimum (around 1620), where the Uso03 and the Sol04 reconstructions underestimate the group SSN levels. Figure 6.6 also shows that the Spörer Minimum is a broader low-activity episode than the Maunder Minimum, with more gradually decreasing and increasing transition phases. Note that the onset of the Maunder Minimum was recently refined, so that it now appears as a more gradual transition than hitherto believed (Vaquero et al., 2011). However, the transition phases associated with the Maunder Minimum appear to be steeper than for the Spörer Minimum, but more gradual than those associated with the Dalton Minimum. Furthermore, in our reconstruction the activity level of the Sun during the Maunder Minimum is lower than during the Spörer and Dalton Minima, in contrast with Uso14, Uso03, and Sol04, where the reconstructed group SSNs during the Spörer Minimum are lower than, or similar to, that observed during the Maunder Minimum.

To a large degree, these discrepancies reflect differences in the underlying data, because the  $^{10}\text{Be}$  flux recorded in the NGRIP ice core displays a slightly different long-term trend than the  $^{10}\text{Be}$  data recorded at Dye-3 and the South Pole. This demonstrates that effects related to climate and transport also influence the deposition of  $^{10}\text{Be}$  on longer time scales and that more  $^{10}\text{Be}$  records are needed to better resolve past solar variability. We emphasize, however, that at the present, only the data from

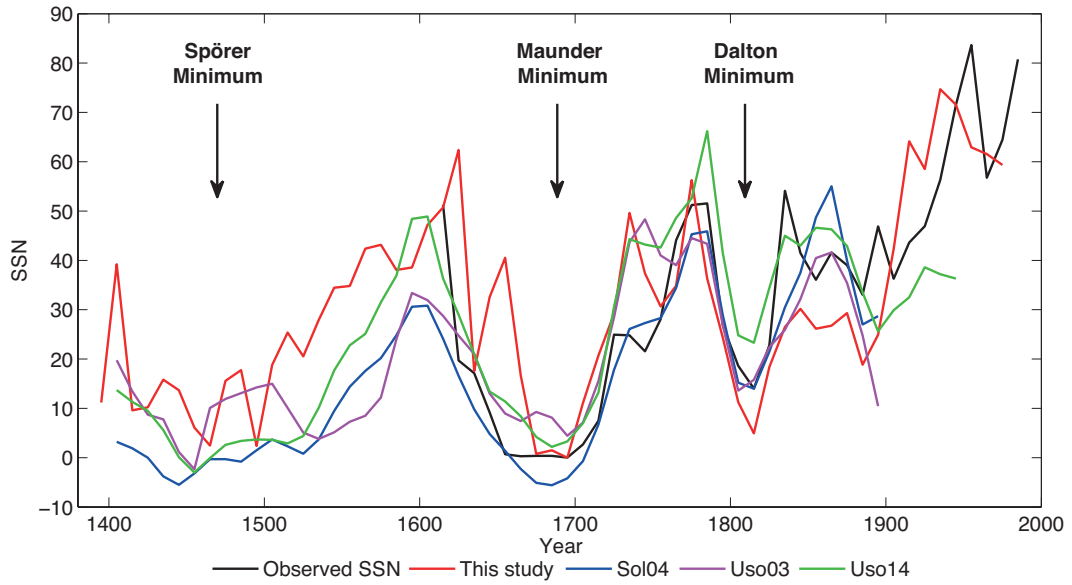


Figure 6.6: Reconstructed group SSNs in this study (10-year average, red line), decadal reconstructions of Usoskin et al. (2014) (Uso14, green line), Usoskin et al. (2003c) (Uso03, magenta line), Solanki et al. (2004) (Sol04, blue line), and decadal SSNs<sub>Obs</sub> (black line).

NGRIP allow reconstructing changes in the 11-year solar cycle, which is the primary objective of this study.

The new reconstruction of SSNs based on the NGRIP  $^{10}\text{Be}$  flux shows that during the Maunder and Spörer Minima, the solar dynamo that drives the 11-year solar cycle did not cease, even though the sunspot observations show that sunspots in the photosphere almost completely vanished during the Maunder Minimum (Figure 6.5). This can explain the modulation effects of the residual magnetic flux on the cosmic rays that reach Earth (Solanki et al., 2002; Usoskin et al., 2003c). The residual magnetic flux remains on the solar surface during its minimum activity level, because the Sun's polarity cycle most likely continues to be active, which leads to a continued modulation of open solar magnetic flux throughout the heliosphere (Owens et al., 2011).

## 6.6 Conclusions

We show that it is possible to reconstruct changes in the annual group SSNs, and we investigated changes in the 11-year solar cycle as well as long- and short-term variations in the magnetic activity level of the Sun using annually resolved  $^{10}\text{Be}$  flux measured in the NGRIP ice core. This was achieved by superimposing changes of the 11-year cycles, modeled with an ellipse approach, on a long-term trend computed with a physics-based model. The ellipse approach we used is based on the hysteresis effect observed between  $\Phi$  and group SSNs. Long-term changes in reconstructed group SSNs based on the NGRIP ice core record agree reasonably well with the other group SSN reconstructions with some discrepancies. These discrepancies result from differences in the underlying proxy data for past solar activity, hereby demonstrating the potential influence of climatic noise. Therefore, to better resolve short-term changes in solar

variability prior to 1610 A.D., which is necessary to improve our understanding of the Sun, we need more high-resolution  $^{10}\text{Be}$  records that extend farther back in time.

**Acknowledgements** Funding for the Stellar Astrophysics Centre is provided by the Danish National Research Foundation (Grant agreement no.: DNRF106). MFK, CK and JO acknowledge support from the Carlsberg Foundation and Villum Foundation. Neutron monitors of the Bartol Research Institute are supported by the United States National Science Foundation (Grant agreement numbers: ANT-0739620 and ANT-0838839), and by the University of Delaware Department of Physics and Astronomy and Bartol Research Institute. Authors are also thankful to Ilya Usoskin for providing his SSN reconstruction. We also thank the referee for comments that greatly improved this manuscript.

## Chapter 7

# Grand solar minima and maxima deduced from $^{10}\text{Be}$ and $^{14}\text{C}$ : Magnetic dynamo configuration and polarity reversal

F. Inceoglu, R. Simoniello, M. F. Knudsen, C. Karoff, J. Olsen, S. Turck-Chiéze, B. H. Jacobsen

*Under revision for resubmission to Astronomy & Astrophysics*

### Abstract

**Aims:** This study aims to improve our understanding of the occurrence and origin of grand solar maxima and minima.

**Methods:** We first investigate the statistics of the peaks and dips simultaneously occurring in the solar modulation potentials reconstructed using the GRIP  $^{10}\text{Be}$  and IntCal13  $^{14}\text{C}$  records for the overlapping time period spanning the last 8250 years. Based on the distribution of these events, we propose a method to identify grand minima/maxima periods. By using waiting time distribution analysis, we investigate the nature of grand minima/maxima periods identified by the criteria as well as the variance and the significance of the Hale cycle during such events throughout the Holocene epoch.

**Results:** The analysis of the grand minima/maxima events simultaneously occurring in the solar modulation potentials reconstructed based on the  $^{14}\text{C}$  and the  $^{10}\text{Be}$  records, shows that these periods are not time-independent memoryless processes, but rather related to accumulation and release of energy. Furthermore, we found that the majority of events characterised by periods of moderate activity levels tend to last less than 50 years, grand maxima periods do not last longer than 100 years, while grand minima can persist a bit longer. The power and the variance of the 22-year Hale cycle increases during grand maxima and decreases during grand minima, compared to periods characterised by moderate activity levels.

**Conclusions:** We present the first reconstruction of the occurrence of grand solar maxima and minima during the Holocene based on simultaneous changes in records of past solar variability derived from tree-ring  $^{14}\text{C}$  and ice-core  $^{10}\text{Be}$ , respectively. Such a robust determination of the occurrence of grand solar minima and maxima periods will enable systematic investigations of the influence of grand solar minima and maxima episodes on Earth's climate. Also, energy accumulation and release origin of grand minima/maxima together with an upper limit on the duration of grand maxima provide useful constraints for solar dynamo models.

## 7.1 Introduction

Sun-like stars are characterised by convective envelopes, where large-scale plasma flows are able to support a self-exciting global dynamo (Parker, 1955a,b) believed to be the root of all phenomena collectively known as stellar activity in Sun-like stars. The multitude of activity-related phenomena, such as star spots in the photosphere, chromospheric plages, coronal loops, UV-X radio emission and flares, are produced with an amplitude modulation that ranges from decadal up to at least centennial time scales. Despite these chaotic complexities, large-scale organized spatial patterns are seen (e.g. Maunder’s butterfly diagram, Joy’s law and Hale’s polarity as observed in the Sun), which support the existence of a large-scale magnetic field within the convection zone. The geometry and behavior of stellar magnetic activity are thought to be globally determined by the stability of dynamo configurations with different symmetries (Brandenburg et al., 1989). For example, the Sun exhibits variations over a wide range of time scales with the most prominent being the roughly 11-year sunspot cycle. This can be explained by a dipole-like dynamo configuration (dynamo mode), which is antisymmetric with respect to the equator and reverses its polarity very near the maximum of the 11-year solar activity cycle (DeRosa et al., 2012). The initial dipolar magnetic configuration (full magnetic cycle) is re-established after about 22 years.

The magnetic activity can be tracked through many observational proxies, from the photosphere to the corona. From 1965 to 2003, The Mount Wilson Observatory carried out a long-term monitoring of the chromospheric activity of one hundred solar-like stars and revealed a correlated pattern between chromospheric changes and rotation rates. Cyclic patterns were observed with a variety of cycle lengths in stars as old as the Sun, and even older stars with slow rotation rates; more erratic activity fluctuations were seen in particularly young stars with high chromospheric activity and rapid rotation rates, while some others had no detectable activity at all (Baliunas et al., 1995). The stars, which do not show any detectable activity could be in the so-called grand minimum state. Within solar dynamo models, grand minima are seen as quiescent intervals of activity that interrupt periods of normal cyclic activity. There are at least two ways to reproduce these intermittent periods in stellar dynamos; stochastic noise (Moss et al., 2008) and non-linearities (Tobias, 1996). Although these two formalisms reproduce some of the observed features of grand minima, they fail to reproduce the frequencies of such events. Depending on assumptions in the dynamo model, grand minima might represent a periodic or a random characteristic of the dynamo. Therefore, a better understanding of the occurrence and origin/nature of such events, would lead us to make a significant step forward in stellar dynamo theory. Within this context, the Sun can play a key role, because answering these questions requires longer data sets that allow detailed studies of variations in solar activity levels over millennia.

Information on solar activity levels during the pre-telescopic era, prior to 1610 A.D., relies mainly on past production rates of cosmogenic radionuclides, such as  $^{10}\text{Be}$  and  $^{14}\text{C}$  (Usoskin, 2013). Cosmogenic radionuclides are mainly produced by spallation reactions occurring when galactic cosmic ray particles from space interact with atoms in the Earth’s atmosphere (Dunai, 2010). The production rates of cosmogenic radionuclides are inversely correlated with solar magnetic activity and the geomagnetic field intensity due to the nonlinear shielding effect of the solar magnetic

field and the geomagnetic dipole field (Heikkilä et al., 2008b). A strengthening of the solar magnetic and geomagnetic fields thus results in a lower production rate of cosmogenic nuclides (Masarik & Beer, 1999).

Earlier attempts to study the occurrences of grand minima and maxima of solar activity are based only on  $^{14}\text{C}$  records (Stuiver, 1980; Stuiver & Braziunas, 1989; Voss et al., 1996; Usoskin et al., 2007), and provide different results on the nature of the process. In the work of Voss et al. (1996), the authors claimed that the occurrences and durations of these minima are random in origin. On the contrary, using a physics-based reconstruction of group sunspot numbers from  $^{14}\text{C}$  measurements in tree rings, Usoskin et al. (2007) suggested that identified grand minimum and maximum solar activity periods occur as a result of a special state of the solar dynamo, implying that the occurrence and the nature of grand minima and maxima might reflect a self-organised criticality or an oscillatory behaviour where the energy is accumulated and released. The following investigation will combine results from  $^{10}\text{Be}$  and  $^{14}\text{C}$  records for an overlapping time period that provides information about past solar activity levels through the Holocene epoch (past  $\sim 11.700$  years), in which the influences of climatic variations and changes in the carbon cycle were minimal (Lockwood, 2013). Our aim is to investigate the signatures of grand minima/maxima as seen in the solar modulation potential, which brings vital information on the solar magnetic field, extracted from  $^{10}\text{Be}$  and  $^{14}\text{C}$  records.

Therefore, we first propose a method to identify grand minima/maxima states of solar activity in the data and then we investigate whether the occurrence of these events are best understood as a random or an oscillatory behaviour, using waiting time distribution analysis. If indeed these events are driven by an oscillatory behaviour, then we expect to see correlated patterns between length variations and the occurrence of grand minima/maxima, as they are not memoryless.

## 7.2 Long term solar variability based on cosmogenic radionuclide data

### Solar potential

The  $^{10}\text{Be}$  and  $^{14}\text{C}$  production mostly takes place within the lower stratosphere and the upper troposphere, but they follow very different pathways in the Earth's system due to differences in their geochemical behaviour. The  $^{10}\text{Be}$  atoms rapidly become adsorbed onto aerosols, mainly atmospheric sulfate particles. After a residence time of 1 to 2 years in the lower stratosphere (Raisbeck et al., 1981), the aerosols are transported into the lower troposphere by air mass exchanges taking place between the troposphere and stratosphere at mid-latitudes (Koch & Rind, 1998). Subsequently, they are deposited at the surface by both dry and wet deposition and become incorporated into geological archives. As a consequence,  $^{10}\text{Be}$  concentrations in *e.g.* ice cores can be influenced by atmospheric mixing, transportation and local, high-frequency meteorological changes (Berggren et al., 2009). In contrast, shortly after its production,  $^{14}\text{C}$  becomes oxidised and joins the atmospheric  $^{12}\text{CO}_2$  reservoir. The atmospheric  $^{12}\text{CO}_2$  reservoir is part of the global carbon cycle, and it exchanges  $^{12}\text{CO}_2$  with Earth's carbon reservoirs, including the oceans, sediments, soils and biosphere (Bard et al., 1997). The amount of  $^{14}\text{C}$  in the atmosphere is influenced by changes in the global production rate, but variations in the  $^{14}\text{C}$  concentration measured in tree rings are attenuated and delayed relative to its production due to the effect of the global carbon inventory (Roth & Joos, 2013). Therefore, these two cosmogenic

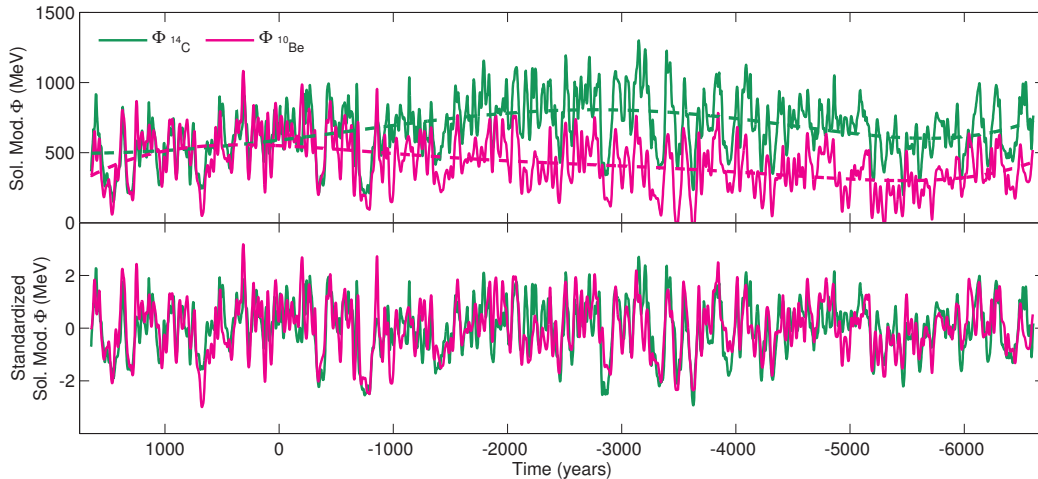


Figure 7.1: Top panel: Solar modulation potential based on the GRIP  $^{10}\text{Be}$  (magenta) and the IntCal13  $^{14}\text{C}$  (green) records. Dashed lines show the long-term trend observed in calculated solar modulation potentials. Bottom panel: Detrended and standardised solar modulation potential based on polynomial fits of degree 5.

radionuclides may also provide independent information on the climate system, other than changes in the activity level of the Sun (Roth & Joos, 2013).

In this study, we use the GRIP (Greenland Ice Core Project)  $^{10}\text{Be}$  (Vonmoos et al., 2006) and IntCal13  $^{14}\text{C}$  (Reimer et al., 2013) records. The GRIP  $^{10}\text{Be}$  record spans the period between around 1650 A.D. to 6600 B.C., with a mean temporal resolution of about 5 years. The available data, which has been filtered using a 61-point binomial filter (Vonmoos et al., 2006), were linearly interpolated at 1-year intervals.

The  $^{14}\text{C}$  values within the overlapping period are calculated based on the  $\Delta^{14}\text{C}$  record associated with the IntCal13 calibration curve. The  $\Delta^{14}\text{C}$  record in the study period, which spans from 1650 A.D to 6600 B.C., has a temporal resolution of 5 years. Even though the IntCal13 calibration curve ends at 1950 A.D., we had to truncate the most recent 300 years of the data in order to obtain a time period that overlaps the GRIP ice core. In this way, we also got rid of the Suess effect, which has caused a significant decrease in the  $^{14}\text{C}/^{12}\text{C}$  ratio as a consequence of admixture of large amounts of fossil carbon into the atmosphere after the industrial revolution (Suess, 1955). The data were linearly interpolated at 1-year intervals.

In order to get rid of the effects of the geomagnetic field intensity on the production rates of the cosmogenic radionuclides and to calculate the solar modulation potential ( $\Phi$ ), based on both  $^{10}\text{Be}$  ( $\Phi_{10\text{Be}}$ ) and  $^{14}\text{C}$  ( $\Phi_{14\text{C}}$ ), we used a well-established relationship between the solar modulation potential, the geomagnetic field intensity, and the production rates of  $^{14}\text{C}$  and  $^{10}\text{Be}$  (Masarik & Beer, 1999). The latter relationship was updated by Knudsen et al. (2009) to take into account a 20% polar enhancement of the solar signal in the  $^{10}\text{Be}$  flux (Field et al., 2006). Following the calculation of  $\Phi_{10\text{Be}}$  and  $\Phi_{14\text{C}}$ , we then adjusted the time scale of  $\Phi_{10\text{Be}}$  according to the time scale of the  $\Phi_{14\text{C}}$  curve using the maxima of the running cross-correlation analysis following the approach of Knudsen et al. (2009).

The resulting reconstructions of the solar modulation potentials are shown in the top panel of Fig. 7.1. Even though there is a good agreement between short-term fluctuations seen in the upper panel of Fig. 7.1, it is also evident from the figure that there are some discrepancies between the long-term variations of the two

reconstructions. The observed long-term differences between the two reconstructions can be caused by long-term changes in the atmospheric transport and deposition of  $^{10}\text{Be}$  and undetected changes in carbon cycle (Vonmoos et al., 2006).

In order to remove the observed long-term trends from the time series, we subtract the values of the long-term trends (as calculated with polynomial fits of degree 5) from the calculated solar modulation potential values. After removal of the long-term trends from the two time series, we standardised the data using their mean and standard deviation values. The lower panel of Fig. 7.1 shows the detrended and standardised solar modulation potential reconstructions based on  $^{10}\text{Be}$  and  $^{14}\text{C}$ . Temporal variations in the detrended solar modulation potential reconstructions are in good agreement, implying that the short-term variations seen in the reconstructions reflect the solar component within the data.

### Classification of solar cycle events

As seen in the lower panel of Figure 7.1, temporal variations of both  $\Phi$  reconstructions show overlapping events, as peaks and dips. There are 160 overlapping events in total, whose onset and ending times are determined using a zero-crossing method. Durations of these events range from 5 years (since the records are interpolated) up to  $\sim 170$  years. In order to define relevant selection criteria regarding the strength of the peaks and dips, which will be used to identify grand minima/maxima states of the Sun, we construct histograms of the 160 events occurring in both  $\Phi$  reconstructions through the Holocene epoch. The bin numbers for the histograms are calculated according to the Freedman-Diaconis rule, which aims to minimise the sum of squared errors between the bar heights and the probability distribution of the underlying data (Freedman & Diaconis, 1981).

The resulting histograms are shown in Fig. 7.2 together with superimposed bimodal gaussian probability density function fits. As observed in Fig. 7.2, the events follow bimodal distributions, which are partly created by the subtraction of polynomials of degree 5, implying that the overlapping events through the Holocene epoch show two modes, peaks and dips, with distinct local maxima in the probability density functions (red line in Fig. 7.2). Based on the local maxima values of the bimodal gaussian fits, we define threshold values regarding the strengths of the overlapping peaks and dips in order to identify grand maximum and minimum episodes among these events. Since the distributions of all events observed for the  $\Phi_{10\text{Be}}$  and  $\Phi_{14\text{C}}$  reconstructions are not symmetrical and hence yield slightly different local maxima values, we determine different threshold values for maximum and minimum periods for each data set separately.

We classified all the events according to their amplitudes in three distinct modes (Usoskin et al., 2014), which are determined by the threshold values found using bimodal gaussian distribution fits: moderate activity level in  $\Phi_{10\text{Be}}$  defined as values within  $-0.92\sigma$  and  $+1.35\sigma$ , low activity level for values smaller than  $-0.92\sigma$  and high activity level for values higher than  $+1.35\sigma$ . For  $\Phi_{14\text{C}}$ , moderate activity level is defined as values between  $-0.67\sigma$  and  $+1.41\sigma$ , low activity level for values smaller than  $-0.67\sigma$  and high activity level for values higher than  $+1.41\sigma$ . Within the low- and high-activity groups, we define grand minima/maxima events as intervals lasting more than two sunspot cycles.

Based on the criteria defined in this study, we identify 32 grand minima and 21 grand maxima periods, which are listed in Table 8.1 and Table 8.2, respectively. In the  $\Phi_{10\text{Be}}$  data, there are two grand minima around 417 A.D. and -2183 B.C. (434 A.D. and -2195 B.C. in  $\Phi_{14\text{C}}$ ) and three grand maxima around 517 A.D., 224 A.D.,

Table 7.1: The list of the grand minima found in solar modulation potential data based on our criteria.

$\Phi_{10Be}$		$\Phi_{14C}$	
Center time (A.D. / B.C.)	Duration (years)	Center time (A.D. / B.C.)	Duration (years)
1463	161	1450	167
1283	75	1300	91
1027	47	1050	65
901	31	900	28
676	107	690	102
417	106	434	54
266	36	261	34
124	31	133	25
-344	82	-348	107
-658	35	-660	22
-790	135	-750	154
-906	43	-895	54
-1190	41	-1189	38
-1358	125	-1370	121
-1488	61	-1491	53
-2125	39	-2132	42
-2183	83	-2195	25
-2453	51	-2461	74
-2901	93	-2874	106
-3088	30	-3080	28
-3344	140	-3330	134
-3479	79	-3492	73
-3627	80	-3627	98
-3699	24	-3695	30
-4231	59	-4224	67
-4317	53	-4322	72
-5193	45	-5205	53
-5298	62	-5298	69
-5459	50	-5466	80
-5606	76	-5610	53
-5718	51	-5713	41
-6445	123	-6425	152

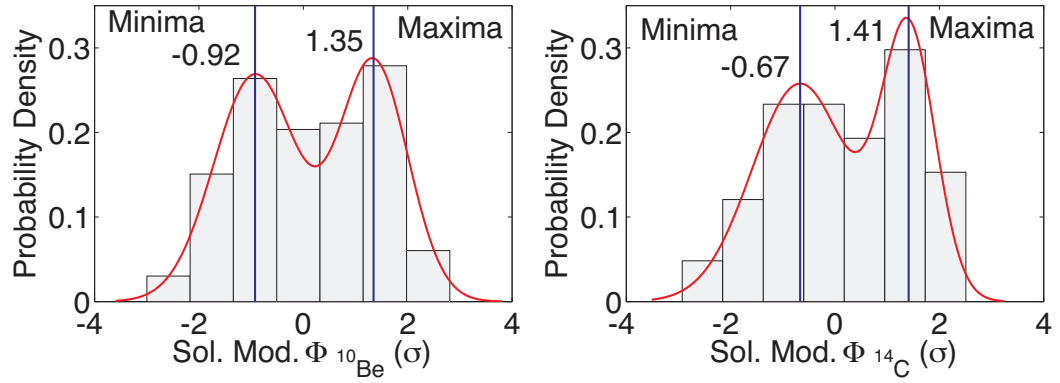


Figure 7.2: The left and the right panels show histograms of all events recorded over the Holocene period, which overlap in solar modulation potential reconstructions based on the GRIP  $^{10}\text{Be}$  and the IntCal13  $^{14}\text{C}$ , respectively. Red line shows the bimodal gaussian distribution fitted to the data, whereas the texts show the threshold values determined for identifying grand minima and maxima.

Table 7.2: The list of the grand maxima found in solar modulation potential data based on our criteria.

$\Phi_{^{10}\text{Be}}$		$\Phi_{^{14}\text{C}}$	
Center time (A.D. / B.C.)	Duration (years)	Center time (A.D. / B.C.)	Duration (years)
1616	82	1604	83
1373	58	1370	36
517	27	521	72
314	72	305	67
224	37	200	88
-200	59	-218	22
-263	43	-241	26
-447	67	-433	94
-1845	57	-1838	39
-2052	71	-2078	63
-2509	46	-2510	43
-2764	72	-2718	40
-2947	62	-2948	75
-3127	76	-3150	70
-3406	70	-3394	83
-3844	104	-3854	78
-4087	56	-4090	63
-4626	65	-4630	51
-4852	48	-4863	70
-6130	49	-6133	104
-6309	86	-6280	80

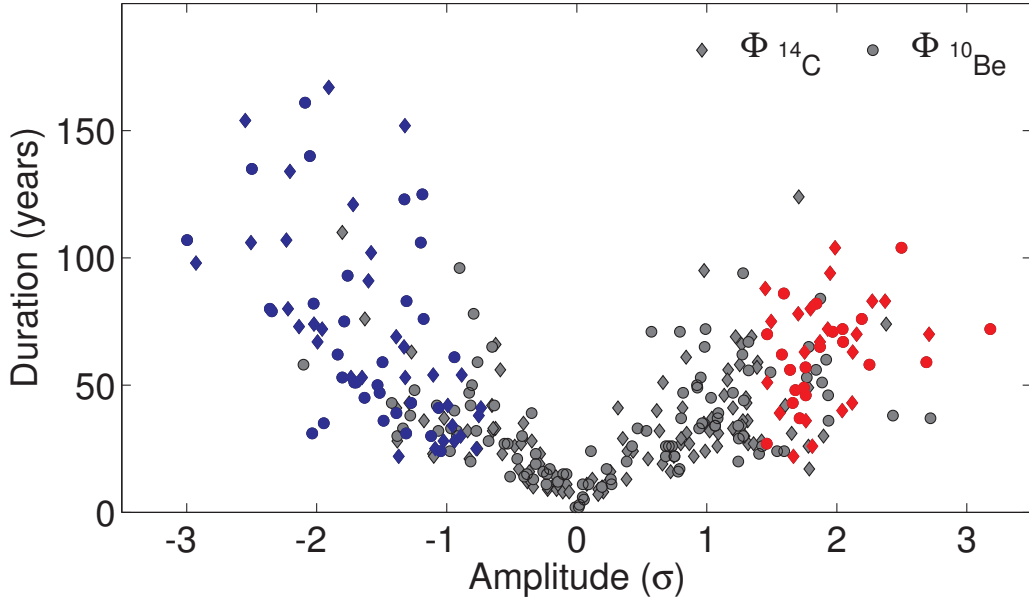


Figure 7.3: The duration as function of strength of all events recorded over the Holocene period. Red and blue colors show identified grand maximum and grand minimum periods, respectively. Grey colour shows moderate activity periods observed in  $\Phi_{14C}$  and  $\Phi_{10Be}$ . Circles and diamonds represents  $\Phi_{14C}$  and  $\Phi_{10Be}$ , respectively.

and -6130 B.C. (521 A.D., 200 A.D., and -6133 B.C. in  $\Phi_{14C}$ ), whose durations show approximately 50 year difference in comparison to those identified in  $\Phi_{14C}$ . The reason for the difference seen in durations can be caused by the different geochemical behaviour of the two radionuclides, which can alter the peak shapes.

According to the results obtained using  $\Phi_{10Be}$ , the Sun spent  $\sim 27\%$  of its time in a grand minimum state and  $\sim 16\%$  of its time in a grand maximum state during the last 8250 years. As for  $\Phi_{14C}$ , these numbers are  $\sim 28\%$  and  $\sim 16\%$ , respectively. The total time spent in a minimum state ( $\sim 27\%$ ) found in this study is higher than that found by Usoskin et al. (2007), whereas our estimate of the time spent in a maximum state lies in between the two estimates obtained by Usoskin et al. (2007) based on two different SSN reconstructions.

Additionally, we have also investigated the dependence of the durations of identified grand minima and grand maxima on their amplitude in order to check whether these grand minima and grand maxima events have any preferred tendency to last longer/shorter with respect to the periods characterised by moderate activity levels. Fig 7.3 clearly suggests that there is a tendency for the grand minima events to last longer than moderate activity periods. For grand maxima, we found an upper limit for the durations of 100 years for the highest amplitudes.

## 7.3 Results

### On the origin of Grand Minima/Maxima

Waiting time is defined as the time interval between two subsequent events. The statistical distribution of the waiting times between discrete events has been broadly used in physical sciences to investigate whether the underlying mechanisms of such

events are random or time-dependent memory-bearing processes (Wheatland, 2000; Lepreti et al., 2001; Wheatland, 2003). An exponential waiting time distribution indicates that the mechanism causing such events is a Poisson process, which is a memoryless, purely random process, where the occurrence of an event is independent of the preceding one (Usoskin et al., 2007). On the other hand, if the waiting time distribution follows a power law, the occurrence is dependent on the previous event, implying that the mechanism has a memory (Clauset et al., 2009), which can be interpreted as self-organising criticality or processes related to accumulation and release of energy like an oscillator (Usoskin et al., 2007). Therefore, in order to investigate the occurrence of the detected grand minimum and maximum activity states of the Sun and durations of these periods, we applied waiting time distribution analyses to the data. Waiting times can be considered as intervals between the ending time of an event to the onset of a subsequent event or alternatively the time intervals between subsequent peaks or dips in activity (Wheatland et al., 1998). In this study, we applied the latter definition.

Prior to the analyses, we constructed complementary cumulative distribution functions of the data, which is defined as the probability that an event "X" with a certain probability distribution will be found at a value more than or equal to "x". The mathematical formulation is shown below (Clauset et al., 2009; Guerriero, 2012);

$$P(X \geq x) = 1 - \int_{-\infty}^x p(x) dx = \int_x^{\infty} p(x) dx \quad (7.1)$$

where P denotes the probability. Following this step, we fit a power law distribution using the code provided by Clauset et al. (2009) and an exponential distribution using the maximum likelihood method (MLM), which takes into account the real distribution of the data. The MLM is robust and generally accurate for estimation of the parameters of the distributions under consideration of this study (Clauset et al., 2009; Guerriero, 2012). The equations used for the power law (Eq. 7.2) and exponential (Eq. 7.3) fits are shown below;

$$p(x) \propto x^{-\alpha} \quad (7.2)$$

$$p(x) \propto \exp\left(\frac{-x}{\tau}\right) \quad (7.3)$$

where  $p(x)$  denotes the probability and  $\alpha$  and  $\tau$  indicate the scaling and the survival parameters, respectively (Virkar & Clauset, 2012). The resulting fits constructed using the MLM are shown in the top panel of Fig. 7.4, whereas their scaling and survival parameters are listed in Table 7.3 together with the Bayesian Information Criterion (BIC) and Akaike Information Criterion (AIC). The BIC was suggested by Schwarz (1978) as an alternative to the AIC (Akaike, 1974). Although both criteria are extensions of the maximum likelihood principle and used to choose the most probable model that better characterises the data, they show some differences in practical manner. The BIC is generally used when the main goal is to build a model that describes the distribution of the data, whereas the AIC is used for more predictive aspects (Neath & Cavanaugh, 2012). The difference between the BIC and the AIC is more pronounced when the sample size is large. Additionally, the model which gives the minimum AIC and/or BIC is selected as the best model. According to the results of the BIC and the AIC, a power law represents the distribution of waiting times seen both in  $\Phi_{14C}$  and  $\Phi_{10Be}$  reconstructions better in comparison to an exponential fit. One interesting feature seen in the top-left panel of Fig 7.4 is that

Table 7.3: The scaling and the survival parameters found for grand minima, maxima and duration of these periods using maximum likelihood method for power-law and exponential fits together with the Bayesian (BIC) and Akaike (AIC) information criterion values.

	Power law			Exponential		
	$\alpha$	BIC	AIC	$\tau$	BIC	AIC
Grand Min.	2.30	648	646	255	815	813
Grand Max.	2.45	443	441	395	562	560

there is an indication of a lumping of the waiting times of grand minima periods into three, *i. e.*, one is around 140 years and the other two are around 250 and 470 years, respectively. For the top-right panel of Fig 7.4, which shows the waiting times of grand maxima periods, these lumps are seen around 250 and 440 years. The observed tendency for lumping in the top panels of Fig 7.4 may indicate that there are different characteristic time scales involved in the system, some of which may potentially be associated with the known periods of  $\sim 150$ ,  $\sim 220$  and  $\sim 400$  years (Knudsen et al., 2009). However, Monte-Carlo tests showed that the observed tendencies for lumping are not statistically significant.

We also run Kolmogorov-Smirnov (KS) tests in order to double-check the results suggested by the BIC and the AIC. For grand minimum and maximum periods, the KS test results suggest that the distributions are better represented by a power law compared to an exponential fit at the 99% significance level, supporting the results of the BIC and AIC analyses.

Additionally, we tested whether the distributions of the durations of grand minima and maxima (the bottom panel of Fig. 7.4) are best represented by normal, lognormal, or bimodal gaussian distributions. Results showed that the durations of grand maxima periods are best represented by a normal distribution with a mean duration of  $\sim 65$  years, while a lognormal distribution represents the distribution of grand minima durations better with a mean duration of  $\sim 70$  years. Usoskin et al. (2007) also suggested that the mean duration for grand minima is 70 years, but claimed that the durations of grand minima shows a bimodal gaussian distribution implying two kinds of minima, *i. e.* 30 to 90 years, similar to the Maunder Minimum, and longer than 110 years, similar to the Spörer Minimum. The results presented here based on both  $^{14}\text{C}$  and  $^{10}\text{Be}$  do not support such a systematic grouping of minima based on their durations.

## Magnetic cycle lengths during Grand Minima/Maxima

Previous studies have shown that the cyclic behaviour of solar magnetic activity does not cease during grand minimum states (Beer et al., 1998; Owens et al., 2012; McCracken et al., 2013). Even more, based on a  $^{10}\text{Be}$  record from the Dye 3 ice core, Fligge et al. (1999), showed that the sunspot cycle lengths during the Spörer Minimum are much longer than 11 years. Hence, we study the cycle length variation of the Hale cycle (22-year magnetic activity) over the whole Holocene period, more specifically during grand minima and maxima. We expect, in fact, to observe systematic trends in the cycle length variation over grand minima and maxima if indeed these events are not memoryless (Tobias, 1998).

The bottom panels of Fig. 7.5 and Fig. 7.6, which are focusing on the identified grand minima and maxima based on the criteria defined in this study, show the resulting local cross-wavelet power spectra of high-pass filtered  $\Phi_{10\text{Be}}$  and  $\Phi_{14\text{C}}$  with a

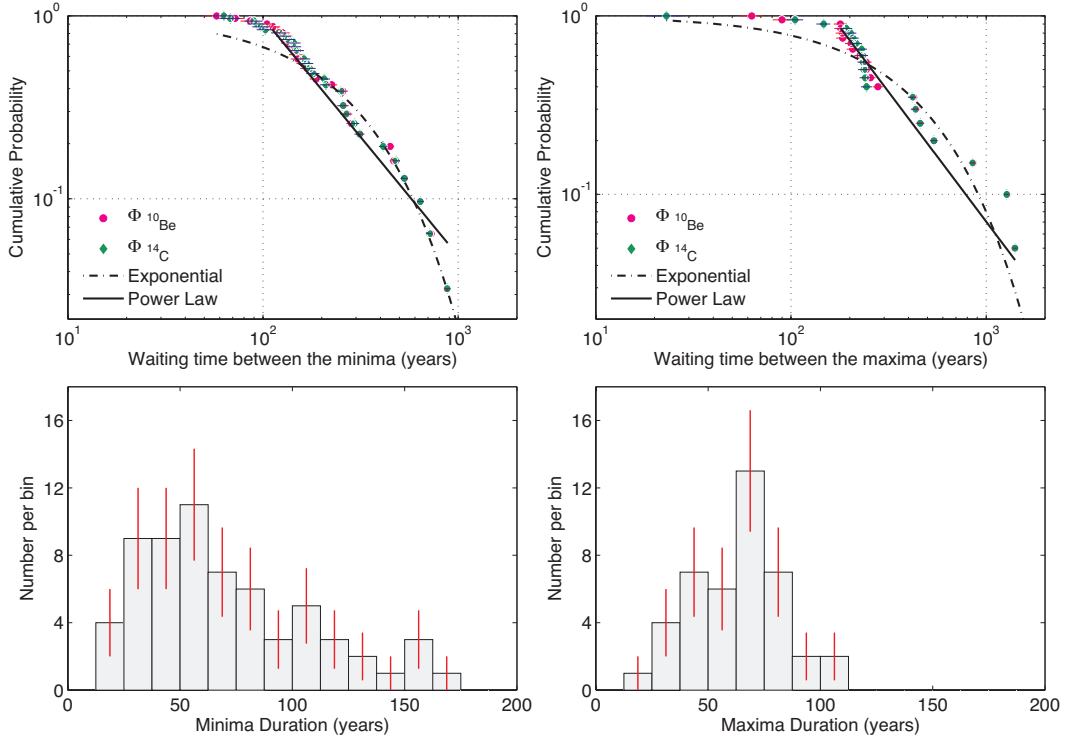


Figure 7.4: The results of the waiting time distribution analyses. Top panels show the complementary cumulative distribution function for grand minima and grand maxima together with the power-law and exponential fits using MLM. Bottom panels show the distributions of durations of the grand minima and maxima, respectively.

cut-off frequency of  $(1/30) \text{ year}^{-1}$  together with the solar modulation potential reconstructions based on  $^{10}\text{Be}$  and  $^{14}\text{C}$ , respectively (top panel). Cross-wavelet analyses are made based on the code provided by Grinsted et al. (2004). In the figures, we also show minimum and maximum solar activity periods identified based on the criteria defined in this study.

One interesting feature observed in the cross-wavelet power spectra of the high-pass filtered solar modulation potential data, is that even though it is difficult to detect the 22-year Hale cycle due to lack of high-resolution data, it is still possible to follow the temporal behaviour of the periods lower than 40 years that are present in the data. When the bottom panels of Fig. 7.5 and Fig. 7.6 are carefully examined, we might observe that the significance of the 22-year Hale cycle during grand minimum/maximum states tends to decrease/increase, respectively, implying that the power of the 22-year periodicity under consideration becomes weaker during grand minima states, whereas the power of the 22-year Hale cycle signal seems stronger during grand maxima states. A similar trend can also be observed for the length of the 22-year Hale cycle, which tends to become longer ( $\sim 30$  years) during grand minima states, while it becomes shorter ( $\sim 20$  years) during grand maxima states.

A similar feature can also be seen in the high-pass filtered data (Fig. 7.7), the variance in the data set tends to be lower during grand minimum periods in contrast to grand maximum periods, in which the variance tends to be higher. We therefore calculate the moving variance of the two high-pass filtered data set using a 25-year moving window, which is also shown in Fig. 7.7. In order to test the significance of our observations statistically, we carried out KS tests, which are based on the null

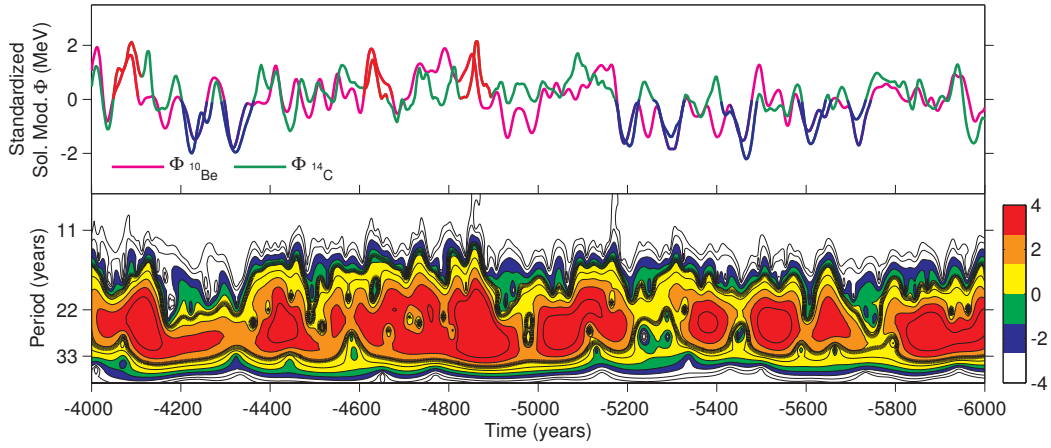


Figure 7.5: Top panel: Temporal change in  $\Phi_{10Be}$  and  $\Phi_{14C}$ . Blue and red lines show identified grand minima and maxima, respectively. Bottom Panel: Local Cross-wavelet spectrum of the high pass filtered  $\Phi_{10Be}$  and  $\Phi_{14C}$  with a cut-off frequency of  $(1/30) \text{ year}^{-1}$ , focusing on identified grand minima periods by criterion defined in this study.

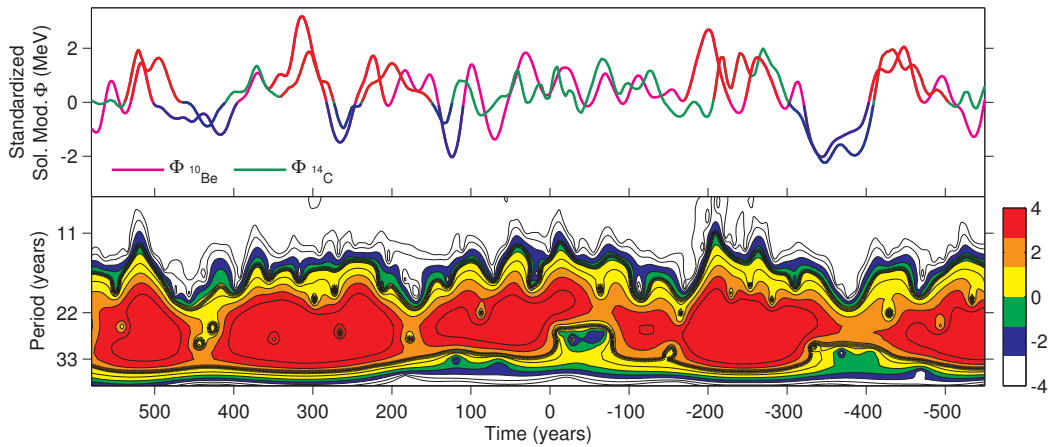


Figure 7.6: Top panel: Temporal change in  $\Phi_{10Be}$  and  $\Phi_{14C}$ . Blue and red lines show identified grand minima and maxima, respectively. Bottom Panel: Local Cross-wavelet spectrum of the high pass filtered  $\Phi_{10Be}$  and  $\Phi_{14C}$  with a cut-off frequency of  $(1/30) \text{ year}^{-1}$ , focusing on identified grand maxima periods by criterion defined in this study.

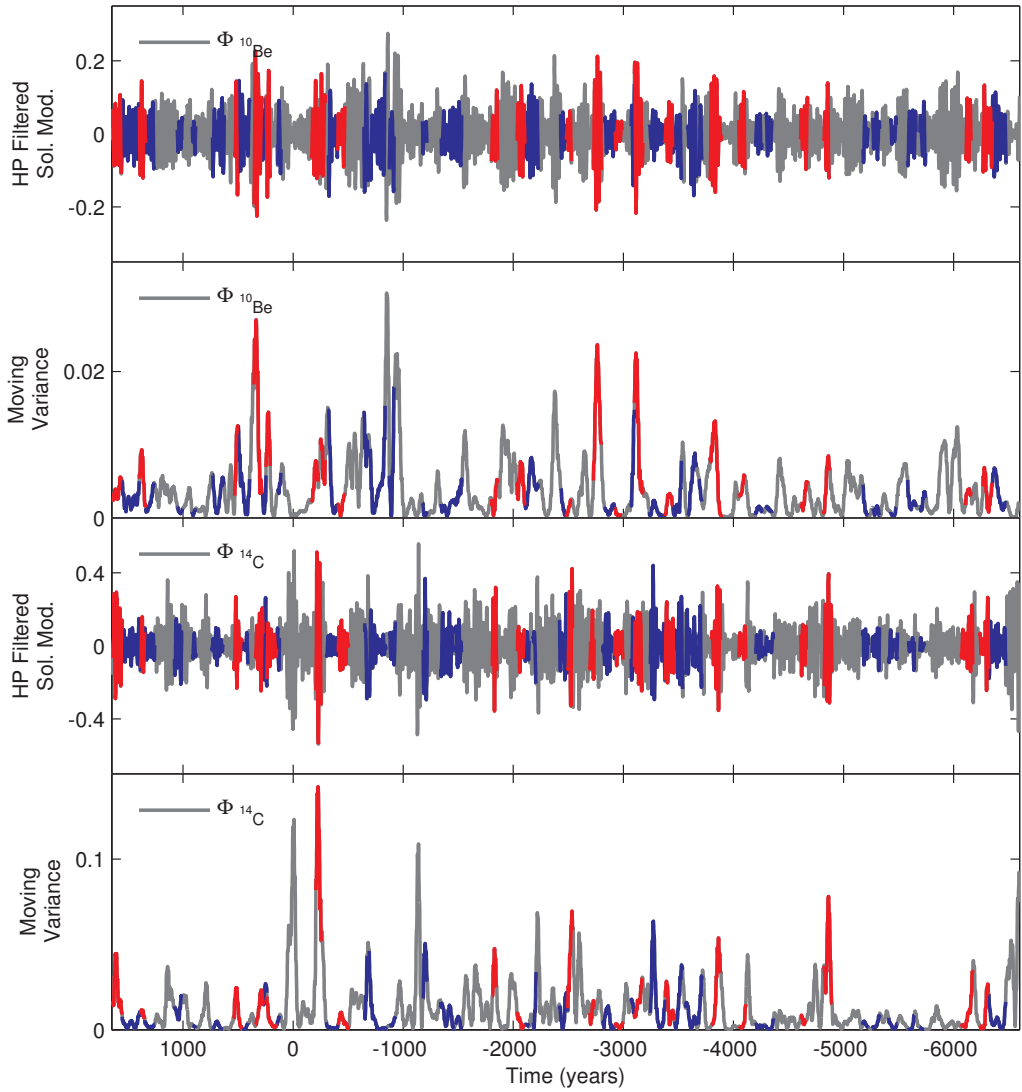


Figure 7.7: Temporal changes in high-pass filtered  $\Phi_{10\text{Be}}$  and  $\Phi_{14\text{C}}$  (first and third row, respectively) with a cut-off frequency of  $(1/30) \text{ year}^{-1}$ . Blue and red lines show identified grand minima and maxima, respectively. The second and fourth panel show the moving variance of high-pass filtered  $\Phi_{10\text{Be}}$  and  $\Phi_{14\text{C}}$ .

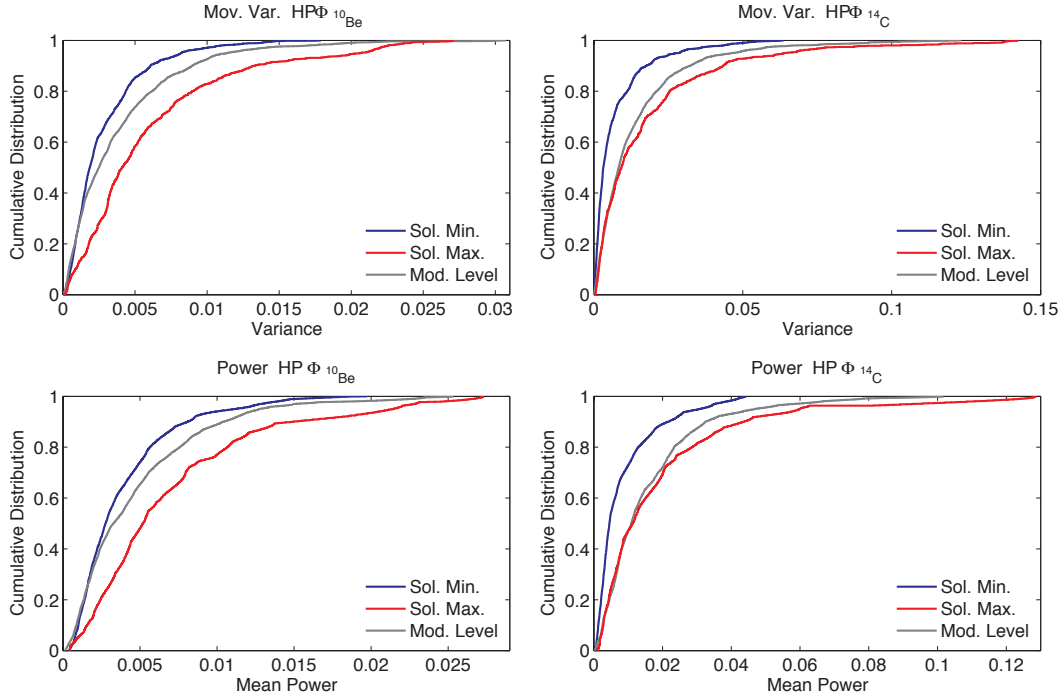


Figure 7.8: Two sample Kolmogorov-Smirnov test results for  $\text{HP}\Phi_{10\text{Be}}$  and  $\text{HP}\Phi_{14\text{C}}$ . Top panels show the results for moving variance, whereas bottom panels show the results for the power seen in  $\text{HP}\Phi_{10\text{Be}}$  and  $\text{HP}\Phi_{14\text{C}}$ , respectively. grand maximum, minimum and isolated periods are shown with red, blue and black lines, respectively.

hypothesis that the two data sets belong to the same continuous distribution. Prior to the KS tests, we separated the moving variance data set into three periods, *i. e.* grand minima, grand maxima and periods characterised by intermediate solar activity levels. We also separated the wavelet power spectra of the high-pass filtered data, which is calculated separately for the  $\text{HP}\Phi_{10\text{Be}}$  and the  $\text{HP}\Phi_{14\text{C}}$ , into the same three periods. After this step we average the power obtained between periodicities of 20 and 40 years. The results of the KS tests are shown in Fig 7.8. Both the power and the variance seen during grand minimum states are lower at the 99% significance level than those observed during grand maximum states and during the moderate activity periods. Additionally, the power and the variance seen during grand maximum states are higher at the 99% significance level compared to those observed during grand minimum states and during moderate periods. These differences observed for the power and the variance are more pronounced in the  $\text{HP}\Phi_{10\text{Be}}$  data in comparison to the  $\text{HP}\Phi_{14\text{C}}$  data. The reason for this difference may be the attenuation effect of the global carbon cycle on the amplitude of the peaks seen in the  $^{14}\text{C}$  measurements. Combining these findings on the power and variance of the 22-year Hale cycle with its cycle length variations during grand minima/maxima periods, we suggest that during grand minima/maxima periods the 22-year Hale cycles tend to show weaker/stronger variability and to be longer/shorter compared to moderate activity periods.

## 7.4 Discussion

Cosmogenic radionuclides, such as  $^{10}\text{Be}$  and  $^{14}\text{C}$ , provide a useful tool to study the nature and occurrence of grand minimum and grand maximum states of solar activity

and to investigate their nature and underlying mechanisms.

Combined results from the analyses of  $^{10}\text{Be}$  and  $^{14}\text{C}$  data show that grand minimum/maximum events are likely to be distinct modes of the solar dynamo, resulted from time-dependent processes related to energy accumulation and release like an oscillator, supporting the results found by Usoskin et al. (2014). We also found that there is an apparent upper limit of  $\sim 100$  years for the duration of grand maxima based on the criteria defined in this study. This can be interpreted as a limit on the solar dynamo capability to sustain higher activity levels for longer periods and this number can be directly compared with predictions based on solar dynamos regarding the length of grand maxima. Furthermore the results of cross-wavelet and KS test analyses suggest that, during grand minima, the power of the 22-year Hale cycle and variance in the data decrease, while they increase during the grand maxima. Keeping in mind that there is a tendency for grand minima and grand maxima to last longer than the periods characterized by moderate activity level, these findings could be interpreted as follows: at the maximum solar activity levels, the poloidal component of the dynamo is at its minimum. As the solar activity level goes into the descending phase, the poloidal component of the dynamo becomes stronger, reaching its maximum at the minimum solar activity. This means that soon after the large-scale dynamo has completed its polarity reversal throughout the whole Sun, the first active regions with opposite polarity compared to the previous cycle starts to emerge. To sustain the polarity reversals over many cycles, the meridional flow <sup>1</sup> is assumed to be faster during more active cycles, while slower during less active ones (Wang et al., 2002). This assumption seems to fit better with the observed trend for the more active cycles to have shorter rise times (Schatten & Hedin, 1984) and a more rapid progression of sunspots toward the equator (Hathaway et al., 2003). However, during grand minima/maxima, there tend to subsequently be less/more active cycles compared to times of moderate activity levels and this might alter the time it takes to reverse the polarity throughout the whole Sun and hence this period might become shorter and longer compared to the periods characterized by moderate activity levels, respectively. It is also noteworthy that over the last grand maxima, which started in  $\sim 1940$  and ended with solar cycle 22 (Usoskin, 2013), there have been 5 solar cycles, whose durations are below 11 years and only one that lasted almost 11.7 years.

Furthermore, during grand minima the power of the 22-year Hale cycle and variance in the data become weaker in comparison to the moderate activity periods, while during grand maxima, the variance in the data and the power of the 22-year Hale cycle tend to be stronger compared to moderate solar activity periods. These observational findings perfectly fit the recent 3-D Magnetohydrodynamic Anelastic Spherical Harmonics Model, which has exhibited long-lasting minima, showing that indeed there is an interval covering 20% of the cycles in which the polarity does not reverse and the magnetic energy is substantially reduced (Augustson et al., 2013).

The time-dependent oscillatory behaviour origin of grand minima/maxima also imposes new constraints on dynamo models. In fact, our study suggests that at the root of these quiescent/extreme active events are not stochastic noise as suggested by Moss et al. (2008) and Usoskin et al. (2009b). We need to make further investigations in order to identify other possible factors that might play a role for the origin of those events. One of these factors can be the quadrupolar component (if any). Observations and non-linear dynamo theory have shown that before entering or leav-

---

<sup>1</sup>transport of magnetic flux at the surface from low latitudes to the polar region, causing the periodic reversals of the global magnetic field, a process important to the prediction of the solar cycles (Dikpati et al., 2010)

ing a grand minimum state, solar cycles might become strongly axisymmetric. This has been interpreted as the result of the quadrupolar component of the solar dynamo (Tobias, 1997). As the dynamo enters a state of low activity, then the energy of the dipole and quadrupole components of the solar dynamo might become comparable in strength and as a consequence the system can enter a quadrupolar configuration. It has been argued that since the Maunder Minimum the magnetic configuration has been strictly dipolar, but recent observations have shown strong asymmetries during the last maximum (solar cycle 23) (Simoniello et al., 2013a,b).

## 7.5 Conclusions

In this study, we used, for the first time, two solar modulation potential reconstructions based on the IntCal13  $^{14}\text{C}$  and the GRIP  $^{10}\text{Be}$  records simultaneously to detect the occurrence of grand minima and maxima periods. In order for a low/high activity period to be considered as a grand minimum/maximum, it has to occur in both records at the same time with a duration longer than 22-years and with an amplitude below/above a certain threshold value (Section 2.2). The performed waiting time distribution analysis shows that the origin of grand minima/maxima periods is likely to be of non-random origin, implying that there is a self-organising physical process governing the occurrence of these periods, rather than stochastic noise. A more robust determination of the observed grand solar minima and maxima periods and better understanding of the physical processes that cause them, will allow more systematic and detailed investigations of the possible influences of grand minima and maxima episodes on the Earth's climate using climate proxy records.

**Acknowledgements** Funding for the Stellar Astrophysics Centre is provided by the Danish National Research Foundation (Grant agreement no.: DNRF106). MFK, CK and JO acknowledge support from the Carlsberg Foundation and Villum Foundation. RS acknowledge the support from the PiCARD collaboration.

## Chapter 8

# Are we entering a Grand Solar Minimum?: Comparison between current and previous solar dynamics

F. Inceoglu, R. Simoniello, M. F. Knudsen, C. Karoff, J. Olsen and S. Turck-Chiéze  
*Submitted to Astronomy & Astrophysics*

### Abstract

**Aims:** We aim at comparing current solar magnetic activity with magnetic activity levels of previous grand minima/maxima observed in solar modulation potential reconstruction based on the IntCal13  $^{14}\text{C}$  record, as the solar modulation potential maintains a memory of the Sun's dipole magnetic field.

**Methods:** We used the IntCal13  $^{14}\text{C}$  data to investigate distinct patterns in the occurrences of grand minima/maxima during the Holocene period. As variations in solar magnetic activity are driven by the Sun's large-scale dipolar magnetic field, we also investigated how the single dipolar component developed over the last decades using the Wilcox Solar Observatory data.

**Results:** The cosmogenic radionuclide data analysis showed that 71% of grand maxima are followed by a grand minimum and it also indicates that the activity level of the Sun, soon after 2000, is comparable to previous grand minima. Over the last three solar cycles, the axial and toroidal components of the Sun's large-scale dipolar magnetic field underwent a steady decrease. Furthermore we also found lines of evidence showing that the axial dipolar component needed longer time to build up its magnetic configuration after 1980.

**Conclusions:** The recent solar dynamics seem to be well represented by the pattern grand maxima followed by a grand minimum, as the Modern Maximum (1914-2000) has ended with Solar cycle 23 and the solar magnetic activity is comparable to previous grand minima since 2000. Therefore, it is possible that the Sun has entered a Modern Minimum state. The occurrence characteristics of grand maxima and minima seem to support the scenario in which the dynamical non-linearity induced by the Lorentz force leads the Sun to act as a relaxation oscillator. Here the large-scale magnetic field of one parity (dipole or quadrupole) drives velocity perturbations and energy is exchanged between the magnetic field and the velocity flow.

Sun: activity–solar–terrestrial relations

## 8.1 Introduction

We are currently at the maximum of Solar cycle 24, which is displaying very muted solar activity. Sunspot observations show that Solar cycle 24 is weaker than Solar cycle 23, with peak sunspot numbers almost half the value of Solar cycle 23. Additionally, geomagnetic activity levels during the ascending phase of Solar cycle 24 were lower in comparison to the rising phases of Solar cycle 17–23, and they are almost comparable to what was observed during descending phases of Solar cycles 17–23 (Richardson, 2013). Fewer coronal mass ejections have been observed during Solar cycle 24 and they tend to be less massive and slower than the ones that occurred during Solar cycle 23 (Wang & Colaninno, 2014). All these observations imply that the current period of reduced magnetic activity already started during the descending phase of solar cycle 23. In fact, after the first sunspot maximum observed in 1999, the dynamics of Solar cycle 23 was characterised by a prolonged descending phase with a small-amplitude secondary peak (Dikpati et al., 2004). The double peak structure is thought to be the typical signature of the Quasi Biennial Periodicity (QBP), which characterises cycle changes in all solar activity proxies (Krivova & Solanki, 2002; Mursula et al., 2003; Vecchio & Carbone, 2008) and in helioseismic data (Fletcher et al., 2010; Simoniello et al., 2012, 2013a). Together with the prolonged descending phase, a significant reduction was observed in the heliospheric magnetic field and the solar wind speed and density during Solar cycle 23 (Owens et al., 2011). It is therefore believed that the Modern Maximum<sup>1</sup> may have ended with Solar cycle 23 in 2000. It has also been speculated that the next solar cycle will even be weaker than Solar cycle 24 as this quiescent period might indicate that we are about to enter (or have already entered) a Modern Minimum state. So far, there are various and contradictory predictions regarding the sunspot peak amplitude and duration of Solar cycle 25, *e. g.*, peak sunspot amplitude of  $\sim 50$  and a duration of around 11 years were suggested by Clilverd et al. (2006), while Hiremath (2008) estimated a peak sunspot amplitude of  $110 \pm 11$  and a duration of 12.5 years.

Therefore, we aim at investigating this future solar behaviour by studying the solar dynamics during the Holocene epoch (the past  $\sim 11700$  years).

Information on solar variations prior to 1610<sup>2</sup> relies on past production rates of cosmogenic nuclides, such as  $^{10}\text{Be}$  and  $^{14}\text{C}$  (Usoskin, 2013), which are produced when galactic cosmic ray (GCR) particles from space interact with atoms in the Earth’s atmosphere (Dunai, 2010). Earlier studies based on the past production rates of cosmogenic radionuclides showed that the Maunder Minimum was not the only quiescent activity period observed over the last  $\sim 10000$  years. Inceoglu et al. (2014c) suggest that during the past  $\sim 8250$  years, the Sun experienced 32 grand minima and 21 grand maxima. Using these grand minima and maxima, we investigate regular patterns of occurrence, characterising solar magnetic activity on multi-millennial time scales. This categorisation may allow us to classify the recent solar dynamics. Additionally, observations of the large-scale solar magnetic field enable us to statistically interpret the future solar dynamics.

---

<sup>1</sup>the period of relatively high solar activity which began with Solar Cycle 15 in 1914. It reached a maximum in Solar cycle 19 during the late 1950s

<sup>2</sup>Sunspot data are available only since 1610

## 8.2 The characterisation of the solar dynamics during the Holocene

### The cosmogenic radionuclide data

The production rates of cosmogenic radionuclides are inversely correlated with solar magnetic activity and the geomagnetic field intensity. This inverse correlation is caused by the non-linear shielding effect of the solar magnetic field and the geomagnetic dipole field (Aldahan et al., 2008). Also, the amount of GCR particles reaching Earth are inversely proportional to, but out of phase with, the 11-year solar cycle. Temporal variations in the GCR intensity display a distinct 11-year periodicity owing to solar modulation of GCRs in the heliosphere (Potgieter, 2013). A strengthening of the solar magnetic and geomagnetic fields results in a lower production rate of cosmogenic nuclides (Masarik & Beer, 1999).

Here, we use the grand solar minima and maxima periods detected in the solar modulation potential (SMP) reconstructions (Inceoglu et al., 2014c) based on the IntCal13  $^{14}\text{C}$  (Reimer et al., 2013) and the GRIP (Greenland Ice Core Project)  $^{10}\text{Be}$  (Vonmoos et al., 2006) records. In their study, Inceoglu et al. (2014c) used the GRIP  $^{10}\text{Be}$  and IntCal13  $^{14}\text{C}$  records for the overlapping period from 1650 AD to 6600 BC to calculate the SMPs and they detected 32 grand minima and 21 grand maxima based on three criteria, *i. e.*, (i) the amplitude of low/high activity period has to be under/over a certain threshold value, (ii) with durations longer than two solar cycles, and (iii) they have to occur simultaneously in the reconstructions based on the GRIP  $^{10}\text{Be}$  and IntCal13  $^{14}\text{C}$  records (see Inceoglu et al., 2014c, for details). Using such a method provides more robust identification of grand minima and grand maxima, since the geochemical behaviour of these two radionuclides are different and their deposition rates can be effected by different processes in the earth system (Roth & Joos, 2013). In addition to the list given in Inceoglu et al. (2014c), we also included the Maunder Minimum (1645 – 1715) to the grand minima list, which could not be included in that study because of the time span of the GRIP  $^{10}\text{Be}$  record, which extends up to 1650 A.D. Therefore, all the numerical results presented here are based on the SMP reconstruction calculated using the IntCal13  $^{14}\text{C}$  record, which extends up to 1950 AD. However, because of the Suess effect, which has caused a significant decrease in the  $^{14}\text{C}/^{12}\text{C}$  ratio as a consequence of admixture of large amounts of fossil carbon into the atmosphere after the industrial revolution (Suess, 1955), we excluded the most recent 100 years.

### Distribution of Grand Minima and Grand Maxima

We investigated the occurrence characteristics of grand maxima and minima and found that 15 out of 21 grand maxima are followed by a grand minimum (Fig. 8.1a), meaning that  $\sim 71\%$  of grand maxima are followed by a grand minimum and almost 47% of the grand minima are preceded by a grand maximum. Table 8.1 lists these events together with their duration.

There are six grand maxima events (29%) that are not followed by a grand minimum and 17 grand minima events (53%) that are not preceded by a grand maximum. Fig. 8.1 shows examples for the four different categorisations based on the statistics we have from  $^{14}\text{C}$  data: (i) grand maxima followed by grand minima either immediately after or after spending some time in a moderate activity (Fig. 8.1a), (ii) six grand maxima events that are followed by another grand maximum after spending some time in a moderate activity activity level (Fig. 8.1b), (iii) six grand minima that

Table 8.1: The list of the grand minima events, which are following grand maxima, with their durations. Minus signs before the dates represent years BC.

Center time	Duration
1695	84
1450	167
690	102
434	54
261	34
133	25
-348	107
-1491	53
-2461	74
-2874	106
-3080	28
-3330	134
-3695	30
-4322	72
-5713	41

are followed by a grand maximum after a period of moderate activity (Fig. 8.1c), and (iv) 11 grand minima, which are all preceded by another grand minimum (Fig. 8.1d)

### Grand Minima preceded by Grand Maxima

The 15 grand maxima events, which are followed by grand minima, may represent the current solar dynamics, as the Modern Maximum is thought to have ended with solar cycle 23. Therefore, we calculated the waiting times between subsequent grand maxima and grand minima. Waiting times can be considered as intervals between subsequent peaks or dips in activity (Wheatland et al., 1998). Fig. 8.2a shows the complementary cumulative distribution function (CCDF) of the waiting times between subsequent grand maxima and minima together with the distributions of durations of maxima periods, which are followed by minima, and durations of grand minima periods, which are following maxima. The CCDF is defined as the probability that an event "X" with a certain probability distribution will be found at a value more than or equal to "x". The mathematical formulation is shown below (Clauaset et al., 2009; Guerriero , 2012);

$$P (X \geq x) = 1 - \int_{-\infty}^x p(x) dx = \int_x^{\infty} p(x) dx \quad (8.1)$$

where  $p(x)$  denotes the probability density (PD). As seen in Fig. 8.2a, the relative probability to have a grand minimum state soon after a grand maximum is higher and the relative probability decreases with increasing time. Longer periods have the lowest relative probability. In Fig. 8.2b, we show the probability densities of the waiting times with a log-normal fit, showing that the relative probability of a grand maximum to be followed by a grand minimum within  $\sim 50$  years is 33%. Based on the probability density distribution of the waiting times between grand maxima and following grand minima, it is noteworthy that all the grand minima, which are following grand minima, occur within 450 years from the peak-time of a grand maximum during the Holocene period. It is also evident from Fig. 8.2b that majority of grand minima occur within 175 years after the peak-time of a grand maximum. We also tested whether the

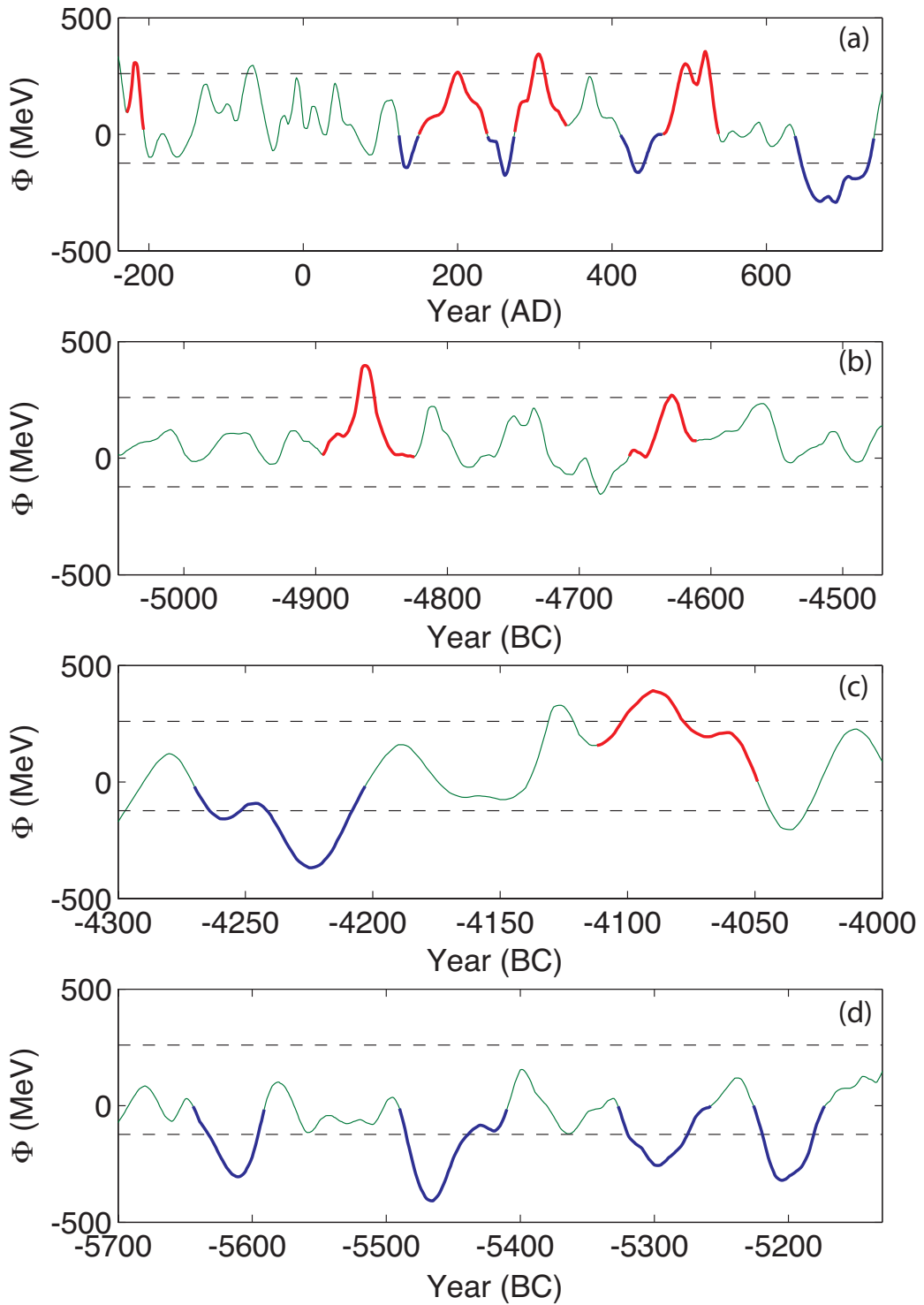


Figure 8.1: The categorisation of grand minima (blue) and grand maxima (red) in four distinct groups: (a) grand maxima followed by grand minima, (b) grand maxima followed by another grand maxima after a period in a moderate activity level (green), (c) grand minima preceded by grand minima and followed by grand maxima, and (d) grand minima preceded by a grand minimum.

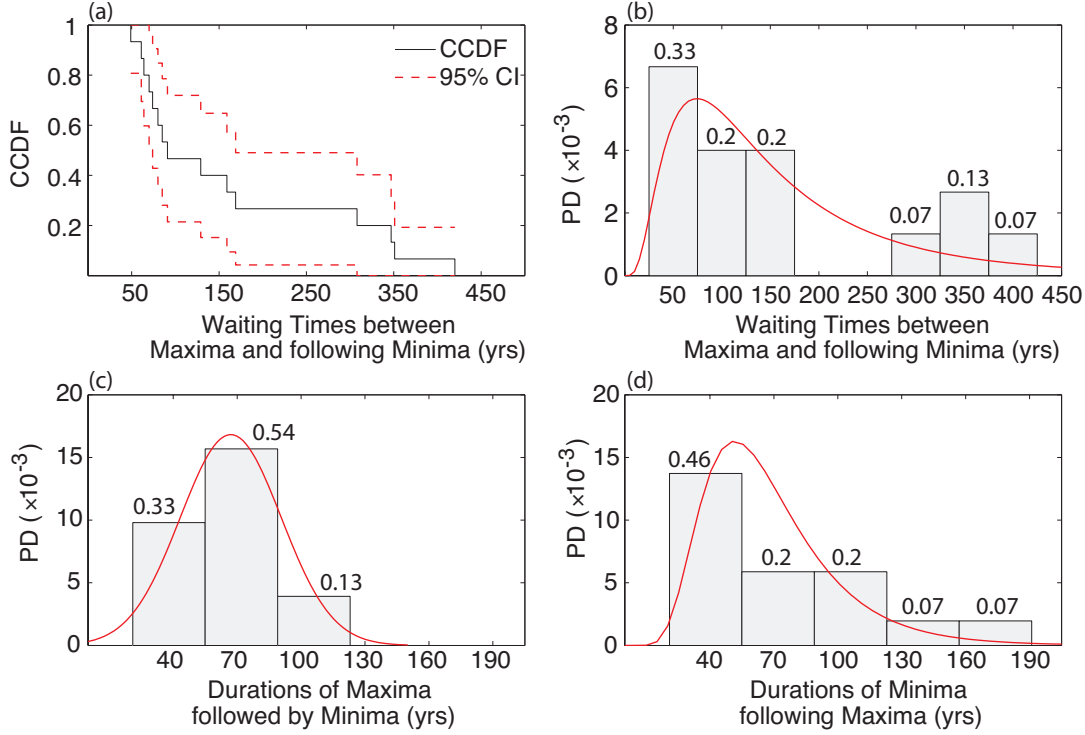


Figure 8.2: (a) The complementary cumulative distribution function (CCDF) of waiting times of subsequent maxima and minima, the probability densities (PD) of waiting times (b), the durations of maxima that are followed by minima (c) and the durations of minima that are following maxima (d) based on  $^{14}\text{C}$  data (see text).

distributions of the durations of grand maxima, which are followed by grand minima (Fig. 8.2c), and grand minima, which are following grand maxima (Fig. 8.2d), are best represented by normal, lognormal, or bimodal gaussian distributions. The results show that the durations of grand maxima periods are best represented by a normal distribution with a mean duration of  $\sim 65$  years, while a lognormal distribution with a mean duration of  $\sim 75$  years represents the distribution of grand minima durations better. Usoskin et al. (2007) also suggested that the mean duration for grand minima is 70 years but claimed that the durations of grand minima shows a bimodal gaussian distribution implying two kinds of minima. Furthermore, we checked whether there is any correlation between the duration of these grand minima and grand maxima. Fig. 8.3 shows the relationship between the durations of grand maxima and following grand minima. We also grouped the durations of grand maxima based on the bin edges in Fig. 8.2c and their following grand minima. As a result, we could not find any significant correlations. We also investigated the waiting time distribution for the other three categories (Figure 8.1b, c and d), however we were not able to detect any tendency due to the poor statistics.

To test the statistical significance of the ratio of the number of grand maxima that are followed by a grand minimum to total number of grand maxima identified using the criteria defined in Inceoglu et al. (2014c), we use two different approaches. In the first approach, we generate a thousand synthetic data sets using normally distributed random number generator. Each data set has a decadal temporal resolution, standard deviation and mean values similar to that of the solar modulation potential record, which was calculated based on IntCal13  $^{14}\text{C}$  record. We then linearly interpolate each

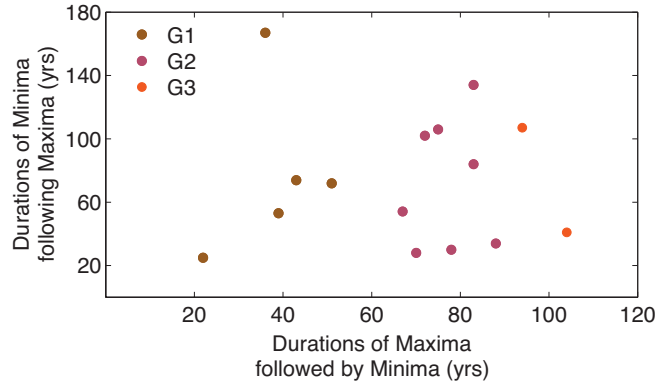


Figure 8.3: The relationship between the durations of grand maxima and their following grand minima grouped based on the bin edges in Figure 8.2c. G1 represents (brown circles) the duration of grand maxima that have a probability of 33% to last  $\sim 40$  years, G2 (purple) shows the ones that have a probability of 54% to last 70 years and G3 (orange) the ones having a probability of 13% to last 100 years.

synthetic data set at an annual resolution.

We also used the random-phase approach. Random-phase is a resampling method in the frequency domain based on Fast Fourier transformation of the data series, which preserves the original power spectrum and the amplitudes of the signals but changes the phase randomly and then back-calculates the data series (Ebisuzaki, 1997; Usoskin et al., 2006). Following the generation of a thousand realisations of the underlying solar modulation potential data, we applied the same procedures, that are applied to the synthetic and real data set.

After generating a thousand synthetic data and a thousand realisations of the real data, we detrend them using a polynomial fit of degree 5, which was applied to the underlying data. Subsequently, we treated the synthetic data and realisations of real data following Inceoglu et al. (2014c) to identify grand maxima and grand minima periods, except from one of the selection criteria requiring that low and high activity periods have to overlap in two datasets. The reason for this exclusion is to increase the number of grand minima and maxima found in the synthetic and resampled data. Inclusion of this criterion results in very small numbers of grand minima and maxima that are overlapping in two synthetic data sets. Additionally, in order to make a better comparison of the results of the synthetic and resampled data to the results of the real data, we also excluded the same selection criterion for the real data. As a result, the analysis of the real data gives 28 grand maxima, 24 of which are followed by a grand minimum.

The resulting probability density functions for the resampled and synthetic data are shown in Fig. 8.4. As seen in Fig. 8.4 for the resampled data (blue), the total number of identified grand minima and the ratio of the number of grand maxima that are followed by a grand minimum to the total number of grand maxima, hereby percentage, are best represented by a gaussian distribution with a mean value of 25 and 0.85, respectively. Analysis of the synthetic data (green) shows that the total number of identified grand maxima is higher in the synthetic data than those observed in the real data by a factor of 2 and the percentage of grand maxima that are followed by a grand minimum is 0.55. These results imply that the 28 grand maxima identified in the real data set and the percentage of 0.86 is not a coincidence, but rather a pattern

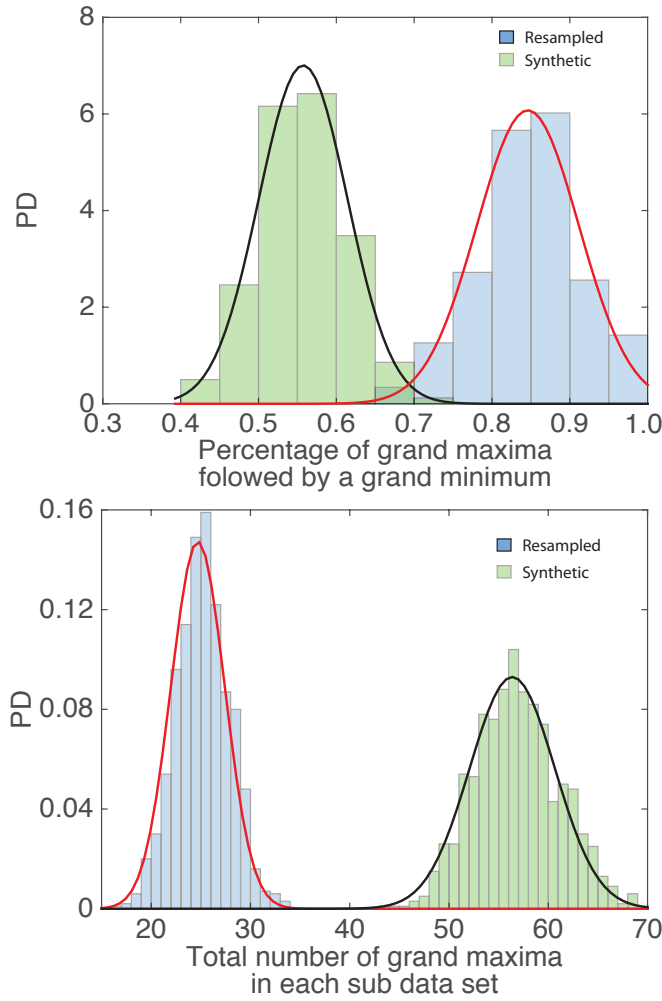


Figure 8.4: Top panel shows the probability densities (PD) of the ratio of the number of grand maxima that are followed by a grand minimum to total number of grand maxima identified in each resampled (blue) and synthetic (green) data. The bottom panel shows the PD of the total number of grand maxima in each resampled (blue) and synthetic (b) data. The red and black lines are showing the gaussian distribution fitted to the distributions. The overlapping area under the two PDFs is 0.028.

inherent in the real data that random fluctuations cannot explain. As seen in the top panel of Fig. 8.4, the overlapping area under the two probability density functions is very small (0.028), which means that it is very unlikely for a random process to generate a distribution (blue) seen in the top panel of Fig. 8.4.

### Comparing the present solar magnetic activity with its past

To compare the current solar dynamics to the previous grand solar minima and maxima observed in the SMP reconstructions based on the  $^{14}\text{C}$  and  $^{10}\text{Be}$  records, we have to use the current SMP values together with the current solar dynamics. To achieve this objective, we use the SMP reconstructions by Muscheler et al. (2007a) (Musch07), Usoskin et al. (2011) (Uso11) and Inceoglu et al. (2014c) (Inc14). Note that we use the SMP reconstruction of Muscheler et al. (2007a), which is normalised

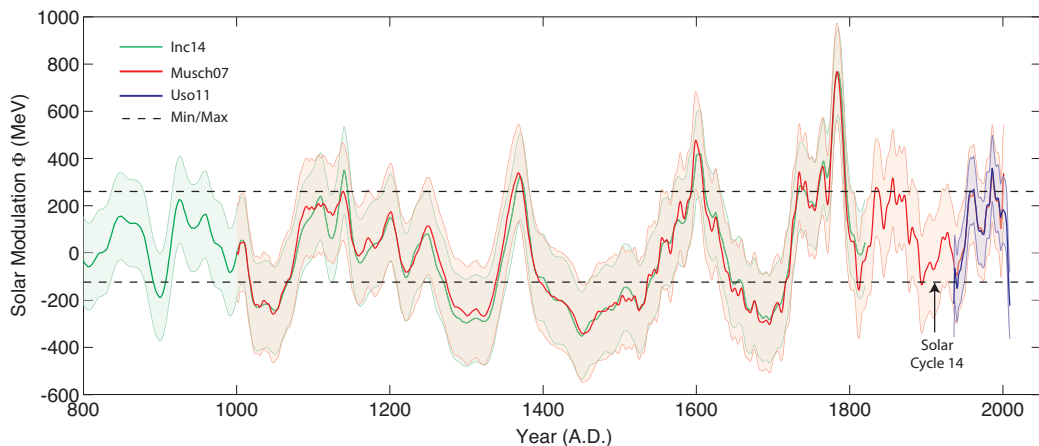


Figure 8.5: Solar modulation potential reconstructions by Inceoglu et al. (2014c) (green line, based on IntCal13  $^{14}\text{C}$ ), by Muscheler et al. (2007a) (red line, based on SHCal  $^{14}\text{C}$ , IntCal04  $^{14}\text{C}$  from 1000 to 1510 AD and annual  $^{14}\text{C}$  data from 1511 to 1950 AD) and by Usoskin et al. (2011) (blue line, based on neutron monitor data). Dashed lines show the threshold values for grand minima and maxima periods. Shaded areas indicate the %68 confidence interval calculated based on each dataset, separately. Note that here we only show the period from 800 to 2009 AD for visual purposes, even though the records extends from 6600 BC to 2009 AD. The arrow indicates solar modulation potential levels during Solar cycle 14.

Table 8.2: The date when the dip of a grand minimum that follows the Modern Maximum is expected and its probability.

Modern Minimum	Probability
2035	0.33
2085	0.53
2135	0.73

to the Cheltenham ionisation chamber data.

In order to remove the long-term trend observed in the SMPs based on  $^{14}\text{C}$  and  $^{10}\text{Be}$ , Inceoglu et al. (2014c) used a polynomial fit of degree 5 (see Inceoglu et al., 2014c, for details). Here, to have the same long-term SMP levels as Inc14, we also detrended the Much07 and Us011 SMP reconstructions as extensions of Inc14, using the same coefficients of the 5<sup>th</sup> degree polynomial found for Inc14. Additionally, we smoothed the Much07 and the Us011 SMP reconstructions using a 11-year moving average to have the same temporal resolution. The resulting SMP reconstructions are represented in Fig. 8.5 together with their  $\pm\sigma$  uncertainties. We also show the minimum/maximum threshold values found in Inceoglu et al. (2014c), which indicate that the SMP levels that define low and high activity levels and hence grand minima and maxima. As seen in Fig. 8.5, the solar modulation potential increased beyond the maximum threshold values around the 1980s, which may be associated with the Modern maximum (Usoskin, 2013), where the current SMP values decreased below the minimum threshold value soon after 2000 AD.

Considering changes in SMP during the Holocene, the current solar dynamics can be understood as a grand maximum followed by a grand minimum. The probability to have a grand minimum as a function of time distance from the peak-time of the Modern Maximum, which is observed in 1980 in SMP reconstruction based on

IntCal13  $^{14}\text{C}^3$  is listed in Table 8.2.

### 8.3 The Sun’s large scale dipolar magnetic field over the last three solar cycles

#### The dipolar component of the magnetic dynamo configuration

The analysis of cosmogenic radionuclide data suggests that, soon after 2000, the solar modulation potential dropped down to magnetic activity levels comparable with previous grand minima. As seen in Fig. 8.5, the solar magnetic activity started to decrease already at the beginning of 1980, the period in which the solar activity reached its maximum according to the cosmogenic radionuclide data. We also show the solar modulation potential levels during Solar cycle 14, which Solar cycle 24 behaves similar to. This is an interesting piece of information as the solar modulation potential is directly related to the dipolar component of the Sun’s magnetic field, and thanks to the Wilcox Solar Observatory we have the chance to verify whether or not the solar magnetic dipole field started to undergo a steady decreasing trend. We thus decided to investigate the temporal evolution of the large-scale dipolar magnetic field over the last three solar cycles. To this aim, we used synoptic photospheric magnetic field maps of the radial magnetic field ( $B_r$ ) obtained from line-of-sight magnetogram observations by the Wilcox Solar Observatory (WSO) (Scherrer et al., 1977).

The WSO data used in this study span the time period between 1976–2014, starting with Carrington rotation (CR) 1642 (27 May 1976), and ending with CR 2149 (4 May 2014). For each map per CR, we carried out harmonic analysis using the Legendre-transform software provided by the PFSS (Potential Field Source Surface) package of SolarSoft following the recipe given in DeRosa et al. (2012). As a result, we obtained the energies of the dipolar and quadrupolar components of the solar magnetic field.

#### The axial and equatorial component of the dipole mode

Fig. 8.6 shows the axial ( $\ell=1, m=0$ ) and equatorial ( $\ell=1, m=1$ ) dipole components of the large-scale solar magnetic field. The equatorial component has dropped during the last two solar maxima (2000 and 2014). Correspondingly, Fig. 8.7 shows the axial dipole component has steadily decreased during the last two solar sunspot maxima. These observational findings are in good agreement with the decreasing trend in solar magnetic activity inferred by the cosmogenic radionuclide data.

The detailed information provided by magnetic field data along with the categorisation of solar magnetic activity, allows the possibility to study features of Solar cycle 25 as well as the future solar magnetic activity. In fact, the strength of the forthcoming cycle is established already at the ongoing solar sunspot maximum, when the axial dipole field is at its minimum. Fig. 8.7 shows the temporal evolution of the axial dipole field in log-scale in order to highlight its behaviour over the minimum phase. There are several interesting features:

- the minimum of the axial component continuously decreased over the last three sunspot maximum and reached its deepest values during the maximum of Solar cycle 24 (Fig. 8.7);
- the way the axial component approached its maximum differs from cycle to cycle;

---

<sup>3</sup>it is important to note that in other study with other proxies the Modern Maximum peaked in 1950

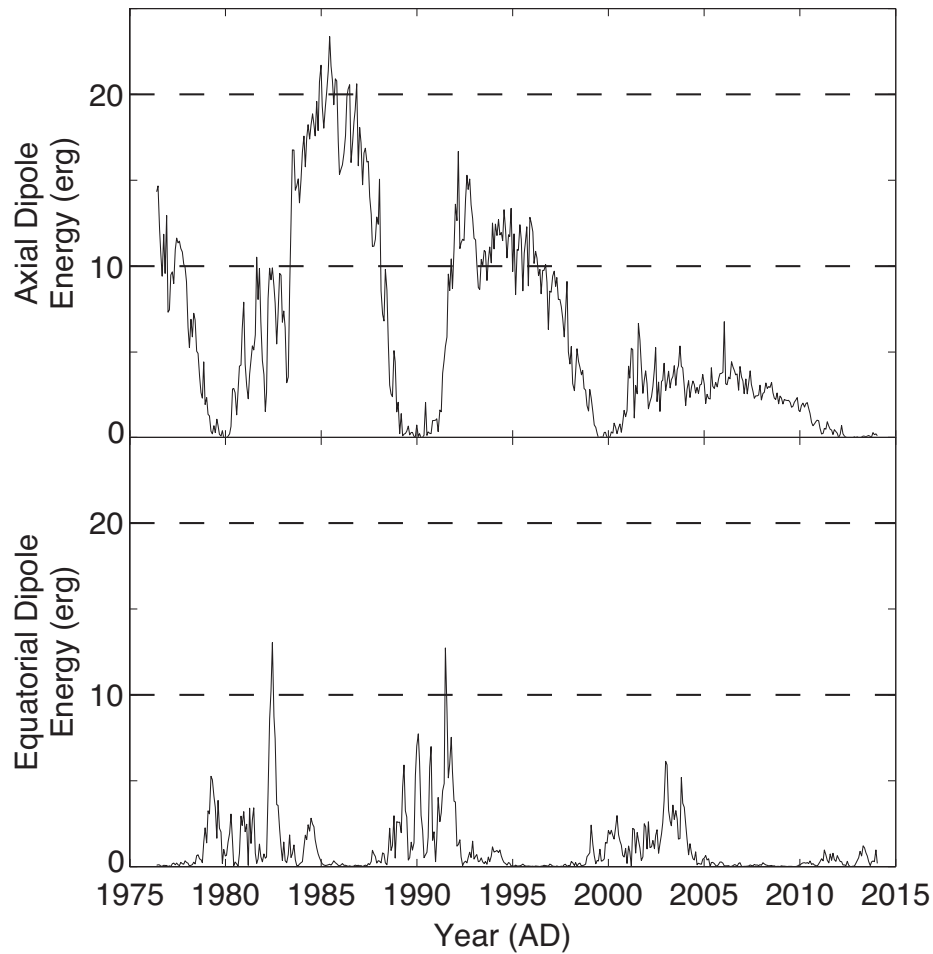


Figure 8.6: The top panel shows the temporal evolution of the total energy in the axial component of the dipole mode of the solar large-scale magnetic field, while the bottom panel represents the temporal evolution of the total energy in the equatorial component of the dipole mode.

- Solar cycles 21, 22 and 23 were stronger compared to Solar cycle 24, and as a consequence, so was the axial dipole field.

Based on these observational findings, to get a measure of the time required for the axial dipole field to recover itself from its lowest value, we compare the current energy in the axial dipole field to those observed during the previous solar cycles. In particular, at the current solar cycle, 0.9 years have elapsed since the axial dipole component was at its minimum. To make a reliable comparison, we determined the energies in the axial dipole component for the previous cycles at the time, when 0.9 years have elapsed after they reached their lowest values. As seen in Fig. 8.7 (red diamonds), the axial dipole component has already recovered itself after 0.9 years from its minimum at the sunspot maximum in 1980, while the recovery time seems increased during the following cycles (Fig. 8.7). This might indicate that the time required for the axial dipole component to reach its moderate/high values during Solar cycle 24 will be longer than that of Solar cycle 23. This may imply that the forthcoming Solar cycle 25 could be even weaker than Solar cycle 24. If this is confirmed, then according to our definition of a grand minimum (Inceoglu et al., 2014c), it can be argued that

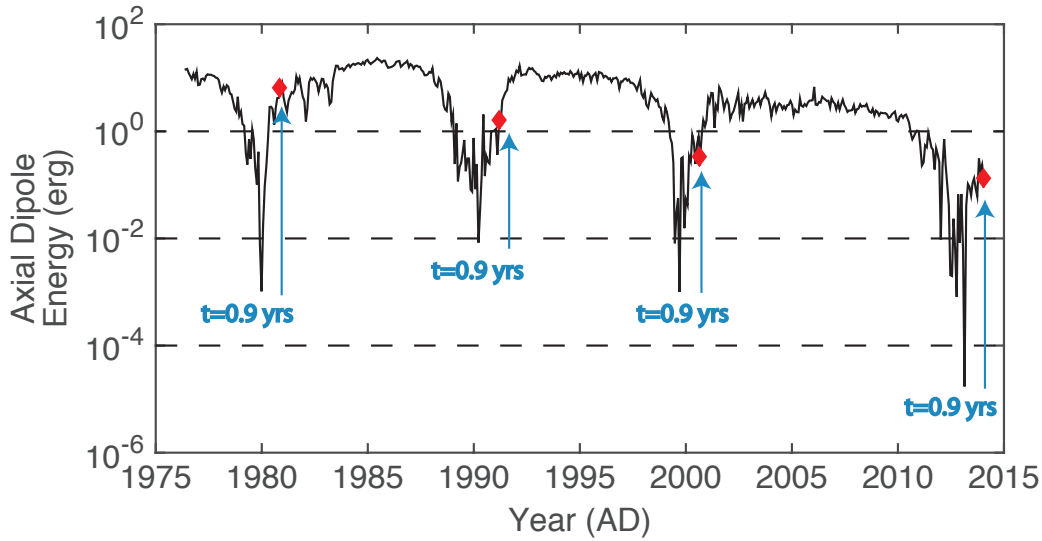


Figure 8.7: The temporal evolution of the energy in the axial component of dipole mode of the solar large-scale magnetic field in log-scale. The red diamond show the energies, where 0.9 years have elapsed (blue arrows) since the axial dipole component reached its lowest value.

the Sun has already entered a Modern Minimum state (Abreu et al., 2008).

## 8.4 Interpreting and Predicting the future solar dynamics

### Dynamical non-linearity

The dynamo-generated magnetic field will, in general, produce a Lorentz force that will tend to oppose the driving fluid motions through velocity fluctuations - the so-called Malkus-Proctor effect (Malkus & Proctor, 1975). These fluctuations can be observed on the Sun as torsional oscillations, pattern of zonal flow bands that migrate toward the equator and poles during the solar cycle (Howard et al., 1980). This mechanism is expected to reduce the amplitude of differential rotation until the effective dynamo falls back to its critical value, at which point the dynamo again saturates. Under this circumstances the Sun is expected to behave as a relaxation oscillator, damped by magnetic changes in the dynamo mode of one fixed polarity (dipole or quadrupole) interacting with the large scale velocity flow.

This back-reaction of the Lorentz force has been shown to lead to a variety of behaviours characterising the long-term solar variability, including amplitude and parity modulation, periodic or aperiodic, as well as intermittency, where grand minima are seen as quiescent intervals of activity that interrupt periods of normal cyclic activity (Tobias et al., 1995; Tobias, 1996, 1997). However, there is also another way to reproduce these intermittent periods in stellar dynamos, *i. e.* stochastic noise (Moss et al., 2008; Usoskin et al., 2009b). Previous studies (Inceoglu et al., 2014c) suggest that the occurrence of the grand minima/maxima periods reflects energy accumulation and release processes. In this work we have provided piece of evidence that the Sun is acting as a relaxation oscillator. (Tobias, 1996). Furthermore there are helioseismic evidences pointing to changes in high-latitude rotation rates during the

rising phase of Solar cycle 24, which can be interpreted as a slowing of the underlying rotation rate at mid to high latitudes (Howe et al., 2013). This might explain a delay in the inversion of the polarity and as further effect even a slowdown in the build-up of the magnetic configuration of the axial dipole components. Additionally, there are lines of evidence suggesting that the total dipole field behaved differently from previous cycles during the minimum of Solar cycle 23–24 (around 2008) compared to Solar cycle 22–23 (around 1996).

Observations of acoustic waves can probe solar magnetic activity in the Sun’s deeper subsurface layers. Acoustic modes propagate in the Sun’s interior and are shaped by changes in magnetic field due to mode conversion (Simoniello et al., 2010). Thanks to highly resolved sunlight observations we can investigate the changes in mode frequency in layers just below the surface. We have used GONG data with spherical degree  $\ell=0,150$ , in a low-frequency band  $1500 \leq \nu \leq 2300 \mu\text{ Hz}$ , medium-frequency band  $2300 \leq \nu \leq 3100 \mu\text{ Hz}$  and high-frequency band  $2300 \leq \nu \leq 3900 \mu\text{ Hz}$  to infer the solar magnetic activity in layers between  $-1500 \text{ Km} \leq \text{depth} \leq -1000 \text{ Km}$ ,  $-1000 \text{ Km} \leq \text{depth} \leq -500 \text{ Km}$  and  $-500 \text{ Km} \leq \text{depth} \leq -100 \text{ Km}$  covering a period that goes from 1996–2012. Fig. 8.8 shows the frequency changes at low-, medium- and high-frequency bands of the acoustic waves. From an helioseismic point of view, the origin of the shift in the subsurface layers reside in the  $\beta = \frac{P_{gas}}{P_{mag}}$  value. This ratio is extremely large in the Sun’s interior, while it becomes smaller as we get closer to the surface and therefore the magnetic field is able to act on the acoustic cavity. Then we expect to observe higher shifts in the high frequency band. Fig. 8.8 shows the frequency changes at the low-, medium- and high-frequency bands of the acoustic waves. We can clearly identify the 11-yr cycle and the typical double peak structure at the solar maximum. It should be noticed that the size of the shift in the higher frequency band is smaller compared to the shift in the low/medium frequency bands at the minimum between Solar cycle 23 and 24. This could suggest that the flux tubes rising up were extremely weak and that they have been pushed down into the deeper layers (Simoniello et al. 2014, in preparation) due to magnetic pumping (Weiss et al., 2004; Thomas et al., 2002). This phenomenon tend to occur over the minimum phase of the solar sunspot cycle, when the equatorial component is at its minimum, while the axial component reaches its maximum.

## 8.5 Discussion and Conclusion

The Sun’s activity influences everyday life on short-and long-time scales. For example, the rate of solar flares correlates with the number of sunspots, and large solar flares or coronal mass ejections can disrupt satellite communications and cause power outages. On long-time scales, long quiescent/higher periods of activity effects the solar energy output which influences the Earth’s climate system.

The recent wealth of information coming from line-of-sight magnetograms, radionuclide data and very accurate helioseismic observations create a fertile ground for a new aspect of solar-terrestrial research. Bringing together information from the Sun and how its variability is seen from Earth might help to explore the topics related to the early Sun’s activity and space weather. This will improve our knowledge about how the star energy output is affected by the surface magnetism and how it effects the evolution of the planet hosted by the star. Within this broad context, we decided to address this topic by bringing together different types of datasets and different techniques. We have used radionuclide data to look at the long-term variability of the Sun, we then used magnetic field data to analyse the recent current dynamics

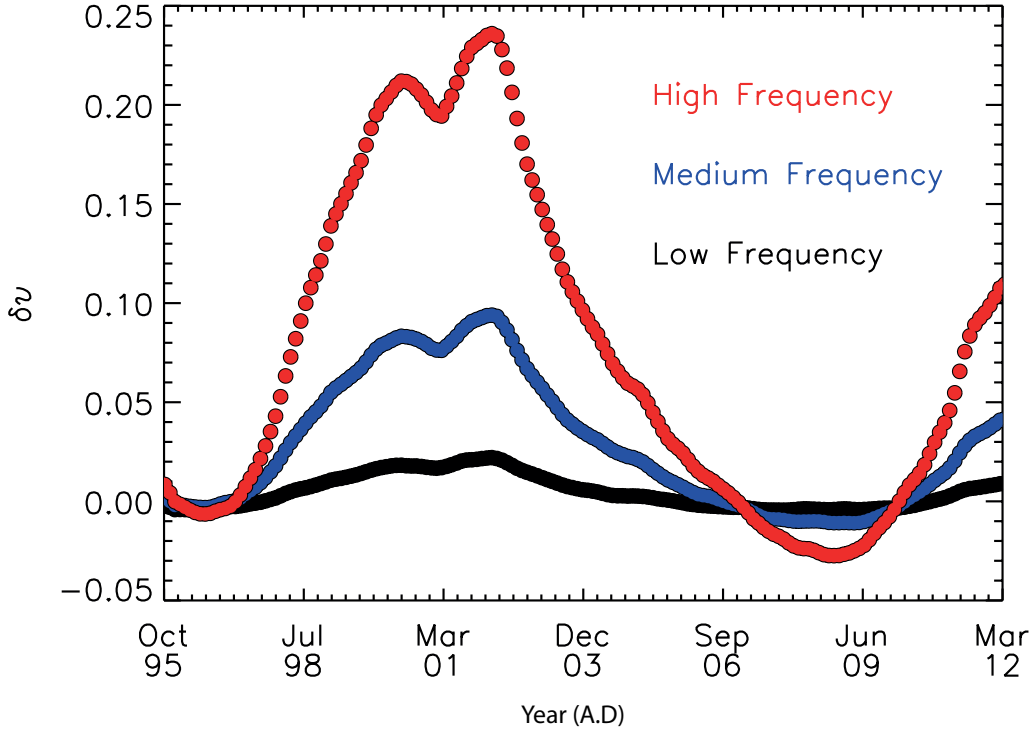


Figure 8.8: Solar cycle changes in acoustic p-mode frequency over the period 1996-2012 (re-adapted from Simoniello et al. 2013).

and we also used helioseismic data to infer the current solar magnetic activity in the deeper layers.

The analysis of cosmogenic radionuclide data has provided evidence that the recent and current solar dynamics seem to be well represented by a Modern Maximum followed by a Modern Minimum. In fact, since the peak in the Modern Maximum in 1980, solar magnetic activity started to steadily decrease and since the end of the Modern Maximum, believed to have occurred in 2000, the magnetic activity has been very modest, reaching levels comparable with previous grand minima. These findings have also been supported by the analysis of the large-scale dipolar magnetic field provided by the Wilcox Solar Observatory. Furthermore, we also found that the time to build up the axial dipole component has increased over the last three solar cycles and in particular over this maximum, the time required to the axial field to recover will likely be longer compared to previous cycles. This led us arguing that even Solar cycle 25 could be comparable or even weaker than Solar cycle 24 and as a consequence we suggest that the Sun has already entered a Modern Minimum State.

The recent behaviour of solar magnetic activity resembles the behaviour of a damped oscillator. This can be viewed as the result of the dynamical non-linearity induced by the Lorentz force that dampens the solar dynamics by inducing zonal flow that slow down the differential rotation, and as a consequence slow down the velocity of the driving fluid motions. We might suspect that such a slow down has also an impact on the time required by the axial dipole field to build up its magnetic configuration. Indeed, we found that over the last three solar cycles, this time has increased and we also found evidence of magnetic pumping, another feature that give a measure of how weak solar activity was during the minimum of Solar cycle 23–24.

These findings, therefore, clearly provide evidence in favour of dynamical non-linearity as the main driver of solar/stellar magnetic variability on short and long time scales and this information is also of vital importance when star-planet interactions are concerned in the search of habitable planets, a research area significantly developed thanks to recent space missions.

**Acknowledgements** Funding for the Stellar Astrophysics Centre is provided by the Danish National Research Foundation (Grant agreement no.: DNRF106). FI acknowledge M. DeRosa for providing his code for calculations of dipolar and quadrupolar energies of solar magnetic field. RS acknowledge the support from the PiCARD collaboration. MFK, CK and JO acknowledge support from the Carlsberg Foundation and Villum Foundation.



## Chapter 9

# A continuous ice core $^{10}\text{Be}$ record from Mongolian mid-latitudes: Influences of solar variability and local climate

F. Inceoglu, M. F. Knudsen, C. Karoff, J. Olsen, P.-A. Herren, M. Schwikowski, A. Aldahan and G. Possnert

*Submitted to Earth and Planetary Science Letters*

### Abstract

Long-term  $^{10}\text{Be}$  records used to estimate atmospheric  $^{10}\text{Be}$  production rates predominantly derive from polar ice cores. Here, we present the first  $^{10}\text{Be}$  record from a mid-latitude ice core located in the Tsambagarav mountain range situated in the Mongolian Altai. The  $^{10}\text{Be}$  concentration spans the period from AD 1550 to 2009, while flux record extends from AD 1816 to 2009. The  $^{10}\text{Be}$  concentration in the Tsambagarav ice core ranges between  $\sim 1.5 \times 10^4$  and  $\sim 10 \times 10^4$  atoms  $\text{g}^{-1}$ , whereas the  $^{10}\text{Be}$  flux changes from  $\sim 0.02$  to  $\sim 0.15$  atoms  $\text{cm}^{-2} \text{ s}^{-1}$ . In general, the long-term trends observed in the Tsambagarav  $^{10}\text{Be}$  concentration and flux records are reasonably similar to those measured in ice cores from polar regions, *i.e.*, the NGRIP and the Dome Fuji  $^{10}\text{Be}$  records. A comparison between the Tsambagarav  $^{10}\text{Be}$  record and group sunspot numbers reveals that grand solar minima, *i.e.*, the Maunder and Dalton Minima, influenced the  $^{10}\text{Be}$  record and moreover that the 11-year solar-cycle signal is present in the Tsambagarav ice core. However, some notable discrepancies are observed between the Tsambagarav  $^{10}\text{Be}$  record and the two  $^{10}\text{Be}$  records from Greenland and the South Pole, potentially due to effects linked to regional meteorological phenomena, such as cyclonic versus anticyclonic conditions and storm tracks affecting the  $^{10}\text{Be}$  deposition in the Tsambagarav region.

*Keywords*;Cosmogenic nuclide; Beryllium 10; Mid-latitude; Past solar activity; Climate

## 9.1 Introduction

Past production rates of cosmogenic nuclides recovered from terrestrial archives, such as  $^{10}\text{Be}$  in ice cores and  $^{14}\text{C}$  in tree rings, are widely used to acquire information on past solar variations during the pre-telescopic era prior to 1610 AD (Bard & Frank,

2006; Muscheler et al., 2007a; Usoskin, 2013; Inceoglu et al., 2014b). Changes in solar activity have also been detected in  $^{10}\text{Be}$  and  $^{14}\text{C}$  records from lake sediments (Staff et al., 2011; Berggren et al., 2013). Cosmogenic nuclides are produced mainly in the lower stratosphere and the upper troposphere by interactions of galactic cosmic ray (GCR) particles from space with atmospheric elements, such as N and O (Masarik & Beer, 1999). Their production rates are inversely correlated with the solar magnetic activity and the geomagnetic field intensity due to the nonlinear shielding effect of the solar magnetic field and the geomagnetic dipole field (Aldahan et al., 2008). A strengthening of the solar magnetic and geomagnetic fields thus results in a lower production rate of cosmogenic nuclides and *vice versa* (Masarik & Beer, 1999).

About 67% of the total atmospheric  $^{10}\text{Be}$  is produced in the stratosphere while the remaining 33% is produced in the troposphere (Baroni et al., 2011). Following its production,  $^{10}\text{Be}$  is rapidly adsorbed mainly onto atmospheric sulfate aerosols. After a residence time around one to two years in the lower stratosphere (Raisbeck et al., 1981; Heikkilä et al., 2013a), the aerosols are transported into the lower troposphere by air mass exchanges taking place between the troposphere and stratosphere at mid-latitudes (Koch & Rind, 1998). Following a residence time around three weeks in the troposphere (Heikkilä et al., 2013a), they are eventually deposited at the surface by both dry and wet deposition. The concentration of  $^{10}\text{Be}$  in terrestrial archives is therefore not only influenced by changes in production rate caused by variable solar activity, but also by transport and deposition processes, atmospheric mixing, scavenging and snow accumulation rates at the coring site (Heikkilä et al., 2008b).

Because atmospheric transport and deposition processes play an important role for  $^{10}\text{Be}$  deposition in terrestrial records, the maximum deposition of  $^{10}\text{Be}$  occurs at temporal latitudes (Field et al., 2006). In contrast, all the currently available high-resolution  $^{10}\text{Be}$  records derive from the polar regions associated with Antarctica and Greenland. In this study, we present  $^{10}\text{Be}$  measurements from a mid-latitude mountain glacier ice core from Tsambagarav, Mongolia, covering the period between ~1550 and 2009. Our new  $^{10}\text{Be}$  record is compared with two  $^{10}\text{Be}$  records from polar ice cores (the NGRIP (Berggren et al., 2009) and the Dome Fuji (Horiuchi et al., 2008)), as well as a regional climate record in order to disentangle the influence of past  $^{10}\text{Be}$  production rate changes from potential regional climatic influences.

The objective is to assess the degree to which solar variability local climatic effects influence  $^{10}\text{Be}$  deposition at mid-latitudes.

## 9.2 Location

The Tsambagarav ice core was collected in 2009 in the Tsambagarav mountain range located in the Mongolian Altai (Figure 9.1, red star, 4130 m asl,  $48^{\circ}39'N$   $90^{\circ}51'E$ ) and it extends back to 6000 B.P. (see Herren et al. (2013) for details).

The climate over the Altai mountain region can generally be characterised by cold and dry winters associated with the Siberian Anticyclone (SA) over the area defined by  $90^{\circ}$ – $110^{\circ}E$  and  $40^{\circ}$ – $55^{\circ}N$  (Sahsamanoglou et al., 1991; Klinge et al., 2003) and relative warm summers, when most of the precipitation occurs in accordance with stationary cyclones, which transport moisture from the Pacific Ocean to the Altai (Aizen et al., 2005). The SA is a high-pressure system, which develops from October to March (Sahsamanoglou et al., 1991).



Figure 9.1: Location of the Tsambagarav coring site in Mongolian Altai (red star, 4130 m asl 48°39′N 90°51′E) and Belukha coring site in the Siberian Altai (black dot, 4062 m asl 49°50′N 86°34′E) (<http://www.geomapapp.org>).

### 9.3 Methods

In order to extract the  $^{10}\text{Be}$  signal stored in the Tsambagarav ice core during the period from 1550 to 2009, we collected 131 continuous ice samples with an average weight of  $\sim 200$  g. The samples were then melted and filtered. Prior to melting the samples,  $100\ \mu\text{l}$  of  $^9\text{Be}$  carrier was added to each sample. The pore size of the filter is important due to the fact that  $^{10}\text{Be}$  can be transported and re-deposited by dust particles. For the long-term record, we used filters with a pore size of  $0.45\ \mu\text{m}$  for the 131 samples, similar to the filters used for the  $^{10}\text{Be}$  extraction procedure of the GRIP (Greenland Ice Core Project) ice core (Yiou et al., 1997). The geochemical sample preparations were carried out both at the Paul Scherrer Institute (PSI), Switzerland, and at the Department of Geosciences, Aarhus University, following the procedures used in Berggren et al. (2009). Following the  $^{10}\text{Be}$  extraction procedure, the  $^{10}\text{Be}$  measurements were performed using the Uppsala University 5 MV AMS system and the NIST SRM 4325 standard ( $^{10}\text{Be}/^9\text{Be} = 3.03 \times 10^{-11}$ , internally standardised value) at machine and statistical errors of  $< 15\%$ . Blanks were prepared following the same sample procedure.

### 9.4 Data

The average time resolution of the Tsambagarav ice core  $^{10}\text{Be}$  record is 3.5 years, varying between annual resolution in the upper section and roughly decadal resolution in the lowermost section of the ice core due to strong thinning of the annual layers in the lower part of the ice core (Herren et al., 2013). The NGRIP and the Dome Fuji records have annual and decadal time resolutions, respectively. The  $^{10}\text{Be}$

concentration and flux records of the Tsambagarav, the NGRIP and the Dome Fuji ice cores were linearly interpolated at 1-year intervals in order to correct the datasets for brief discontinuities observed in the  $^{10}\text{Be}$  records of the three ice cores. We also used observed annual group sunspot numbers (SSNs), ranging from 1610 to the present (Hoyt and Schatten, 1998), as well as major ion ( $\text{Ca}^{2+}$ ,  $\text{Mg}^{2+}$ ,  $\text{Na}^+$ ,  $\text{Cl}^-$ ,  $\text{SO}_4^{2-}$ ,  $\text{NH}_4^+$ ,  $\text{HCOO}^-$ ,  $\text{K}^+$ ,  $\text{NO}_3^-$ ) and  $\delta^{18}\text{O}$  records measured in the Belukha ice core from the Siberian Altai (Figure 9.1, black dot) (Eichler et al., 2009), located in relative close proximity to Tsambagarav. The Belukha major ion records extend from 1255 to 1995, while the Belukha  $\delta^{18}\text{O}$  record ranges between 1255–1975. These records have decadal time resolutions.

## 9.5 Results

### $^{10}\text{Be}$ Concentration and Flux

The Tsambagarav  $^{10}\text{Be}$  concentration is presented in Figure 9.2 together with the NGRIP and Dome Fuji  $^{10}\text{Be}$  concentrations, group SSNs and the Belukha  $\text{Ca}^{2+}$  and  $\text{Mg}^{2+}$  records, which are standardised using their individual mean and standard deviation values. The  $^{10}\text{Be}$  concentration in the Tsambagarav ice core ranges between  $\sim 1.5 \times 10^4$  and  $\sim 10 \times 10^4$  atoms  $\text{g}^{-1}$ , with a mean concentration of  $\sim 4.6 \times 10^4$  atoms  $\text{g}^{-1}$ . The average  $^{10}\text{Be}$  concentration in the NGRIP ice core is  $\sim 1.8 \times 10^4$  atoms  $\text{g}^{-1}$ , while it is  $\sim 9.4 \times 10^4$  atoms  $\text{g}^{-1}$  in the Dome Fuji ice core.

The Tsambagarav  $^{10}\text{Be}$  fluxes were calculated for the period ranging between 1816 and 2009, since the accumulation rates are only known at sufficient resolution during this period (Herren et al., 2013). The  $^{10}\text{Be}$  fluxes calculated for the Tsambagarav ice core are shown in Figure 9.3, together with the  $^{10}\text{Be}$  fluxes obtained from the NGRIP and Dome Fuji ice cores and group SSNs. The  $^{10}\text{Be}$  fluxes in the Tsambagarav ice core vary between  $\sim 0.02$  and  $\sim 0.15$  atoms  $\text{cm}^{-2} \text{ s}^{-1}$  with an average of  $\sim 0.04$  atoms  $\text{cm}^{-2} \text{ s}^{-1}$ . The average fluxes for the Dome Fuji and the NGRIP ice cores are  $\sim 0.01$  atoms  $\text{cm}^{-2} \text{ s}^{-1}$ .

Figure 9.4 presents the smoothed  $^{10}\text{Be}$  concentrations and the fluxes associated with the three ice cores along with the observed group SSNs, which are smoothed using an 11-year moving average window. The  $^{10}\text{Be}$  concentrations and fluxes of each ice core and the group SSNs are standardised according to their individual mean and standard deviation values. In the top panel of Figure 9.4, the  $^{10}\text{Be}$  concentrations in the Tsambagarav ice core shows a slight increase towards the recovering phase of the Dalton Minimum ( $\sim 1825$ ), whereas it is more pronounced and spanning the full duration of the Dalton Minimum in the Dome Fuji record. The  $^{10}\text{Be}$  concentration in the NGRIP ice core seems insensitive to changes in solar activity during this period. For the Maunder Minimum, while both the Tsambagarav and the NGRIP  $^{10}\text{Be}$  concentration records show clear almost overlapping peaks related to the low activity level of the Sun, there is a slight decrease in the  $^{10}\text{Be}$  concentrations measured in the Dome Fuji ice core. The Maunder Minimum signal in the Tsambagarav  $^{10}\text{Be}$  concentration record is relatively narrow in comparison to the NGRIP record, where it is slightly wider. The middle panel of Figure 9.4 shows the  $^{10}\text{Be}$  fluxes of the Tsambagarav together with the NGRIP and the Dome Fuji ice cores. The Tsambagarav  $^{10}\text{Be}$  fluxes, similar to the  $^{10}\text{Be}$  concentrations, show an increase during the ascending phase of the Dalton Minimum ( $\sim 1825$ ) as defined by changes in the group SSNs. The NGRIP  $^{10}\text{Be}$  flux record shows a clear increase related to the decrease in the solar activity level during the Dalton Minimum, even though there was not any change in its  $^{10}\text{Be}$  concentrations during this period.

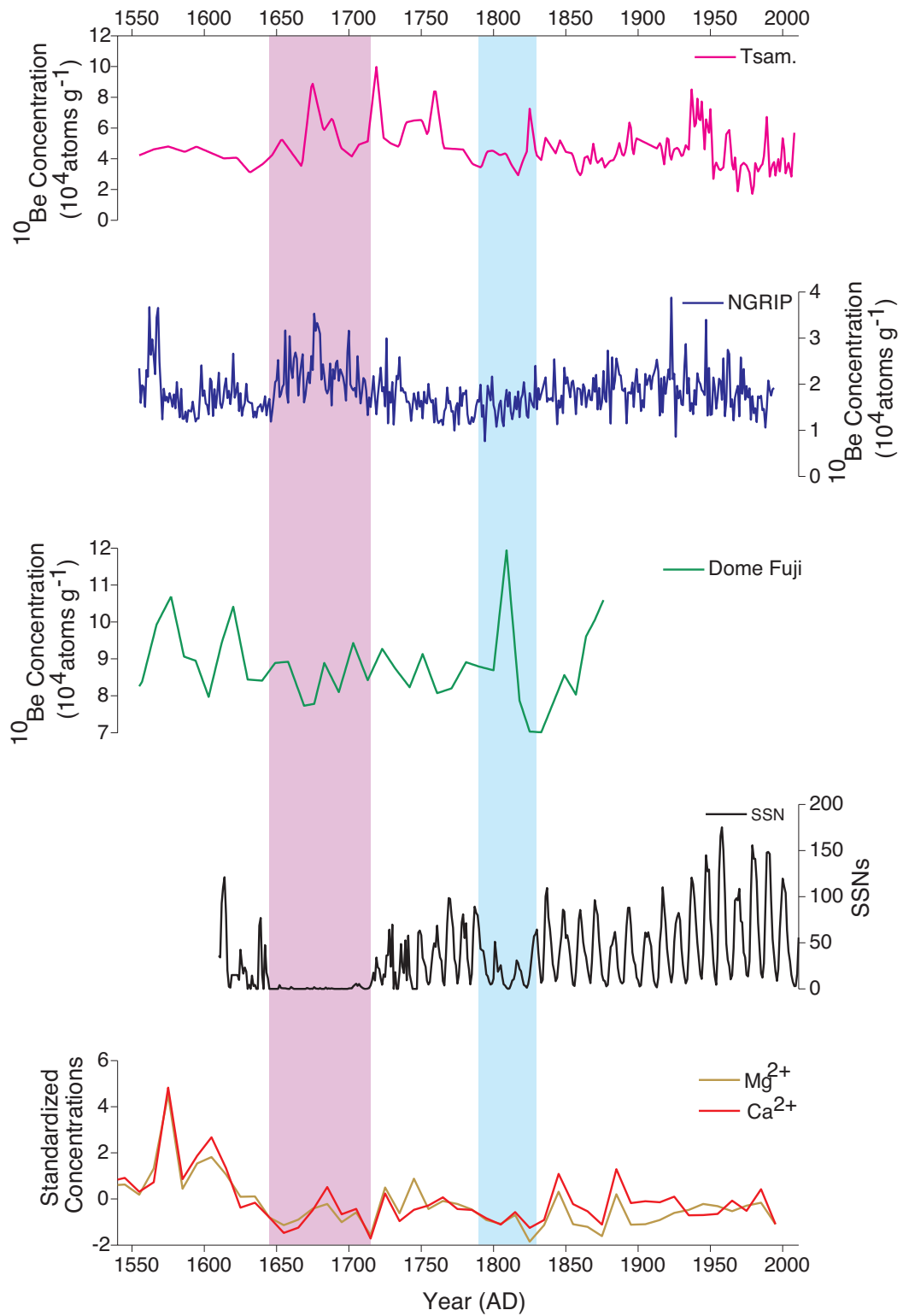


Figure 9.2: From top to bottom: The  $^{10}\text{Be}$  concentrations measured in the Tsamgarav (magenta), the NGRIP (blue) and the Dome Fuji (green) ice cores and group SSNs (black). The brown and red lines show standardized  $\text{Mg}^{2+}$  and  $\text{Ca}^{2+}$  records from the Belukha ice core. The purple and the blue bands show The Maunder Minimum (1645–1715) and the Dalton Minimum (1790–1830), respectively.

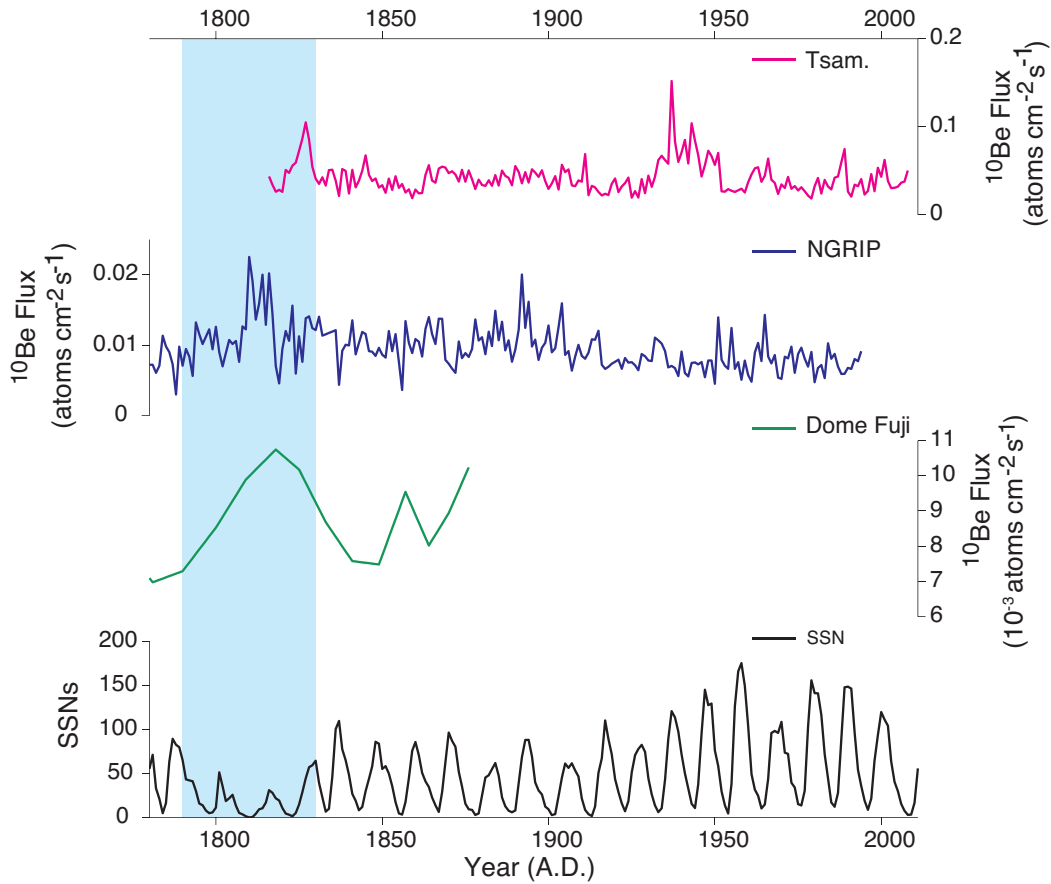


Figure 9.3: From top to bottom: The calculated  $^{10}\text{Be}$  fluxes of the Tsambagarav (magenta), the NGRIP (blue) and the Dome Fuji (green) ice cores and group SSNs (black). The blue band show the Dalton Minimum (1790–1830).

### $^{10}\text{Be}$ Flux in the $(1/8)$ – $(1/15)$ $\text{year}^{-1}$ Band

In order to investigate whether the Tsambagarav  $^{10}\text{Be}$  flux record contains the 11-year solar signal and to get rid of any possible high-frequency climatic noise and any long-term trend, we band-pass filtered the Tsambagarav  $^{10}\text{Be}$  fluxes using a Butterworth filter of degree 10 within a frequency band of  $(1/8)$ – $(1/15)$   $\text{year}^{-1}$  because the length of the 11-year solar cycle changes from 9 to 14 years (Friis-Christensen & Lassen, 1991). We also band-pass filtered the  $^{10}\text{Be}$  flux record from the NGRIP and the group SSNs to compare the general behaviour of the two ice cores in relation to the solar activity cycles. We used standardised  $^{10}\text{Be}$  fluxes of the Tsambagarav and the NGRIP ice cores and the group SSNs for the band-pass filter analyses. Figure 9.5 shows the band-pass filtered  $^{10}\text{Be}$  fluxes and observed group SSNs. Because the time resolution of the Dome Fuji ice core is similar to the duration of 11-year solar cycles, we excluded the Dome Fuji  $^{10}\text{Be}$  flux record from the band-pass filtering.

As seen in Figure 9.5, the 11-year sunspot cycle signal is present in the Tsambagarav  $^{10}\text{Be}$  flux record. Variability in the band-pass filtered group SSNs is small during the Dalton Minimum. The band-pass filtered Tsambagarav  $^{10}\text{Be}$  flux data shows a large variation during the termination of the Dalton Minimum ( $\sim 1825$ ), while the variability in the NGRIP record does not show any different behaviour throughout the Dalton Minimum (1790 – 1830).

We also applied cross-correlation analysis to investigate any possible phase lag

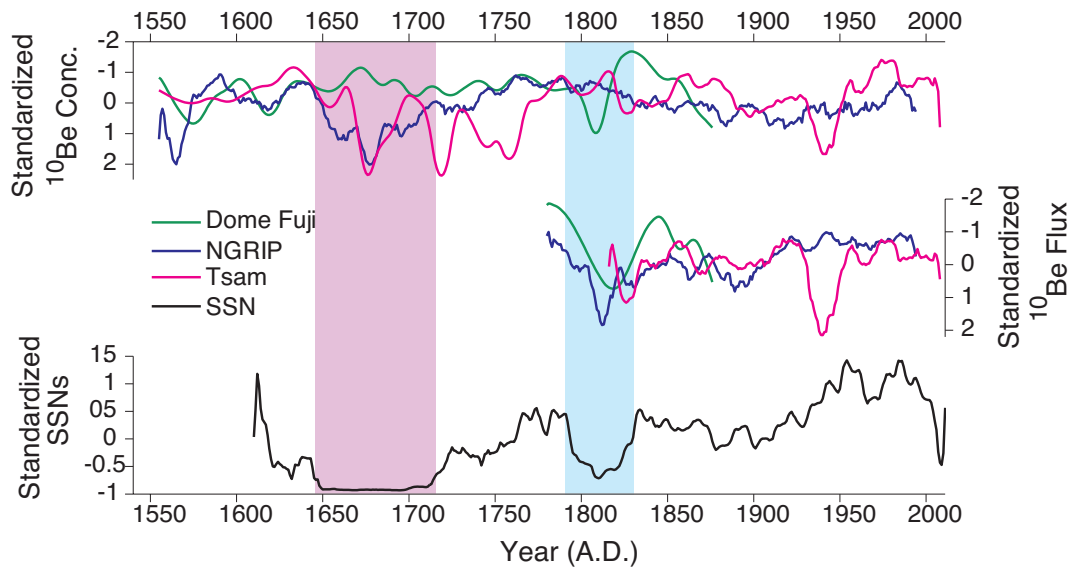


Figure 9.4: The top panel shows 11-year moving average values of the  $^{10}\text{Be}$  concentrations measured in the Tsambagarav (magenta), the NGRIP (blue) and the Dome Fuji (green) ice cores, whereas the middle panel shows the  $^{10}\text{Be}$  fluxes of the three ice cores. Notice that the x-axes of the top and mid-panels are reversed. The bottom panel shows 11-year moving average values of the observed group sunspot numbers. The purple and the blue bands show the Maunder Minimum and the Dalton Minimum, respectively.

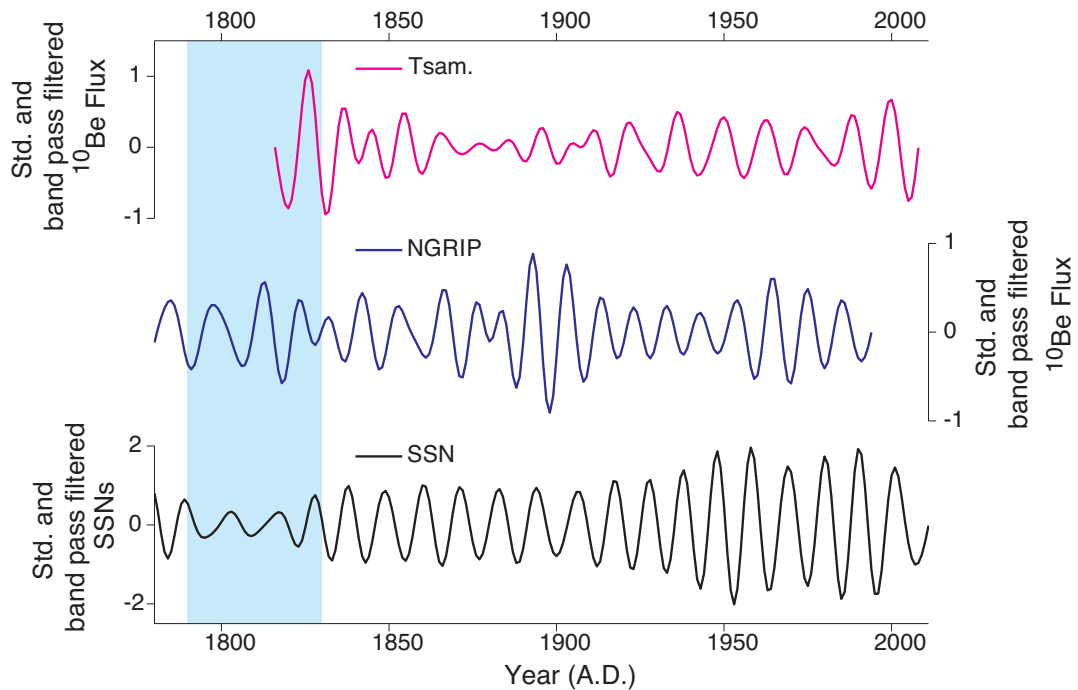


Figure 9.5: From top to bottom: Standardized and band-pass filtered  $^{10}\text{Be}$  fluxes calculated for the Tsambagarav (magenta) and the NGRIP (blue) ice cores, and group SSNs (black) using a Butterworth filter of degree 10 within a frequency range of  $(1/8)$ – $(1/15)$  year $^{-1}$ . The blue band shows the Dalton Minimum (see text).

Table 9.1: Multiple regression coefficients of Tsambagarav  $^{10}\text{Be}$  concentrations for the period from 1625 to 1975 and of Tsambagarav  $^{10}\text{Be}$  fluxes for the period from 1825 to 1975.

Coefficients	$^{10}\text{Be}$ concentrations	$^{10}\text{Be}$ fluxes
Constant	$-2.6 \times 10^{-16}$	$-5.3 \times 10^{-16}$
$\delta^{18}\text{O}$	<b>-0.415</b>	0.680
$\text{HCOO}^-$	-0.095	-0.147
$\text{Cl}^-$	-0.154	0.031
$\text{NO}_3^-$	-0.297	0.420
$\text{SO}_4^{2-}$	-0.114	-0.633
$\text{Na}^+$	<b>-0.309</b>	-0.208
$\text{NH}_4^+$	-0.031	-0.635
$\text{K}^+$	0.004	-0.138
$\text{Mg}^{2+}$	<b>0.417</b>	<b>2.315</b>
$\text{Ca}^{2+}$	0.138	<b>-2.133</b>
SSN	0.002	<b>-1.685</b>

between the band-pass filtered Tsambagarav  $^{10}\text{Be}$  flux and group SSN data, as well as between the band-pass filtered NGRIP  $^{10}\text{Be}$  flux and group SSN data. The results show that there is a two-year lag between the band-pass filtered Tsambagarav  $^{10}\text{Be}$  flux and group SSN data, while there is a lag of one year between the band-pass filtered NGRIP  $^{10}\text{Be}$  flux and group SSN data. Given a residence time of  $^{10}\text{Be}$  in the stratosphere of one to two years (Raisbeck et al., 1981; Heikkilä et al., 2013a), our results are completely in line with expectations because a large fraction of the  $^{10}\text{Be}$  atoms deposited at mid-latitudes are produced in the stratosphere. A phase lag of two-years at mid-latitudes and smaller time lag at polar latitudes is therefore highly consistent with model simulations of  $^{10}\text{Be}$  production and transport in the atmosphere. This, in turn, strongly suggests that the 11-year variability found in this frequency band does not represent an arbitrary variability, but rather that it is driven by the solar signal.

### Multiple Regression Analysis

To further investigate the possible influences of local climate on the Tsambagarav  $^{10}\text{Be}$  record and compare them to the effects of solar activity, we have applied multiple regression analysis to the Tsambagarav  $^{10}\text{Be}$  concentrations and fluxes. To achieve this, we use the major ion and  $\delta^{18}\text{O}$  records measured in the Belukha ice core as well as the group SSNs. We first averaged the group SSNs and the Tsambagarav  $^{10}\text{Be}$  concentrations and fluxes over a decade, in order to have the same time resolution as the major ion and  $\delta^{18}\text{O}$  records measured in the Belukha ice core. Subsequently, we standardised each data set using their individual mean and standard deviation values. The resulting coefficients of the two multiple regression analyses for the Tsambagarav  $^{10}\text{Be}$  concentration for the overlapping period from 1625 to 1975 and for the Tsambagarav  $^{10}\text{Be}$  flux record for the overlapping period between 1825–1975 are represented in Table 9.1 and their relevant statistics are shown in Table 9.2.

The results of the multiple regression analysis applied to the Tsambagarav  $^{10}\text{Be}$  concentrations for the overlapping period showed that 44% ( $r^2=0.44$ ) of the variation in the Tsambagarav  $^{10}\text{Be}$  concentration can mainly be explained by changes in  $\delta^{18}\text{O}$ ,  $\text{Mg}^{2+}$  and  $\text{Na}^+$ , while the effect of solar variability is relatively small (contributions

Table 9.2: Statistics of the two multiple regression analyses; Tsambagarav  $^{10}\text{Be}$  concentrations for the period from 1625 to 1975 and Tsambagarav  $^{10}\text{Be}$  fluxes for the period from 1825 to 1975.

Model	$R^2$	F-statistic	p-value	Error Variance
$^{10}\text{Be}$ Conc.	0.44	1.710	0.131	0.818
$^{10}\text{Be}$ Flux	0.82	1.675	0.327	0.669

from the other major ions are also small). For the Tsambagarav  $^{10}\text{Be}$  flux record, the multiple regression analysis showed that 82% ( $r^2=0.82$ ) of variations in the Tsambagarav  $^{10}\text{Be}$  fluxes are mainly explained by  $\text{Ca}^{2+}$ ,  $\text{Mg}^{2+}$  and SSNs. These results may imply that there is an additional input of re-mobilised mineral dust over the coring site. We also investigated the relative influences of  $\text{Ca}^{2+}$ ,  $\text{Mg}^{2+}$  and SSNs on the Tsambagarav  $^{10}\text{Be}$  fluxes by adding and removing these variables to the multiple regression analysis. When we remove the group SSNs from the multiple regression analysis, but keeping all the other variables, the resulting  $R^2$  value decreases to 0.60. In the absence of  $\text{Ca}^{2+}$  record, while keeping the rest of the variables in the multiple regression analysis, the  $R^2$  value decreases back to 0.48. When we remove  $\text{Mg}^{2+}$  record, but keeping the rest of the variables in the multiple regression analysis, the  $R^2$  value decreases back to 0.43. Therefore, the results may imply that the influences of dust related mineral-particles plays a major role on the observed variations in the Tsambagarav  $^{10}\text{Be}$  fluxes during the periods, where there is not a significant decrease in the solar activity. However, during the quiescent periods of solar activity such as the Dalton and Maunder Minima, the effect of SSNs on the Tsambagarav  $^{10}\text{Be}$  fluxes in the regression analysis becomes more pronounced.

## 9.6 Discussion

The new  $^{10}\text{Be}$  concentration and flux records from Tsambagarav support the model work by Field et al. (2006), who suggest that maximum  $^{10}\text{Be}$  deposition takes place at mid-latitudes, because the high precipitation rates within the mid-latitude storm tracks together with  $^{10}\text{Be}$ -rich stratospheric air injection to the troposphere may enhance the  $^{10}\text{Be}$  deposition flux (Field et al., 2006; Heikkilä et al., 2008a). The injection of stratospheric air into the upper layers of the troposphere occurs during cyclonic conditions causing stratosphere-to-troposphere air mass exchange, which will introduce stratospheric aerosols into the upper troposphere (Zanis et al., 2003). However, the air from the upper troposphere is transported into the lower layers of the troposphere under anticyclonic conditions, resulting in higher concentrations of  $^{10}\text{Be}$  in the lower troposphere (Zanis et al., 2003; Yamagata et al., 2010).

Even though there is a general agreement between the concentration and flux records of the three ice cores (Figure 9.2 and Figure 9.3), there are some notable discrepancies among the records. The peaks occurring roughly around 1936 in the Tsambagarav  $^{10}\text{Be}$  concentration and flux records are present neither in the NGRIP nor in the Dome Fuji record. Further, there are two peaks in the Tsambagarav  $^{10}\text{Be}$  concentration around 1719 (one data point) and 1759 (one data point), which too are not observed in the polar ice cores.

Sahsamanoglou et. al. (1991) investigated the temporal evolution of the central atmospheric pressure values of the SA using monthly-mean sea-level pressure grid-point data spanning the period between 1873–1988. As a result, the authors suggest that the central pressure of the SA was relatively weak between 1910-1940, with two

minima occurring in the central pressure of the SA around January 1920 and 1945, and a maximum around January 1935. The abrupt increase observed in Tsambagarav  $^{10}\text{Be}$  concentrations and the fluxes around 1936 coincides with marked variations in the strength of the Siberian Anticyclone. The peak observed in  $^{10}\text{Be}$  concentrations maintains high values until  $\sim 1950$  and then shows a gradual decrease, while a clear peak can be observed in the  $^{10}\text{Be}$  fluxes. This can be explained by effects linked to accumulation rates at the coring site. The abrupt increases observed in the Tsambagarav  $^{10}\text{Be}$  record around 1936, 1719 and 1759 are likely associated with variations in the strength of the SA.

The results of the multiple regression analysis applied to the Tsambagarav  $^{10}\text{Be}$  concentration and flux records suggest that 44% of the variation in the Tsambagarav  $^{10}\text{Be}$  concentration during 1625 to 1975 is mainly explained by changes in  $\delta^{18}\text{O}$ ,  $\text{Mg}^{2+}$  and  $\text{Na}^+$ , while 82% of variations in the Tsambagarav  $^{10}\text{Be}$  fluxes spanning the period 1825–1975 can be explained by  $\text{Ca}^{2+}$ ,  $\text{Mg}^{2+}$  and SSNs. The ions  $\text{Mg}^{2+}$ ,  $\text{Ca}^{2+}$  and  $\text{Na}^+$  are typically dust-related mineral particles, which may imply that there is a redeposition process involved over the coring site.

Overall, the  $^{10}\text{Be}$  concentration record from the Tsambagarav Mountain Region in the Mongolian Altai is influenced by atmospheric processes, cyclonic versus anticyclonic conditions, atmospheric transport, redeposition, etc., while the effect of the solar activity variations is relatively small. However, for the Tsambagarav  $^{10}\text{Be}$  flux record, the influence of solar variability is visible, particularly as positive anomalies during solar minima, *i. e.* the Maunder and Dalton Minima, and through its influence on the 11-year periodicity, which lags the group SSNs by two years as expected from model simulations.

## 9.7 Conclusions

The Tsambagarav record provides the first long-term  $^{10}\text{Be}$  archive from a mid-latitude ice core. The general trends observed in the Tsambagarav  $^{10}\text{Be}$  concentration and flux records are similar to those from polar ice cores, but with some notable differences. The  $^{10}\text{Be}$  fluxes calculated for the Tsambagarav ice core is higher than the fluxes obtained from polar ice cores, supporting the results of the model work by Field et al. (2006). Multiple regression analysis shows that variations in the Tsambagarav  $^{10}\text{Be}$  concentrations are influenced by local climatic conditions, such as the strength of the Siberian Anticyclone and atmospheric transport mechanisms, while the effect of solar variability is small. However, for the Tsambagarav  $^{10}\text{Be}$  flux record, the influence of solar variability becomes significant, particularly as positive anomalies during the Maunder and Dalton Minima. In addition to showing long-term changes related to solar activity, the band-pass filtered Tsambagarav  $^{10}\text{Be}$  flux record shows that significant variability corresponding to the 11-year solar cycle signal is also present.

It is difficult to assess whether the effects of regional meteorological phenomena, such as cyclonic versus anticyclonic conditions and storm tracks, on the  $^{10}\text{Be}$  concentration and fluxes are general across the mid-latitudes. In order to disentangle and better understand these regional meteorological effects and to achieve a global perspective on past  $^{10}\text{Be}$  production rates, more long-term, high-resolution  $^{10}\text{Be}$  records from mid-latitudes are needed.

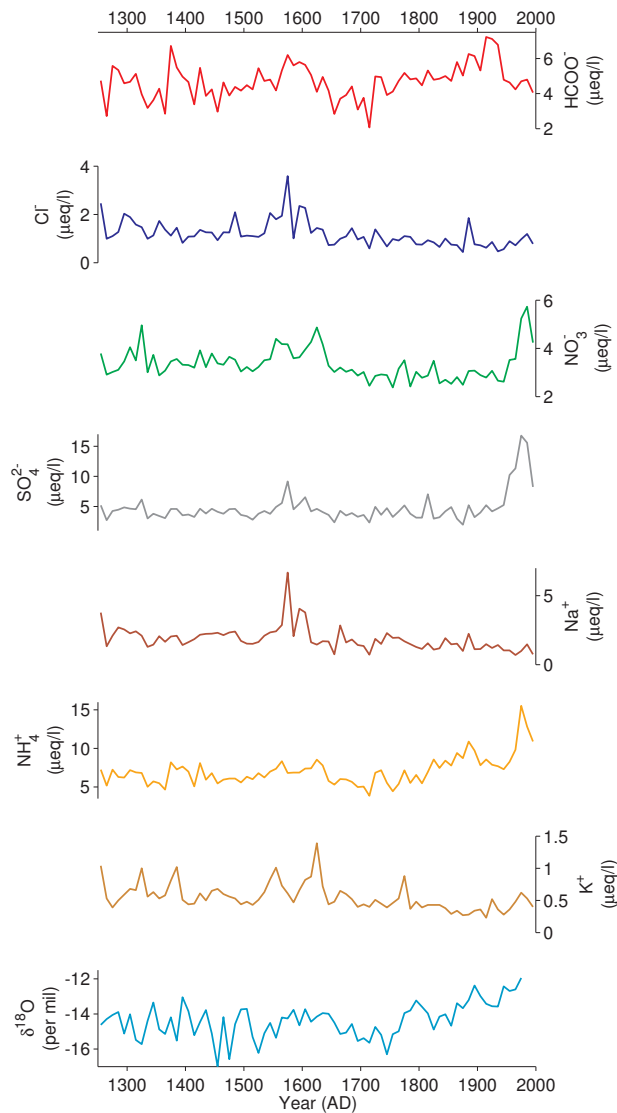


Figure 9.6: From top to bottom:  $\text{HCOO}^-$ ,  $\text{Cl}^-$ ,  $\text{NO}_3^-$ ,  $\text{SO}_4^{2-}$ ,  $\text{Na}^+$ ,  $\text{NH}_4^+$ ,  $\text{K}^+$  and  $\delta^{18}\text{O}$  records measured in the Belukha ice core from Siberian Altai (Eichler et al., 2009).

## 9.8 Supplementary

Figure 9.6 represents the Belukha major ion ( $\text{HCOO}^-$ ,  $\text{Cl}^-$ ,  $\text{NO}_3^-$ ,  $\text{SO}_4^{2-}$ ,  $\text{Na}^+$ ,  $\text{NH}_4^+$ ,  $\text{K}^+$ ) and  $\delta^{18}\text{O}$  records used in the multiple regression analysis in Section 9.5.

## Acknowledgments

FI is grateful to Ann-Marie Berggren and Anna Sturevik Storm for help during the  $^{10}\text{Be}$  chemistry work at Uppsala University. Funding for the Stellar Astrophysics Centre is provided by the Danish National Research Foundation (Grant agreement no.: DNRFF106). MFK, CK and JO acknowledge support from the Carlsberg Foundation and Villum Foundation.



## Chapter 10

# The lost sunspot cycle: New support from $^{10}\text{Be}$ measurements

C. Karoff, F. Inceoglu, M. F. Knudsen, J. Olsen, A. Fogtman-Schulz  
*Under revision for resubmission to Astronomy & Astrophysics*

### Abstract

It has been suggested that the Dalton minimum (1790 – 1830) might hide a lost sunspot cycle, sometimes referred to as cycle 4b. Here we reanalyse  $^{10}\text{Be}$  measurements with annual resolution from the NGRIP ice core in Greenland in order to investigate if the hypothesis about a lost sunspot cycle is supported by these measurements. Specifically, we make use of the fact that the Galactic cosmic rays, responsible for forming  $^{10}\text{Be}$  in the Earth's atmosphere, are affected differently by the solar open magnetic field during even and odd solar cycles. This fact enables us to evaluate if the numbering of cycles earlier than cycle 5 is correct. For the evaluation we use Bayesian analysis, which reveals that the lost sunspot cycle hypothesis is likely to be correct. We also discuss if this cycle 4b is a real cycle or a phase catastrophe and what implications this has for our understanding of stellar activity cycles in general.

Sun: activity, sunspots

### 10.1 Introduction

It was first suggested by Loomis (1870) based on auroral observations that a sunspot cycle was lost in the 1790s in the original sunspot record by Wolf. This suggestion has since caused some scientific debate. Part of the reason for this is that the parity of the solar cycles does have consequences for our understanding of the solar dynamo, as the 11-year solar cycle covers only half of the 22-year magnetic polarity Hall cycle. Therefore, using various parameters, it is possible to distinguish between even and odd solar cycles and an extra cycle thus clearly change the parity of earlier cycles.

Loomis' idea from 1870 was taken up again by Usoskin et al. (2001b) who used the group sunspot number (GSN) calculated by Hoyt & Schatten (1998) to show that not only did a cycle 4b scenario agree better with the GSN, it also made it possible to extend the Gnevyshev-Ohl (GO) rule (Gnevyshev & Ohl, 1948) to cycles before the Dalton minimum. The GO rule describes how even cycles typically have smaller amplitudes than the following odd cycles. A plausible explanation for the GO rule is that the Sun's magnetic field consists of both a dynamo and a fossil field. During odd cycles, the Sun's poloidal magnetic field is aligned with the fossil field whereas

it is misaligned during even cycles (see i.e. Charbonneau, 2010). The 2001 Usoskin et al. study was followed up by Usoskin et al. (2002c) who demonstrated how  $^{10}\text{Be}$  measurements from Dye 3, South Greenland, with annual resolution did not exclude the cycle 4b scenario and how the Waldmeier relation (see i.e. Charbonneau, 2010) was also improved by including a lost cycle. These results were, however, called into question by Krivova et al. (2002) who reexamined both the GSN,  $^{10}\text{Be}$  measurements,  $^{14}\text{C}$  measurements from tree rings and auroral records without finding any statistical evidence for a lost cycle. Krivova et al. (2002) did not call into question the improved extension of the GO rule, but argued that this only suggested a phase shift and not a lost cycle. A reply to the criticism by Krivova et al. (2002) was provided by Usoskin et al. (2003a), who argued that the negative results by Krivova et al. (2002) were mainly caused by the fact that they did not properly account for the uncertainties of the GSN and used arithmetic averages rather than weighted averages. Finally, Usoskin et al. (2009c) claim to have resolved the mystery using recovered solar drawings from the Dalton minimum by Staudacher and Hamilton (Arlt, 2008, 2009a,b). These drawings were used to reconstruct the solar butterfly diagram during the Dalton minimum which shows the presence of high-latitude sunspots around 1793 which strongly suggest that a new cycle started around this year.

In this paper, we will reanalyse  $^{10}\text{Be}$  measurements from the NGRIP ice core from North Greenland (Berggren et al., 2009) in order to reevaluate the lost cycle hypothesis. The analysis takes advantage of the so-called hysteresis effect, which has been reported by various authors (Mavromichalaki & Petropoulos, 1984; Marmatsouri *et al.*, 1995; Gupta et al., 2006; Mavromichalaki et al., 2007; Inceoglu et al., 2014a). The hysteresis effect describes how Galactic cosmic rays (GCR) are modulated differently by the solar open magnetic field during even and odd solar cycles due to the polarity of the field. During the declining phase of even cycles and the onset of odd cycles, when the polarity is positive the GCR will experience an inward drift over the heliographic poles and an outward drift at equator, while the opposite will be the case when the polarity is negative. This means that the flux of GCR particles at the Earth’s orbit will recover faster from the strong open solar magnetic field associated with cycle maxima after even cycles compared to odd cycles. For odd cycles, this can be observed as a delay of up to two years between changes in the open solar magnetic fields and the flux of GCRs at the Earth’s orbit (the hysteresis effect), while the relation is linear for the even cycles (Inceoglu et al., 2014a) – i.e. no delays.

Inceoglu et al. (2014a) used the hysteresis effect to make an improved reconstruction of the solar modulation strength based on  $^{10}\text{Be}$  measurements from NGRIP. In this study, a parametric form of the ellipse equation was used to model the hysteresis effect and the results were then used in the physical model of Usoskin et al. (2002a, 2004) to evaluate the long-term trend (cycle-to-cycle) of the GSN. Here, we present a method to model the hysteresis effect using differential equations that does not cause problems when linking even and odd cycles [encountered by Inceoglu et al. (2014a,a)] and we adjust the physical model by Usoskin et al. (2002a, 2004) to work on a sub-cycle time scale. This makes it possible for us to compare two reconstructions of the GSN around the Dalton minimum – one with the lost cycle and one without. One of the advantages of our evaluation of the  $^{10}\text{Be}$  measurements compared to the evaluations by Usoskin et al. (2002c) and Krivova et al. (2002) is that we do not only rely on the years 1785–1805 to evaluate the hypothesis as it is not just cycle 4 that is affected by the lost cycle in our analysis, but, as in the evaluation of the GO rule, it is all cycles around the Dalton minimum that are affected.

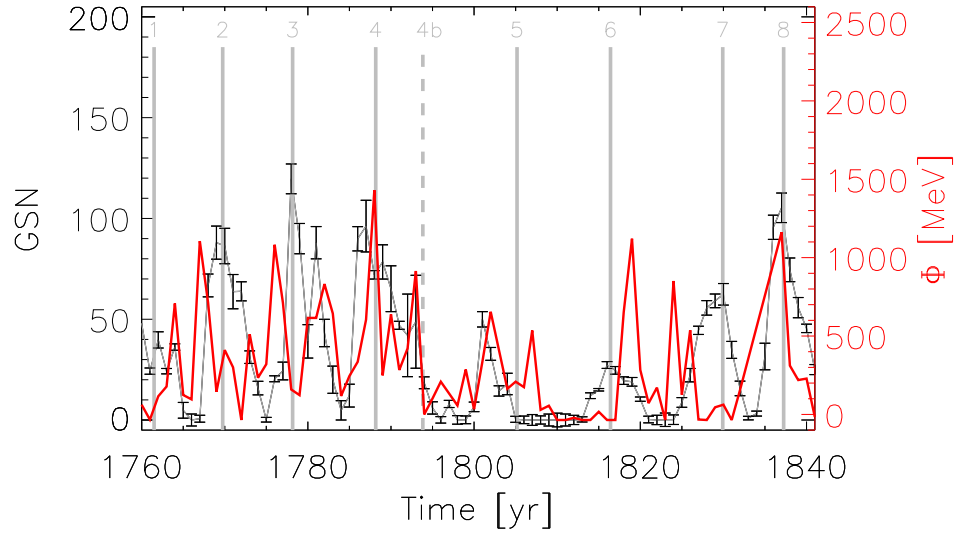


Figure 10.1: Comparison between the observed GSN (black line and left axis) and the solar modulation potential  $\Phi$  reconstructed from  $^{10}\text{Be}$  measurements from the NGRIP ice core on Greenland (red line and right axis). The solid grey lines indicate the midpoints of the canonical solar cycles, whereas the dashed line indicates the midpoint of cycle 4b.

## 10.2 Observations

Two different sets of observations are used in this analysis - the GSN record and the solar modulation potential of GCRs calculated based on  $^{10}\text{Be}$  concentrations in the NGRIP ice core.

### The group sunspot number record

There are mainly two reasons why the GSN is used in this study, and not the Wolf sunspot number (WSN): firstly, sunspot groups are more easily identified than individual spots and secondly, the GSN relies on all available observers, whereas the WSN only relies on a primary observer. The GSN was compiled by Hoyt & Schatten (1998) based on the WSN and 65,941 additional observations from 117 observers active before 1874.

As the  $^{10}\text{Be}$  measurements only have annual resolution, we also only need the GSN calculated with annual resolution. The most simple way to calculate the annual value of the GSN and the uncertainty of this value would be to just calculate the arithmetic mean and the uncertainty as the uncertainty of the mean. Unfortunately, as showed by Usoskin et al. (2003b) this is not the correct way to calculate the annual value of the GSN and its uncertainty. The main reason is that not all daily or even weekly or monthly values have the same quality and in order to take this into account, the annual values should be calculated as weighted mean values, where the weights are calculated based on the quality of the monthly values (which again are calculated based on the quality of the weekly and daily values). Apart from this, we are left with another critical problem for our analysis that is related to the fact that the Bayesian analysis relies heavily on the uncertainties and especially on the uncertainties of GSNs

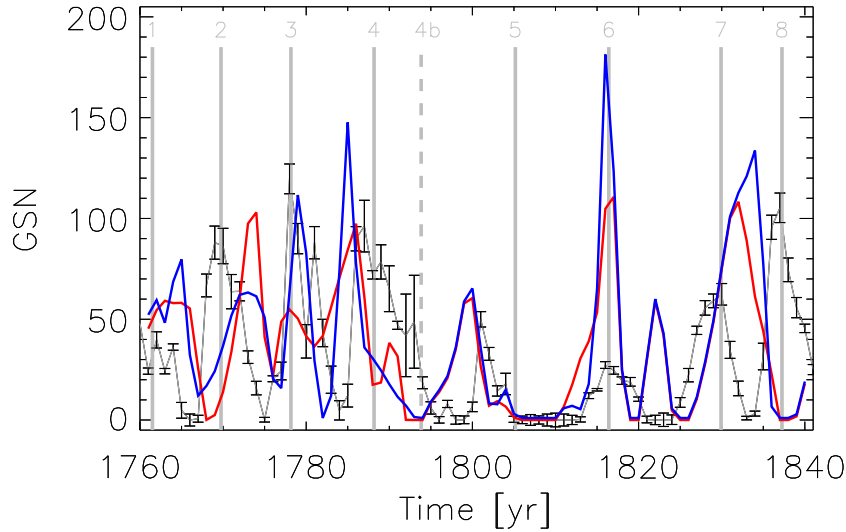


Figure 10.2: Comparison between the observed GSN (black line), the GSN calculated based on  $^{10}\text{Be}$  measurements and assuming a cycle 4b (blue line) and the GSN calculated based on  $^{10}\text{Be}$  measurements and not assuming a cycle 4b (red line). The calculation including cycle 4b is supported by the Bayesian analysis. Again, the solid grey lines indicate the midpoints of the canonical solar cycles, whereas the dashed line indicates the midpoint of cycle 4b.

in years with GSNs very close to zero. In a year where no sunspots are observed at all, then the annual value of the GSN will be zero, but the uncertainty of the annual value will in principle (if it is calculated as the uncertainty of the mean) also be zero – independent of how many observations the annual value is based on. This does not work in the Bayesian analysis. We therefore apply the recipe by Usoskin et al. (2003b) for calculating the annual GSN and its uncertainty. Especially, we also truncate the uncertainty of the weekly GSN (that is used to calculate the monthly and annual GSN) at 0.51. This is supported by the statistics of the weekly GSN value and implies that no weekly values of the GSN will have an uncertainty below 0.51. The calculated GSNs and the associated uncertainties are plotted in Figs. 1 & 2.

## Modulation potential

The solar modulation potential (or strength)  $\Phi$  is a quantity that measures the solar modulation of GCR particles in the heliosphere and it can be calculated from the  $^{10}\text{Be}$  flux based on the recipe in Knudsen et al. (2009), which corrects for any changes in the Earth’s magnetic field (though these are negligible, but we still use the recipe for converting from  $^{10}\text{Be}$  flux to modulation potential). Note that as our  $^{10}\text{Be}$  record has annual and not 5-year resolution, and as we do not apply a 61-point binomial filter to the record we do have a few years with such a high  $^{10}\text{Be}$  flux that it corresponds to slightly negative modulation potentials (i.e. 1772, 1810, 1811, 1813, 1814, 1816, 1817, 1823, 1828 and 1831). This is of course not physical and we therefore truncate all these years to a modulation potential of zero. We do not apply the linear interpolation to the  $^{10}\text{Be}$  fluxes as used by Inceoglu et al. (2014a) for correcting the data set for discontinuities as these can be handled by the Bayesian analysis.

The calculated modulation potential is plotted in Fig. 1.

### 10.3 Analysis

For the analysis we need a model that can be used to calculate the GSN from the modulation potential. The model we use is based on the *physical model* by Usoskin et al. (2004), but we include an extra step to account for the hysteresis effect. This means that our model cannot be completely physical in the sense that we need some empirical relation in order to account for the hysteresis effect. The reason is that we, currently, do not know exactly what causes the hysteresis effect (see e.g. discussion in Inceoglu et al., 2014a), which makes it difficult to model it. On the other hand, it is really clear from observations that the effect is real and significant (Inceoglu et al., 2014a), and it is straight forward to describe the observed effect mathematically – with some constants that will then have to be constrained from observations – empirically. We therefore construct a model, as described in details below, with four free parameters. These parameters are then constrained for the time period from 1850 to 1950. Using these parameters we then evaluate the lost cycle hypothesis using observations from 1750 to 1850.

#### The model

The hysteresis effect is included in the model by exchanging the step in the approach by Usoskin et al. (2004) where the open magnetic flux  $F_0$  is calculated:

$$F_0 = 0.023 \cdot \bar{\Phi}^{0.9} \quad (10.1)$$

with:

$$F_0 = g \int_0^{\tau_h} \Phi dt \quad (10.2)$$

where  $\Phi$  is the modulation potential and  $g$  is a free parameter we call the gain. The hysteresis lag  $\tau_h$  has to depend on whether we are considering an even or an odd cycle. We did test different functional forms for  $\tau_h$  – i.e. a simple step function, a triangular function or a sine function etc. and found that the best result was obtained with a smoothed step function. This means that:

$$\tau_t = \begin{cases} \tau_0 & \text{if cycle number} = \text{odd} \\ \tau_1 & \text{if cycle number} = \text{even} \end{cases} \quad (10.3)$$

where  $\tau_0$  and  $\tau_1$  are free parameters that are constrained from the observations spending the time period 1850 to 1950. The smoothing is done as:

$$\tau_h = \sum_{i-s}^{i+s} \frac{\tau_t}{2s} \quad (10.4)$$

where  $s$  is the smoothing width, which is constrained along with  $g$ ,  $\tau_0$  and  $\tau_1$  using the observations from the time period 1850 to 1950.

After the  $^{10}\text{Be}$  has been produced in the Earth's atmosphere, the atoms become adsorbed by aerosols and stay for 1 to 2 years in the lower stratosphere (Raisbeck et al., 1981). This delay is not modelled in the recipe by Knudsen et al. (2009) and has so far not been taken into account in the physical model by Usoskin et al. (2004). Here, we do not take the delay explicitly into account, but it is accounted for by  $\tau_0$

and  $\tau_1$ . If there were no delay in the transport of  $^{10}\text{Be}$  in the atmosphere,  $\tau_0$  should be close to zero (or one as we work with annual resolution), but because there is a delay,  $\tau_0$  is, as we will see larger than two. This also explains why Inceoglu et al. (2014a) found that the GSN was better modelled with an ellipse-ellipse than with a ellipse-linear relationship.

Note that  $F_0$  in the formulation by Usoskin et al. (2004) is given in  $10^{14}$  Wb. In our formulation this factor and the 0.023 constant is included in the gain factor  $g$ .

In the next step, we follow Usoskin et al. (2004) and use the relation from Solanki et al. (2000) to calculate the source function  $S$  from the open magnetic flux:

$$\frac{dF_0}{dt} = S - \frac{F_0}{\tau_s}, \quad (10.5)$$

where  $\tau_s = 4$  years represents the characteristic decay time of the open network flux. As noted by Usoskin et al. (2004), taking the time derivative of relatively noisy observations as the  $^{10}\text{Be}$  measurements can lead to fluctuations from one point to the next. This is of course a problem if the aim is to visually match solar cycles, but this is not the aim of this analysis. Here, the aim is to do a statical test of the lost cycle hypothesis and the statical test will account for such fluctuations. We do therefore not apply the 11-year smoothing for calculating the source functions as done by Usoskin et al. (2004)

The last step is to calculate the GSN from the source term. This is done as in Usoskin et al. (2004), solving the following equation:

$$S(\text{GSN}) = \alpha \cdot (24.35 + 22 \cdot \text{GSN} - 0.061 \cdot \text{GSN}^2), \quad (10.6)$$

where  $\alpha = 1.95 \cdot 10^{11}$  Wb/yr

## The Bayesian analysis

In order to evaluate the model we use a Bayesian inference tool (MULTINEST, Feroz & Hobson, 2008; Feroz et al., 2009). MULTINEST uses Bayes' theorem that states:

$$\Pr(\Theta | D, H) = \frac{\Pr(D, \Theta | H) \Pr(\Theta | H)}{\Pr(D | H)} \quad (10.7)$$

where  $\Pr(\Theta | D, H)$  is the posterior probability distribution of the parameters  $\Theta$  given the observations  $D$  and a model  $H$ ,  $\Pr(D, \Theta | H)$  is the likelihood,  $\Pr(\Theta | H)$  is the prior (assumed in all cases to be uniform) and  $\Pr(D | H) \equiv \mathcal{Z}$  is the Bayesian evidence. Here, the advantage compared to conventional statistical tools is that the calculated Bayesian evidence is properly normalised to the number of free parameters in the model. This is also the idea known as Occam's razor: *a simpler theory with compact parameter space will have a larger evidence than a more complicated one, unless the latter is significantly better at explaining the data* (Feroz & Hobson, 2008). This is exactly what we want to investigate here: Does an extra sunspot cycle lead to a significantly better explanation of the relation between the  $^{10}\text{Be}$  measurements and the GSN?

Having calculated the Bayesian evidence for a model including cycle 4b, lets call this  $\mathcal{Z}_1$ , and a model not including cycle 4b, lets call this  $\mathcal{Z}_2$ , we can calculate the Bayes' factor  $\mathcal{K}$ :

$$\mathcal{K} = \frac{\mathcal{Z}_1}{\mathcal{Z}_2} \quad (10.8)$$

Here, the lost cycle hypothesis is supported if  $\ln \mathcal{K}$  is larger than zero and, according to Jeffreys (1961), the evidence for the hypothesis is decisive if  $\ln \mathcal{K}$  is larger than 5.

In order to calculate the Bayesian evidence we need to define a function for the likelihood  $\Pr(D, \Theta | H)$ . If we assume that the errors between the model and the GSN are given by a normal distribution (see e.g. Corsaro et al., 2013) :

$$f = \prod_{i=1}^n \frac{1}{\sqrt{2\pi}\sigma_i} e^{-\frac{(D_i - H_i)^2}{2\sigma_i^2}} \quad (10.9)$$

where  $D$  represents the observations (the GSN),  $H$  is the model and  $\sigma$  is the uncertainty of  $D$ , then we obtain the following logarithmic likelihood function:

$$\ell = \ln f = -\sum_{i=1}^N \ln \sqrt{2\pi}\sigma_i - \frac{1}{2} \sum_{i=1}^N \left( \frac{\ln D_i - \ln H_i}{\sigma_i} \right)^2 \quad (10.10)$$

The assumption that the errors between the model and the GSN are given by a normal distribution is based on the central limit theorem, but we stress that this is an assumption. We did test other likelihood functions – i.e. functions assuming  $\chi^2$  distribution with two or more degrees of freedom (Appourchaux, 2003). These tests all supported the conclusions of this paper, independent of the choice of likelihood function.

In this study we use eq. 7 for two different proposes. First we use it for parameter optimisation (in section 3.3) in order to calibrate the model described in eqs. 1–6. This is done using a *control period* (1850–1950). Then we use it for model selection (in section 3.4) in order to evaluate the lost cycle hypothesis. This is done using observations from the *evaluation period* (1750–1850). The use of a control period that is different from the evaluation period for the calibration of the model ensures that free parameters are not chosen in a way that can influence the model evaluation.

## Calibration of the Model

In order to use the model to evaluate the lost cycle hypothesis we need to calibrate the model. This means that we need to constrain the four free parameters  $\tau_0$ ,  $\tau_1$ ,  $s$  and  $g$  in the model (see eq. 2–4). This is done by using the modulation potential (calculated from the  $^{10}\text{Be}$  measurements) as input to the model in order to reproduce the GSN for the period 1850–1950. The other free parameters in the model, apart from  $\tau_0$ ,  $\tau_1$ ,  $s$  and  $g$ , are the midpoints of the sunspot cycles during the period. Here, the first guess was taken as the maxima of a smoothed version of the GSN and the midpoints could then vary by  $\pm 2$  years – the prior of the midpoint was uniform around the midpoint  $\pm 2$  years. Both the calibration and evaluation of the model were very robust against how the priors on the midpoints were chosen.

As the model is cumulative to the extent that the modelling of one cycle depends on the previous (and in fact also on the successor) - the model has memory, we only calculate the likelihood function for the years 1860–1940, though we do reconstruct the GSN for the whole period from 1850–1950. This, of course means that the midpoints of the first and last cycle are very poorly determined, but these are not the aim of this study anyway.

MULTINEST (or the PYTHON implementation of it) contains a number of optimisation parameters that we in general do not use, one exception being the parameter called `SAMPLING_EFFICIENCY`. This parameter determines, as the name indicates, how effective the sampling should be – i.e. how likely is it that a given parameter set, with a given likelihood, will be considered for the posterior probability distribution.

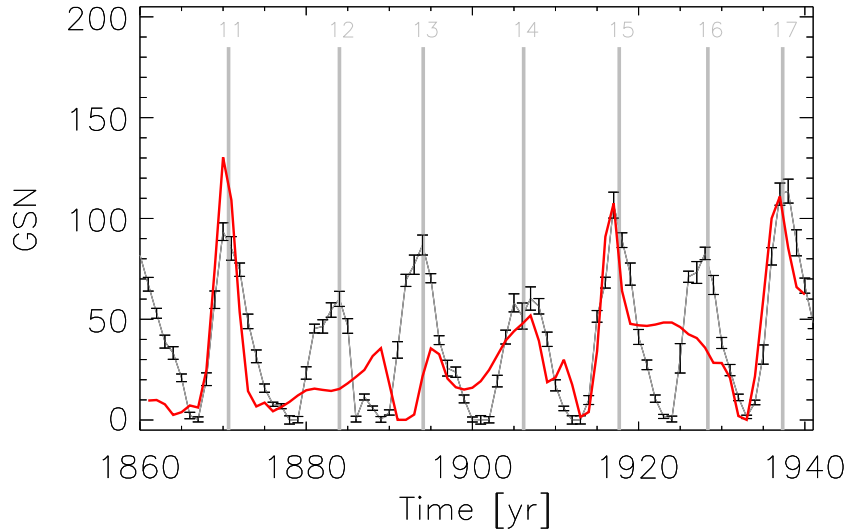


Figure 10.3: Comparison between the observed GSN (black line) and the GSN calculated based on  $^{10}\text{Be}$  measurements (red line). This comparison is used to constrain the four free parameters. The solid grey lines indicate the midpoints of the canonical solar cycles.

For the calibration of the model – where the aim is to constrain the free parameters, a sampling efficiency of 0.3 is chosen, whereas we choose a sampling efficiency of 0.9 for the evaluation of the lost cycle hypothesis where the aim is evidence evaluation.

Fig. 3 shows the modelled GSN based on the NGRIP  $^{10}\text{Be}$  measurements for the period 1850–1950. For the four free parameters we obtained the following results:  $\tau_0 = 2.54^{+0.18}_{-0.11}$  years,  $\tau_1 = 4.58^{+0.39}_{-0.46}$  years,  $s = 1.8^{+0.7}_{-0.5}$  days and  $g = 0.062^{+0.003}_{-0.003} \cdot 10^{14}$  Wb/MeV<sup>2</sup>.

### Evaluation of the Lost Cycle Hypothesis

For the evaluation of the lost cycle hypothesis, we run two models that are identical except for one point: one of them (model 1) includes an extra cycle, 4b. We use the time period 1750–1850 for the evaluation, which includes cycles 0–9. The uniform priors are given in Table 1 and a sampling efficiency of 0.3 was used.

## 10.4 Results

The results of the modelling are shown in Fig. 2, where the model including cycle 4b is shown in blue and the model without is shown in red.

We obtain the following evidence and Bayes’ factor:

$$\ln\mathcal{K} = \ln\mathcal{Z}_1 - \ln\mathcal{Z}_2 = 620.3 \pm 0.2 - 614.0 \pm 0.2 = 6.3 \pm 0.3 \quad (10.11)$$

which implies that the lost cycle hypothesis is decisively supported by the  $^{10}\text{Be}$  measurements from the NGRIP ice core.

Table 10.1: Midpoints of cycles

Cycle nr.	Prior [yr]	model 1 [yr]	model 2 [yr]
0	1750.0±2.0	1750.0 ±1.1	1750.0±1.1
1	1761.5±2.0	1761.4 ±1.1	1761.5±1.1
2	1769.8±2.0	1768.7 ±0.6	1770.8±0.7
3	1778.4±2.0	1778.8 ±1.0	1777.4±0.8
4	1786.2±2.0	1784.9 ±0.6	1786.4±1.1
4b	1795.0±2.0	1796.2 ±0.5	–
5	1805.2±2.0	1805.0 ±1.1	1805.0±1.1
6	1816.4±2.0	1814.8 ±0.3	1814.9±0.3
7	1829.9±2.0	1828.6 ±0.5	1828.6±0.5
8	1837.3±2.0	1837.8 ±0.7	1837.9±0.7
9	1848.2±2.0	1848.2 ±1.1	1847.7±1.1

## 10.5 Discussion

Though we have shown that the lost cycle hypothesis is decisively supported by the  $^{10}\text{Be}$  measurements, there are still a number of explanations that we cannot rule out. What we can conclude, assuming that the hysteresis effect was working during the Dalton minimum as it has been working for the last 60 years, where we have continuous monitoring of GCRs with neutron counting monitors, is that it is decisively more likely that the Sun possessed an extra cycle 4b than it did not.

Another possible explanation for the Dalton minimum is the phase catastrophe scenario (Kremlivsky, 1994). Here, the idea is that the sunspot numbers can be explained as a low-dimensional chaotic system with a periodical 11-year component. This system is unstable and can, under the right conditions, drop into a laminar low-activity stage. Grand minima represents the lowest of these stages. The change from a chaotic to a laminar low system will happen through a so-called phase catastrophe, where the falling branch of a cycle will be extended thereby breaking the phase preservation. Usoskin (2013) provides a nice review of the low-dimensional chaotic system idea and the criticism of it. Especially, he notes that different models of the sunspot numbers based on low-dimensional chaotic systems provide rather different results and that the general problem is that the sunspot record is too short to allow a proper determination of the parameters in the low-dimensional chaotic system. To this it could be added that the concept of low-dimensional chaotic systems is a purely mathematical concept – it provided no direct explanation of the physical processes leading to the variability in the sunspot record – except that the processes must be chaotic. Nevertheless, the phase catastrophe scenario for the onset of the Dalton minimum is tempting as it is capable of reproducing a number of the observed features. Along these lines, it is not clear if the phases would be preserved during a phase catastrophe. If they are not preserved, it would explain both our results and the results related to the GO rule by Usoskin et al. (2001b) without the need to include an extra cycle.

The phase catastrophe scenario also becomes particularly interesting in the light of the recent extended minimum between solar cycle 23 and 24, which has some characteristics similar to the beginning of the Dalton minimum. On the other hand, it is clear that the parity of the global solar magnetic field has changed as normal between cycle 23 and 24. Whether or not cycle 24 will be followed by 2–3 low amplitude cycles, as cycle 4 was, is still to be revealed.

Another possible explanation for the Dalton minimum is that the configuration of

the dynamo changed from a dipolar to a quadrupolar configuration during this period (Simoniello et al., 2013b). Dynamo theory does suggest this as a valid explanation for grand minima (?) and recent analysis of helioseismic observations suggest that it is likely that the Sun contains both a dipolar and a quadrupolar dynamo mode, where the dipolar mode is responsible for the 11-year cycle and the quadrupolar mode is responsible for the biannual variability (Simoniello et al., 2012, 2013a). In this scenario, the hysteresis effect as we know it would no longer work during the Dalton minimum as the hysteresis effect relies on a dipolar configuration of the solar open magnetic field. We do not know how the modulation of GCR would be for a quadrupolar configuration of the open solar magnetic field, but for most of the possible explanations of the hysteresis effect (see e.g. discussion in Inceoglu et al., 2014a), the modulation would be different and the hysteresis effect would therefore most likely not apply.

A possible stellar connection to these questions comes from the study of the star  $\epsilon$  Eridani by Metcalfe et al. (2013) where the authors identified both a 3-year and a 13-year activity cycle in a re-analysis of both archive and new Ca HK activity measurements. In the record, which extends from 1962 to 2013, they also identify a possible *Maunder minimum-like state for the short cycle* during the early 1990s. An interesting feature of this possible Maunder minimum-like state, is that it takes place just after a cycle with an extended falling branch – as suggested in the phase catastrophe scenario. In other words,  $\epsilon$  Eridani might be showing the same phenomenon as the Sun was showing during the Dalton minimum and it is also not clear if this is due to an extra low amplitude cycle or to a phase catastrophe.

Progress in our understanding of both grand minima and extended cycle minima would thus be possible if we could either identify a way to measure the parity of the stellar cycles observed in other stars, mainly from the Mount Wilson (Baliunas et al., 1995) and Lowell (Hall et al., 2007) observatories, or if we could identify a way to test if the phase is preserved in the Sun over grand minima like the Maunder minimum – i.e. if all even cycles are followed by odd cycles.

#### **Acknowledgements**

The Danish National Research Foundation (Grant agreement no.: DNRF106). The projects has been supported by the Villum Foundation.

# Bibliography

- Abreu, J. A., Beer, J., Steinhilber, F., Tobias, S. M., & Weiss, N. O. 2008, *Geophysical Research Letters*, 35, 20109. 104
- Akaike, H., 1974, *IEEE Transactions on Automatic Control*, AC-19, 6. 85
- Alanko-Huotari, K., Usoskin, I. G., Mursula, K., Kovaltsov, G. A. 2007, *Journal of Geophysical Research*, 112, 8101. 47
- Aizen, V. B., Aizen, E., Fujita, K., Nikitin, S. A., Kreutz, K. J., Takeuchi, L. N.. 2005, *Journal of Glaciology*, 51,(175), 637. 110
- Ahluwalia, H. S., Ygbuhay, R. C. 2012, *Advances in Space Research*, 49, 493. 45, 46
- Aldahan, A., Hedfors, J., Possnert, G., et al. 2008, Atmospheric impact on beryllium isotopes as solar activity proxy, *Geophysical Research Letters*, 35, 21812. 95, 110
- Appourchaux, T. 2003, *Astronomy & Astrophysics*, 412, 903. 127
- Arlt, R. 2008, *Solar Physics*, 247, 399. 122
- Arlt, R. 2009, *Astronomische Nachrichten*, 330, 311. 122
- Arlt, R. 2009, *Solar Physics*, 255, 143 122
- Augustson, K., Brun, A. S., Miesch, M. S., Toomre, J. 2013, arXiv:1310.8417. 91
- Baliunas, S. L., Donahue, R. A., Soon, W. H., et al. 1995, *The Astrophysical Journal*, 438, 269. 78, 130
- Bard, E., Frank, M. 2006, *Earth and Planetary Science Letters*, 248, 1. 6, 21, 44, 109
- Bard, E., Raisbeck, G. M., Yiou, F., Jouzel, J. 1997, *Earth and Planetary Science Letters*,150, 453. 11, 21, 62, 79
- Bard, E., Raisbeck, G. M., Yiou, F., Jouzel, J. 2007, *Quaternary Science Reviews*, 26, 2301. 21
- Baroni, M., Bard, E., Petit, J.-R., Magand, O., Bourlès, D. 2011, *Geochimica et Cosmochimica Acta*, 75, 7132. 9, 11, 19, 44, 62, 63, 110
- Belov, A. 2000, *Space Science Reviews*, 93, 79. 46
- Beer, J., Tobias, S., Weiss, N. 1998, *Solar Physics*, 181, 237. 66, 86
- Berdyugina, S. V.. 2005, *Living Reviews in Solar Physics*, 2, 8.

- Berggren, A.-M., Beer, J., Possnert, G., Aldahan, A., Kubik, P., Christl, M., Johnsen, S. J., Abreu, J., Vinther, B. M. 2009, *Geophysical Research Letters*, 36, 11801. 32, 33, 62, 63, 66, 79, 110, 111, 122
- Berggren, A.-M., Aldahan, A., Possnert, G., Haltia-Hovi, E., and Saarinen, T. (2013), *Nuclear Instruments and Methods in Physics Research B*, 294, 524. 110
- Blandford, R., Eichler, D. 1987, *Physics Reports*, 154, 1. 7
- Bond, G. C., Showers, W., Elliot, M., et al. 1999, Washington DC American Geophysical Union Geophysical Monograph Series, 112, 35. 19, 35
- Bond, G., Kromer, B., Beer, J., et al. 2001, *Science*, 294, 2130. 18
- Brandenburg, A., Krause, F., Meinel, R., Moss, D. Tuominen, I., 1989, *Astronomy and Astrophysics*, 213, 411. 78
- Brajša, R., Wöhl, H., Hanslmeier, A., Verbanac, G., Ruždjak, D., Cliver, E., Svalgaard, L., Roth, M. 2009, *Astronomy and Astrophysics*, 496, 855. 62
- Braun, H., Christl, M., Rahmstorf, S., et al. 2005, *Nature*, 438, 208. 18
- Bridgman, H. A., Oliver, J. E., 2006, Cambridge University Press. 17
- Broecker, W. S., Peteet, D. M., Rind, D. 1985, *Nature*, 315, 21. 36
- Brun, A. S., Browning, M. K., Dikpati, M., Hotta, H., Strugarek, A. 2013, *Space Science Reviews*, 100.
- Bryden, H. L., Longworth, H. R., Cunningham, S. A. 2005, *Nature*, 438, 655. 19
- Castro-Diez, Y., D. Pozo-Vazquez, F. S. Rodrigo, M. J. Esteban-Parra 2002, *Geophysical Research Letters*, 29, 8. 17
- Charbonneau, P. 2010, *Living Reviews in Solar Physics*, 7, 3. 4, 6, 62, 122
- Chowdhury, P., Kudela, K., Dwivedi, B. N. 2013, *Solar Physics*, 286, 577. 49
- Clauset, A., Rohilla Shalizi, C., Newman, M. E. J. 2009, *Society for Industrial and Applied Mathematics Rev.*, 51, 4. 28, 85, 96
- Clilverd, M. A., Clarke, E., Ulich, T., Rishbeth, H., & Jarvis, M. J. 2006, *Space Weather*, 4, 9005. 94
- Corsaro, E., Fröhlich, H.-E., Bonanno, A., et al. 2013, *Monthly Notices of Royal Astronomical Society*, 430, 2313. 127
- Dansgaard, W., Johnsen, S. J., Clausen, H. B., et al. 1993, *Nature*, 364, 218. 19, 35
- DeRosa, M. L., Brun, A. S., Hoeksema, J. T. 2012, *The Astrophysical Journal*, 757, 96. 5, 78, 102
- Dikpati, M., de Toma, G., Gilman, P. A., Arge, C. N., & White, O. R. 2004, *The Astrophysical Journal*, 601, 1136. 94
- Dikpati, M., Gilman, P. A., de Toma, G., Ulrich, R. K. 2010, *Geophysical Research Letters*, 37, 14107 91

- Dunai, T. J.: 2010, *Cosmogenic Nuclides: Principles, Concepts and Applications in the Earth Surface Sciences*, Cambridge University Press, Cambridge, 2. 8, 44, 62, 78, 94
- Ebisuzaki, W. 1997, *Journal of Climate*, 10, 2147. 71, 99
- Eichler, A., Brütsch, S., Olivier, S., Papina, T., Schwikowski, M. 2009, *Geophysical Research Letters*, 36, 18813. 32, 112, 119
- Feroz, F., & Hobson, M. P. 2008, *Monthly Notices of Royal Astronomical Society*, 384, 449. 33, 126
- Feroz, F., Hobson, M. P., & Bridges, M. 2009, *Monthly Notices of Royal Astronomical Society*, 398, 1601. 33, 126
- Field, C. V., Schmidt, G. A., Koch, D., Salyk, C. 2006, *Journal of Geophysical Research (Atmospheres)*, 111, 15107. 11, 14, 21, 31, 63, 80, 110, 117, 118
- Fletcher, S. T., Broomhall, A.-M., Salabert, D., et al. 2010, *The Astrophysical Journal Letters*, 718, L19. 94
- Fligge, M., Solanki, S. K., Beer, J. 1999, *Astronomy and Astrophysics*, 346, 313 . 86
- Foukal, P. V. 2004, *Solar Astrophysics*, 2nd, Revised Edition, by Peter V. Foukal, pp. 480. ISBN 3-527-40374-4. Wiley-VCH , April 2004. 3
- Freedman, D., Diaconis, P. 1981, *Zeitschrift für Wahrscheinlichkeitstheorie und Verwandte Gebiete*, 57, 453. 81
- Friis-Christensen, E., Lassen, K. 1991 *Science*, 254, 698. 5, 114
- Fröhlich, C. 2006, *Space Science Reviews*, 125, 53. 14
- Gleeson, L. J., Axford, W. I. 1968, *The Astrophysical Journal*, 154, 1011. 12, 64
- Gnevyshev, M. N. & Ohl, A. I. 1948, *Astron. Zh.*, 25(1), 18. 121
- Gosse, J. C., Phillips, F. M. 2001, *Quaternary Science Reviews*, 20, 1475. 8
- Gray, L. J., Beer, J., Geller, M., et al. 2010, *Reviews of Geophysics*, 48, 4001. 13, 14, 15, 16, 19, 40
- Grinsted, A., Moore, J. C., Jevrejeva, S. 2004, *Nonlinear Processes in Geophysics*, 11, 561. 87
- Guerriero, V., 2012, *Journal of Modern Mathematics Frontier*, 1, 21. 85, 96
- Gupta, M., Mishra, V. K., Mishra, A. P. 2006, *Journal of Astrophysics and Astronomy*, 27, 455. 33, 49, 122
- Haigh, J. D. 1994, *Nature*, 370, 544. 15
- Haigh, J. D. 1996, *Science*, 272, 981. 15
- Haigh, J. D. 1999, *Journal of Atmospheric and Solar-Terrestrial Physics*, 61, 63. 15
- Haigh, J. D. 2001, *Science*, 294, 2109. 19

- Haigh, J. D. 2007, Space Weather : Research Towards Applications in Europe 2nd European Space Weather Week (ESWW2), 344, 65. 13, 14, 15
- Hale, G. E., Ellerman, F., Nicholson, S. B., Joy, A. H. 1919, Astrophysical Journal, 49, 153. 45
- Hall, J. C., Lockwood, G. W., & Skiff, B. A. 2007, The Astrophysical Journal, 133, 862 130
- Hathaway, D. H., Nandy, D., Wilson, R. M., Reichmann, E. J. 2003, The Astrophysical Journal, 589, 665. 91
- Hathaway, D. H. 2010, Living Reviews in Solar Physics, 7, 1. 7, 8
- Heinrich, H. 1988, Quaternary Research, 29, 142. 19, 35
- Heikkilä, U., Beer, J., Feichter, J. 2008, Atmospheric Chemistry Physics, 8, 2797. 117
- Heikkilä, U., Beer, J., Jouzel, J., Feichter, J., Kubik, P. 2008, Geophysical Research Letters, 35, 5817. 9, 10, 44, 62, 63, 79, 110
- Heikkilä, U., Beer, J., Abreu, J. A., Steinhilber, F. 2013, Space Science Reviews, 176, 321. 11
- Heikkilä, U., Phipps, S. J., and Smith, A. M. 2013, Climate of the Past, 9, 2641–2649. 110, 116
- Herbst, K., Kopp, A., Heber, B., Steinhilber, F., Fichtner, H., Scherer, K., Matthiä, D. 2010, Journal of Geophysical Research, 115, 0. 12, 64
- Herren, P.-A., Eichler, A., Machguth, H., Papina, T., Tobler, L., Zapf, A., Schwikowski, M. 2013, Quaternary Science Reviews, 69, 59. 32, 110, 111, 112
- Hiremath, K. M. 2008, Astrophysics and Space Science, 314, 45. 94
- Hoffmann, D. L., Warren Beck, J., Richards, D. A., Smart, P. L., Singarayer, J. S., Ketchmark, T., & Hawkesworth, C. J. 2010, Earth and Planetary Science Letters, 289, 1. 35
- Horiuchi, K., Uchida, T., Sakamoto, Y., Ohta, A., Matsuzaki, H., Shibata, Y., Motoyama, H. 2008, Quaternary Geochronology, 3, (3), 253. 32, 110
- , Howe, R., Christensen-Dalsgaard, J., Hill, F. et al., 2013, The Astrophysical Journal, 767, L20. 105
- Howard, R. and La Bonte, B.J., The Astrophysical Journal Letters, 239, L33. 104
- Hoyt, D. V., Schatten, K. H. 1993, Journal of Geophysical Research, 98, 18895. 44
- Hoyt, D. V., Schatten, K. H.: 1998, Solar Physics, 179, 189. 7, 24, 32, 63, 112
- Hoyt, D. V., & Schatten, K. H. 1998, Solar Physics, 181, 491. 121, 123
- Hughen, K., Southon, J., Lehman, S., Bertrand, C., Turnbull, J. 2006, Quaternary Science Reviews, 25, 3216. 35
- Inceoglu, F., Knudsen, M. F., Karoff, C., Olsen, J. 2014, Solar Physics, 289, 1387. 8, 24, 26, 33, 63, 66, 67, 73, 122, 124, 125, 126, 130

- Inceoglu, F., Knudsen, M. F., Karoff, C., Olsen, J. 2014, *Solar Physics*, 102. 6, 110
- Inceoglu, F., Simoniello, R., Knudsen, M. F., Karoff, C., Olsen, J., Turck-Chiéze, S., Jacobsen, B. H. 2014, *submitted*, *Astronomy & Astrophysics*. 30, 94, 95, 98, 99, 100, 101, 103, 104
- Ineson, S., Scaife, A. A., Knight, J. R., et al. 2011, *Nature Geoscience*, 4, 753. 15
- IPCC, 2007: *Climate Change 2007: The Physical Science Basis. Contribution of Working Group I to the Fourth Assessment Report of the Intergovernmental Panel on Climate Change* [Solomon, S., D. Qin, M. Manning, Z. Chen, M. Marquis, K.B. Averyt, M. Tignor and H.L. Miller (eds.)]. Cambridge University Press, Cambridge, United Kingdom and New York, NY, USA, 996 pp. 13
- Jeffreys, H. 1961, *Theory of Probability*, 3rd edn. (Oxford University Press). 127
- Johnsen, S. J., Dahl-Jensen, D., Gundestrup, N., et al. 2001, *Journal of Quaternary Science*, 16, 299.
- Jokipii, J. R., Levy, E. H., Hubbard, W. B. 1977, *Astrophysical Journal*, 213, 861. 46
- Jokipii, J. R.: 2011, In: *The 2011 Heliophysics Summer School*, Boulder [http://www.vsp.ucar.edu/Heliophysics/pdf/2011\\_Jokipii\\_Cosmic-Rays-Lecture.pdf](http://www.vsp.ucar.edu/Heliophysics/pdf/2011_Jokipii_Cosmic-Rays-Lecture.pdf).
- Klinge, M., Böhner, J., Lehmkühl, F. 2003, *Erdkunde*, 57 (4), 296-308. 110
- Koch, D. and D. Rind. 1998, *Journal of Geophysical Research*, 103(D4), 3907–3917. 9, 79, 110
- Knudsen, M. F., Riisager, P., Donadini, F., et al. 2008, *Earth and Planetary Science Letters*, 272, 319. 11
- Knudsen, M. F., Riisager, P., Jacobsen, B. H., et al. 2009, *Geophysical Research Letters*, 36, 16701. 6, 7, 19, 25, 63, 65, 80, 86, 124, 125
- Kremliovsky, M. N. 1994, *Solar Physics*, 151, 351. 129
- Krivova, N. A., and Solanki, S. K. 2002, *Astronomy and Astrophysics*, 394, 701. 5, 94
- Krivova, N. A., Solanki, S. K., & Beer, J. 2002, *Astronomy and Astrophysics*, 396, 235. 122
- Lal D. and Peters B.: 1967, Cosmic ray produced radioactivity on the Earth, In *Handbuch der Physik* (ed S. Flugge), Springer, pp. 551–612. 9, 11
- Lamb, P. J., Pepler, R. A. 1987, *Bulletin of the American Meteorological Society*, 68, 1218. 17
- Lean, J. 2000, *Geophysical Research Letters*, 27, 2425. 4, 44
- Lean, J. L., Wang, Y.-M., Sheeley, N. R. 2002, *Geophysical Research Letters*, 29, 2224. 4
- Lepreti, F., Carbone, V., Veltri, P. 2001, *Astrophysical Journal Letters*, 555, L133 28, 85

- Lockwood, M. 2001, *Journal of Geophysical Research*, 106, 16021. 6
- Lockwood, M. 2013, *Living Reviews in Solar Physics*, 10, 4. 4, 79
- Loomis, E. 1870, *Am. J. Sci.*, 2nd Ser, 50, 153. 121
- Malkus, W. V. R., & Proctor, M. R. E. 1975, *Journal of Fluid Mechanics*, 67, 417. 104
- Maris, G., Oncica, A., Popescu, M. D. 2001, *Romanian Astronomical Journal*, 11, 13.
- Marmatsouri, L., Vassilaki, A., Mavromichalaki, H., Petropoulos, B. 1995, *Advances in Space Research*, 16, 245. 33, 49, 122
- Masarik, J., Beer, J. 1999, *Journal of Geophysical Research*, 104, 12099. 9, 11, 12, 62, 79, 80, 95, 110
- Matthiä, D., Herbst, K., Heber, B., Berger, T., Reitz, G. 2013, *Space Science Reviews*, 176, 333 8
- Mavromichalaki, H., Belehaki, A., Rafios, X. 1998, *Astronomy and Astrophysics*, 330, 764. 46
- Mavromichalaki, H., Belehaki, A., Rafios, X., Tsagouri, I. 1996, *Astrophysics and Space Science*, 246, 7. 46
- Mavromichalaki, H., Marmatsouri, E., Vassilaki, A. 1990, *Solar Physics*, 125, 409. 60
- Mavromichalaki, H., Paouris, E., Karalidi, T. 2007, *Solar Physics*, 245, 369. 33, 49, 122
- Mavromichalaki, H., Petropoulos, B. 1984, *Astrophysics and Space Science*, 106, 61. 9, 33, 47, 122
- Mavromichalaki, H., Petropoulos, B. 1987, *Earth, Moon, Planets*, 37, 79. 56
- McCracken, K., Beer, J., Steinhilber, F., Abreu, J. 2013, *Space Science Reviews*, 176, 59. 86
- Merkel, A. W., Harder, J. W., Marsh, D. R., et al. 2011, *Geophysical Research Letters*, 38, 13802. 16
- Metcalf, T. S., Buccino, A. P., Brown, B. P., et al. 2013, *Astrophysical Journal Letters*, 763, L26. 130
- Miyahara, H., Masuda, K., Muraki, Y., Kitagawa, H., Nakamura, T. 2006, *Journal of Geophysical Research (Space Physics)*, 111, 3103.
- Moss, D., Sokoloff, D., Kuzanyan, K., Petrov, A. 2004, *Geophysical and Astrophysical Fluid Dynamics*, 98, 257.
- Moss, D., Sokoloff, D., Usoskin, I., Tutubalin, V. 2008, *Solar Physics*, 250, 221. 78, 91, 104
- Murshudov, G. N., Vagin, A. A., Dodson, E. J. 1997, *Acta Crystallograpica*, D53, 240.

- Mursula, K., Zieger, B., and Vilppola, J. H. 2003, *Solar Physics*, 212, 201–5, 94
- Muscheler, R., Beer, J. 2006, *Geophysical Research Letters*, 33, 20706. 18
- Muscheler, R., Joos, F., Beer, J., et al. 2007, *Quaternary Science Reviews*, 26, 82. 6, 7, 21, 30, 100, 101, 110
- Muscheler, R., Joos, F., Beer, J., et al. 2007, *Quaternary Science Reviews*, 26, 2304. 21
- Nagashima, K., Morishita, I. 1980, *Planetary and Space Science*, 28, 195. 47
- Neath, A. A., Cavanaugh, J. E., 2012, *WIREs Comput Stat*, 4, 199. 85
- Neff, U., Burns, S. J., Mangini, A., et al. 2001, *Nature*, 411, 290. 17
- Oberländer, S., Langematz, U., Matthes, K., et al. 2012, *Geophysical Research Letters*, 39, 1801. 16
- Olsen, J., Anderson, N. J., Knudsen, M. F. 2012, *Nature Geoscience*, 5, 808. 17
- Olsen, J., Rasmussen, T.L., Reimer, P.J., 2014, North Atlantic marine radiocarbon reservoir ages through the Heinrich 4 event developed with a new method for marine age model construction in: Austin, W.E.N., Abbott, P.M., Davies, S.M., Pearce, N.J.G., Wastegard, S. (Eds.), *Marine Tephrochronology*. Geological Society, London, Special Publications. Geological Society, London, London. 35
- Otaola, J. A., Perez-Enriquez, R., Valdes-Galicia, J. F. 1985, 19th Int. Cosmic Ray Conference, 4, 493. 47
- Owens, M. J., Lockwood, M., Barnard, L., & Davis, C. J. 2011, *Geophysical Research Letters*, 38, 19106. 94
- Owens, M. J., Usoskin, I., Lockwood, M. 2012, *Geophysical Research Letter*, 39, 19102. 44, 86
- Owens, M. J., Crooker, N. U., Lockwood, M. 2011, *Journal of Geophysical Research*, 116, 4111. 75
- Parker, E. N., 1955a, *The Astrophysical Journal*, 122, 293. 78
- Parker, E. N., 1955b, *The Astrophysical Journal*, 121, 491. 78
- Parker, E. N. 1965, *Planetary and Space Science*, 13, 9. 8, 45, 64
- Paouris, E., Mavromichalaki, H., Belov, A., Gushchina, R., Yanke, V. 2012, *Solar Physics*, 280, 255. 49
- Passos, D., Nandy, D., Hazra, S., Lopes, I. 2013, arXiv:1309.2186.
- Potgieter, M. S., Burger, R. A., Ferreira, S. E. S. 2001, *Space Science Reviews*, 97, 295. 46
- Potgieter, M. 2013, *Living Reviews in Solar Physics*, 10, 3. 8, 62, 64, 95
- Priest, E. R. 1981, *Geophysics and Astrophysics Monographs Series Volume 21: Solar Magnetohydrodynamics*, 1st Edition, by E. R. Priest, pp. 487. ISBN-13: 978-90-277-1833-4. Kluwer-VCH, 1981. 4

- Rahmstorf, S. 2002, *Nature*, 419, 207. 19
- Raisbeck, G. M., F. Yiou, M. Fruneau, J. M. Loiseaux, M. Lieuvin, J. C. Ravel, C. Lorius, 1981, *Geophysical Research Letters*, 8, 1015–1018. 9, 62, 66, 79, 110, 116, 125
- Ramsey, C. B., Staff, R. A., Bryant, C. L., Brock, F., Kitagawa, H., van der Plicht, J., Schlolaut, G., Marshall, M. H., Brauer, A., Lamb, H. F., Payne, R. L., Tarasov, P. E., Haraguchi, T., Gotanda, K., Yonenobu, H., Yokoyama, Y., Tada, R., Nakagawa, T. 2012, *Science*, 338, 370. 35
- Reimer, P. J., Baillie, M. G. L., Bard, E., Bayliss, A., Beck, J. W., Blackwell, P. G., Ramsey, C. B., Buck, C. E., Burr, G. S., Edwards, R. L., Friedrich, M., Grootes, P. M., Guilderson, T. P., Hajdas, I., Heaton, T. J., Hogg, A. G., Hughen, K. A., Kaiser, K. F., Kromer, B., McCormac, F. G., Manning, S. W., Reimer, R. W., Richards, D. A., Southon, J. R., Talamo, S., Turney, C. S. M., van der Plicht, J., Weyhenmeyer, C. E., 2009, *Radiocarbon*, 51, 4. 35
- Reimer, P. J., Bard, E., Bayliss, A., Beck, J. W., Blackwell, P. G., Ramsey, C. B., Buck, C. E., Cheng, H., Edwards, R. L., Friedrich, M., Grootes, P. M., Guilderson, T. P., Hafliadon, H., Hajdas, I., Hatté, C., Heaton, T. J., Hoffmann, D. L., Hogg, A. G., Hughen, K. A., Kaiser, K. F., Kromer, B., Manning, S. W., Niu, M., Reimer, R. W., Richards, D. A., Scott, E. M., Southon, J. R., Staff, R. A., Turney, C. S. M., van der Plicht, 2013, *Radiocarbon*, 55, 1869. 80, 95
- Richardson, I. G. 2013, *Journal of Space Weather and Space Climate*, 3, A8 94
- Roth, R., Joos, F. 2013, *Climate of the Past*, 9, 1879. 11, 62, 79, 80, 95
- Roudier, Th., Malherbe, J.M., Vigneau, J. and Pfeiffer, B., 1998, *Astronomy and Astrophysics*, 330, 1133-1144.
- Ruddiman, W. F. 2007, W.F. W.H Freeman and Co., NY. 13, 17, 19
- Sahsamanoglou, H. S., Makrogiannis, T. I., Kallimopoulos, P. P. 1991, *International Journal of Climatology*, 11, 827. 110, 117
- Schatten, K. H., Hedin, A. E. 1984, *Geophysical Research Letters*, 11, 873. 91
- Scherrer, P. H., Wilcox, J. M., Svalgaard, L., et al. 1977, *Solar Physics*, 54, 353. 102
- Schwarz, G., 1978, *The Annals of Statistics*, 6, 461. 85
- Schulz, M. 2002, *Paleoceanography*, 17, 1014. 18
- Simoniello, R., Finsterle, W., García, R.A. et al. 2010, *Astronomy & Astrophysics*, 516, 30. 105
- Simoniello, R., Finsterle, W., Salabert, D., et al. 2012, *Astronomy and Astrophysics*, 539, A135. 94, 130
- Simoniello, R., Jain, K., Tripathy, S. C., et al. 2013, *The Astrophysical Journal*, 765, 100. 5, 6, 92, 94, 130
- Simoniello, R., Jain, K., Tripathy, S. C., et al. 2013, *Astronomical Society of the Pacific Conference Series*, 478, 167. 92, 130

- Singarayer, J. S., Richards, D. A., Ridgwell, A., et al. 2008, *Geophysical Research Letters*, 35, 14707. 35
- Singh, M., Singh, Y. P., Badruddin, , 2008, *Journal of Atmospheric and Solar-Terrestrial Physics*, 70, 169. 8, 46
- Snowball, I., & Muscheler, R. 2007, *The Holocene*, 17, 851.
- Solanki, S. K., Schüssler, M., Fligge, M. 2000, *Nature*, 408, 445. 4, 64, 126
- Solanki, S. K., Schüssler, M., Fligge, M. 2002, *Astronomy and Astrophysics*, 383, 706. 75
- Solanki, S. K., Usoskin, I. G., Kromer, B., Schüssler, M., Beer, J. 2004, *Nature*, 431, 1084. 6, 21, 26, 44, 62, 74, 75
- Soukharev, B. E., & Hood, L. L. 2006, *Journal of Geophysical Research (Atmospheres)*, 111, D20314. 15, 16
- Southon, J., Noronha, A. L., Cheng, H., Edwards, R. L., Wang, Y. 2012, *Quaternary Science Reviews*, 33, 32. 35
- Staff, R. A., Ramsey, C. B., Bryant, C. L., Brock, F., Payne, R. L., Schlolaut, G., Marshall, M. H., Brauer, A., Lamb, H. F., Tarasov, P., Yokoyama, Y., Haraguchi, T., Gotanda, K., Yonenobu, H., Nakagawa, T., Suigetsu 2006 Project Members, 2011, *Radiocarbon*, 53, 3, 511–528. 110
- Steinhilber, F., Abreu, J. A., Beer, J. 2008, *Astrophysics and Space Sciences Transactions*, 4, 1. 12, 64
- Steinhilber, F., Abreu, J. A., Beer, J., Brunner, I., Christl, M., Fischer, H., Heikkilä, U., Kubik, P. W., Mann, M., McCracken, K. G., Miller, H., Miyahara, H., Oerter, H., Wilhelms, F. 2012, *Proceedings of the National Academy of Sciences*, 109, 5967. 62
- Stuiver, M., Polach, H. A., 1977, *Radiocarbon*, 19(3), 355. 35
- Stuiver, M. 1980, *Nature*, 286, 868. 79
- Stuiver, M., Braziunas, T. F. 1989, *Nature*, 338, 405. 79
- Suess, H. E. 1955, *Science*, 122, 415. 80, 95
- Thomas, J. H., Weiss, N. O., Tobias, S. M., & Brummell, N. H. 2002, *Nature*, 420, 390. 105
- Thomas, B. C., Melott, A. L., Arkenberg, K. R., & Snyder, B. R. 2013, *Geophysical Research Letters*, 40, 1237. 40
- Thompson, D. W. J., Wallace, J. M. 1998, *Geophysical Research Letters*, 25, 1297. 17
- Tobias, S. M., Weiss, N. O., & Kirk, V. 1995, *Monthly Notices of Royal Astronomical Society*, 273, 1150. 104
- Tobias, S. M. 1996, *Astronomy and Astrophysics*, 307, L21. 78, 104
- Tobias, S. M. 1997, *Astronomy and Astrophysics*, 322, 1007. 92, 104

- Tobias, S. M. 1998, *Monthly Notices of the Royal Astronomical Society*, 296, 653. 86
- Usoskin, I. G. 2013, *Living Reviews in Solar Physics*, 10, 1. 8, 62, 78, 91, 94, 101, 110, 129
- Usoskin, I. G., Bobik, P., Gladysheva, O. G., Kananen, H., Kovaltsov, G. A., Kudela, K. 2001, *Advances in Space Research*, 27, 565. 44
- Usoskin, I. G., Mursula, K., & Kovaltsov, G. A. 2001, *Astronomy and Astrophysics*, 370, L31. 121, 129
- Usoskin, I. G., Gladysheva, O. G., Bobik, P., Kudela, K., Kananen, H. 1999, *Czech Journal of Physics*, 12, 49. 44
- Usoskin, I. G., Kananen, H., Mursula, K., Tanskanen, P., Kovaltsov, G. A. 1998, *Journal of Geophysical Research*, 103, 9567. 44, 47
- Usoskin, I. G., Solanki, S. K., Kovaltsov, G. A. 2007, *Astronomy and Astrophysics*, 471, 301. 6, 28, 62, 79, 84, 85, 86, 98
- Usoskin, I. G., Hulot, G., Gallet, Y., Roth, R., Licht, A., Joos, F., Kovaltsov, G. A., Thébault, E., Khokhlov, A. 2014, *Astronomy and Astrophysics*, 562, L10. 26, 62, 74, 75, 81, 91
- Usoskin, I. G., Alanko, K., Mursula, K., Kovaltsov, G. A. 2002b, *Solar Physics*, 207, 389. 64
- Usoskin, I. G., Mursula, K., & Kovaltsov, G. A. 2002b, *Geophysical Research Letters*, 29, 2183. 122
- Usoskin, I. G., Solanki, S. K., Schüssler, M., Mursula, K., Alanko, K. 2003, *Physical Review Letters*, 91, 211101. 6, 26, 62, 64, 74, 75
- Usoskin, I. G., Mursula, K., & Kovaltsov, G. A. 2003a, *Astronomy and Astrophysics*, 403, 743. 122
- Usoskin, I. G., Mursula, K., & Kovaltsov, G. A. 2003b, *Solar Physics*, 218, 295. 123, 124
- Usoskin, I. G., Mursula, K., Solanki, S. K., Schüssler, M., Kovaltsov, G. A. 2002a, *Journal of Geophysical Research*, 107, 1374. 24, 33, 63, 122
- Usoskin, I. G., Mursula, K., Arlt, R., Kovaltsov, G. A. 2009, *The Astrophysical Journal*, 700, L154. 67, 122
- Usoskin, I. G., Sokoloff, D., Moss, D. 2009, *Solar Physics*, 254, 345. 91, 104
- Usoskin, I. G., Mursula, K., Arlt, R., & Kovaltsov, G. A. 2009, *The Astrophysical Journal Letter*, 700, L154. 67, 122
- Usoskin, I. G., Mursula, K., Solanki, S., Schüssler, M., Alanko, K. 2004, *Astronomy and Astrophysics*, 413, 745. 24, 33, 63, 64, 122, 125, 126
- Usoskin, I. G., Voiculescu, M., Kovaltsov, G. A., Mursula, K. 2006, *Journal of Atmospheric and Solar-Terrestrial Physics*, 68, 2164. 71, 99
- Usoskin, I. G., Bazilevskaya, G. A., & Kovaltsov, G. A. 2011, *Journal of Geophysical Research (Space Physics)*, 116, 2104. 30, 100, 101

- Vaquero, J. M., Gallego, M. C., Usoskin, I. G., Kovaltsov, G. A. 2011, *The Astrophysical Journal Letters*, 731, L24. 74
- Van Allen, J. A. 2000, *Geophysical Research Letters*, 27, 2453. 45, 46
- van Meerbeeck, C. J., Renssen, H., Roche, D. M. 2009, *Climate of the Past*, 5, 33. 36, 37
- Vecchio, A., & Carbone, V. 2008, *The Astrophysical Journal*, 683, 536. 94
- Vecchio, A., Carbone, V. 2009, *Astronomy and Astrophysics*, 502, 981. 5
- Vinther, B. M., Clausen, H. B., Johnsen, S. J., Rasmussen, S. O., Andersen, K. K., Buchardt, S. L., Dahl-Jensen, D., Seierstad, I. K., Siggaard-Andersen, M.-L., Steffensen, J. P., Svensson, A. M., Olsen, J., Heinemeier, J. 2006, *Journal of Geophysical Research*, 111, 13102. 26, 66, 73
- Virkar, Y., Clauaset, A. 2012, arXiv:1208.3524 . 85
- Vonmoos, M., Beer, J., Muscheler, R. 2006, *Journal of Geophysical Research*, 111, 10105. 27, 62, 65, 66, 80, 81, 95
- Voss, H., Kurths, J., Schwarz, U. 1996, *Journal of Geophysical Research*, 101, 15637. 79
- Wang, Y.-M., Lean, J., Sheeley, N. R., Jr. 2002, *The Astrophysical Journal Letters*, 577, L53. 91
- Wang, Y.-M., Sheeley, N. R., Jr. 1991, *The Astrophysical Journal*, 375, 761. 4
- Wang, Y.-M. 2004, *Solar Physics*, 224, 21. 4
- Wang, Y.-M., & Colaninno, R. 2014, *The Astrophysical Journal Letters*, 784, L27. 94
- Wang, Y., Cheng, H., Edwards, R. L., He, Y., Kong, X., An, Z., Wu, J., Kelly, M. J., Dykoski, C. A., Li, X., 2005, *Science*, 308, 854. 17, 18
- Webber, W. R., Lockwood, J. A. 1988, *Geophysical Research Letters*, 93, 8735. 45
- Webber, W. R., Highbie, P. R., McCracken, K. G. 2007, *Journal of Geophysical Research*, 112, 10106. 63
- Weiss, N. O., Thomas, J. H., Brummell, N. H., & Tobias, S. M. 2004, *The Astrophysical Journal*, 600, 1073. 105
- Wheatland, M. S., Sturrock, P. A., McTiernan, J. M. 1998, *The Astrophysical Journal*, 509, 448. 28, 85, 96
- Wheatland, M. S. 2000, *The Astrophysical Journal Letters*, 536, L109. 28, 85
- Wheatland, M. S. 2003, *Solar Physics*, 214, 361. 28, 85
- Wild, M., Folini, D., Schär, C., et al. 2013, *Climate Dynamics*, 40, 3107. 14
- Wolff, E. W., Chappellaz, J., Blunier, T., Rasmussen, S. O., Svensson, A. 2010, *Quaternary Science Reviews*, 29, 2828. 19
- Yamagata, T., Sugihara, S., Morinaga, I., Matsuzaki, H., Nagai, H. 2010, *Nuclear Instruments and Methods in Physics Research B*, 268, 1135. 117

- Yiou, F., Raisbeck, G. M., Baumgartner, S., et al. 1997, *Journal of Geophysical Research*, 102, 26783. 111
- Zanis, P., Gerasopoulos, E., Priller, A., Schnabel, C., Stohl, A., Zerefos, C., Gäggeler, H. W., Tobler, L., Kubik, P. W., Kanter, H. J., Scheel, H. E., Luterbacher, J., Berger, M. 2003, *Journal of Geophysical Research*, 108 (D12), 8520. 117
- Zaqarashvili, T. V., Carbonell, M., Oliver, R., Ballester, J. L. 2010, *The Astrophysical Journal*, 709, 749. 5